Université de Toulouse

THÈSE

En vue de l'obtention du

DOCTORAT DE L'UNIVERSITÉ DE TOULOUSE

Délivré par :
Institut National des Sciences Appliquées de Toulouse (INSA Toulouse)

Discipline ou spécialité :

Matériaux, Technologies et Nano-Electronique

Présentée et soutenue par :
Steffen WIEDMANN

le : vendredi 1octobre 2010

Titre :

Nouvelles propriétés de transport dans les systèmes d'électrons multicouches
(Novel transport properties in multilayer electron systems)

JURY

G. Le LAY, Professeur, CINaM-CNRS, Marseille
M. DYAKONOV, Professeur, LPTA-CNRS, Montpellier (Rapporteur)
A. RAYMOND, Professeur, GES-CNRS, Montpellier (Rapporteur)
G. BREMOND, Professeur, INL-CNRS, INSA, Lyon
R. JALABERT, Professeur, IPCMS-DMONS, Strasbourg
J. C. PORTAL, Professeur, IUF-INSA Toulouse, CNRS LNCMI, Grenoble (Directeur)

Ecole doctorale :
Génie Electrique, Electronique et Télécommunications (GEET)

Unité de recherche :
LNCMI Grenoble, UPR 3228, CNRS-INSA-UJF-UPS

Directeur(s) de Thèse :

Jean-Claude PORTAL

Rapporteurs :

Michel DYAKONOV, André RAYMOND

Meiner Familie

Bourse de thèse GEET-INSA Toulouse (2007-2010)
[Bourse MENRT]

COFECUB-USP Uc Ph 109/08
EuroMagNET, EU contract n° 228043

Microwave facilities used from ANR MICONANO

Contents

La thèse en français - sommaire substantiel

Introduction générale

Les technologies de l'information et des dispositifs micro-électroniques sont principalement basées sur les semi-conducteurs. Ces technologies utilisent intensivement le transport de l'électricité par les électrons. Avant de pouvoir envisager de nouveaux dispositifs, il est nécessaire de connaître en détail les processus de transport des électrons en présence d'un champ magnétique ainsi que la réponse des électrons aux ondes électromagnétiques à haute fréquence.

Les systèmes électroniques multicouches bidimensionnels sont particulièrement intéressants, puisqu'ils possèdent un nouveau degré de liberté quantique grâce au couplage des électrons qui se trouvent dans différentes couches. Une variété de phénomènes intéressants apparaît, qui ne sont pas observés lorsque les électrons se propagent dans une seule couche. Grâce aux progrès de la croissance en épitaxie par jets moléculaires (MBE) des semi-conducteurs, la fabrication de multi-puits quantiques de haute qualité et très proches les uns des autres est devenue possible.

L'objectif de cette thèse est d'étudier pour la première fois l'influence du nouveau degré de liberté quantique, causé par le couplage tunnel entre les couches, sur les propriétés de transport des multi-puits quantiques dans un champ magnétique et sous irradiation micro-onde. En outre, ce travail présente la recherche de nouveaux états corrélés dans les champs magnétiques intenses dans ces systèmes.

Grâce à une proche et fructueuse collaboration avec Oleg Raichev, physicien théorique de l'Institut de Physique des semi-conducteurs à Kiev (NAS of Ukraine), au cours de ce projet, nous sommes capables d'analyser et de discuter les résultats expérimentaux obtenus en connexion avec la théorie.

Dans la première partie de ce sommaire substantiel, nous donnons un résumé des effets qui ont été observés lorsque nos systèmes sont irradiés par les micro-ondes à faible champ magnétique. La deuxième partie décrit les résultats obtenus dans un champ magnétique intense, nous montrons en particulier des études sur les nouveaux états corrélés dans les triples puits quantiques. Nous décrirons finalement brièvement les techniques expérimentales et l'extraction du champ électrique dans les expériences sous irradiation micro-onde.

Notons que ce sommaire substantiel présente et discute seulement les résultats les plus importants obtenus durant cette thèse. De plus, nous avons ajouté quelques images clés pour mieux décrire les observations. Ce sommaire ne remplace pas la thèse entière écrite en anglais.

Partie I

(Correspondant aux chapitres 1 à 5 du manuscrit complet)

Introduction

Il est bien connu qu'à bas champ magnétique (B <0.3 T) et sous irradiation micro-ondes, la résistance électrique d'un gaz-2D commence à osciller et peut même devenir nulle si la qualité de l'échantillon est suffisante (grande mobilité). Une résistance nulle (*en anglais:* zero-resistance state - ZRS) est un phénomène rare en physique de la matière condensée. Heike Kamerlingh Onnes fut le premier à observer une résistance nulle, quand il a découvert la supraconductivité dans le mercure en 1911. Presque 70 ans plus tard, Klaus von Klitzing a observé l'effet Hall quantique accompagnant la disparition de la résistance longitudinale dans les systèmes électroniques bidimensionnels [vonKlitzing80]. La réponse oscillatoire d'un gaz-2D à l'irradiation micro-onde a été découverte par Michael Zudov (Université de l'Utah) [Zudov01a]. Plus tard et grâce à l'amélioration continue de la qualité des échantillons, les états de résistance nulle ont été découverts par Ramesh Mani (travaillant à cette période au Max-Planck-Institut de Stuttgart) et ses collègues [Mani02] et indépendamment par Michael Zudov et Rui-Rui Du [Zudov03]. En outre, ces découvertes ont aussi attiré beaucoup d'intérêt théorique et plusieurs mécanismes microscopiques ont été présentés qui vont être décrits et utilisés dans cette thèse [Ryzhii70, Ryzhii86, Durst03, Dorozhkin03, Dmitriev05].

Dans cette première partie, nous présentons d'abord nos systèmes bidimensionnels (puits et doubles puits quantiques) et le transport électronique en présence d'un champ magnétique appliqué perpendiculairement au plan du gaz-2D. Nous avons aussi effectué des expériences dans des puits quantiques en présence d'un champ magnétique perpendiculaire et sous irradiation micro-ondes pour confirmer les magnéto-oscillations induites par les micro-ondes (oscillations MIRO, *en anglais*: microwave-induced resistance oscillations). De plus, nous montrons que dans quelques conditions particulières, on observe le phénomène des oscillations FMIRO (oscillations MIRO fractionnaires, *en anglais*: fractional microwave-induced resistance oscillations).

Ensuite, nous nous intéressons au transport électronique sous irradiation micro-onde dans les doubles et larges puits quantiques avec deux sous-bandes peuplées d'électrons. A bas champ magnétique et sous irradiation micro-onde, les propriétés de transport électronique dans un système avec deux sous-bandes peuplées peuvent être décrites par l'interférence des oscillations entre les sous-bandes et des oscillations induites par l'irradiation micro-ondes [Wiedmann08]. Dans les larges puits quantiques, grâce à la meilleure qualité du système, les oscillations induites par l'irradiation micro-onde évoluent jusqu'à des états de résistance nulle. Ces études nous permettent d'identifier les mécanismes microscopiques proposés par la théorie et d'effectuer des expériences pour connaître l'origine de ces phénomènes en changeant les paramètres fréquence, puissance micro-onde (champ électrique) et température.

Finalement, nous développons une théorie générale pour les oscillations entre les sous-bandes et les oscillations induites par l'irradiation micro-onde. Cette théorie va être appliquée dans les systèmes de triples puits quantiques.

Magnétotransport dans les systèmes du gaz-2D - puits et doubles puits quantiques

(Correspondant au chapitre 1 du manuscrit complet)

Les échantillons étudiés dans cette thèse sont des puits quantiques semi-conducteurs dont le point commun est le piégeage des électrons, qui s'effectue dans l'arséniure de gallium (GaAs). GaAs est un semi-conducteur modèle intensivement étudié principalement en raison de la grande pureté qu'il est possible d'obtenir dans un tel matériau. La pureté de ces matériaux garantit un désordre suffisamment faible, ce qui permet d'avoir accès aux propriétés électroniques fondamentales. On parle d'un gaz électronique bidimensionnel (gaz-2D) pour désigner un ensemble d'électrons confinés selon une direction de l'espace, mais dont la liberté est préservée dans un plan perpendiculaire à l'axe de confinement. Une possibilité pour réaliser un gaz-2D par épitaxie de jets moléculaires est de créer un puits quantique AlGaAs/GaAs/AlGaAs. L'aluminium est utilisé pour former le composé ternaire AlGaAs.

Les électrons qui constituent le gaz-2D ne peuvent se déplacer que selon le plan x-y. Les électrons sont confinés dans la direction de l'axe de croissance z et sont libre dans leur mouvement dans le plan x-y. Ce confinement spatial entraîne l'apparition de sous-bandes d'énergie avec une densité d'états (DOS) constante. L'état fondamental d'un système est défini comme un système à l'équilibre constitué de N électrons à T=0 K. Lorsque cet équilibre est rompu, certains états d'énergie, vides à l'origine, se peuplent. On peut calculer la densité n_s d'électrons en utilisant la densité d'état et la distribution de Fermi-Dirac.

L'application d'un champ magnétique change profondément les propriétés des systèmes d'électrons bidimensionnels. Lorsqu'un champ magnétique B est appliqué au système, la densité d'état se transforme dans une séquence de pics séparés par l'énergie $\hbar\omega_c$ où $\omega_c = eB/m^*$ est la fréquence cyclotron avec m^* la masse effective des électrons et e la charge de l'électron. Les niveaux d'énergie dans un champ magnétique sont appelés niveaux de Landau. Notez bien que le couplage du spin et du champ magnétique se traduit par un terme supplémentaire, l'énergie Zeeman $\Delta_z = g^*\mu_B B$, avec g^* le facteur de Landé effectif (g^*=-0.44 pour "bulk GaAs") et μ_B le magnéton de Bohr.

Le premier modèle du transport électrique fut le Modèle de Drude [Drude00]. Il présente les porteurs de charge comme se déplaçant, à l'équilibre, librement entre des collisions sur des impuretés. Pour des problèmes plus complexes, on applique l'équation de Boltzmann. Si un champ magnétique B est appliqué perpendiculairement au système bidimensionnel, les électrons sont soumis à la force de Lorentz. Si le champ magnétique varie d'une façon

continue, l'espacement entre les niveaux de Landau augmente. Le niveau de Fermi croise donc successivement les différents niveaux de Landau en fonction de la valeur du champ magnétique. La résistance longitudinale R_{xx} de l'échantillon, qui est proportionnelle à la densité d'états au niveau de Fermi, présente donc des oscillations qui suivent une périodicité de $1/B$. C'est l'effet Shubnikov-de Haas [SdH30].

Donc, dans les études de magnéto-transport, on observe dans la résistance longitudinale les oscillations Shubnikov-de Haas (SdH) à bas champ magnétique qui permettent d'avoir un accès direct au temps de vie quantique (*en anglais*: quantum lifetime) et qui sont très sensibles à la température [cf. équation (0.1)]. Si on augmente le champ magnétique, le gap cyclotron devient assez grand et par conséquent, on observe une résistance longitudinale qui devient nulle et en même temps un plateau dans la résistance de Hall si le niveau de Fermi se trouve dans le gap. Donc, la résistance de Hall reste constante. La valeur de la résistance de Hall R_{xy} est quantifiée et donnée par $h/\nu e^2$, où ν, le facteur de remplissage est un entier supérieur ou égal à 1. C'est l'effet Hall quantique entier mis en évidence par von Klitzing sur des Si-MOSFETs [vonKlitzing80]. A la suite de la découverte de l'effet Hall quantique entier, Tsui et al. observent en explorant le domaine des champs magnétiques intenses une quantification de la résistance de Hall R_{xy} d'un gaz-2D pour des facteurs de remplissage non-entiers du système [Tsui82]: c'est l'effet Hall quantique fractionnaire qui va être traité dans la deuxième partie de ce sommaire substantiel.

Dans un double puits quantique, les puits sont très proches et séparés par une barrière d'AlGaAs. Si la barrière est suffisamment mince, les deux puits sont couplés par l'effet tunnel. Ces systèmes peuvent être vus comme deux couches électroniques de deux dimensions couplées par cet effet tunnel (cf. insert sur la figure 0.2). Celui-ci modifie la magnétorésistance et de nouvelles oscillations entre les sous-bandes (oscillations MIS, en anglais : magneto-intersubband oscillations) apparaissent (cf. insert sur la figure 2 à 1.4 K) [Mamani08]. Celles-ci sont la conséquence du passage des niveaux de Landau à l'énergie de Fermi si on augmente le champ magnétique perpendiculaire. La périodicité est décrite avec la séparation Δ qui est l'énergie entre les deux niveaux quantiques symétrique (S) et asymétrique (AS): $\Delta = E_{AS} - E_S$. Ces oscillations MIS survivent à haute température et nous nous permettrons d'extraire le temps de vie quantique où les oscillations SdH sont déjà absentes. Pour obtenir le couplage maximal, nous utilisons dans ce mémoire une barrière mince de d_b =1.4 nm.

Notez bien que dans un large puits quantique de haute densité, en raison de la redistribution des électrons, on obtient deux puits à l'interface séparés par une barrière de potentiel électrostatique. Par conséquent, deux sous-bandes apparaissent dans les larges puits quantiques avec une barrière mince due à la pénétration des ondes d'électrons. La qualité du gaz-2D est meilleure.

Gaz-2 D sous irradiation micro-onde - puits quantiques

(Correspondant au chapitre 2 du manuscrit complet)

De nouvelles oscillations dans la résistance longitudinale R_{xx} d'un gaz d'électron bidimensionnel dans les échantillons de haute mobilité sont induites par l'irradiation micro-onde avec de fréquence ω sous champ magnétique perpendiculaire (oscillations MIRO). Ces oscillations apparaissent en dessous de la gamme du champ magnétique des oscillations SdH et ont une période déterminée par le rapport ω/ω_c [Zudov01a]. Si on augmente soit l'intensité de l'irradiation soit la mobilité des porteurs, la résistance devient nulle (*en anglais*: zero-resistance state [Mani02, Zudov03, Willett04]). Ce phénomène dû aux propriétés de magnéto-transport fait actuellement l'objet d'un très intense effort dans la recherche scientifique. Plusieurs modèles théoriques ont été proposés. Dans ce mémoire, nous présentons deux modèles largement discutés dans la littérature et appliqués plus tard dans les multi-puits quantiques. Les micro-ondes influencent fortement les collisions entre les électrons et les impuretés (mécanisme de déplacement, *en anglais*: displacement mechanism), proposé par Victor Ryzhii [Ryzhii70, Ryzhii86, Durst03]. En outre, les micro-ondes modifient la distribution en énergie des électrons (*en anglais*: inelastic mechanism), discuté par Sergey Dorozhkin [Dorozhkin03] et développé par Ivan Dmitriev et ses collègues [Dmitriev05], et basé sur l'équation quantique de Boltzmann. Le mécanisme de déplacement prend en compte celui des électrons si on applique un champ dc avec une absorption des micro-ondes. Le mécanisme repose sur le fait qu'un gaz-2D sous champ magnétique et irradié par une onde électromagnétique d'énergie $\hbar\omega$, entraîne la création d'un courant dû aux collisions entre les électrons photo-excités et les impuretés. L'énergie du photon est absorbée par l'électron qui subit une transition directe et de même énergie dans la bande de conduction jusqu'à un état libre au dessus du niveau de Fermi. Ce mécanisme décrit la période pour les oscillations MIRO et conduit à une conductivité localement négative. Le modèle du "mécanisme inélastique" développé par I. A. Dmitriev [Dmitriev05] part du principe que les magnéto-oscillations observées sur la conductivité d'un gaz-2D seraient dues à une modulation de la fonction de distribution électronique. En effet, le comportement oscillatoire à bas champ magnétique de la densité d'état ajouté à la modulation de la fonction de distribution serait l'explication des oscillations observées sur la photoconductivité dc. La périodicité ainsi que la phase des oscillations sont similaires et respectent le comportement expérimental observé, ce qui confirme la validité en première approximation de ce modèle. De plus, ce modèle est fortement dépendant de la température et du temps de relaxation inélastique $\tau_{in} \propto T^{-2}$. Notez bien que les effets électrodynamiques sont aussi reliés à des phénomènes observés, par exemple, l'absorption des micro-ondes par le gaz-2D [Studenikin05].

Dans le cadre de cette thèse, notre analyse expérimentale est basée sur des études de systèmes 2D de haute densité électronique et de mobilité modérée en changeant plusieurs paramètres comme la puissance micro-onde (champ électrique), la fréquence et la température. Dans la figure 0.1(a) nous présentons les oscillations induites par les micro-

ondes pour une fréquence de 140 GHz (atténuation 0 dB) et en même temps, les oscillations SdH à 1.4 K. La résistance ne change pas si $\omega = n \cdot \omega_c$ (n=1, 2, ...). Pour cet échantillon, on observe trois oscillations MIRO.

Dans les expériences, il est important de prendre en compte le chauffage des électrons due à l'irradiation micro-onde, ce qui est reflété dans la température électronique T_e. Cet effet est visible dans la diminution de l'amplitude des oscillations SdH [cf. figure 0.1(a)].

En augmentant l'intensité des micro-ondes (le champ électrique), on peut observer les oscillations MIRO qui sont reliés à un rapport fractionnaire avec la condition $\epsilon = \omega/\omega_c = n/m$, n, m sont des nombres entiers. Deux mécanismes théoriques ont été proposés [Dmitriev07b, Pechenezhskii07]. A ce jour, seuls quelques résultats expérimentaux ont été annoncés sur les oscillations FMIRO par d'autres groupes que le nôtre et le travail expérimental (jusqu'à ϵ=1/4) et la théorie ne sont pas capables de décrire tous les phénomènes observés. Les figures 0.1(b) et (c) désignent les oscillations FMIRO pour deux fréquences et leur dépendance en fonction de la température à une fréquence fixe de 75 GHz et de 66 GHz. Nous avons observé plusieurs oscillations FMIRO d'ordre haut (jusqu'à ϵ=1/8) [Wiedmann09a]. Si on analyse les figures 0.1(b) et (c), on constate qu'une température plus élevée est plus favorable pour l'apparition de ce phénomène. Les oscillations FMIRO sont plus prononcées à T=6.5 K.

Parmi les deux mécanismes théoriques possibles, l'absorption simultanée de plus que deux photons est constatée comme un événement rare [Dmitriev07b]. Donc, l'explication la plus plausible est l'absorption graduelle de photons [Pechenezhskii07]. Mais, ce mécanisme n'explique pas l'observation des oscillations FMIRO de haut ordre, par exemple n/m=1/8, à cause des restrictions de conservation d'énergie, quand l'espace entre les niveaux de Landau excède l'énergie des photons. De plus, il faut constater que l'amplitude des oscillations FMIRO diminue radicalement pour des hautes fréquences (micro-ondes). On pourrait croire que les oscillations FMIRO précèdent les oscillations MIRO mais celles-ci restent visibles à de plus hautes fréquences [Smet05, Mani08].

Pour conclure, nous avons confirmé l'observation d'oscillations MIRO très prononcées dans nos échantillons. Nous avons trouvé que des conditions particulières, notamment haute température et puissance élevée, favorisent l'apparition des oscillations FMIRO [Wiedmann09a].
Quelques oscillations qui sont attribuées aux oscillations FMIRO, par exemple n/m=2/5 qui montre une dépendance étrange en augmentant la puissance, peuvent être expliquées avec une interférence entre les oscillations MIRO fractionnaire et les oscillations des phonons (*en anglais*: phonon induced resistance oscillations [Zudov01b]).
Même en prenant en compte ce phénomène d'interférence, il n'est pas possible d'expliquer l'apparition des oscillations FMIRO de haut ordre.

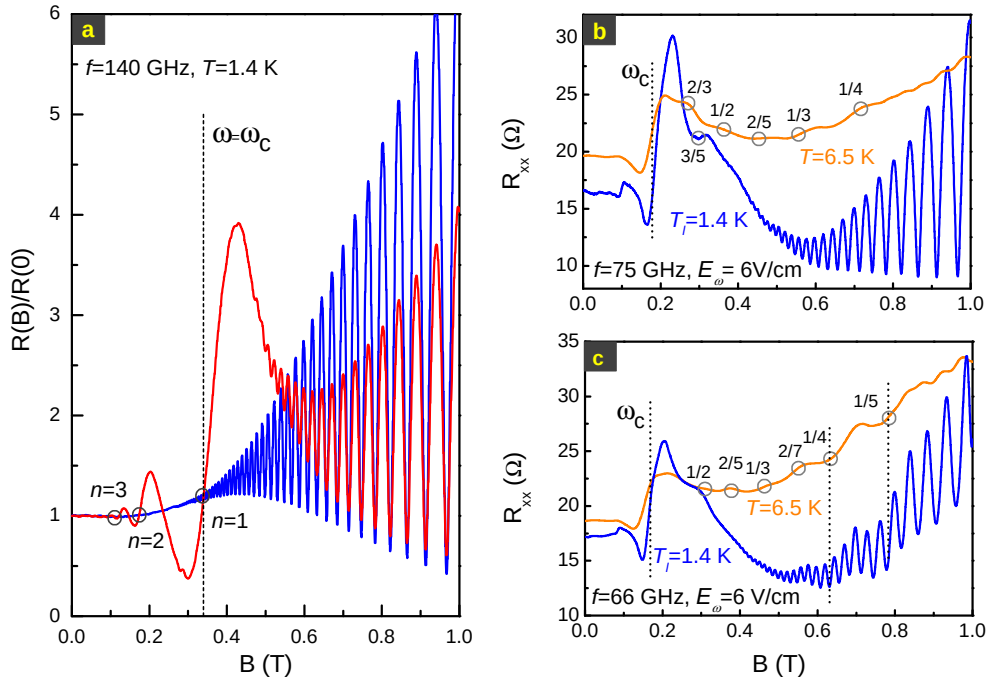

Figure 0.1: (a) Résistance longitudinale d'un échantillon exposé à une irradiation micro-ondes (rouge) à 140 GHz (0 dB) et sans irradiation micro-ondes (bleu). Les oscillations MIRO apparaissent à faible champ magnétique lorsque les oscillations SdH sont absentes. (b) Oscillations FMIRO pour 75 GHz à une température de 1.4 et 6.5 K, et (c) pour 66 GHz exposé par le même champ électrique et pour la même température.

Double puits quantiques sous irradiation micro-ondes

(Correspondant au chapitre 3 du manuscrit complet)

Cette section présente pour la première fois les propriétés de magnéto-transport d'un système avec deux sous-bandes peuplées par des électrons, réalisé dans les doubles puits quantiques et exposée à une irradiation micro-onde. Nous avons déjà montré que dans un tel système, des oscillations entre les sous-bandes (oscillations MIS) apparaissent en raison d'un alignement des niveaux de Landau de deux puits au niveau de Fermi en augmentant le champ magnétique perpendiculaire [Mamani08]. Les doubles puits quantiques sont séparés par une barrière étroite et les deux sous-bandes sont couplées par l'effet tunnel (cf. insert sur la figure 0.2). Pour avoir le couplage maximal, nous utilisons pour les expériences sous irradiation micro-ondes une barrière avec une épaisseur de d_b=1.4 nm (Δ=3.67 meV).

Sans irradiation micro-onde, la magnétorésistance d'un double puits quantique montre les oscillations MIS qui commencent à B=0.1 T et qui se superposent avec des oscillations SdH à basse température (insert sur la figure 0.2). Sous irradiation micro-ondes, de nou-

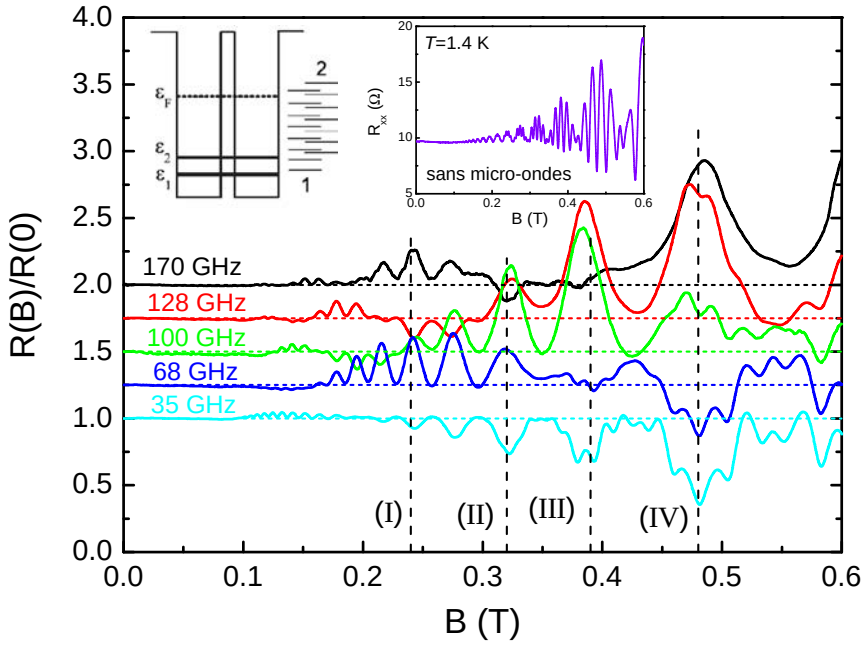

Figure 0.2: Magnétorésistance d'un double puits quantique sous irradiation micro-onde pour différentes fréquences, 35 à 170 GHz (les courbes sont décalées vers le haut pour plus de clarté, sauf celle correspondant à 35 GHz). La température est 1.4 K et le champ électrique 2.5 V/cm. Les inserts montrent un double puits quantique, séparé par une barrière avec les deux paliers des niveaux de Landau en champ magnétique perpendiculaire. Deux sous-bandes avec l'énergie ε_1 et ε_2 sont peuplées. De plus, la magnétorésistance à 1.4 K est également représentée sur l'insert (sans irradiation micro-onde).

veaux effets sont observés: la suppression et/ou l'inversion des oscillations MIS ou même quelques groupes d'oscillations MIS dont l'amplitude est continuellement augmentée par l'irradiation. La figure 0.2 montre le comportement des oscillations MIS sous irradiation micro-onde pour différentes fréquences. Si l'on regarde par exemple l'oscillation (IV), on peut voir une augmentation pour 170 GHz mais si on diminue la fréquence, cette oscillation est inversée. Le même effet peut être observé pour d'autres oscillations MIS. A 35 GHz, seule l'amplitude du groupe des oscillations MIS à B=0.1 T est augmentée alors que toutes les autres oscillations MIS ont changé de signe. L'irradiation micro-onde diminue aussi les oscillations SdH en raison du chauffage par les micro-ondes.

Grâce aux mesures effectuées à différentes fréquences, nous avons confirmé que les oscillations MIS sont fortement corrélées avec la fréquence micro-onde (périodicité en ω/ω_c). Cela nous permet d'attribuer l'effet observé à un phénomène MIRO. L'explication théorique de ces résultats est basée sur le modèle de Dmitriev [Dmitriev05] (mécanisme inélastique), généralisé au cas de deux sous-bandes et amélioré par la considération des effets électrodynamiques dans l'absorption d'un système bidimensionnel [Studenikin07]. Ce modèle théorique a été formulé par Oleg Raichev. Ici, en bref, nous présentons le

modèle du résultat théorique sur la résistivité dc pour un système avec deux sous-bandes peuplé par des électrons [Wiedmann08]. La résistivité dc s'écrit:

$$\frac{\rho_d}{\rho_0} = 1 - 2d\mathcal{T}\sum_{j=1,2}\cos\frac{2\pi(\varepsilon_F-\varepsilon_j)}{\hbar\omega_c} + d^2(1-A_\omega)\left[1+\cos\frac{2\pi\Delta}{\hbar\omega_c}\right], \tag{0.1}$$

$$\mathcal{T} = \frac{X}{\sinh X}, \quad X = \frac{2\pi^2 T_e}{\hbar\omega_c}, \quad A_\omega \simeq \frac{\mathcal{P}_\omega(2\pi\omega/\omega_c)\sin(2\pi\omega/\omega_c)}{1+\mathcal{P}_\omega\sin^2(\pi\omega/\omega_c)},$$

où $\rho_0 = m^*/e^2 n_s \tau_{tr}$ est la résistivité à champ nul et $\Delta = \varepsilon_2 - \varepsilon_1$ est la séparation des sous-bandes. Le deuxième terme, proportionnel au facteur de Dingle, $d = \exp(-\pi/\omega_c\tau)$ et au facteur d'atténuation de la température $\mathcal{T}$ décrit les oscillations SdH. Le troisième terme, quadratique en d, décrit les oscillations MIS et leur modification à cause de l'irradiation. Le facteur $\mathcal{P}_\omega$ [Dmitriev05] est proportionnel au carré du champ électrique E_ω^2 et au rapport de τ_{in} (temps de relaxation inélastique) et au temps de transport τ_{tr}. Bien sûr, il faut tenir compte du chauffage d'électrons par le champ électrique et de la dépendance en température des temps caractéristiques τ_{in}, τ_{tr} et τ_q. Ce modèle du mécanisme inélastique décrit complètement nos résultats obtenus dans cette gamme de température (cf. figure 0.3).

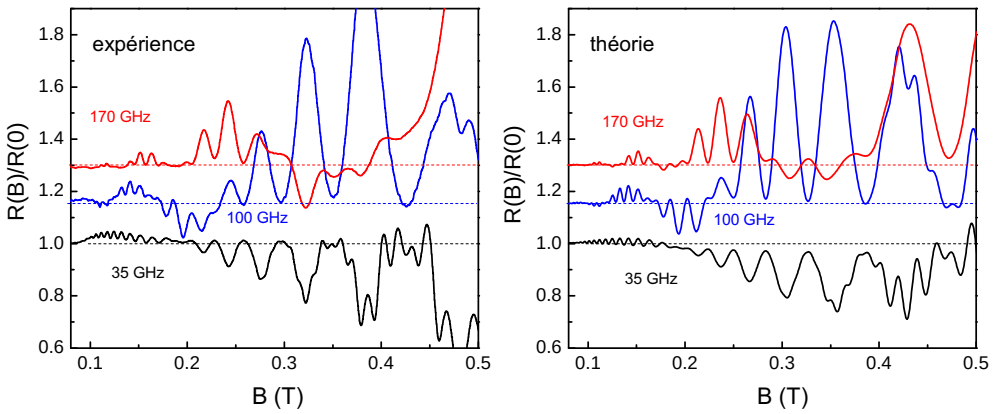

Figure 0.3: Magnétorésistance expérimentale et calculée d'un double puits quantique sous irradiation micro-onde pour différentes fréquences : 35, 100 et 170 GHz à 1.4 K. La théorie est en accord avec l'expérience.

Grâce à ce modèle [équation (0.1)], nous sommes capables aussi d'extraire le champ électrique des micro-ondes dans l'expérience et d'étudier le temps de relaxation inélastique τ_{in}. L'intensité de l'irradiation (champ électrique) est aussi estimée en comparant les amplitudes des oscillations SdH (oscillations de la magnétorésistance) avec un champ dc.

En augmentant la température lorsque l'échantillon est exposé à un champ électrique (pas trop élevé) et une fréquence fixe, nous avons trouvé une déviation du mécanisme inélastique qui ne décrit plus les observations pour T >4 K [Wiedmann10a]. Les auteurs

d'une étude similaire, faite dans un puits quantique simple [Hatke09a] ont trouvé que le mécanisme de déplacement ne peut pas être négligé pour les températures supérieures à 2 K. Bien que la magnétorésistance soit plus compliquée dans un système à deux sous-bandes qu'un système avec une seule sous-bande peuplée, nous avons certains avantages dans l'analyse des effets micro-ondes. En effet, la composante quantique de la magnétorésistance, qui est "visualisée" par les micro-ondes dans les doubles puits quantiques, a une période généralement plus petite que la période des oscillations MIRO. Nous commençons avec de basses températures et l'échantillon est irradié par une fréquence fixe et un champ électrique faible. Ces conditions permettent d'analyser les résultats avec le mécanisme inélastique qui explique nos résultats précédents [Wiedmann08]. Pour une température supérieure à 4 K, la contribution du mécanisme inélastique seul ne peut pas expliquer la magnétorésistance sous irradiation micro-ondes. Nous prenons cela en compte en remplaçant le temps inélastique par le temps τ_{in}^{*} comprenant les contributions du mécanisme inélastique et celle du mécanisme de déplacement. Le calcul théorique montre que le mécanisme du déplacement seul n'est pas capable d'expliquer les expériences, mais il ajoute une certaine contribution [Wiedmann10a].

De plus, nous avons démontré que sous certaines conditions, notamment aux températures élevées et une exposition à un fort champ électrique, une interférence existe entre les oscillations FMIRO et les oscillations MIS.

Pour conclure, nous avons étudié la réponse d'un gaz-2D à l'irradiation micro-ondes. Le mécanisme responsable pour des oscillations induites à basses températures est le mécanisme inélastique. La présence du produit des facteurs oscillants $\cos(2\pi\Delta/\hbar\omega_c)$ et $\sin(2\pi\omega/\omega_c)$, cf. équation (0.1), qui correspond respectivement aux oscillations MIS et à la partie micro-ondes peut être interprétée comme une interférence des oscillations MIS avec les oscillations MIRO.

Etats de résistance nulle sous irradiation micro-ondes - larges puits quantiques

(Correspondant au chapitre 4 du manuscrit complet)

Cette partie décrit la découverte et l'analyse des états de résistance nulle observés dans un système avec deux sous-bandes peuplées, réalisé dans un large puits quantique. L'avantage de ce système par rapport aux doubles puits quantiques est une plus grande qualité (mobilité des électrons). Les états de résistance nulle (*en anglais*: zero-resistance states - ZRS) apparaissent si un gaz-2D de haute qualité est exposé à une irradiation micro-ondes. Jusqu'à présent, les expériences de ZRS ont été menées seulement dans les systèmes à haute mobilité (puits quantiques simples ou hétérojonctions) avec une seule sous-bande peuplée. Les études incluent l'effet de la température, de la puissance et de la fréquence micro-onde, et toutes les expériences et travaux théoriques se concentrent sur ces systèmes.

Il est absolument nécessaire que les matériaux aient une pureté (haute mobilité des électrons) suffisante et que la puissance des micro-ondes permette d'obtenir une résistance nulle induite par irradiation micro-ondes. Malgré la pureté des doubles puits quantiques, on observe seulement une interférence entre les oscillations MIS et MIRO [Wiedmann08]. Par contre, dans les larges puits quantiques avec une barrière mince dû à la pénétration des ondes d'électrons, la qualité du gaz-2D est meilleure et nous observons les ZRS même en présence d'un mécanisme de collisions supplémentaires entre les sous-bandes qui donne lieu aux oscillations MIS.
Si la densité des électrons dans un large puits quantique (w=45 nm) est importante (n_s=9.1 · 10^{11} cm^2 dans nos échantillons), deux sous-bandes sont peuplées. Les fonctions d'onde symétrique (S) et asymétriques (AS) sont tracées dans l'insert de la figure 4. Nous confirmons cette configuration dans la figure 0.4 puisque l'on peut voir les oscillations MIS sans excitations micro-ondes ("sans m-o").

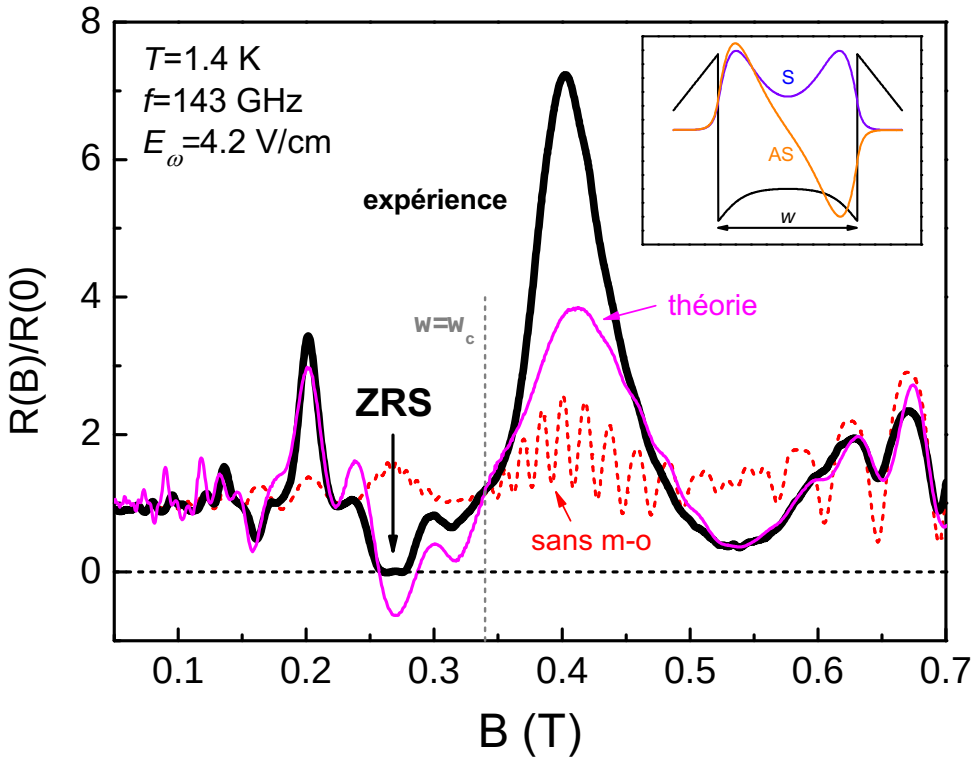

Figure 0.4: Magnétorésistance en l'absence d'irradiation micro-onde (rouge). Résistance nulle induite par des micro-ondes de fréquence 143 GHz à 1.4 K; en noir la courbe expérimentale, en rose la théorie (courbe rouge, hachurée: magnétorésistance sans irradiation micro-ondes). Le champ électrique est extrait de l'équation (0.1). L'insert montre les fonctions d'ondes des électrons, symétrique (S) et asymétrique (AS).

Sous irradiation micro-onde, on peut voir que l'état de résistance nulle correspond au maximum d'une oscillation MIS sans irradiation. Ceci est illustré par la figure 0.4 pour

B=0.27 T. Pour cette fréquence, cette oscillation MIS particulière est inversée et elle devient nulle pour un certain champ électrique. Nous avons observé que pour différentes fréquences, d'autres oscillations MIS sont inversées et montrent des ZRS, au total quatre oscillations MIS entre 68.5 et 155 GHz.

Pour l'analyse théorique, nous appliquons notre modèle pour deux sous-bandes peuplées [équation (0.1)]. Notez bien que, nos observations permettent de résoudre la question concernant le mécanisme quantique responsable de ces observations parmi les modèles qui ont été proposés [Ryzhii70, Durst03, Vavilov04a, Dmitriev05], est en particulier l'apparition des "domaines de courant" (*en anglais*: current domains) [Andreev03]. Pour cette basse température (T <4 K) et pour un champ électrique pas trop élevé, nous sommes capables d'expliquer nos résultats avec le mécanisme inélastique. Le mécanisme de déplacement devient important pour un champ électrique plus élevée. Un champ électrique de 4.2 V/cm est obtenu pour l'expérience montrée dans la figure 0.4. Une série d'expériences révèle des propriétés des ZRS pour différents champs électriques et températures [Wiedmann10b].

Les ZRS dans un système avec deux sous-bandes peuplées est distinct des systèmes monocouches et les états de résistance nulle sont développés pour les oscillations MIS qui sont inversées par l'irradiation micro-onde. Les intervalles de résistance nulle sont étroits et très sensibles à la fréquence micro-onde. Les résultats expérimentaux sont comparés à la théorie et nous avons constaté que dans des conditions où la résistivité est négative, nos calculs basés sur le mécanisme inélastique de la photorésistance sont en corrélation avec l'apparition de ZRS. Il s'agit de la première comparaison quantitative de l'expérience avec la théorie. Les ZRS observés peuvent être décrits par une conséquence de la formation des domaines de courant [Andreev03]. Une preuve de l'existence de domaines de courant dans un échantillon qui présente des ZRS est une condition nécessaire à une compréhension complète de ce phénomène.

Pour résumer, ce résultat décrit la première étape d'une généralisation des ZRS pour les systèmes au-delà du cas d'une seule sous-bande peuplée et rend possibles des études expérimentales et théoriques de ZRS à trois dimensions puisque nous avons montré qu'une diffusion additionnelle, notamment responsable de l'apparition des oscillations MIS, n'est pas un obstacle à l'observation des ZRS [Wiedmann10b].

Oscillations dans les systèmes de multi-puits quantiques

(Correspondant au chapitre 5 du manuscrit complet)

L'objet de cette étude est de généraliser les théories du magnéto-transport et de la magnétorésistance sous irradiation micro-ondes, formulées par Oleg Raichev. Pour vérifier le modèle théorique, nous présentons des études dans des puits quantiques triples en présence d'un champ magnétique perpendiculaire et sous irradiation micro-ondes. Les résultats sont récapitulés dans la figure 0.5.

Les oscillations MIS se produisent en raison de la modulation périodique de la probabil-

ité des transitions d'électrons entre les sous-bandes si on augmente le champ magnétique perpendiculaire quand différents niveaux de Landau de deux sous-bandes sont consécutivement alignés au niveau de Fermi. L'expression de la magnétorésistance pour un système de multi-puits quantiques est :

$$\rho_d = \rho_d^{(0)} + \rho_d^{(1)} + \rho_d^{(2)}, \tag{0.2}$$

où $\rho_d^{(0)}$ est la résistivité classique (résistivité de Drude), $\rho_d^{(1)}$ est la contribution du premier ordre décrivant les oscillations SdH et $\rho_d^{(2)}$ est la contribution du deuxième ordre contenant les oscillations MIS [Wiedmann09b]. Maintenant, nous considérons trois sous-bandes avec les énergies ε_j ($j = 1, 2, 3$), cf. figure 0.5(a). Les triples puits constituent un système symétrique qui se compose de trois puits quantiques couplés par effet tunnel. Le puits quantique central a une largeur de 23 nm et les puits latéraux font 10 nm de large. Ces puits sont séparés par des barrières d'épaisseur d_b= 1.4 nm ou d_b= 2.0 nm. Les trois couches sont connectées par les mêmes contacts ohmiques. Afin d'augmenter la mobilité, nous avons produit des échantillons de haute densité électronique. Les oscillations MIS pour un triple puits quantique sont illustrées dans la figure 0.5(b) pour des barrières de 1.4 nm. Pour T <3.2 K, les oscillations MIS sont superposées aux oscillations SdH.
Si un triple puits quantique est exposé à une irradiation micro-onde, cette irradiation provoque aussi une suppression et/ou une inversion des oscillations MIS.
Apres avoir appliqué avec succès le mécanisme inélastique aux systèmes à deux sous-bandes peuplées Wiedmann08, nous généralisons ce modèle et nous l'utilisons au cas des puits quantiques triples. Le modèle pour un nombre de sous-bandes arbitraires se trouve dans la référence [Wiedmann09b]. Les densités partielles dans les sous-bandes sont n_j et la densité totale est donc $n_s = n_1 + n_2 + n_3$. Dans le régime classique et dans un fort champ magnétique, nous utilisons une approche simple avec des densités égales dans chaque puits ($n_1 = n_2 = n_3 = n_s/3$) et nous supposons que $\nu_{jj'}^{tr}$ (*en anglais*: scattering rates) et les facteurs de Dingle $d_j = e^{-\alpha_j}$ ($\alpha_j = \pi\nu_j/\omega_c$) sont égaux ($d_j = d$). En négligeant les oscillations SdH, on peut écrire:

$$\begin{aligned}\frac{\rho_d^{MW}(B)}{\rho_d(0)} \simeq 1 + \frac{2}{3}(1 - A_\omega)d^2 \Bigg[1 + \frac{2}{3}\cos\left(\frac{2\pi\Delta_{12}}{\hbar\omega_c}\right) \\ + \frac{2}{3}\cos\left(\frac{2\pi\Delta_{13}}{\hbar\omega_c}\right) + \frac{2}{3}\cos\left(\frac{2\pi\Delta_{23}}{\hbar\omega_c}\right)\Bigg],\end{aligned} \tag{0.3}$$

Cette équation décrit la contribution des oscillations MIS avec les gaps d'énergie Δ_{12}, Δ_{13} et Δ_{23} en incluant la modification par l'irradiation micro-onde donnée par le facteur A_ω, cf. équation (0.1). La magnétorésistance sans irradiation peut être calculée avec A_ω=0. La comparaison entre l'expérience et la théorie est montrée dans les figures 0.5(c) et (d) à 1.4 K et à différentes fréquences. Le champ électrique varie autour de 3 V/cm. La théorie est en accord avec l'expérience [Wiedmann09b].
Pour conclure, nous avons étudié les oscillations MIS et leur interférence avec les oscillations MIRO dans les systèmes de triple puits quantiques de haute densité électronique.

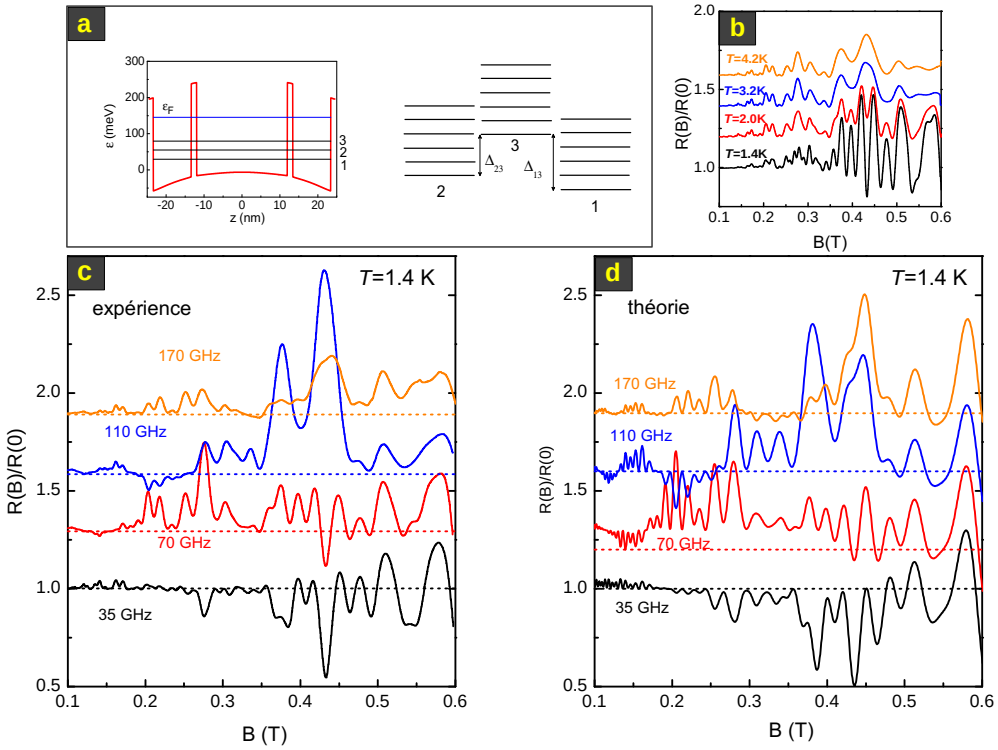

Figure 0.5: Schémas d'un triple puits quantique avec trois sous-bandes peuplées et niveaux de Landau dans un champ magnétique perpendiculaire. (b) Evolution des oscillations MIS avec la température. Triple puits quantique sous irradiation micro-ondes: (c) courbes expérimentales et (d) théoriques (les courbes sont décalées vers le haut pour plus de clarté, sauf celle correspondant à 35 GHz).

Les oscillations dépendent fortement de la fréquence et peuvent être décrites par le mécanisme inélastique à basses températures. Notre théorie peut être appliquée aux études expérimentales avec un nombre arbitraire de sous-bandes.

Partie II

(Correspondant au chapitre 6 du manuscrit complet)

Introduction

Un système Hall quantique multi-composants, composé de multiples puits quantiques séparés par des barrières minces, permet l'observation d'une variété de phénomènes intéressants qui ne sont pas observés si une seule sous-bande est peuplée [QH-effects97]. Si les puits quantiques sont proches, l'interaction électron-électron crée de nouveaux états corrélés dans un champ magnétique intense. De telles études ont été lancées il y a 20 ans dans les doubles puits quantiques avec un intérêt particulier concernant l'état du

facteur de remplissage total ν=1 [Eisenstein92a, Murphy93]. En outre, le champ magnétique parallèle a une influence particulière sur les phénomènes de transport dans un système de multi-puits quantiques, ceci a pu être montré dans les doubles puits quantiques [Eisenstein92a, Murphy93, Eisenstein95, Giudici08]. Un thème récurrent dans les études des effets Hall quantiques entier et fractionnaire est la recherche des nouveaux états quantiques qui existent dans les systèmes multicouches et qui n'apparaissent pas dans les systèmes contenant une seule couche mais deux sous-bandes peuplées. Il y a déjà de nombreuses études sur des systèmes bicouches mais très peu de résultats (expérimentaux et théoriques) sur les puits quantiques triples. En fait, la théorie propose une variété très riche de nouveaux états incompressibles en champ magnétique intense dans ces systèmes si au moins deux couches sont suffisamment proches pour que les interactions entre couches soient importantes [MacDonald90]. Afin de créer des conditions favorables pour des états corrélés, la localisation des électrons doit être augmentée. Cela peut être fait en appliquant un champ magnétique parallèle au plan des couches 2D qui supprime l'effet tunnel des électrons entre les couches. Dans cette thèse, nous étudions les triples puits quantiques à haute densité électronique pour garantir que les trois sous-bandes restent peuplées même dans un champ magnétique intense. Expérimentalement, nous utilisons une température entre 50 et 100 mK et un champ magnétique intense jusqu'à 34 T.

Nouveaux états de l'effet Hall quantique fractionnaire

Dans cette thèse, nous effectuons des études dans les triples puits quantiques. En raison d'une action combinée de la répulsion des électrons due au confinement, les électrons ont tendance à se concentrer surtout dans les puits latéraux. Afin de peupler le puits central, nous avons augmenté sa largeur ; sa densité est estimée 30% plus faible que celle des puits qui le bordent. Les échantillons sont les mêmes que ceux utilisés pour les études sous irradiation micro-ondes (cf. partie qui correspond au chapitre 5). Nous avons ici une séquence des sous-bandes $E_1 < E_2 < E_3$ [Gusev09]. Dans la résistance longitudinale, nous observons que le minimum de ν=6 correspond au gap cyclotron, le minimum ν=3 au gap de Zeeman et les minima de ν=1, ν=2, ν=4, and ν=5 aux gaps entre les sous-bandes du premier niveau de Landau.

L'observation la plus intrigante est la suppression complète du minimum attribué au facteur de remplissage entier ν=4 à $\theta \simeq 40°$. θ est l'angle d'inclinaison entre le champ magnétique B est la composante perpendiculaire $B_\perp$, cf. insert de la figure 0.6(a). Dans la figure 0.6(a) nous montrons cet effet à $\theta \simeq 46.3°$. Nos calculs montrent que pour un angle d'inclinaison de $\theta \simeq 40°$, le champ magnétique parallèle correspond au champ critique $B_\parallel^c$ pour supprimer exponentiellement l'effet tunnel entre les puits (sous-bandes). La condition de l'apparition des nouveaux états corrélés est maintenant satisfaite, car l'effet tunnel est supprimé d'une façon exponentielle et le mouvement des électrons est limité à une seule couche (puits). Par conséquent, la corrélation entre les électrons

devient possible et est responsable de ces nouveaux états dans l'effet Hall quantique fractionnaire. D'autre part, le champ magnétique n'a aucune influence sur l'état ν=5 pour de plus grands angles d'inclinaison. Dans la figure 0.6(a), la résistance longitudinale et la résistance de Hall sont tracées pour $\theta = 0°$ et $\theta = 46.3°$. Nous observons trois nouveaux minima accompagnés de plateaux quantifiés avec un dénominateur de trois (13/3, 11/3 et 10/3) et l'un des plateaux est très profonde avec le facteur de remplissage ν=10/3. La sensibilité différente pour différents facteurs de remplissage avec $B_{\|}$ s'explique par une suppression de l'amplitude de l'effet tunnel ($t \to 0$) si le gap entre les deux sous-bandes les plus basses de chaque niveau de spin $E_1 \to E_2 = \varepsilon_s$) est fermé, tandis que le gap diminue entre les sous-bandes supérieures et moyennes, mais ne disparaît pas ($E_3 \to \varepsilon_c$). Ces états ont été observés pour deux épaisseurs de barrières différentes [Gusev09].

Maintenant nous discutons le magnéto-transport pour les angles inclinés pour les facteurs de remplissage inférieurs à ν=4 (d_b= 2.0 nm, figure 0.6). Nous trouvons de nouveaux états de l'effet Hall quantique fractionnaire qui se produisent dans des champs magnétiques intenses (ν <5/2). Quelques expériences en fonction de l'angle d'inclinaison sont présentées dans la figure 0.6(b). Les états pour ν <5/2 sont présents pour tous les angles inclinés mais on observe seulement des effets intéressants pour les états ν >5/2, en particulier ν=7/3 et ν=12/5. L'état ν=8/3 est visible tout le temps en augmentant la composante du champ magnétique parallèle et un nouvel état à ν=13/5 apparaît. L'état ν=7/3 présente l'effet de réentrance et nous observons un nouvel état à ν=12/5 si l'on augmente la composante du champ magnétique parallèle, cf. figure 0.6(b). L'état ν=7/3 est présent pour $\theta = 0°$, disparaît à $\theta = 46.3°$ et est de nouveau observable à $\theta = 55°$. Chaque nouvel état (minimum dans la résistance longitudinale), s'accompagne d'une résistance de Hall quantifiée.

Dans ces études, nous avons toujours un effet lié aux deux composantes du champ magnétique, perpendiculaire et parallèle. Un champ magnétique perpendiculaire mène à une dépopulation consécutive des sous-bandes tandis qu'une composante parallèle contrôle le couplage entre celles-ci. La cohabitation entre les composantes parallèle et perpendiculaire peut expliquer la suppression de ν=7/3 et l'apparition de ν=12/5 par un transfert de charge entre le puits au centre et les puits latéraux, mais n'explique pas la réentrée de ν=7/3 avec l'augmentation de l'angle. Cet état pourrait être attribué à un nouvel état corrélé [Gusev09].

En conclusion, cette thèse a présenté les premières études expérimentales dans les systèmes d'électrons réalisés dans les triples puits quantiques de haute densité. Dans un champ magnétique incliné, trois nouveaux états à ν=10/3, 11/3, et 13/3 ont été trouvés à la place du facteur de remplissage entier ν=4. L'observation de l'effondrement de ν=4, ν=2, et l'émergence d'autres facteurs de remplissage fractionnaires dans les champs magnétiques inclinés pour nos systèmes de triples puits quantiques ont été démontrées. Ces états sont développés de plus en plus si on augmente le champ magnétique parallèle qui supprime l'effet tunnel, et certains d'entre eux peuvent être attribués aux nouveaux états

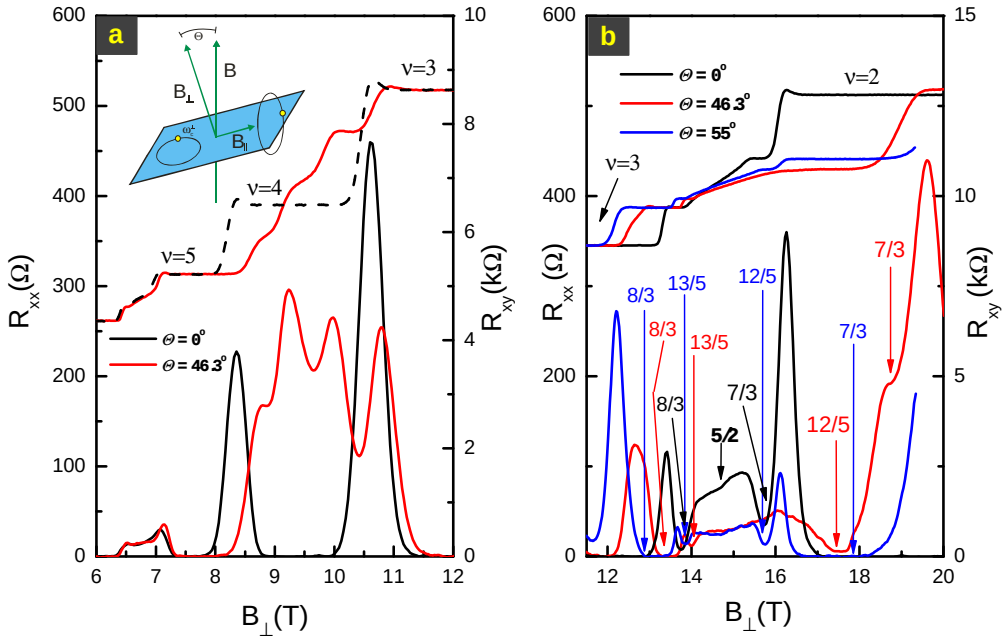

Figure 0.6: (a) Nouveaux états d'effet Hall quantiques fractionnaire qui remplacent le plateau ν=4 pour un angle de Θ=46.3°. (b) Effet Hall quantique fractionnaire dans un triple puits quantique en fonction de l'angle T ≃100 mK, barrière 20 Å). Les expériences pour Θ=0° (noir) Θ=46.3° (rouge) et Θ=55° (bleu) montrent le comportement de ce phénomène: le plateau 7/3 est réprimé pour Θ=46.3° mais réapparaît et s'élargit pour Θ=55°. Le plateau 12/5 est large pour Θ=46.3° et étroit pour Θ=55°.

corrélés. L'état ν=7/3 montre l'effet de réentrance et nous avons observé un comportement non monotone avec l'augmentation du champ parallèle de l'état ν=12/5. Avec ces études, nous pensons avoir ouvert une discussion sur de nouveaux états corrélés dans les systèmes de multi-puits quantiques.

Partie III

(Correspondant à l'appendix B du manuscrit complet)

Dispositif expérimental - expériences sous irradiation micro-onde

Les systèmes cryogéniques utilisés pendant la thèse sont un cryostat ^{4}He à température variable pour des températures de mesure entre 1.4 K et 280 K, un cryostat ^{3}He (300 mK - 4.2 K) et un réfrigérateur à dilution (40 mK - 1.4 K). Dans ce sommaire, nous ne présentons que le système utilisé pour des expériences sous irradiation micro-ondes. Le principe est d'irradier, d'une manière continue, un échantillon qui se trouve dans le cryostat à partir d'une source extérieure d'irradiation micro-onde. Nous avons

deux cannes et la seule différence entre les deux est que l'une d'entre elles est équipée d'un système de rotation. On peut ainsi tourner l'échantillon de 180° dans son plan pour les expériences avec polarisation linéaire. Les sources micro-ondes utilisées sont des générateurs d'ondes électromagnétiques de type "carcinotron" (de modèle G440XE) fourni par ELMIKA. Les sorties des guide d'onde sont rectangulaires (WR), leur taille varie avec la gamme de fréquence. Un atténuateur de puissance avec entrée et sortie également en guide d'onde rectangulaire, est connecté à chaque générateur. La gamme d'atténuation de ces atténuateurs est de 0 à -75 dB. La longueur totale du guide est de 4.5 m et le diamètre interne de sa section circulaire est de 1 cm. L'échantillon est placé à 1-2 mm de la sortie du guide d'onde.

Pour toutes les expériences avec polarisation non déterminée, le guide d'onde coté échantillon est ouvert et pour contrôler la polarisation linéaire, nous utilisons une transition circulaire-rectangulaire à la sortie du guide d'ondes. Pour pouvoir adapter la sortie rectangulaire du générateur au guide d'onde circulaire, nous avons utilisé des pièces de transitions de guide d'onde. La détermination du champ électrique des micro-ondes est une question fondamentale des mesures des gaz-2D sous irradiation micro-ondes. Nous avons montré que nous sommes capables de calculer le champ électrique in-situ de nos mesures expérimentales en comparant l'expérience avec la théorie dans les multi-puits quantiques.

Une méthode bien connue pour estimer le champ électrique est de comparer les oscillations SdH dans la magnétorésistance sous excitation micro-ondes avec des mesures où seulement un champ dc (courant continu) est appliqué. Cette idée est largement abordée dans la littérature et a été appliquée aux mesures dans les systèmes à simple couche [Wiedmann09a]. Nous avons également comparé cette méthode avec la procédure pour les multi-puits quantiques et nous avons trouvé un accord raisonnable [Wiedmann08].

Un dernier commentaire sur la puissance des micro-ondes. En général, cette puissance (en mW) à la sortie du guide d'onde peut être calculée en tenant compte des pertes dans celui-ci pour chaque fréquence. Pour nos quatre générateurs, nous avons une puissance différente pour chaque fréquence sans atténuation (0 dB). Les tableaux fournis par ELMIKA peuvent être utilisés pour estimer la puissance (en mW) à la sortie du guide d'onde. Néanmoins pour plus de rigueur nous utilisons, dans ce travail, la valeur de l'atténuation en décibels (dB) pour mesurer la puissance dans les expériences. Cette atténuation est ensuite traduite en un champ électrique

Conclusion générale et perspectives

Cette thèse a présenté les études expérimentales et théoriques dans des puits quantiques multiples exposés à une irradiation micro-ondes en continu. En raison de deux sous-bandes peuplées ou plus à deux dimensions, nous observons des oscillations de magnétorésistance entre les sous-bandes qui sont un signe du couplage entre les électrons dans des puits quantiques différents. Le magnétotransport sous irradiation micro-

ondes est fortement modifié. En particulier nous avons observé pour la première fois des états de résistance nulle dans des systèmes multicouches. Nous avons expliqué les résultats expérimentaux par une généralisation de la théorie aux systèmes d'électrons multicouches. Nous avons trouvé que, à basse température, le mécanisme inélastique joue le rôle dominant [Wiedmann08, Wiedmann09b]. En particulier, les états de résistance nulle apparaissent dans les conditions de résistivité négative prédites par le mécanisme inélastique. Cette observation est en accord avec la formation de domaines de courants. Dans la communauté scientifique, il existe une controverse: ces micro-ondes induites apparaissent-elles dues à des phénomènes "bulk" ou en raison d'effets de contact? Dans le cadre de cette thèse, nous avons apporté notre contribution en réalisant de nouvelles expériences qui ont permis d'élucider le traitement théorique des mécanismes microscopiques (phénomènes "bulk ") [Wiedmann10b]. En outre, nous avons effectué des études en transport jusqu'à un champ magnétique intense de 34 T dans le Laboratoire National des Champs Magnétiques Intenses (LNCMI). Ces expériences à la plus basse température possible (T <100 mK), nous ont permis d'observer de nouveaux états d'effet Hall quantique fractionnaire dans les triples puits quantiques se produisant en présence d'une composante parallèle au champ magnétique et qui pourraient être attribués à de nouveaux états corrélés [Gusev09].

En ce qui concerne les expériences fondamentales sur l'effet d'un champ électrique qui affecte le transport d'électrons dans les systèmes multicouches, l'étape suivante consiste, par conséquent, à étudier la réponse des systèmes multicouches soumis aux micro-ondes et à un champ électrique dc. Ce genre d'études a été réalisé dans les systèmes avec une sous-bande peuplée [Hatke08, Khodas08, Lei08]. De plus, l'influence des micro-ondes sur la résistance de Hall doit être étudiée plus précisément. Une analyse au Microscope électronique (Scanning Hall Probe Microscopy) à balayage pourrait permettre de donner plus d'informations sur la distribution du courant dans le cas d'échantillons montrant des états à résistance nulle.

La recherche de nouveaux états dus aux interactions électron-électron sont au début de la recherche expérimentale et théorique dans les systèmes de multiples puits quantiques. De nouveaux modèles théoriques ont été proposés [Levin09].

La réponse d'un système d'électrons de basse dimension exposé à une haute fréquence électromagnétique peut être utilisée pour identifier et détecter la fréquence et la valeur du champ électrique. Cette propriété pourrait être utilisée dans les détecteurs de fréquence et de dispositifs à haute fréquence car il a été démontré dans ce travail que les systèmes électroniques multicouches sont extrêmement sensibles à la fréquence de l'irradiation. Cela laisse envisager des applications industrielles dans le domaine de la détection du champ électromagnétique de haute fréquence.

L'objectif principal, au-delà des études fondamentales et en s'appuyant sur de nouveaux modèles théoriques, est de contrôler l'effet tunnel entre les couches par des grilles extérieures. Cette manipulation par un champ électrique externe peut également être utilisée pour contrôler la polarisation de spin qui est l'aspect fondamental de la "spin-

tronique". Ainsi, les effets peuvent être utilisés dans l'application de divers dispositifs d'électronique de spin.

Introduction

Information technology and microelectronic devices are mainly based on semiconductor technology. The development of Molecular Beam Epitaxy (MBE) enabled scientists, to create and define low-dimensional structures in semiconductor materials owing to a confinement of electrons. In order to make the application of new devices possible, a detailed knowledge of the underlying electron transport processes in the presence of a magnetic field and the response of electrons to high-frequency electromagnetic fields are of crucial importance.

Among the various realizations of low-dimensional systems made of semiconductors, multilayer electron systems are of particular interest, since they possess a new quantum degree of freedom due to interlayer coupling. This leads to a variety of interesting phenomena which are not observed in conventional single-layer two-dimensional (2D) systems. New effects like tunneling of electrons and correlation between electrons in different layers become important. Owing to the progress of modern semiconductor growth technologies, fabrication of high-quality multiple 2D layers in a close proximity to each other became possible. Fundamental research is mostly carried out in semiconductor materials based on gallium arsenide sandwiched by aluminium gallium arsenide forming a quantum well structure, which is one possible realization of a 2D electron system. In order to obtain multilayer systems, quantum wells are separated by aluminium gallium arsenide barriers. Variation of the barrier thickness and/or aluminium concentration strongly affects coupling between electrons in different layers.
In the presence of a perpendicular magnetic field and at low temperatures, motion of electrons becomes quantized (Landau level quantization). The modulation of the density of states by the applied magnetic field changes the conductivity of a two-dimensional system. The resultant oscillations in the longitudinal resistance are called Shubnikov-de Haas oscillations [SdH30]. In high magnetic fields, remarkable phenomena like integer quantum Hall effect [vonKlitzing80] and fractional quantum Hall effect [Tsui82] accompanied by vanishing longitudinal resistance have been discovered.

The objective of this thesis is to study the influence of the quantum degree of freedom caused by the tunnel coupling on transport properties of multilayer electron systems in magnetic fields and under microwave excitation. Within the scope of this thesis, multilayer electron systems exposed to a continuous microwave irradiation are investigated for the first time. In addition, this work presents studies of new correlated states in high magnetic fields in these systems.

It is generally known that in low magnetic fields (B <0.3 T) and under microwave (MW) irradiation, the resistance of a 2D semiconductor starts to oscillate and can even reach zero for low temperature, depending on the mobility of the sample, whereas the transverse Hall resistance remains essentially unaffected. Indeed, zero-resistance is a rare phenomenon in condensed matter systems and the first transition has been found by Kamerlingh Onnes when he discovered superconductivity in mercury in 1911. In semiconductor physics, Klaus von Klitzing observed the quantum Hall effect accompanying vanishing longitudinal resistance in a single-layer 2D electron system at high magnetic fields [vonKlitzing80]. It was first Michael Zudov (University of Utah) who observed microwave-induced resistance oscillations, governed by the ratio of the radiation frequency to the cyclotron frequency [Zudov01a]. In later experiments and due to continuing improvements in sample quality, zero-resistance states have been discovered by Ramesh Mani (at this time at Max-Planck-Institut in Stuttgart) and colleagues [Mani02] and independently by Michael Zudov and Rui-Rui Du [Zudov03].
This discovery has also attracted much theoretical interest. In general it is assumed that this phenomenon is related to the bulk properties of a 2D electron system and several microscopic mechanisms have been presented. Among them, displacement mechanism, proposed by Victor Ryzhii [Ryzhii70, Ryzhii86, Durst03], and inelastic mechanism, discussed by Sergey Dorozhkin [Dorozhkin03] and developed by Ivan Dmitriev and collegues [Dmitriev05], are the dominant mechanisms, widely discussed in literature. In addition, electrodynamic effects are connected to the observed phenomena, e.g. the absorption of microwaves by the 2D electron system [Mikhailov04, Studenikin05].
In scientific community, there is a controversy wheater these microwave-induced phenomena occur due to bulk-like [Ryzhii70, Ryzhii86, Durst03, Dorozhkin03, Dmitriev05] or near-contact effects [Mikhailov06, Andreev08]. Within the framework of this thesis, new data will elucidate the theoretical background of microscopic mechanisms.

The main idea of Chapter 1 is to introduce fundamentals of a 2D electron system and its properties as well as transport in the presence of a perpendicular magnetic field. In addition, basic properties and magnetotransport for a bilayer electron system are explained, which is the simplest multilayer system. Bilayer electron systems can be formed by either two quantum wells separated by a narrow barrier or high-density wide single quantum wells owing to charge redistribution, where the two wells near the interface are separated by an electrostatic potential barrier. As a result, two subbands appear due to tunnel hybridization of 2D electron states. In magnetotransport, a bilayer system exhibits magneto-intersubband oscillations due to an alignment of Landau levels from both wells at the Fermi level with increasing perpendicular magnetic field [Mamani08]. We will present own results to illustrate all transport phenomena.

The experimental studies of magnetoresistance in single, bi- and multilayer electron systems exposed to microwave irradiation are the topic of the Chapters 2-5. Owing to a close and successful collaboration with Oleg Raichev, theoretical physicist from the

Institute of Semiconductor Physics in Kiev (NAS of Ukraine), during this project, we were able to analyze and discuss the obtained experimental results within a theoretical framework.

Chapter 2 introduces basics of magnetotransport in the presence of microwave irradiation in single-layer systems. The relevant microscopic models will be illustrated in detail for studies of multilayer electron systems. To confirm microwave-induced resistance oscillations, experiments in high-density samples will be shown. Additionally, we will demonstrate that under certain conditions (high temperature and microwave power), fractional microwave-induced resistance oscillations become well-developed showing the highest denominators so far observed in experiments.

The response of a bilayer electron system to microwave excitation is studied for the first time and is the topic of Chapter 3. Magneto-intersubband oscillations observed in dark magnetoresistance are enhanced, damped or even inverted under microwave irradiation. The observed effects are strongly correlated with the radiation frequency. Experiments will demonstrate the response of double quantum wells to microwave excitation and their dependence on various parameters such as temperature, power and MW frequency. We will show that the inelastic mechanism of photoresistance which is applied to the case of bilayers (two subbands) is the dominant contribution for low temperature.

Whereas no zero-resistance states have been observed in bilayer systems formed by a double quantum well, wide quantum wells exhibit this remarkable phenomenon due to a higher quality of the samples which is the topic of Chapter 4. It must be pointed out that the results in Chapter 4 are the first experimental observation of zero-resistance states for a system which is different from a single-layer system. It will be shown that zero-resistance states in bilayers are distinct from single-layer systems. Theoretical calculations demonstrate that the inelastic mechanism fully explains the appearance of zero-resistance in bilayer electron systems.

Due to the continuous improvement of sample quality, this thesis presents the investigation of a trilayer electron system in low-magnetic fields and exposed to microwave irradiation in Chapter 5. In extension to investigations of magneto-intersubband oscillations in two-subband systems, we will show here both experimental and theoretical studies of such phenomena in three-subband systems realized in triple quantum wells. We point out that owing to a superposition of several oscillating contributions, dark magnetoresistance and magnetoresistance exposed to MW irradiation exhibit a qualitatively different oscillation picture. Finally, we present a general theory that is valid for an arbitrary number of subbands.

Another aim of this thesis is to investigate multilayer electron systems in high magnetic fields. Multicomponent quantum Hall systems exhibit new many-body states or many-body ground states which are absent in single-layer electron systems owing to interlayer electron-electron interaction. In this work, magnetotransport studies in high

quality (mobility) and high-density trilayer systems will be presented. For experimental investigations, we require high-density samples to ensure a population of all three subbands in high magnetic fields. We can achieve such high fields within the facilities of the Laboratoire National des Champs Magnétiques Intenses (LNCMI). Experiments up to a static magnetic field of 35 T can be performed this day. In multiple two-dimensional systems new states are theoretically predicted if the layers are in close proximity to each other [MacDonald90].
Experimental evidence for correlated states is nowadays mostly restricted to bilayer systems. In Chapter 6, we will demonstrate in experiments suppression of integer quantum Hall states, reentrance effect and the appearance of new emergent fractional quantum Hall states in tilted magnetic fields. The discovery of new states might be attributed to novel correlated states owing to many-body phenomena since the tunneling is suppressed by the parallel magnetic field. This result might be also considered as the first experimental evidence for many-body states in a multilayer system which is different from bilayer electron systems.

In Appendix A, the concept of high-electron density samples by using a superlattice structure will be briefly discussed. For all samples studied in this work, this concept has been applied. For readers interested in the experimental technique, Appendix B describes the cryogenic systems which have been used during this thesis. In addition, we give detailed information about the experimental methods for microwave experiments, in particular, the determination of the microwave electric field strength.

Chapter 1

Properties of magnetotransport in 2D electron gases

Two-dimensional electron systems have been extensively studied during the last decades and remarkable effects at low temperature and in the presence of a magnetic field have been discovered [vonKlitzing80, Tsui82]. This chapter gives a general introduction in two-dimensional (2D) electron systems and their transport properties in order to understand photoresistance studies in single- and bilayer electron systems in the following chapters. Basics of integer and fractional quantum Hall effect are also introduced for the experiments performed in trilayer electron systems in the last chapter.

Physics of 2D electron systems become interesting when a magnetic field is applied perpendicular to the 2D plane and electron motion is quantized in discrete energy levels. The gap between these energy levels leads to the quantum Hall effect (QHE) [vonKlitzing80] which exhibits a quantization of the Hall resistance accompanied by oscillations in the longitudinal resistance. Studies of both phenomena are sensitive to temperature and provide an important tool for transport studies. However, fractional quantum Hall effect (FQHE) [Tsui82] can not be described in a single electron picture and physics of electron-electron interactions become important.

Beyond investigations in a pure 2D electron system where motion of electrons occurs in one single layer, bilayer electron systems, which can be realized in either double quantum well (DQW) or high-density wide quantum well (WQW) structures, are of great interest in the scientific community. Bilayer electron systems possess an extra degree of freedom leading to a variety of interesting phenomena which are absent in single layer electron systems. Owing to the quantum-mechanical penetration of the wavefunctions through a thin barrier, a bilayer system can be viewed as two 2D layers coupled by tunneling. Magnetotransport in bilayer electron systems with two occupied 2D subbands exhibits magneto-intersubband (MIS) oscillations due to additional intersubband scattering in a perpendicular magnetic field when different Landau levels of the two subbands are sequentially aligned at the Fermi level. To understand this phenomenon, we introduce basics of MIS oscillations and their theoretical description.

1.1 Fundamentals of 2D electron gases

Starting from three-dimensional (3D) semiconductor materials, a low dimensional electron system is achieved by geometric confinement in one, two or three directions. This is well-known as "quantum confinement". The semiconductor materials used in this thesis are gallium arsenide (GaAs) and aluminium gallium arsenide (AlGaAs). Both semiconductors have similar lattice constants and can be grown[1] together in layers to create a very clean high-quality crystal with few defects. GaAs and AlGaAs have different conduction band energies in the conduction band profile in the dimension perpendicular to the 2D layers where band electrons become trapped and have discrete energy levels. The combination of both semiconductors can form a 2D electron gas (2DEG) either as a heterostructure (triangular well) or a quantum well (QW) if a GaAs layer is sandwiched by AlGaAs. Additional doping ensures to have a very high mobility in such 2D systems.

1.1.1 Basic properties

In 2DEGs, free electron motion is confined along the crystal growth direction and the energy states are called two-dimensional subbands. Electron motion in the QW-plane (in these two dimensions) remains unconstrained. Thus, a single QW provides a single layer of two-dimensional electrons. If one considers the 2DEG in a "single electron picture", the Schrödinger equation can be written as

$$\left[-\frac{\hbar^2}{2m^*}\nabla^2 + V(z)\right]\Psi(x,y,z) = \varepsilon\Psi(x,y,z), \tag{1.1}$$

with m^* the effective electron mass of conduction band electrons (m^*=0.067m_e in GaAs/$Al_xGa_{1-x}As$, essentially the effective mass of bulk GaAs) and $V(z)$ the potential of the 2DEG perpendicular to the boundary layer. $\Psi(x,y,z)$ is the wavefunction. The electrons in the QW-potential (z-direction) are confined and we have free electron motion in the x-y-plane. With the ansatz $\Psi(x,y,z) = \Psi_n(z)\exp[(ik_xxk_yy)]$ the total energy of each electron is given by

$$\varepsilon(k_x,k_y) = \varepsilon_i + \frac{\hbar^2}{2m^*}(k_x^2+k_y^2); \qquad i = 0,1,2,\ldots, \tag{1.2}$$

where ε_i is the energy of the lowest subband ($i = 0$) and k_i is the electron wavevector in i-direction. For low temperatures, $k_BT \ll \Delta\varepsilon$ (subband energy), all electrons will be confined to the lowest energy state (lowest subband) ε_0. For 2D systems, the density of states (DOS) is

$$\mathcal{D}(\varepsilon) = \mathcal{D}_0\sum_n \Theta(\varepsilon-\varepsilon_n), \tag{1.3}$$

with $\mathcal{D}_0 = g_sg_vm^*/2\pi\hbar^2$ (g_s and g_v are spin and valley degeneracy, respectively; for GaAs: g_s =2, g_v=1) a constant density of states for each subband. Θ is the Heavyside

[1] 2DEGs are fabricated by Molecular Beam Epitaxy (MBE) in which crystals are grown one atomic layer at time with a control over the composition of each layer.

function.
The electron density n_s is expressed as

$$n_s = \int \mathcal{D}(\varepsilon) f(\varepsilon) d\varepsilon, \tag{1.4}$$

with the Fermi-Dirac electron distribution function $f(\varepsilon)$ in the thermodynamic equilibrium

$$f(\varepsilon) = \frac{1}{\exp\left(\frac{\varepsilon - \mu_F}{k_B T}\right) + 1} \tag{1.5}$$

where k_B is the Boltzmann constant and μ_F the chemical potential. $f(\varepsilon)$ describes the probability of an electron which occupies a band state with energy ε at a temperature T. This implies, that for T=0, the probability to find an electron with $\varepsilon < \varepsilon_F$ is 1 and no electrons with $\varepsilon > \varepsilon_F$ exist. Fermi energy is the energy of the highest occupied state. At T=0, the chemical potential μ_F is equal to the Fermi energy ε_F. For a finite temperature, electrons which are close to ε_F can occupy free energy states $\varepsilon > \varepsilon_F$ and these electrons are responsible for the transport properties. With a constant DOS, the Fermi energy is determined by the electron density as

$$\varepsilon_F = n_s \frac{\pi \hbar^2}{m^*}. \tag{1.6}$$

1.1.2 2DEG in a perpendicular magnetic field

When a magnetic field B is applied perpendicular to the 2DEG, the Lorentz force $\vec{F_L} = -e(\vec{v} \times \vec{B})$ forces electrons on circular orbits. With the Hamiltonian

$$\mathcal{H} = \frac{1}{2m^*}(\vec{p} - e\vec{A})^2 \tag{1.7}$$

for a charged particle, ignoring spin, in a magnetic field, Schrödinger equation has the form

$$\left[\frac{1}{2m^*}(\vec{p} - e\vec{A})^2 + V(z)\right] \Psi(x, y) = \varepsilon \Psi(x, y), \tag{1.8}$$

where $\vec{p} = -i\hbar\nabla$ is the generalized momentum of the particle and $\vec{A}$ the vector potential, such that $\vec{B} = \nabla \times \vec{A}$. By definition, electron motion is in the x-y-plane, thus the magnetic field will be perpendicular to the plane $\vec{B} = B\hat{z}$ and by using the Landau gauge, the vector potential is $\vec{A} = -yB\hat{x}$. Eq. (1.8) can be transformed in a Schrödinger equation for a one-dimensional harmonic oscillator with the frequency $\omega_c = eB/m^*$, called cyclotron frequency. Due to the particle motion into cyclotron orbits, DOS in the x-y-plane obeys an additional quantization giving rise to a sequence of δ-like energy levels (see Figure 1.1), separated by the energy $\hbar\omega_c$. These energy levels are called Landau levels (LLs). DOS and energy spectrum are obtained as

$$\mathcal{D}(\varepsilon) = \frac{g_s}{2\pi l_B^2} \sum_{i,n} \delta(\varepsilon - \varepsilon_{i,n}) \tag{1.9}$$

and

$$\varepsilon_{i,n} = \varepsilon_i + \hbar\omega_c(n + \frac{1}{2}); \qquad i, n = 0, 1, 2, \ldots , \tag{1.10}$$

respectively, with the Dirac function δ, ε_n, the confinement energy and $\hbar\omega_c(n+1/2)$ the Landau level energy. i is the subband level and n the Landau quantum number. Here l_B is the magnetic length with $l_B = \sqrt{\hbar/eB}$ and g_s the spin degeneracy. The degeneracy of a Landau level n_L which is defined as the allowed number of states in each Landau level per unit area, can be calculated as the number of flux quanta $\Phi_0 = h/e$ per unit area:

$$n_L = \frac{eB}{h} = \frac{1}{2\pi l_B^2}. \tag{1.11}$$

If n_s is the total carrier density, one can introduce a filling factor ν, given by

$$\nu = \frac{n_s}{n_L} = \frac{h}{eB} \cdot n_s. \tag{1.12}$$

The filling factor ν gives the number of fully occupied Landau levels.

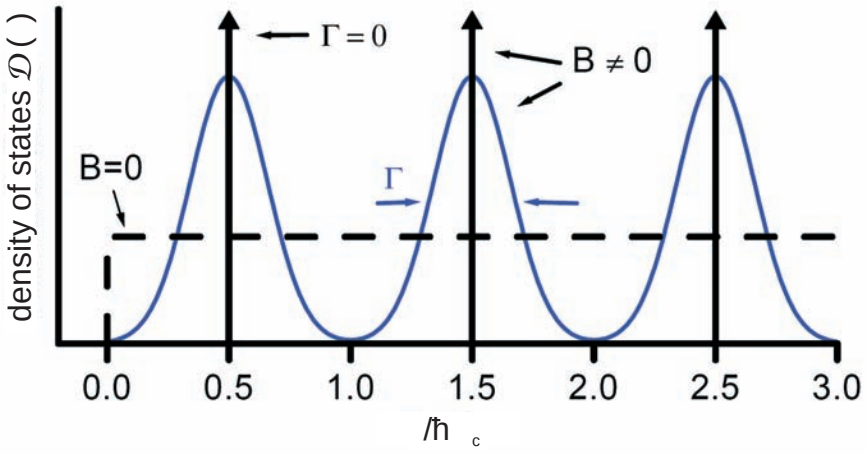

Figure 1.1: A magnetic field introduces a quantization into δ-like Landau levels with the broadening parameter Γ. Without a magnetic field, B=0, the DOS is constant.

Introducing the spin of electrons, the coupling of spin and magnetic field gives rise to an additional term with the Zeeman energy $\Delta_z = g^*\mu_B B$, with g^* the effective Landé-factor (g^*=-0.44 for bulk GaAs) and μ_B the Bohr magneton. The energy spectrum, extended by the Zeeman term is

$$\varepsilon_{i,n,s} = \varepsilon_i + \hbar\omega_c(n + \frac{1}{2}) + s\mu_B g^* B; \qquad s = \pm\frac{1}{2}. \tag{1.13}$$

In the ideal case, the DOS consists of δ-functions. In real conditions, Landau levels are broadened due to electron-electron, impurity or phonon scattering. An inclusion of scattering gives rise to a finite lifetime τ_q of electrons between a scattering event. This lifetime is called quantum lifetime τ_q or single particle relaxation time and can be identified as the lifetime of an electronic eigenstate, here a Landau eigenstate in a magnetic field[2]. The scattering broadens a Landau level with an energy width $\Gamma = \hbar/\tau_q$

[2]The distinction of τ_q and τ_{tr}, which is related to the mobility, is important, because in the presence of small-angle scatterers, τ_{tr} is significantly larger than τ_q. Typical experimental values for τ_{tr}/τ_q in GaAs heterostructures are 6 to 14 [Beenakker91].

(see Figure 1.1), which is commonly assumed as a Lorentzian or a Gaussian profile. The density of states can be calculated then using the self-consistent Born approximation (SCBA) where in the linear approximation all scattering events are taken into account and the DOS for each Landau level is a sum of semielliptic functions with the widths $\Gamma_{n,s}$:

$$D(\varepsilon) = \frac{1}{2\pi l_B^2} \sum_{i,n,s} \frac{2}{\pi \Gamma_{n,s}} \left[1 - \left(\frac{\varepsilon - \varepsilon_{i,n,s}}{\Gamma_{n,s}} \right)^2 \right]^{1/2}. \tag{1.14}$$

$\Gamma_{n,s}$ is the nth Landau level broadening with the spin quantum number s and is proportional to the Landau level index, the spin quantum number and to the square root of the magnetic field ($\Gamma_{n,s} \propto \sqrt{B}$).
Oscillations of the DOS result in magnetoresistance oscillations in 2D systems and can be measured in the longitudinal resistivity ρ_{xx}. In high magnetic fields, the spin degeneracy is lifted giving rise to the occurrence of the *odd*-integer quantum Hall effect. The lowest Landau level (ν=1) is a spin-split level. All electrons have their spin aligned in the same direction, thus spin polarization is achieved. Both phenomena will be discussed in the next section.

1.2 Theory of magnetotransport

1.2.1 Classical approach: Drude Model

In the classical approach, electron transport in a crystal is described by the Drude model where electrons are considered as classical particles [Drude00]. The interaction between electrons and the periodic lattice potential is included in the effective electron mass m^*. The collisions of electrons in the relaxation approach are included by a scattering time τ, the average time between two collisions. The Drude model is only valid for small magnetic fields and overlapping Landau levels ($\omega_c \tau \ll 1$), where the Landau quantization is neglected. The motion of electrons can be described by Newton's equation of motion

$$m^* \frac{d\vec{v_D}}{dt} + \frac{m^*}{\tau} \vec{v_D} = -e[\vec{E} + (\vec{v_D} \times \vec{B})] \tag{1.15}$$

where the electrons move with a drift velocity $\vec{v_D}$ in a homogenous electric field $\vec{E}$, perpendicular to the magnetic field $\vec{B}$. In the static case, the velocity is $\vec{v_D} = e\tau\vec{E}/m^*$ and we can define the mobility μ of a 2D system as

$$\mu = \frac{|\vec{v_D}|}{\left|\vec{E}\right|} = \frac{e\tau_{tr}}{m^*}. \tag{1.16}$$

The mobility gives rise to the quality of a sample. It should be noticed that the scattering time between two collisions is the elastic transport scattering time τ_q. In contrast, τ_{tr} is a measure of the amount of time a carrier remains moving in a particular direction. In calculating τ_q, the inclusion of a factor 1-cos Θ, where Θ is the scattering angle, is related to the importance of large angle over small angle scattering events.

In addition, we can derive Drude conductivity with the Ohmic law from

$$\sigma_0 = \frac{n_s e^2 \tau}{m^*}. \tag{1.17}$$

The parameters density n_s and mobility μ characterize a 2D system.
With the current density $\vec{j} = -en_s\vec{v_D}$, a connection between the current density $\vec{j}$ and the electric field $\vec{E}$ can be obtained via the conductivity tensor $\widehat{\sigma}$:

$$\begin{pmatrix} j_{xx} \\ j_{xy} \end{pmatrix} = \begin{pmatrix} \sigma_{xx} & \sigma_{xy} \\ \sigma_{yx} & \sigma_{yy} \end{pmatrix} \begin{pmatrix} E_x \\ E_y \end{pmatrix}. \tag{1.18}$$

In an isotropic system the tensor components can be written as $\sigma_{xx} = \sigma_{yy}$ and $\sigma_{xy} = -\sigma_{yx}$. The resistivity tensor $\widehat{\rho}$ is obtained by a simple tensor inversion of $\widehat{\sigma}$ to

$$\begin{pmatrix} \rho_{xx} & \rho_{xy} \\ -\rho_{xy} & \rho_{xx} \end{pmatrix} = \frac{1}{\sigma_{xx}^2 + \sigma_{xy}^2} \begin{pmatrix} \sigma_{xx} & \sigma_{xy} \\ -\sigma_{xy} & \sigma_{xx} \end{pmatrix} \tag{1.19}$$

and the tensor components ρ_{xx} and ρ_{xy} from Eq. (1.19) are

$$\rho_{xx} = \frac{\sigma_{xx}}{\sigma_{xx}^2 + \sigma_{xy}^2} = \frac{1}{en_s\mu} \tag{1.20}$$

and

$$\rho_{xy} = \frac{\sigma_{xy}}{\sigma_{xx}^2 + \sigma_{xy}^2} = \frac{B}{en_s}. \tag{1.21}$$

In the high field limit when $\sigma_{xx} \ll \sigma_{xy}$, one can write a simple expression for ρ_{xx} and σ_{xx}:

$$\rho_{xx} \sim \frac{\sigma_{xx}}{\sigma_{xy}^2} \quad , \quad \sigma_{xx} \sim \frac{\rho_{xx}}{\rho_{xy}^2}. \tag{1.22}$$

A standard magnetotransport measurement is presented in Figure 1.2 for an arbitrary sample in Hall-bar geometry in a perpendicular magnetic field where longitudinal resistance R_{xx} and transverse resistance R_{xy} are measured at the same time.
By rescaling the longitudinal resistance R_{xx} by the dimensions length L and width W, the longitudinal resistivity in Hall-bar geometry can be calculated via

$$\rho_{xx} = R_{xx} \cdot \frac{W}{L}, \quad \texttt{and} \quad \rho_{xy} = R_{xy}. \tag{1.23}$$

Now, density by Eq. (1.21) and mobility

$$\mu = \frac{1}{neR_{xx}(B=0)} \cdot \frac{L}{W} \tag{1.24}$$

can be calculated and the 2D system is characterized. In van-der Pauw geometry (square specimens), longitudinal resistance R_{xx} must be multiplied with factor 4.5 to obtain correct resistivity.

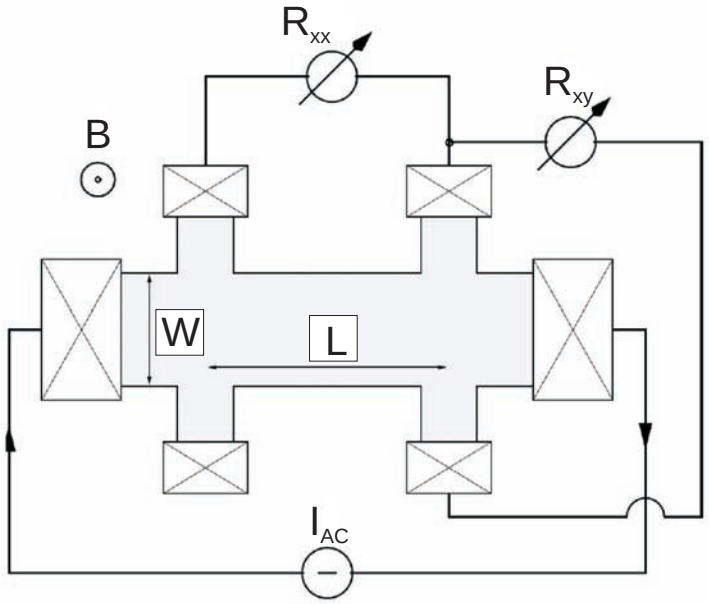

Figure 1.2: Sketch of a measurement of longitudinal and transverse resistance in a sample in Hall-bar geometry.

1.2.2 The Boltzmann equation

The Boltzmann equation (or Boltzmann transport equation) is used to treat complex electric and thermal transport properties in solid state physics. This equation gives a microscopic description of the evolution of an electron system, determined by the electron distribution function $f(\vec{r}, \vec{k}, t)$:

$$\left[\frac{\partial}{\partial t} + \vec{v} \cdot \nabla_{\vec{r}} + \frac{e}{\hbar}\vec{F} \cdot \nabla_{\vec{k}}\right] f(\vec{r}, \vec{k}, t) = \left(\frac{\partial f}{\partial t}\right)_{coll}, \tag{1.25}$$

where $\vec{F}$ is the total external force and $\vec{v}$ the velocity of particles. The Boltzmann equation is valid for time intervals longer than the interaction duration and for distances longer than the size of the interaction domain. In solid state physics, we consider three mechanisms which affect free electron motion:

- **impulsive external forces** caused by external electric and magnetic fields or temperature gradients
- **dissipative effects** due to scattering
- **diffusion** due to fluctuations in the spatial electron density.

If scattering is neglected, each electron represents a closed subsystem and would completely determine the distribution function of an electron. The term $(\partial f/\partial t)_{coll}$ is called collision integral. The collision integral is defined as the rate of change of the distribution function, $(\partial f/\partial t)_{coll}\, d\vec{r}d\vec{k}/(2\pi)^3$, which is the change of the electron number per unit time in the phase space volume $d\vec{r}d\vec{k}$ due to scattering. Usually, Boltzmann equation is solved numerically or under the relaxation-time approximation (RTA) which is a

good approximation for isotropic scattering and elastic scattering for low-field transport. Within RTA, Boltzmann equation for electrons takes the following form:

$$\left[\frac{\partial}{\partial t} + \vec{v}\cdot\nabla_{\vec{r}} + \frac{e}{\hbar}\vec{F}\cdot\nabla_{\vec{k}}\right] f = \frac{f_0 - f}{\tau_{in}} \tag{1.26}$$

with the inelastic relaxation time τ_{in}. The temperature gradient and, e.g. the external electric field are small so that the deviation from equilibrium distribution f_0 is small, i.e. $f - f_0 \ll f_0$. The application of Boltzmann equation to an electron gas (2DEG) can also be called Boltzmann kinetic equation. For calculations, the collision integral has to be found. Generally, each scattering mechanism is described by a scattering rate $1/\tau$ which can be obtained using the quantum mechanical scattering theory for an electron and the scattering center.

1.2.3 Shubnikov-de Haas oscillations

As it was already mentioned, modulation of the DOS by an applied magnetic field leads to resistance oscillations in the conductance. This has been referred to as Shubnikov-de Haas (SdH) oscillations, discovered by Shubnikov and de Haas in 1930 [SdH30]. SdH oscillations are also an indication for the relevance of quantum phenomena in transport measurements of 2D electrons in a strong magnetic field and their study provides an important tool in semiconductor physics. The origin of SdH oscillations results from the oscillating DOS. Maxima in the density of states pass through the Fermi energy ε_F with increasing magnetic field, which results in resistance oscillations, periodic in the inverse magnetic field $1/B$. The experimental observation of SdH oscillations requires the following conditions:

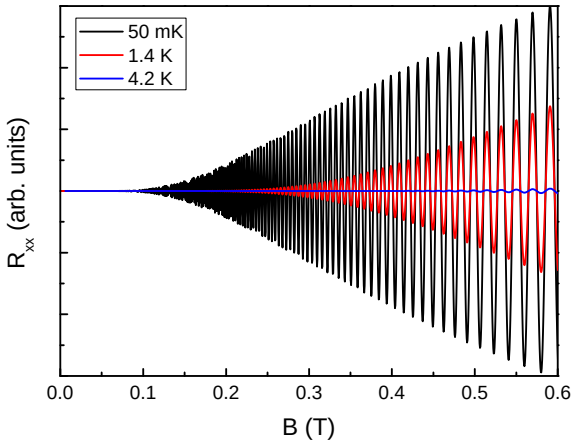

Figure 1.3: Temperature dependent SdH oscillations for 50 mK, 1.4 and 4.2 K. The parameters for this theoretical traces are $\varepsilon_F = 26$ meV and τ_q=2.2 ps (2.0 ps for 1.4 K and 1.5 ps for 4.2 K).

- The broadening of the Landau levels Γ has to be smaller than the separation between adjacent Landau levels $\hbar\omega_c$: $\Gamma \ll \hbar\omega_c$ or $\omega_c\tau_q \gg 1$.

- The thermal blurring of the Fermi energy ε_f must be small compared to the separation of Landau levels and the separation of Landau levels must be less than the Fermi energy: $k_BT \ll \hbar\omega_c < \varepsilon_F$.

If one assumes that the transport scattering time τ_{tr}, which results from electron mobility, is equal to the collision scattering time (quantum lifetime of electrons) τ_q, one can write for the first requirement $\mu B \gg 1$. The conclusion of the conditions given above is that one requires low temperatures and magnetic fields values which satisfy the condition $(\hbar eB/m^*) < \varepsilon_F$. Properties of a 2D system like period, effective g-factor, effective mass m^* or the Dingle temperature T_D can be determined from SdH oscillations. As it can be seen in Figure 1.3, calculated with Eq. (1.27), SdH oscillations are very sensitive to temperature. For a QW with high density (see parameters in inset of Figure 1.3), a Fermi energy $\varepsilon_F = 26$ meV and a quantum lifetime τ_q=2.2 ps for T <1.0 K has been used. Quantum lifetime of electrons can be extracted by comparing amplitude of SdH oscillations from experiment and theory using the Lifshits-Kosevich (Ando) formula [Lifshits56, Coleridge89]

$$\Delta\rho_{xx} \simeq 4\rho_0 \mathcal{T} \cdot \exp\left(-\frac{\pi}{\omega_c \tau_q}\right) \cos\left(\frac{2\pi\varepsilon_f}{\hbar\omega_c}\right). \tag{1.27}$$

Here, ρ_0 is the zero-field resistivity (Drude resistivity), $\mathcal{T} = X/\sinh X$ the temperature damping factor with $X = 2\pi^2 T_e/\hbar\omega_c$ (T_e is the electron temperature) and $d = \exp(-\pi/\omega_c\tau_q)$ is called the Dingle factor which includes the quantum lifetime τ_q.
Finally, Figure 1.4 presents longitudinal resistance up to a magnetic field of 5 T. SdH oscillations start to appear at a magnetic field of $B \simeq$0.5 T. A further increase in perpendicular magnetic field reveals spin splitting for $B \geq$1.5 T, and in high magnetic fields, spin splitting is completely resolved and one can distinguish between the Landau energy gap $\hbar\omega_c$ and the Zeeman gap Δ_Z.

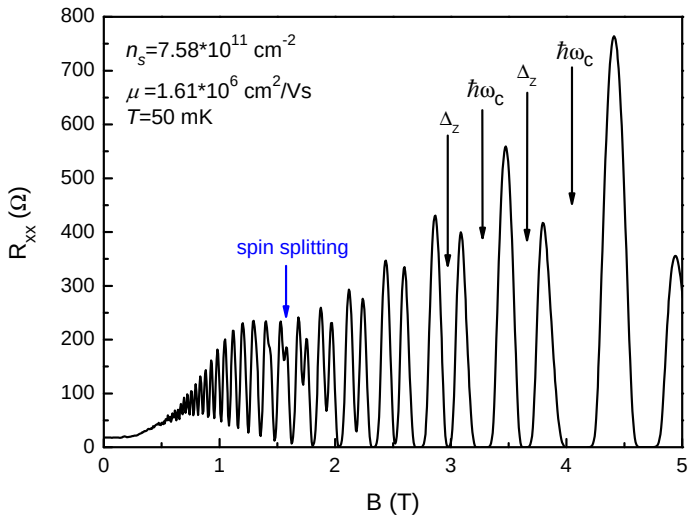

Figure 1.4: Longitudinal resistance of a quantum well up to 5 T at a temperature of 50 mK. Clear SdH oscillations are visible starting from 0.5 T. Spin splitting starts at $B \simeq$1.5 T (see blue arrow). For B >3 T, one can see Zeeman gaps Δ_Z and Landau energy gaps $\hbar\omega_c$.

1.2.4 Integer Quantum Hall Effect

Quantum Hall effect (QHE) is one of the most remarkable condensed-matter phenomena discovered in the second half of the 20th century. For the so-called integer quantum Hall effect (IQHE), discovered by VON KLITZING in 1980 [vonKlitzing80], the quantum number ν (filling factor) is an integer with a precision of about 10^{-10} and an absolute accuracy of about 10^{-8}. Klaus von Klitzing has found this effect in the Grenoble High Magnetic Field Laboratory in a Si-MOSFET structure. The Drude picture holds for low magnetic fields (overlapping Landau levels) where the density of states and thus the longitudinal resistance is constant and the Hall resistance has a linear slope given by $R_{xy} = B/en_s$ with the carrier density n_s. In an intermediate regime, when cyclotron energy exceeds the Landau Level broadening, the DOS starts to oscillate (see Figure 1.1) as a function of energy and SdH oscillations appear. A further increase in magnetic field reveals vanishing longitudinal resistance ($R_{xx} \rightarrow 0$) which implies no scattering. The Landau levels are completely separated and accompanied by plateaus, quantized in h/e^2, in the transverse resistance:

$$R_{xy} = \frac{1}{\nu}\frac{h}{e^2} \tag{1.28}$$

with integer ν. Due to the integer filling factor, this QHE is called integer QHE (IQHE) which refers to the number of fully occupied Landau levels below the Fermi energy. The measurement of Hall resistance is independent of the sample material. It is also used to define the so-called *von Klitzing constant*, $R_K{=}h/e^2{=}25812.807\ \Omega$. The origin of the QHE can be explained by the existence of localized electron states in the 2D system. As already discussed before, δ-functions of the DOS are broadened because of the random potential due to the structural disorder (defects, impurities, etc.). Now, the DOS peaks are divided into localized states (electrons not mobile) and in delocalized states (mobile electrons), see Figure 1.5. Thus, in a strong magnetic field a part of the localized electrons, at low temperatures, does not contribute to the conductivity, only delocalized states do. The sketch of the quantization is shown in Figure 1.5. All states up to the Fermi energy ε_F are occupied. The picture corresponds to the filling factor $\nu = 2$. By increasing the magnetic field, the Landau levels pass one after the other the Fermi energy. If ε_F is in the range of localized states, the QHE is maintained by the electrons within the delocalized states with a Landau level energy below ε_F. The Hall resistivity ρ_{xy} shows a plateau and ρ_{xx} is vanishingly small or zero for low temperatures. If the Fermi energy is in the narrow range of the delocalized states, ρ_{xy} shows a transition between two adjacent plateaus whereas a maximum for ρ_{xx} occurs. In this picture, the QHE can be understood as a phase transition of localization and delocalization. Experimental data for the QH-Effect and the longitudinal resistance which exhibits SdH oscillations, is presented in Figure 1.6.

The microscopic explanation is provided by the Landauer-Büttiker theory [Buettiker88]. Büttiker uses the picture of edge states propagating at the boundary of, e.g., a Hall-bar structure. The concept of edge channels has been introduced to describe the contribution

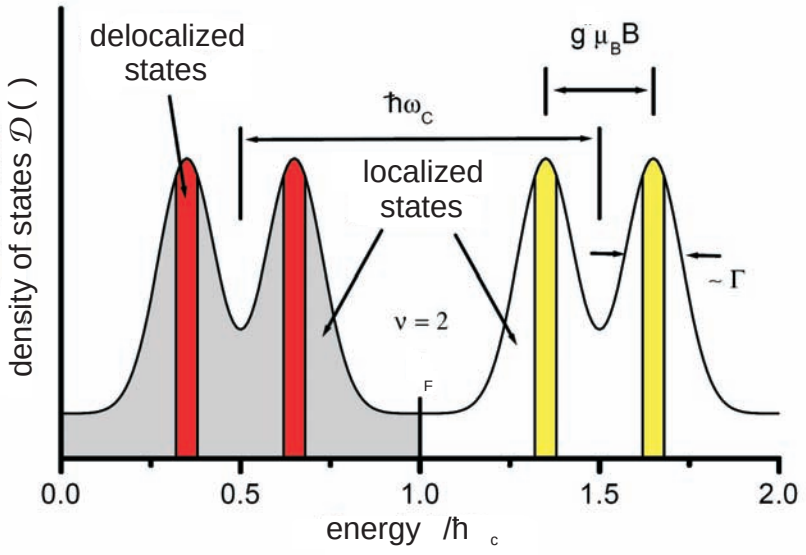

Figure 1.5: Sketch of the DOS for a 2D system in a magnetic field where the position of the Fermi energy corresponds to the filling factor $\nu = 2$. Only the delocalized states contribute to conduction.

to the edge currents from the wave functions of different Landau levels. The filling factor ν is given directly by the number of fully occupied Landau levels in Büttiker's model. This approach describes electrical transport by transmission and reflection at the contacts and uses the Landauer approach of transport. A comprehensive review of the edge-state transport has been published by Haug [Haug93]. The edge states arise due to the fact that boundaries exist in a real sample and along these boundaries, the electron density goes to zero (depletion). As a consequence, the potential rises near to the edges and Landau levels bend upward and cross the Fermi level. All Landau levels below the Fermi level (bulk) have occupied edge states at the Fermi level. The edge states along the boundary are assumed to be responsible for the electrical transport. The current into the ith contact in a sample with several contacts (Hall-bar) is given by

$$I_i = \frac{e}{h}(N - R_i) \cdot \mu_i - \sum_j T_{ij}\mu_j \tag{1.29}$$

with N the number of channels, R_i is the reflection coefficient at contact i, T_{ij} the sum of transmission coefficients from contact j to contact i and μ_i is the chemical potential. This formalism is easy to handle and can be applied to many geometries.

The edge state picture does not account for electrostatic screening effects of a 2DEG. Latest scanning force microscopes reveal convincing evidences for the existence of compressible and incompressible stripes in the depletion region at the sample edges. These experiments have shown that compressible and incompressible stripes also exist at the border between ohmic contacts and the 2DES (e.g. see Refs. [vonKlitzing04, Chklovskii92]).

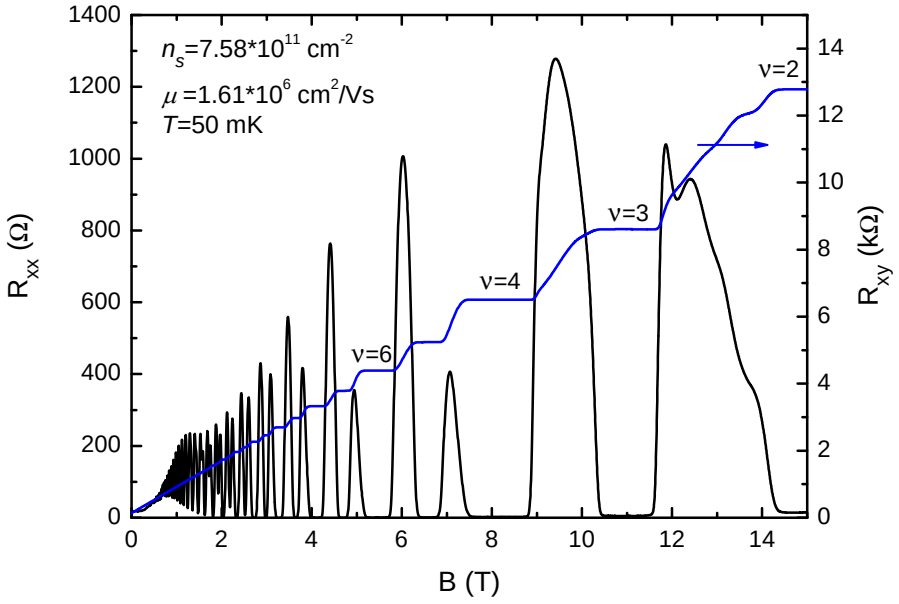

Figure 1.6: Longitudinal resistance and QH-Effect (transverse resistance) in a single-layer system formed by a quantum well.

1.2.5 Fractional Quantum Hall Effect

Apart from the integer QH-Effect which can be explained by single-particle physics, Tsui *et al.* discovered a Hall-resistance quantization at ν=1/3 in high mobility samples in 1982 [Tsui82]. FQHE is the result of quite different underlying physics involving correlations among the electrons and strong Coulomb interactions. Electron-electron correlations mediated by the Coulomb interaction are responsible for the existence of a gap at the Fermi energy giving rise to the FQHE. The particles condense into special quantum states whose excitations have the bizarre property of being described by fractional quantum numbers $\nu = p/q$ with integer values of p and q and q is odd (see original figure 1.7 taken from [Stoermer92]), including fractional charge and fractional statistics that are intermediate between ordinary Bose and Fermi statistics.
Here, only an introduction of FQHE is given which helps to understand basics for multilayer electron systems and experimental studies in trilayer electron systems (Chapter 6) which exhibit new effects due to an extra degree of freedom. As for the integer QHE, the plateaus at fractional filling factors occur because of energy gaps in the DOS. Laughlin proposed a fermionic many-body ground state wavefunction for the most pronounced FQHE states at $\nu = 1/q$ of the form (see [Laughlin83])

$$\chi(1/q) = \prod_{i<j} \left(\frac{z_i - z_j}{l_B} \right)^q \exp\left[-\frac{1}{4} \sum_i \frac{|z_i^2|}{l_B^2} \right] \tag{1.30}$$

where $z_i = x_i + \mathrm{i}y_i$ are the electron positions in the complex notation. The Laughlin wavefunction describes a homogenous incompressible state in the lowest Landau level.

This wavefunction also correctly describes the first observed FQH state at ν=1/3. Using electron-hole symmetry arguments, filling factors $\nu = 1 - 1/q$ can also be explained. The remaining odd-denominator fractional states require analogous condensations of the fractionally charged quasiparticle excitations of the Laughlin states. This is called the "hierarchy model" [Eisenstein90]. Two aspects can not be explained by Laughlin's

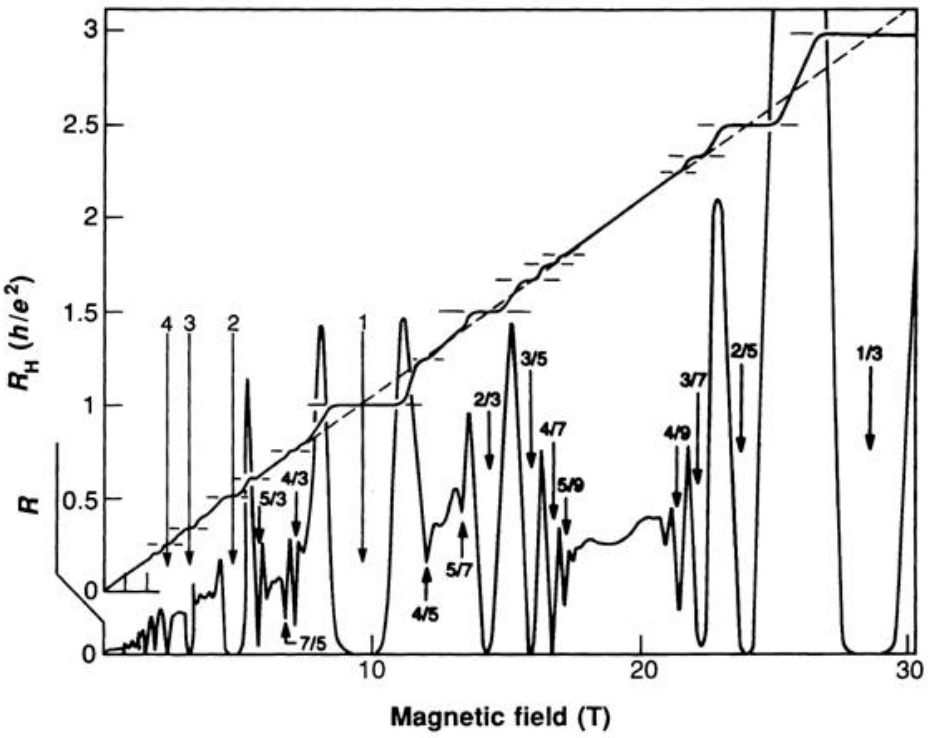

Figure 1.7: Additionally to the plateaus of the IQHE in R_{xy} and the vanishing longitudinal resistance R_{xx}, fractional QHE shows these features for filling factors $\nu = p/q$ with integer values of p and q, q is odd (figure taken from [Stoermer92]).

wavefunction: the system at ν=1/2 which does not display a FQHE and the even-denominator states ν=5/2, ν=7/2. Jain proposed a new kind of quasi-particles, so-called Composite Fermions (CFs) [Jain89]. With these CFs, one can understand FQHE in terms of IQHE of these particles. An even number of flux tubes (each of unit strength Φ_0) is attached to every electron in a 2DEG. The resulting composite particles are CFs with Fermi statistics. Within this model, ν=1/2 can be explained because the average of the statistical flux cancels the external magnetic flux [Halperin93]. Other FQH states, e.g. ν=2/5 or ν=3/7 are part of the series $p/(2sp \pm 1)$, with integers s and p, and a compelling interpretation can be found within CF theory according to which the FQHE may be viewed as an IQHE of a novel quasi-particle that consists of an electron that "captures" an even number of flux quanta [Jain89, Jain90]. In 1987, the states ν=5/2, ν=7/2 with even denominator have been observed [Willett87]. Up to this moment only states $\nu = p/q$ with odd denominators had been observed in monolayer systems. From a theoretical point of view, it was shown in [Moore91] and [Greiter91] that this FQH states could be described in terms of a very particular, so-called Pfaffian

wavefunction, involving particle pairing and the excitations which are anyons with non-Abelian statistics. The state ν=5/2 is also called "Pfaffian-state". These particles are intensively studied in today's research because they may play a relevant role in quantum computation.
Experimental observation of FQHE requires high mobility samples because this effect is sensitive to disorder[3]. The excitation gap and thus the corresponding energy is much smaller compared to cyclotron and Zeeman gap (usually, tenth or hundreds of mK). Fractional states with higher denominator have smaller excitation gaps, therefore they are weaker and need lower temperature. In general it is assumed that high magnetic fields facilitate the observation of FQHE.

1.2.6 Phonon induced resistance oscillations - PIROs

Beyond SdH oscillations which arise owing to a magnetic field induced modulation of the DOS at the Fermi level ε_F, Zudov *et al.* [Zudov01b] have found another magnetoresistance oscillation which is called magnetophonon resonance (MPR). In earlier works [Gurevich61, Tsui80] it has been reported that MPR appears due to longitudinal optical phonons under the condition $\omega_{LO} = n \cdot \omega_c$ with ω_{LO} the optical and ω_c the cyclotron frequency, respectively and n is an integer number. These oscillations can be observed only at relatively high temperatures (100 K< T <180 K) [Tsui80].
In contrast to this high-temperature observation of MPR, Zudov *et al.* have observed magnetoresistance oscillations in a high-mobility 2DEG in a narrow temperature range between 2 K and 9 K [Zudov01b]. Data is interpreted in terms of a magnetophonon resonance mediated by thermally excited *interface-acoustic phonon* modes. The oscillations are also periodic in the inverse magnetic field. Zudov *et al.* explain that high LL electrons interact with interface phonons which carry a wavevector q =$2k_F$, where k_F is the Fermi wavevector of the 2DEG at zero magnetic field. Therefore, one can introduce a condition for resonance absorption or emission of an interface phonon given by

$$2k_F s = n\omega_c, \qquad n = 1, 2, 3, \ldots \quad . \tag{1.31}$$

Eq. (1.31) determines the values of B for maxima of these phonon-induced resistance oscillations (PIROs). s is the sound velocity. The authors also report that negative and positive magnetoresistance occurs and that its strength and even its sign is largely cooling-cycle dependent. Since the Fermi wavevector depends on carrier density by $k_F = \sqrt{2\pi n_s}$, MPRs shift to higher magnetic fields with increasing density. In a recent publication, Hatke *et al.* studied PIROs in a very-high mobility 2DEG [Hatke09b]. PIROs persist to much lower temperatures than predicted in the first observation in Ref. [Zudov01b] due to low disorder in these samples. Additionally, an ideal temperature for PIROs has been found where particular oscillations are best developed increasing with $\sqrt{B}$ and attributed to electron-electron interaction effects modifying the quantum scattering rate.

[3]Note that the disorder, on the other hand, is essential for the existence of the quantum Hall effects as the plateaus' width is determined by the disorder.

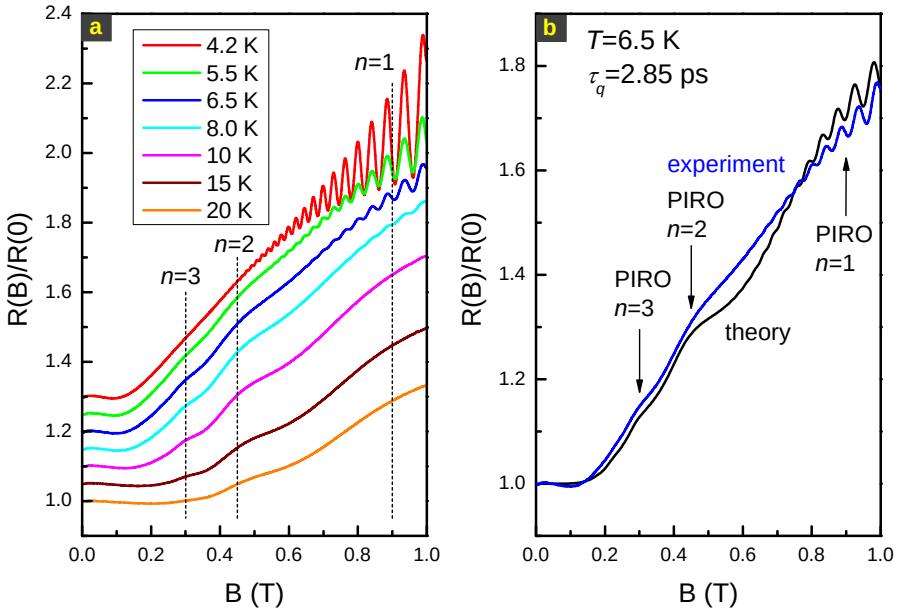

Figure 1.8: (a) Temperature dependence of PIROs from 4.2 to 20 K exhibits n=1, 2 and 3 (traces are shifted up for clarity, except the one for 20 K.). (b) Experiment and theoretical calculation at a constant temperature of 6.5 K.

For the samples investigated in this thesis, PIROs can also be observed in a certain temperature range, presented in Figure 1.8(a). The best features are observed for 5.5 K$< T <$20 K whereas PIROs do not occur at 4.2 K. Taking into account the high density of the samples and a large well width, the main contribution is due to longitudinal-acoustic (LA) phonons while transversal-acoustic (TA) phonons are less active and can be neglected. PIROs up to n=3 are observed and the longitudinal sound velocity s_{LA}=5.3 km/s is calculated with Eq. (1.31). A comparison of both experiment and theory for 6.5 K using a quantum lifetime of τ_q=2.85 ps, extracted from experiment, is shown in Figure 1.8(b) [Raichev09].

1.3 Magnetotransport in bilayer electron systems

In this section, basics of magnetotransport in bilayer electron systems, realized in double quantum wells (DQWs), are introduced. DQWs contain an extra degree of freedom in the growth direction giving rise to new transport phenomena, different from single quantum wells. The first part introduces general properties of DQW systems. The second part focuses on the peculiar magneto-intersubband (MIS) oscillations owing to additional intersubband scattering when Landau levels, which pass sequentially the Fermi energy with increasing perpendicular magnetic field, become in alignment at ε_F.

1.3.1 Basic properties of double quantum wells

Double quantum wells consist of two quantum wells separated by a narrow potential barrier. Two layers of GaAs are grown separated by a thin AlGaAs barrier via MBE-technique. Owing to the quantum-mechanical penetration of the wavefunctions of electrons through the thin barrier (tunneling effect), DQWs can be viewed as two parallel two-dimensional electron layers coupled by tunneling. This coupling induces a new quantum degree of freedom leading to a variety of interesting phenomena which can not be observed in conventional 2D single layer-systems.
In a simple tight-binding perturbation calculation where single isolated square QW-wavefunctions Ψ_1 and Ψ_2 are used as bias wavefunctions, an approximative solution to the Schrödinger equation can be found. Both isolated QWs are identic, each with an eigenenergy ε_{QW}. An infinite well-approximation can not be applied to the DQW situation because the wavefunctions are zero outside both single QWs, thus no coupling between the QWs can be achieved if they are in close proximity. If one assumes a coupled QW wavefunction Ψ, i.e. a linear combination of the isolated QW-wavefunctions, the result is $\Psi = a \cdot \Psi_1 + b \cdot \Psi_2$. Solving this Schrödinger equation results in energy levels, separated by a symmetric-antisymmetric energy gap Δ_{SAS}. The lower (higher) energy state is the (anti)symmetric combination of the basis wavefunction with the energy ε_S (ε_{AS}), see Figure 1.9. It should be added that this simple method does not include band bending which moves the wavefunctions to the outside of the QWs, reducing their overlap and thus Δ_{SAS}. A DQW-system is called balanced when the electron densities between the two wells are balanced (equal). In the energy diagram, the energy gap $\Delta_{12} = \Delta_{SAS}$ ($\Delta_{SAS} = \varepsilon_{AS} - \varepsilon_S$) leads to an additional splitting in a magnetic field. Figure 1.10 sketches the energy and the Landau fan diagram for a DQW. The energy

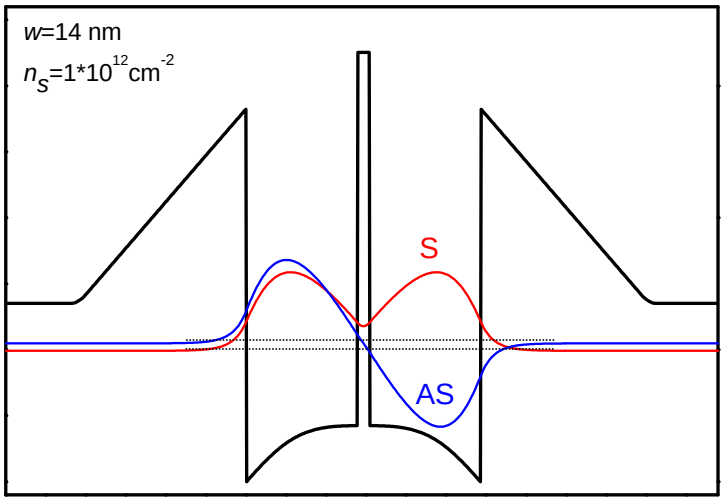

Figure 1.9: Sketch of the DQW-system with the symmetric and antisymmetric wavefunctions for the lowest two occupied subbands (Hartree-Fock calculation).

diagram shows the hierarchy of the energy gaps in a strong magnetic field. Additionally to the cyclotron energy gap ($\hbar\omega_c$) and the Zeeman energy gap (Δ_Z) which appears due to the spin splitting, DQWs exhibit a symmetric-antisymmetric energy gap (Δ_{SAS}). The Landau fan diagram consists of two sets of spin split Landau levels separated by the symmetric-antisymmetric energy gap (Δ_{SAS}). Δ_{SAS} is also a measure of the coupling strenght of the two QWs separated by a barrier. An increase in the barrier width decreases coupling. The samples in this work have barrier widths between 14 Å and 50 Å which results in a theoretically calculated Δ_{SAS} of 4.0 meV and 0.3 meV, respectively [Mamani08]. Hence, the systems here represent fairly strong coupling and strong tunneling[4]. The energies, sketched in Figure 1.10 can be resolved in high magnetic field

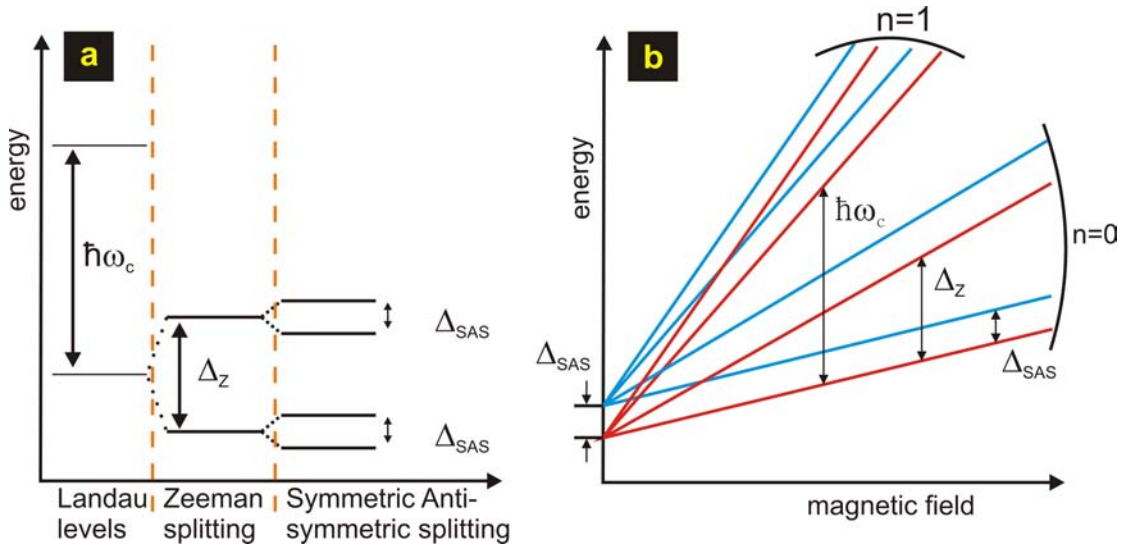

Figure 1.10: (a) Energy diagram with the cyclotron energy ($\hbar\omega_c$), Zeeman energy ($\Delta_Z = g^*\mu_B B$) and symmetric-antisymmetric energy (Δ_{SAS}). (b) Landau fan diagram for a DQW.

measurements and give rise to new transport phenomena with an increase of the parallel component ($B_\parallel$) of the magnetic field. These effects will be discussed in Chapter 6.

1.3.2 Magneto-intersubband oscillations (MIS oscillations)

Shubnikov-de Haas oscillations originate from a sequential passage of Landau levels through the Fermi level. These SdH oscillations are always present in 2D systems. In a 2DEG with more than one occupied 2D subband, the probability of intersubband transitions leads to a new kind of magnetoresistance oscillations. These oscillations are called MIS oscillations and can be observed in wide or high-density single QWs. For a high carrier concentration, electrons can populate more than one subband. Nevertheless, DQWs with high electron mobility seem to be the most appropriate system for experimental studies of this phenomenon. A small subband separation, a reasonably large

[4]DQW systems can be classified in different coupling regimes: a "no coupling regime" where the electron wavefunctions in the individual QWs do not overlap and without Coulomb interaction in opposite QWs, a "Coulomb coupling regime" where Coulomb interactions occur without tunneling between the two QWs, and a "weak coupling regime" ("strong coupling regime") with weak (strong) tunneling.

quantum lifetime of electrons, and a strong tunnel coupling between the wells enables a high probability of intersubband scattering. In the case of two occupied subbands, the energy levels ε_1 and ε_2 are below the Fermi energy ε_F. With increasing magnetic field, Landau levels of both energy levels pass consequtively the Fermi energy. This is illustrated in Figure 1.11. The MIS oscillation peaks correspond to the subband alignment $\Delta = k\hbar\omega_c$ with Δ the subband separation and k an integer number. An analytical theory can be found in Ref. [Raikh94]. In this system it is also possible to control the intersubband energy gap and probabilities of intersubband transitions in a wide range by biasing the structure with an external gate or otherwise by changing the barrier width.

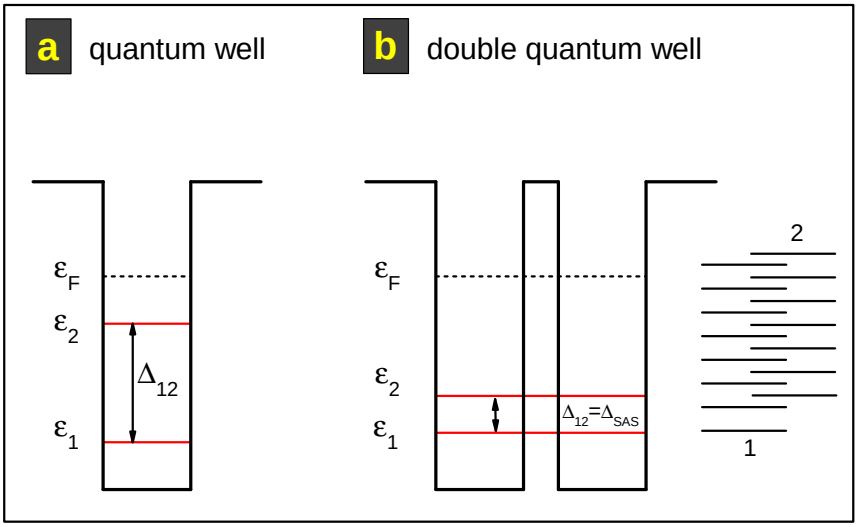

Figure 1.11: (a) QW with two occupied 2D subbands and (b) DQW-system with two occupied 2D subbands and staircase of Landau levels giving rise to MIS oscillations.

In this thesis, high density ($n_s \simeq 10^{12}$ cm^{-2}) balanced DQWs are investigated with high electron mobility ($\mu \simeq 10^6$ cm^2/V s). For balanced DQWs, we have $\Delta = \Delta_{SAS}$ [Raichev08]. Magnetoresistance measurements which describe all properties of balanced DQWs are summarized in Figure 1.12. Figure 1.12(a) presents the difference of normalized magnetoresistance $R(B)/R(0)$ of a QW and a balanced DQW for T=50 mK. Whereas the QW shows SdH oscillations, periodic in $1/B$ starting at B=0.2 T, the DQW exhibits MIS oscillations superimposed on SdH oscillations. With increasing temperature, see Figure 1.12(b), the small-period SdH oscillations are strongly suppressed. The remaining long-period oscillations are the MIS oscillations, also periodic in $1/B$. By further increasing temperature, the thermal broadening of the Fermi distribution exceeds the cyclotron energy $\hbar\omega_c$ and SdH oscillations are strongly damped whereas MIS oscillations are still visible since the physical origin of the MIS oscillation is not related to the position of Landau levels with respect to the Fermi energy. Inset (1) in Figure 1.12(b) indicates the last two peaks (k=1, 2) at T=15 K of the Landau level alignment condition. The densities can be extracted by using a simple Fast Fourier

transform (FFT) of the magnetoresistance data as a function of $1/B$. In the balanced case, see top trace in Figure 1.13 which corresponds to a gate voltage $V_g = 0\ V$, two peaks occur for each occupied subband. By adding the two densities from the FFT analysis, a rough agreement with the density extracted from the low-field Hall resistance is obtained. It must be noticed that the symmetric and antisymmetric states have unequal electron densities but the two QWs still have equal electron densities.

The fact that MIS oscillations survive at high temperature can be used to obtain information about quantum lifetime τ_q of electrons where SdH oscillations are already absent. The extracted data in inset (2) of Figure 1.12(b) presents temperature dependence of τ_q up to 10 K extracted by comparing amplitude of MIS oscillations in experiment and theory. Since MIS oscillations survive up to temperatures of 30 K (see [Mamani08]), the temperature range chosen here corresponds to the microwave experiments in DQW structures in Chapter 3 where effects due to microwave irradiation persist up to T=10 K. The temperature dependence of the quantum lifetime τ_q can be fitted by $\tau_q(T) = \tau_q(0)/\left[1 + \lambda(T/T_0)\right]$, where $T_0 = \sqrt{\varepsilon_f \hbar/\tau_q(0)}$ and λ a numerical constant in the order of unity, here λ=3.5. Fermi energy is calculated to ε_F=18 meV and $\hbar/\tau_q$=0.2 meV, respectively.

The mechanism leading to the observed oscillations relies on intersubband scattering, resonantly modulated by the Landau quantization. The quantitative description of magnetotransport in DQWs which takes elastic scattering into account is based on a Hamiltonian $\mathcal{H}$, a 2×2 matrix in the single-well eigenstate basis, see [Mamani08]. In the regime of classically strong magnetic fields, the symmetric part of the diagonal resistivity, ρ_d is given by the expression

$$\begin{aligned}\frac{\rho_d}{\rho_0} &= 1 - 2\mathcal{T}\tau_{tr} \sum_{j=1,2} \nu_j^{tr} d_j \cos\frac{2\pi(\varepsilon_F - \varepsilon_j)}{\hbar\omega_c} \\ &\quad + \tau_{tr}\left[\sum_{j=1,2} \frac{2n_j}{n_s}\nu_{jj}^{tr} d_j^2 + 2\nu_{12}^{tr} d_1 d_2 \cos\left(\frac{2\pi\Delta_{12}}{\hbar\omega_c}\right)\right] \end{aligned} \tag{1.32}$$

where the sums are taken over both subbands $j = 1, 2$ with energies ε_j separated by $\Delta_{12} = |\varepsilon_2 - \varepsilon_1|$. The second term is the first-order quantum correction describing the SdH oscillations ($\varepsilon_F = \hbar^2\pi n_s/2m^*$ is the Fermi energy). The third term is the equilibrium second-order quantum correction containing the MIS oscillations. In Eq. (1.32), $\rho_0 = m^*/e^2 n_s \tau_{tr}$, τ_{tr} is the averaged transport time defined as $1/\tau_{tr} = (\nu_1^{tr} + \nu_2^{tr})/2$, $1/\tau^* = (\nu_1^* + \nu_2^*)/2$, $d_j = \exp(-\pi\nu_j/\omega_c)$ are the Dingle factors, $\mathcal{T} = X/\sinh X$ with $X = 2\pi^2 T_e/\hbar\omega_c$ is the thermal suppression factor, and n_j are the partial densities in the subbands ($n_1 + n_2 = n_s$). T_e is the electron temperature. The subband-dependent quantum relaxation rates ν_j and $\nu_{jj'}$, as well as the scattering rates ν_j^{tr}, ν_j^*, $\nu_{jj'}^{tr}$, and $\nu_{jj'}^*$ are defined according to

$$\begin{aligned}\nu_j = \sum_{j'=1,2} \nu_{jj'}, \quad \nu_j^{tr} = \sum_{j'=1,2} \frac{n_j + n_{j'}}{n_s}\nu_{jj'}^{tr}, \\ \nu_j^* = \sum_{j'=1,2} \left(\frac{n_j + n_{j'}}{n_s}\right)^2 \nu_{jj'}^*, \end{aligned} \tag{1.33}$$

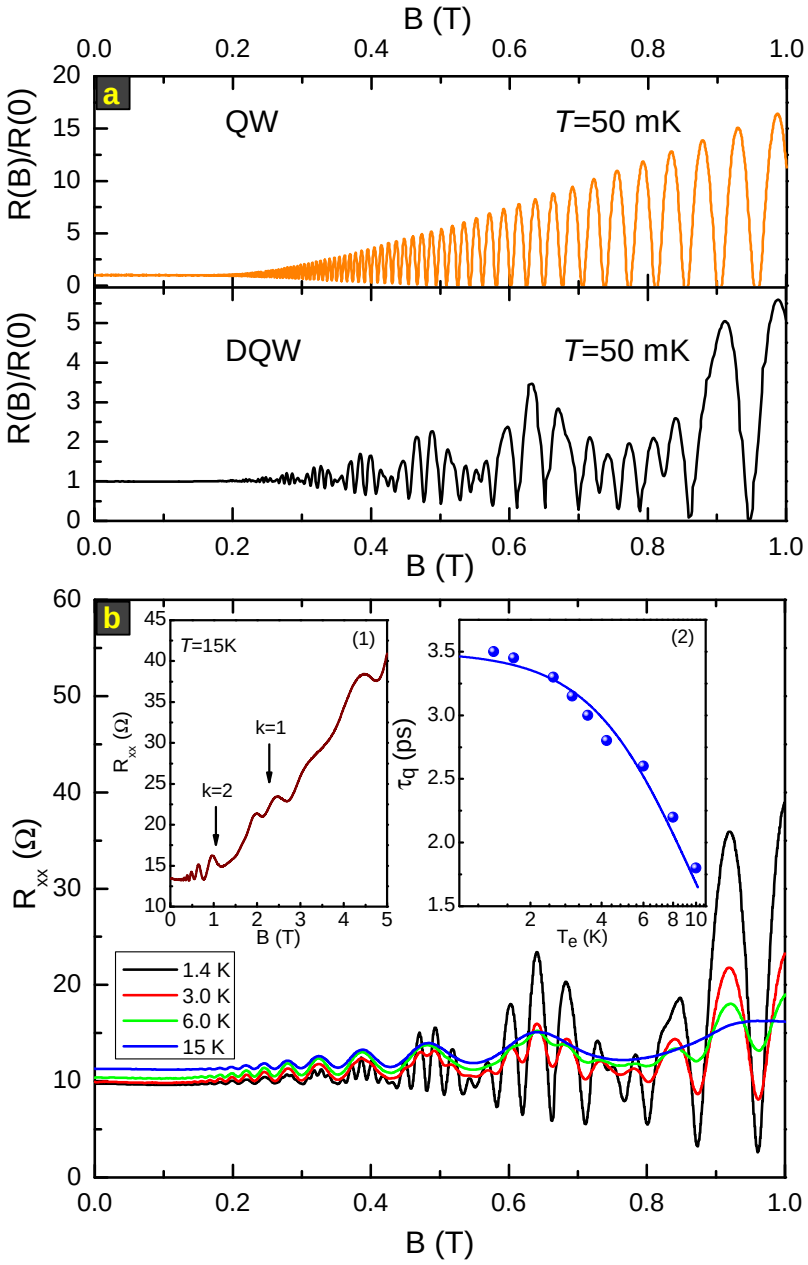

Figure 1.12: (a) Normalized longitudinal resistance for a QW and a DQW (d_b=14 Å) at T=50 mK. The DQW shows well-pronounced MIS oscillations, superimposed on SdH oscillations. (b) Temperature dependence of MIS oscillations: MIS survive at high temperatures, k=1,2 are marked by arrows [inset (1)] and the quantum lifetime τ_q is extracted by comparing amplitude of MIS oscillations of experiment and theory with Eq. (1.35) [inset (2)].

and

$$\left.\begin{matrix}\nu_{jj'}\\ \nu^{tr}_{jj'}\\ \nu^{*}_{jj'}\end{matrix}\right\} = \int_0^{2\pi}\frac{d\theta}{2\pi}\nu_{jj'}(\theta)\times\left\{\begin{matrix}1\\ F_{jj'}(\theta)\\ F^2_{jj'}(\theta)\end{matrix}\right. , \tag{1.34}$$

$$\nu_{jj'}(\theta) = \frac{m}{\hbar^3}w_{jj'}\left(\sqrt{(k_j^2+k_{j'}^2)F_{jj'}(\theta)}\right),$$

where $w_{jj'}(q)$ are the Fourier transforms of the correlators of the scattering potential, $F_{jj'}(\theta) = 1 - 2k_j k_{j'} \cos\theta/(k_j^2 + k_{j'}^2)$, θ is the scattering angle, and $k_j = \sqrt{2\pi n_j}$ is the Fermi wavenumber for subband j. The general expression is now considerably simplified in the case relevant to our high-density DQWs, when $\Delta_{12}/2$ is much smaller than the Fermi energy ε_F and the interlayer correlation of scattering potentials can be neglected[5]. In this case one may approximate $n_1 \simeq n_2 \simeq n_s/2$ and $\nu_{11} \simeq \nu_{22}$, $\nu_{11}^{tr} \simeq \nu_{22}^{tr}$, $\nu_{11}^{*} \simeq \nu_{22}^{*}$, which leads also to $\nu_1 \simeq \nu_2$, $d_1 \simeq d_2$, $\nu_1^{tr} \simeq \nu_2^{tr} \simeq 1/\tau_{tr}$, and $\nu_1^{*} \simeq \nu_2^{*} \simeq 1/\tau^{*}$. Moreover, in balanced DQWs which have been used in this thesis one has $\nu_{12}^{tr} \simeq \nu_{jj}^{tr}$ and $\nu_{12}^{*} \simeq \nu_{jj}^{*}$ [Raichev08]. Applying these approximations to Eq. (1.32), one can rewrite it in the form

$$\frac{\rho_d}{\rho_0} \simeq 1 - 2\mathcal{T} d \sum_{j=1,2} \cos\frac{2\pi(\varepsilon_F - \varepsilon_j)}{\hbar\omega_c} + d^2 \left[1 + \cos\frac{2\pi\Delta_{12}}{\hbar\omega_c}\right]. \tag{1.35}$$

The second-order quantum contribution (the last term in this expression) is reduced to the corresponding single-subband form Eq. (1.27) if the MIS oscillation factor $1 + \cos(2\pi\Delta/\hbar\omega_c)$ is replaced by 2. The amplitude of this contribution is determined by the single squared Dingle factor $d^2 = \exp(-2\pi/\omega_c\tau_q)$, where the quantum lifetime is defined as $1/\tau_q \equiv (\nu_1 + \nu_2)/2$.

Finally, low-field magnetotransport is discussed if the density in a DQW is controlled by an external gate. By applying a positive or a negative gate voltage, first the upper quantum well is penetrated. Here, only the case of a negative gate voltage will is mentioned. Negative gate biases raise the conduction band at the surface of the sample and deplete electron layers under the gate, i.e. in a DQW system first the upper well is affected. Figure 1.13 presents longitudinal resistance up to 1 T. Without an external gate voltage, the total density of the DQW system is $n_s = 8.9 \cdot 10^{11}$ cm^{-2}, therefore each well has an electron density of $n_s = 4.45 \cdot 10^{11}$ cm^{-2} - the system is in balance or in resonance, see Figure 1.13(1). The FFT spectra shows the densities for that case. By decreasing the gate voltage, the upper well is slowly depleated whereas the density in the lower well remains constant. Figure 1.13(2) presents this situation where also a positive magnetoresistance occurs for a density of $n_s = 5.2 \cdot 10^{11}$ cm^{-2}. Figure 1.13(3) shows the case where the upper well is completely depleted and only the electrons in the lower well can contribute to the transport. Here, the FFT spectra clearly demonstrates that only one subband is occupied with a density of $n_s = 3.9 \cdot 10^{11}$ cm^{-2}. By further decreasing the gate voltage, one can even affect and depleate the lower quantum well. It has been recently shown in Ref. [Mamani09a] that both classical and quantum contributions of magnetotransport are necessary to explain the large positive magnetoresistance [Figure 1.13(b)] in a bilayer electron system when the latter is driven from a double to a single layer configuration by an external gate.

[5] This is valid in our samples because the scattering occurs mostly by the impurities placed in the side barriers and interface roughness.

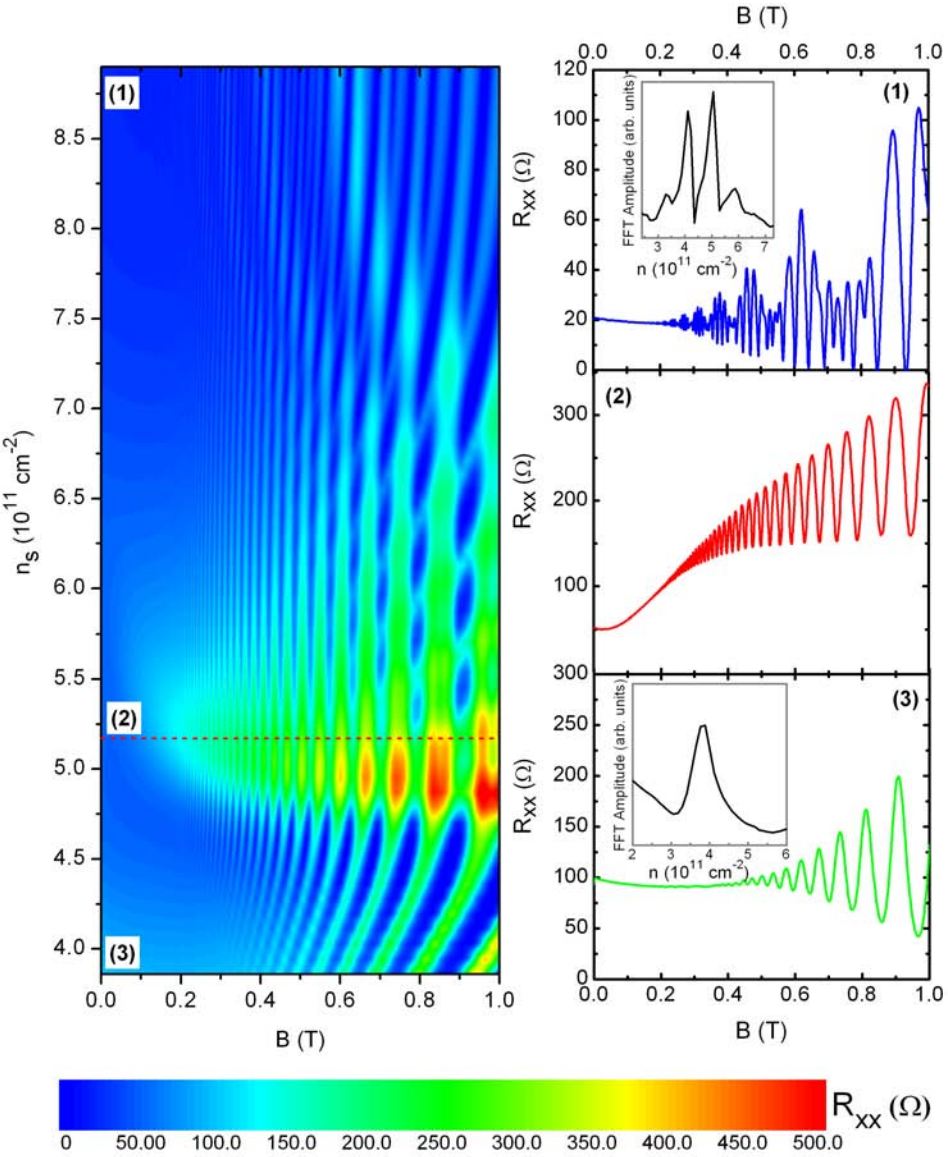

Figure 1.13: By applying a negative gate voltage V_g on the topgate of the sample, the balanced DQW (1) becomes first imbalanced (2) and for a high negative gate voltage, the upper QW in the DQW systems is completely depleted (3). The FFT spectra, taken from the longitudinal resistance are shown in (1) and (3) in the insets.

Summary

This chapter has given a basic introduction in two-dimensional electron systems. Low-field magnetotransport phenomena like Shubnikov-de Haas oscillations and magneto-

intersubband oscillations, which occur in systems with two occupied two-dimensional subbands, have been introduced. Both resistance oscillation phenomena will be dramatically changed if samples are exposed to a continuous microwave irradiation which is the topic of the following chapters and studies.
Finally, the most remarkable phenomena in condensed matter physics, quantum Hall effect and fractional quantum Hall effect have been introduced in single layer electron systems. Chapter 6 will give an introduction into physics of QH-effects in multilayer electron systems (double and triple quantum wells).

Chapter 2

2D systems under microwave irradiation in magnetic fields

This chapter is dedicated to introduce non-equilibrium magnetotransport phenomena in two-dimensional electron systems under microwave (MW) irradiation (usually in the GHz range).
The resistivity shows qualitative new features, strongly dependent on frequency and intensity of the microwaves. These new oscillations are called microwave-induced resistance oscillations (MIROs) and have been discovered by Zudov *et al.* [Zudov01a] in 2001. MIROs are governed by the ratio of the radiation frequency ω to the cyclotron frequency ω_c. For a sufficiently high MW intensity and for samples with ultrahigh electron mobility, MIROs evolve into "zero-resistance states" (ZRS), experimentally discovered by Mani *et al.* [Mani02] and Zudov *et al.* [Zudov03]. The first section presents the discovery of MIROs and ZRS.
Both ZRS and MIROs have also attracted much theoretical interest and several microscopic mechanisms being responsible for these phenomena have been proposed. Two mechanisms, widely discussed in literature, produce similar results concerning MIRO phase and periodicity: displacement mechanism and inelastic mechanism. Both mechanisms will be discussed in this chapter. The role of electrodynamic effects will also be mentioned. Experiments on high-electron density samples with a moderate mobility have been carried out and present all qualitative and quantitative properties of the MIRO phenomenon.
In the second part, we introduce fractional microwave induced resistance oscillations (fractional MIROs or FMIROs). With increasing microwave power, novel MIRO features associated with fractional ratios $\epsilon = \omega/\omega_c = n/m$ where n and m are integer appear. We present new experimental observations in high-density 2D systems up to a denominator m=8 which are analyzed and discussed in connection with two existing theoretical models for FMIROs.

2.1 Discovery of MIROs and ZRS

One fundamental issue in physics of correlated systems is the electrodynamic response of a quantum Hall system. The first experimental observation of microwave-induced resistance oscillations (MIROs) in longitudinal resistance was published by Zudov *et al.* [Zudov01a] at a temperature of 1.7 K (with MW irradiation) and in samples with low density ($n_s \simeq 2.0 \cdot 10^{11}$ cm^{-2}) and high mobility ($\mu \geq 3.0 \cdot 10^6$cm^2/V s). It has been found that, in a 2DEG (formed by either a quantum well or a heterostructure) exposed to microwave irradiation in a perpendicular magnetic field, MIROs satisfy a resonance condition in which the cyclotron energy $\hbar\omega_c = \hbar eB/m^*$ is an *integer multiple* n of the radiation energy $\hbar\omega$, where n is the difference between the indices of participating Landau levels:

$$\hbar\omega = n \cdot \hbar\omega_c, \qquad n = 1, 2, 3, \ldots . \tag{2.1}$$

MIROs, like SdH oscillations are periodic in the inverse magnetic field $1/B$. For ultra-high mobility samples ($\mu \geq 1.5 \cdot 10^7$cm^2/V s), these MIROs evolve into "zero-resistance states" discovered by Mani *et al.* [Mani02] and Zudov *et al.* [Zudov03] with a vanishing longitudinal resistance whereas Hall resistance does not show a plateau. Both discov-

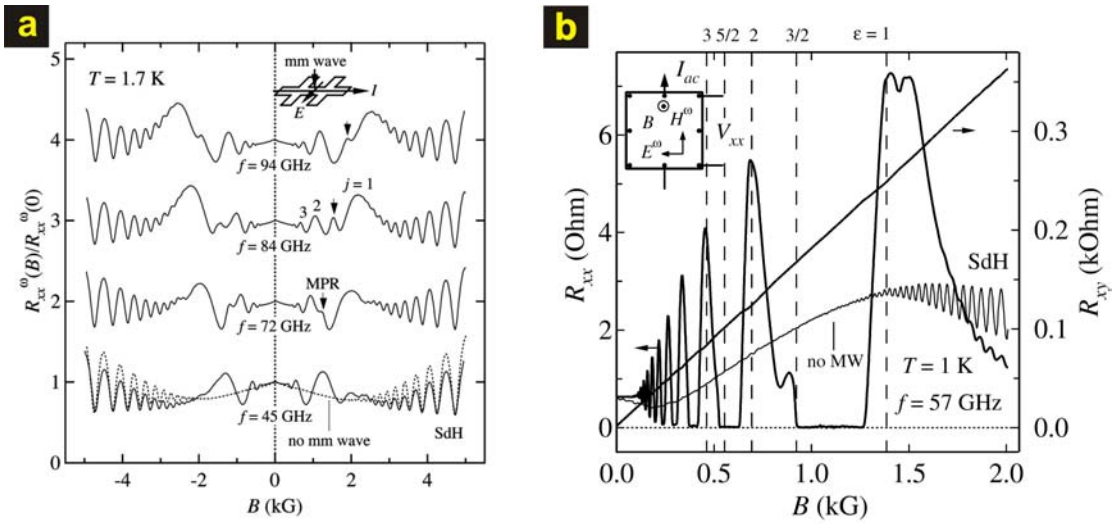

Figure 2.1: (a) Normalized resistance exposed to MW irradiation exhibits MIROs, presented for different frequencies (taken from Ref. [Zudov01a]). The arrows mark a magnetoplasmon resonance (MPR) signal. (b) Resistance exposed to MW irradiation in an ultrahigh mobility sample shows ZRS (measurement by Zudov *et al.*, taken from Ref. [Zudov03]).

eries of MIROs and ZRS by Zudov *et al.* are presented in Figure 2.1. In Figure 2.1(a) an additional feature occurs, marked with arrows which indicate a magnetoplasmon resonance signal (MPR) [Vasiliadou93]. The resonance response occurs at frequency f_{res} with $f_{res}^2(B) = f_{res}^2(B=0) + f_c^2$ where f_c^2 is the cyclotron frequency. This photoresponse is dominated by collective plasmon excitations confined within the width of the Hall-bar structure. More details can be found in Ref. [Vasiliadou93].

2.2 Theory of microwave-induced resistance oscillations (MIROs)

The observations of MIROs and ZRS attracted much theoretical interest and different microscopic mechanisms responsible for both phenomena have been proposed. Magnetoresistance oscillations appear under MW irradiation arising from a correction to the magnetoresistance owing to resonant absorption of MW radiation. The correction, or MW-induced photoresistance (simply called "photoresistance" in literature) is defind as $\Delta R_{xx}(B) = R_{xx}^{MW}(B) - R_{xx}(B)$.
Ryzhii and co-workers have published two papers ([Ryzhii70, Ryzhii86]) thinking about a calculation of the conductivity to second order in the radiation with a prediction of negative conductivity. This mechanism, known as "displacement mechanism" was later once again found by Durst *et al.* after the discovery of MIROs and ZRS [Durst03]. A second mechanism, widely discussed in literature was introduced by Dorozhkin [Dorozhkin03] and Dmitriev *et al.* [Dmitriev05]: the "inelastic mechanism", associated with a microwave-generated non-equilibrium oscillatory component of the electron distribution function. Beyond these mechanisms, which produce similar results concerning phase and periodicity of MIROs, MIROs can also appear due to the "photovoltaic mechanism" and to the "quadrupole mechanism" which leads to an oscillatory contribution to the Hall resistivity. In the following sections, displacement and inelastic mechanism will be introduced and a general description of photoresistance in a 2D system with one occupied subband is presented. In the theoretical part, $\hbar = k_B = 1$. Finally, electrodynamic effects are mentioned which are connected to MIRO physics.

2.2.1 Displacement mechanism

This mechanism explains magnetoresistance oscillations under microwave irradiation in 2D systems as a consequence of photoexcited disorder-scattered electrons which contribute to the dc resistivity in an oscillatory manner inherited from a broadened Landau level structure of the energy spectrum. The disorder-mediated current depends on the ratio of MW energy to the cyclotron energy and flows either parallel or antiparallel to the applied electric field. The model is sketched in Figure 2.2 which gives a qualitative understanding of this mechanism. If an external electric field is applied in the x-direction the Landau level energy has a spatial gradient

$$\varepsilon_n \simeq n\omega_c + eE_{dc}x, \tag{2.2}$$

and the Landau levels are tilted (thick grey lines). Electrons absorb photons and are excited by the energy ω. These photoexcited electrons are scattered by disorder and kicked to the right or to the left by a distance $\pm\Delta x$. It should be noticed that the scattering probability is equal for Δx and $-\Delta x$. The total current density j depends only on the available final states. In detail, the prefered scattering direction is determined by the closest tilted Landau level: if the absorbed MW energy is a bit more than the distance

between Landau levels ($\hbar\omega \geq n \cdot \hbar\omega_c$), the scattering event is in the opposite direction of the electric field and the conductivity decreases, otherwise the favored direction is along the electric field and conductivity increases.

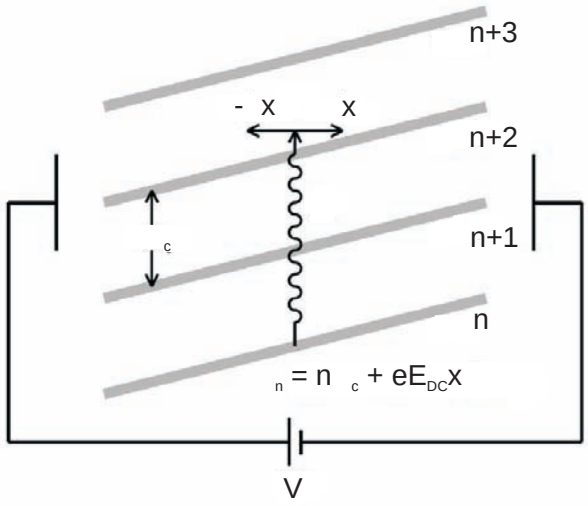

Figure 2.2: Simple picture of the displacement mechanism: Absorption of microwaves with an energy ω via scattering parallel (anti-parallel) to the Landau levels which are tilted by the applied dc electric field. Therefore, conductivity is either increased or decreased, dependent on the absorbed MW energy. Figure taken from Ref. [Durst03].

The total current measured in the experiments is the sum of j_0 and the radiation induced contribution Δj:

$$j = j_0 + \Delta j. \tag{2.3}$$

By calculating the rate w at which the electron is scattered and including the average over disorder (see details in Ref. [Durst03]), the density of states can be written as

$$\mathcal{D}(\varepsilon) = \mathcal{D}_0 + \mathcal{D}_1 \cos\frac{2\pi\varepsilon}{\omega_c} \tag{2.4}$$

where $\mathcal{D}_i$ is the average local density of states. Now, the additional conductivity $\Delta\sigma_{xx}$ can be simplified to

$$\Delta\sigma_{xx} \quad \propto \quad \left.\frac{\partial\mathcal{D}}{\partial\varepsilon}\right|_{\varepsilon=\omega} \propto -\sin\frac{2\pi\omega}{\omega_c}. \tag{2.5}$$

The displacement mechanism gives a correct period of radiation-induced resistivity oscillations and leads to a locally negative conductivity. Temperature dependence enters in the displacement mechanism via τ_q/τ_{tr} which is a slow function of T for low temperatures.

2.2.2 Inelastic mechanism

This theory, developed by Dmitriev and co-workers explains the occurring resistance oscillations under microwave irradiation with an oscillatory part of the electron distribution function [Dmitriev05]. This approach of kinetics of a 2DEG exposed to MW

irradiation and in a magnetic field is based on the quantum Boltzmann equation (QBE) for a semiclassical distribution function at higher Landau levels. 2D electrons in a classically strong magnetic field and in the presence of a random potential are considered under a dc electric field E_{dc} and a microwave electric field E_ω.
The measured longitudinal resistivity ρ_{ph} in a sample exposed to a microwave electric field is connected to the photoconductivity via $\rho_{ph} \simeq \rho_{xy}^2 \sigma_{ph}$, see Eq. (1.22). The photoconductivity per spin is given by

$$\sigma_{ph} = \int d\varepsilon \; \sigma_{dc}\left(\varepsilon\right) \left[-\partial_\varepsilon f(\varepsilon)\right], \tag{2.6}$$

where $f(\varepsilon)$ is the electron distribution function and

$$\sigma_{dc}\left(\varepsilon\right) = \sigma_{dc}^D \cdot \tilde{\nu}^2\left(\varepsilon\right) = \frac{e^2 \nu_0 v_F^2}{2\omega_c^2 \tau_{tr}} \cdot \frac{\nu\left(\varepsilon\right)}{\nu_0} \tag{2.7}$$

determines the contribution of electrons with energy ε to the dissipative transport. σ_{dc}^D is the Drude conductivity, $\nu_0 = m^*/2\pi$ is the density of states[1] at B=0. $\nu(\varepsilon)$ represents the oscillations in the density owing to the Landau quantization whereas $\tilde{\nu}^2\left(\varepsilon\right)$ is a dimensionless DOS, $\tilde{\nu}\left(\varepsilon\right)$=$\nu(\varepsilon)/\nu_0$. The dominant effect is due to a nontrivial energy dependence of the non-equilibrium distribution function $f(\varepsilon)$. Now, the latter can be found as a solution of the stationary kinetic equation (QBE, zero angular harmonic of the distribution function)

$$St_\omega\{f\} + St_{dc}\{f\} = -St_{in}\{f\} \tag{2.8}$$

where the terms on the left side represent the effect of microwaves $St_\omega\{f\}$ and dc fields $St_{dc}\{f\}$. The right side is the collision integral $St_{in}\{f\}$. The calculation and assumption for both microwave and dc field $St_\omega\{f\}$ and $St_{dc}\{f\}$, respectively, can be found in Ref. [Dmitriev05]. Then the kinetic equation (2.8) is written as

$$E_\omega^2 \frac{\sigma_\omega^D}{2\omega^2\nu_0} \sum_{\pm} \tilde{\nu}(\varepsilon \pm \omega)[f(\varepsilon \pm \omega) - f(\varepsilon)] + E_{dc}^2 \frac{\sigma_{dc}^D}{\nu_0 \tilde{\nu}(\varepsilon)} \partial_\varepsilon [\tilde{\nu}^2(\varepsilon) \partial_\varepsilon f(\varepsilon)] = \frac{f(\varepsilon) - f_T(\varepsilon)}{\tau_{in}} \tag{2.9}$$

with the Fermi distribution $f_T(\varepsilon)$ and where the inelastic processes are included in the relaxation time approximation. Now one can introduce dimensionless units for the strength of microwave and dc electric fields:

$$\mathcal{P}_\omega = \frac{\tau_{in}}{\tau_{tr}} \left(\frac{eE_\omega v_F}{\omega}\right)^2 \frac{\omega_c^2 + \omega^2}{\left(\omega^2 - \omega_c^2\right)^2}, \tag{2.10}$$

$$\mathcal{Q}_{dc} = \frac{2\tau_{in}}{\tau_{tr}} \left(\frac{eE_{dc} v_F}{\omega_c}\right)^2 \left(\frac{\pi}{\omega_c}\right)^2, \tag{2.11}$$

with E_ω the strength of the microwave electric field and E_{dc} the strength of the dc electric field. It should be added that both factors are governed by the ratio of τ_{in}/τ_{tr}

[1] Here, the same notation for the density of states is used as in the theoretical work (Ref. [Dmitriev05]).

and depend strongly on temperature via $\tau_{in} \propto T^{-2}$. Using the dimensionless units in Eq. (2.10) and Eq. (2.11), the kinetic equation can be written as

$$\frac{\mathcal{P}_\omega}{4}\sum_{\pm}\tilde{\nu}(\varepsilon\pm\omega)[f(\varepsilon\pm\omega)-f(\varepsilon)]+\frac{\mathcal{Q}_{dc}\omega_c^2}{4\pi^2\tilde{\nu}(\varepsilon)}\partial_\varepsilon[\tilde{\nu}^2(\varepsilon)\partial_\varepsilon f(\epsilon)]=f(\varepsilon)-f_T(\varepsilon) \tag{2.12}$$

In the case of overlapping Landau levels the DOS is given by

$$\tilde{\nu}=1-2d\cos\frac{2\pi\varepsilon}{\omega_c},\qquad d=\exp\left(-\frac{\pi}{\omega_c\tau_q}\right)\ll 1. \tag{2.13}$$

Here, d is the Dingle factor containing τ_q, the quantum lifetime which is smaller than the transport time τ_{tr} ($\tau_q \ll \tau_{tr}$) in high mobility systems. Now, the kinetic equation (2.12) is solved to the first order in d in the form

$$f=f_0+f_{osc}+O(d^2),\qquad f_{osc}\equiv d\Re[f_1(\varepsilon)\exp(i2\pi\varepsilon/\omega_c)]. \tag{2.14}$$

The electron distribution function f gets an additional part f_{osc}

$$f_{osc}(\varepsilon)=d\frac{\omega_c}{2\pi}\cdot\frac{\partial f_T}{\partial\varepsilon}\cdot\sin\frac{2\pi\varepsilon}{\omega_c}\left[\frac{\mathcal{P}_\omega\frac{2\pi\omega}{\omega_c}\sin\frac{2\pi\omega}{\omega_c}+4\mathcal{Q}_{dc}}{1+\mathcal{P}_\omega\sin^2\frac{\pi\omega}{\omega_c}+\mathcal{Q}_{dc}}\right], \tag{2.15}$$

assuming that the MW electric field and dc field are not too strong. The oscillating electron distribution function $f(\varepsilon)$ and density of states $\nu(\varepsilon)$ are presented in Figure 2.3.

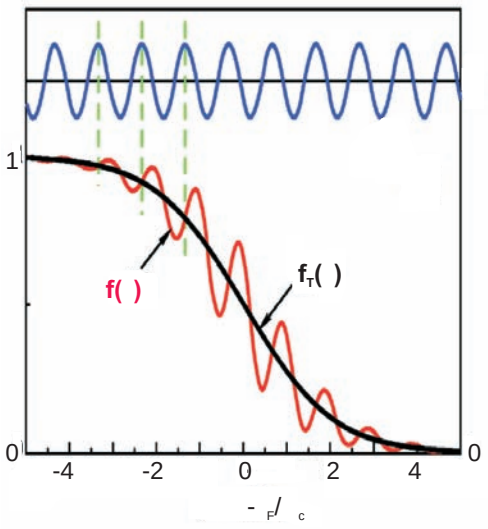

Figure 2.3: Sketch of the schematic behavior of radiation induced oscillations in the distribution function $f(\varepsilon)$ and oscillatory density of states.

The central result of this calculation is the oscillatory photoconductivity

$$\frac{\sigma_{ph}}{\sigma_{dc}^D}=1+2d^2\left[1-\frac{\mathcal{P}_\omega\frac{2\pi\omega}{\omega_c}\sin\frac{2\pi\omega}{\omega_c}+4\mathcal{Q}_{dc}}{1+\mathcal{P}_\omega\sin^2\frac{\pi\omega}{\omega_c}+\mathcal{Q}_{dc}}\right] \tag{2.16}$$

including microwave and dc fields in the case of overlapping LLs. The denominator in Eq. (2.16) accounts for saturation. Notice, that in MW experiments without a strong

dc field, $\mathcal{Q}_{dc}$=0 in Eq. (2.16). In the case of a linear response regime, i.e. a moderate strength of microwave electric field, Eq. (2.16) yields to a correction of the dark dc conductivity, linear in the microwave power

$$\frac{\sigma_{ph}-\sigma_{dc}}{\sigma_{dc}} = -4d^2\mathcal{P}_\omega \frac{\pi\omega}{\omega_c}\sin\frac{2\pi\omega}{\omega_c}. \tag{2.17}$$

The result of the inelastic mechanism describes phase, intensity and period of the MIROs. The most important aspect is that temperature dependence of MIROs and ZRS is well explained by this mechanism due to $\tau_{in} \propto T^{-2}$. If one considers the dependence of σ_{ph} on the dc field E_{dc} at a sufficiently strong microwave power $\mathcal{P}_\omega > \mathcal{P}^*_\omega$ with $\mathcal{P}^*_\omega >0$ corresponding to the negative linear-response photoconductivity, it is obvious from Eq. (2.16) that for a large E_{dc}, the conductivity approaches the Drude value and is positive $\sigma_{ph} = (1-6d^2\sigma^D_{dc}) >0$. At a certain value of E^*_{dc}, σ_{ph} changes sign. This state with negative conductivity $E_{dc} < E^*_{dc}$ is not stable with respect to the formation of domains with a spontaneous electric field of magnitude E^*_{dc} [Andreev03] and leads to ZRS.
The final step is now to calculate the inelastic relaxation time τ_{in}. The dominant mechanism of inelastic scattering are electron-electron (e-e) collisions for not too high temperatures. This e-e scattering leads to relaxation of the oscillatory term f_{osc} in Eq. (2.15) and therefore determines temperature dependence of oscillating photoresistance. This effect is taken into account in calculations by replacing the collision integral on the right-hand side in Eq. (2.8) by the collision integral $St_{ee}\{f\}$. In the case of overlapping Landau levels, Dmitriev *et al.* calculate then the inelastic relaxation rate $1/\tau_{in}$ replaced by $1/\tau_{ee}$

$$\frac{1}{\tau_{in}} = \frac{1}{\tau_{ee}} = \frac{\pi^2T_e^2+\epsilon^2}{4\pi\varepsilon_F}\ln\frac{\kappa v_F}{\omega_c\sqrt{\omega_c\tau_{tr}}} \simeq \frac{T_e^2}{\varepsilon_F} \tag{2.18}$$

with $\kappa = 4\pi e^2/\nu_0$ the inverse screening length of the dynamically screened Coulomb potential. This thesis will show that inelastic mechanism explains well all experimental results for multilayer electron systems (in experiments for double and triple quantum wells) at low temperatures.

2.2.3 General description of microwave photoconductivity

After an introduction of displacement and inelastic mechanism, which are widely discussed in literature, Dmitriev *et al.* have developed a systematic study of MIROs and have found two additional mechanisms: "photovoltaic" and "quadrupole" mechanism [Dmitriev07a]. In this section, a general qualitative theoretical description of MIROs is given. The contribution of each mechanism to either longitudinal or transverse resistance is illustrated in the photoconductivity tensor $\widehat{\sigma}_{ph}$. Finally, photoresistance at elevated and ultrahigh MW power is briefly discussed, i.e. the contribution and interplay of all mechanisms of photoconductivity [Dmitriev07a].
The general description is again based on solving the QBE but in Ref. [Dmitriev07a], angular harmonics $F_{\nu n}$ of the distribution function $f(\varepsilon,\varphi,t)$ are included:

$$f(\varepsilon,\varphi,t) = \sum_{\nu n} F_{\nu n}(\varepsilon)e^{(i\nu\varphi+in\omega t)}. \tag{2.19}$$

φ is the angle of the kinetic momentum. First, we discuss the difference between inelastic and displacement mechanism, also including experimental possibilities how to distinguish between these mechanisms. Both mechanisms have in common that the oscillations appear due to oscillations in the DOS of disorder-broadened Landau levels with changing ε. In the inelastic contribution, oscillations in the dc current are generated by the isotropic (time-independent) part F_{00} of the electron distribution function whereas in the displacement mechanism MW irradiation affects the first angular harmonic F_{10}. In the linear regime, both mechanisms sum up independently but at low temperatures, the inelastic mechanism is the dominant one due to the ratio $\tau_{in}/\tau_q \simeq 100$ at (T=1 K) with $\tau_{in} \propto T^{-2}$ whereas displacement contribution is constant and quasi T-independent. Note that the inelastic relaxation time τ_{in} is governed by electron-electron scattering. Ref. [Dmitriev07a] also predicts that one can distinguish between both mechanisms by using linear polarization since only displacement mechanism is sensitive to the relative orientation of the microwave and dc fields.

An increase in MW power leads to different nonlinear regimes for MIROs. Due to feedback effects in a regime called "saturated inelastic contribution", see Ref. [Dmitriev07a], displacement contribution changes sign which leads to a nonmonotonic behavior of MIROs. In the case of ultrahigh MW power, the classical Drude conductivity tensor is restored due to a competition of feedback and multiphoton effects[2]. In this non-linear interplay of inelastic and displacement mechanism two additional microwave mechanisms are found. First, the photovoltaic mechanism, a combined action of dc and MW electric fields which produces non-zero temporal harmonics F_{01} and F_{20}. Second, quadrupole mechanism, where the dc response in the state with non-zero F_{20} yields to an oscillatory contribution to the Hall part of the photoconductivity tensor $\widehat{\sigma}_{ph}$. This leads to a violation of the Onsager-Casimir relations, which are a consequence at a macroscopic scale of microscopic time-reversal symmetry [Onsager31, Casimir45]. The current $\vec{j} = \widehat{\sigma}_{ph}\vec{E}_{dc}$ in the linear regime is calculated via the photoconductivity tensor $\widehat{\sigma}_{ph}$ which is given by

$$\widehat{\sigma}_{ph} = -4\sigma_{dc}^{D}\begin{pmatrix} d^s + d^a & h^s + h^a \\ h^s - h^a & d^s - d^a \end{pmatrix}, \tag{2.20}$$

where the contribution of each mechanism for longitudinal and transverse conductivity is visible. σ_{dc}^{D} is the Drude conductivity. $\widehat{\sigma}_{ph}$ is parametrized with four functions d^s, d^a and h^s, h^a with

$$d^s = d^s_{di} + d^s_{in} + d^s_{pho}, \qquad d^a = d^a_{di} + d^a_{pho} \tag{2.21}$$

where d^s is the diagonal isotropic and d^a the diagonal anisotropic part of $\widehat{\sigma}_{ph}$ with the displacement d^s_{di}, inelastic d^s_{in} and photovoltaic d^s_{pho} contributions. d^a is the diagonal anisotropic contribution which consists of a displacement d^a_{di} and a photovoltaic d^a_{pho} contribution. The nondiagonal symmetric term h^s generated by the quadrupole mechanism h^s_{qu} and the antisymmetric part arises due to the photovoltaic mechanism h^a_{pho}:

[2]Theoretical description of fractional MIROs is also based on multiphoton effects which occur for elevated MW power. This theory will be introduced later in this chapter.

$$h^s = h^s_{qu}, \qquad h^a = h^a_{pho}. \tag{2.22}$$

For this thesis three main aspects concerning MIRO theory should be kept in mind:

1. At low temperatures, inelastic mechanism is the dominant one due to $\tau_{in} \propto T^{-2}$.
2. The contribution of displacement mechanism is quasi-temperature independent.
3. Only quadrupole and photovoltaic mechanisms contribute to corrections in the Hall conductivity, where h^s_{qu} violates the Onsager relations $[\sigma_{ik}(B) \neq \sigma_{ki}(-B)]$.

One remark about an experimental work [Hatke09a] connected to a theoretical work [Dmitriev09] is finally discussed. An experimental study of temperature dependent photoresistance in a sample with ultrahigh mobility has been analyzed with the conclusion, that the contribution of displacement mechanism has to be taken into account down to a temperature of 2.0 K. This is explained by short-range scatters which increase the displacement contribution. Note, that in the above description for the inelastic mechanism only smooth disorder is considered. Theory in Ref. [Dmitriev09] takes this short-range scatterers into account and the crossing found in Ref. [Hatke09a] might be attributed to the crossing of inelastic and displacement mechanism. We have carried out temperature dependent measurements in double quantum wells in order to check these results. These experimental results and a comparison with both works [Hatke09a] and [Dmitriev09] is presented in Chapter 3.

2.2.4 Electrodynamic effects

The theoretical mechanisms in the previous sections discuss the MIRO phenomenon within electron scattering events or a non-equilibrium electron distribution function and its angular harmonics. In both models, electrodynamic effects are not taken into account. The importance of electrodynamic effects is now first discussed based on Ref. [Mikhailov04] and further on absorption/reflection experiments based on Ref. [Studenikin05].
Three main physical effects are mentioned in Ref. [Mikhailov04]: radiative decay, plasma oscillations and retardation effects.

- Radiative decay is the reaction of a medium, here a 2DEG, to radiation, i.e. an oscillating electric field E_ω of incident waves forces 2D electrons to oscillate in the 2D plane which results in a current therein. Thus the oscillating electrons emit a secondary radiation from the 2DEG (coherent dipole retardation). The system loses energy and the cyclotron resonance (CR) gets an additional contribution to its linewidth. This contribution can be calculated by solving Maxwell equations for electromagnetic waves passing through the 2DEG, see Ref. [Chiu76]. This effect has been observed in the absorption experiment by Studenikin *et al.* [Studenikin05] and is more pronounced in high-electron-mobility systems.

- In finite-size samples, the magnetoplasmon resonance (MPR) has been observed [Vasiliadou93]. If electromagnetic (microwave) irradiation passes through a 2DEG in a magnetic field, one would observe CR at $\omega = \omega_c$. In finite-size samples with lateral dimensions W, CR is shifted to a higher frequency, given by:

$$f_{res}^2(B) \;=\; f_{res}^2(B=0) + f_c^2 \tag{2.23}$$

  with f_c^2 the cyclotron frequency $f_c = \omega_c/2\pi$ and $f_{res} = n_e^2 e^2 k/8\pi^2 \epsilon_{eff}\epsilon_0 m^*$. The plasmon wavevector is $k = \pi/W$.

- Retardation effects become important when the velocity of light c is approached by the velocity of 2D plasmons and these effects modify the absorption spectra of a 2DEG.

Studenikin *et al.* have measured reflection and absorption on high mobility samples exposed to MW irradiation. In the reflection experiment, simultaneously done with a measurement of MIROs, they compared the response of a MW sensor, placed in proximity of the sample, with photoresistance and observed a signal which is different from photoresistance. The position of a broad minimum in the reflection experiment corresponds roughly to the CR. The position and waveform of the reflection signal depends only on the MW frequency and not on temperature or MW power. They attribute this signal to bulk edge plasmons due to the finite size of the sample. For the absorption measurements, they placed the MW sensor behind the sample. They observed a maximum at the CR, broader then theoretical calculations and no resonant absorption at CR harmonics. The absence of absorption features at the harmonics of ω_c has also been found in Ref. [Smet05]. It should be added that absorption decreases also with increasing mobility. Both experiments provide qualitative information about electrodynamic effects which can not be disregarded for the MIRO phenomenon.

Finally, one experimental work by Smet *et al.* has to be mentioned because they have performed a detailed polarization (circular and linear polarization) study in order to assist in isolating the proper microscopic picture of the MIRO and ZRS phenomena [Smet05]. The observation is not in agreement with proposed theories because deviations between different polarizations occur only near ω_c. For both displacement and inelastic mechanism, the sence of circular polarization enters through the ac Drude conductivity σ_ω^D owing to the proportionality of σ_ω^D to either $(\omega+\omega_c)^{-2}$ or $(\omega-\omega_c)^{-2}$. This intriguing experiment has been unfortunately not performed by other groups. In this thesis, circular polarization can not be studied and experiments will be performed only with indeterminate or linear polarization.

Beyond these theoretical models which are used in this thesis to explain all features of photoresistance, there exist also other theoretical models of MIROs which can be found in literature, e.g. microwave-driven electron orbit dynamics [Iñarrea05], many-

body electron-electron interaction mechanism [Sedrakyan08] and a classical explanation of MIROs due to perturbated cyclotron motion [Vavilov04a].

2.3 Experimental investigations - MIROs in high density samples

In contrast to all previous studies with high or ultrahigh electron mobility and low density ($< 4 \cdot 10^{11}$ cm^{-2}), samples with high electron density and moderate mobility have been investigated during this thesis. The density is about $n_s = 7.5 - 10 \cdot 10^{11}$ cm^{-2} and the mobility $\mu < 2.0 \cdot 10^6$ cm^2/V s, respectively. Now, all properties of MIROs are presented including power, frequency and temperature dependence. For all samples, no ZRS have been observed. First, Figure 2.4(a) presents microwave-induced resistance oscillations for a constant lattice temperature 1.4 K at a fixed frequency of 140 GHz. Three minima and maxima can be observed, attributed to MIROs. The circles mark corresponding integer numbers $n = 1, 2, 3$ for $\omega = n \cdot \omega_c$. For an integer n of ω/ω_c, the

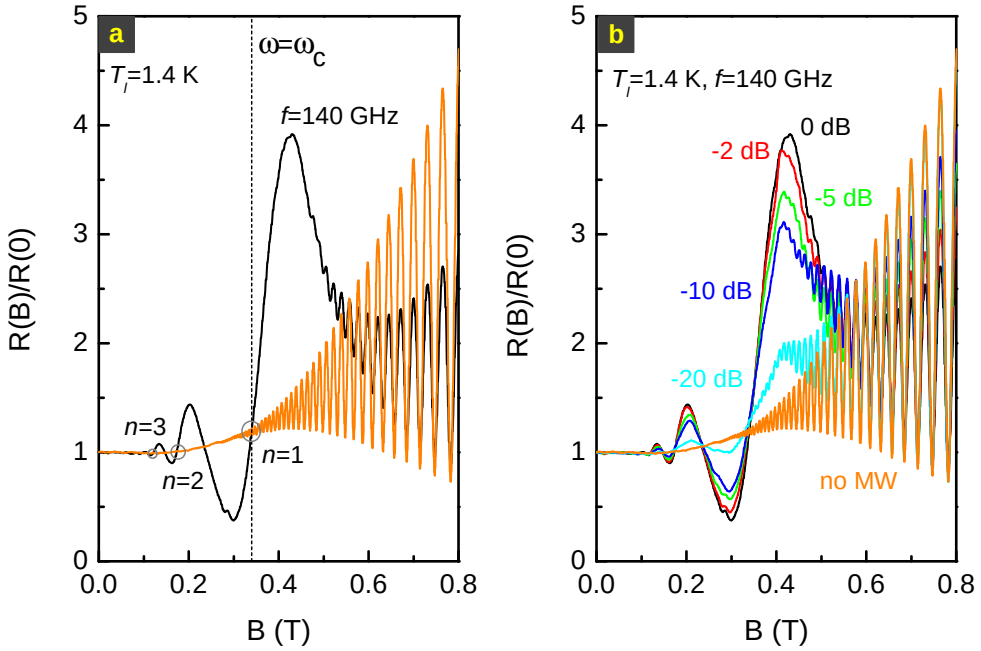

Figure 2.4: (a) Longitudinal resistance exposed to MW irradiation (black) for 140 GHz (0 dB) and without microwave irradiation (orange). MIROs appear in a low magnetic field where SdH oscillations are absent. (b) Dependence of magnetoresistance upon MW power (that is, attenuation from -20 dB to 0 dB) at 140 GHz.

resistance remains unchanged, i.e. $\Delta R_{xx} = R_{xx}^{MW} - R_{xx}$=0. At magnetic fields, where

$\omega/\omega_c = n \pm \varphi$ (φ=1/4)[3], one can observe maxima (+) or minima (-) in photoresistance. The oscillating behavior can be simulated by Eq. (2.17). Figure 2.4(b) illustrates power dependence[4] (that is, attenuation factor in decibels (dB)→0) for a fixed frequency of 140 GHz. With increasing MW power, maxima in resistance increase and the minima become deeper. The inelastic mechanism yields to a MW correction to the dark magnetoresistance which is linear in MW power (quadratic in the MW electric field). This power dependence has been presented for ZRS in Ref. [Zudov03]. It is obvious [see Figure 2.4(b)] that the behavior of MIRO amplitude is sublinear and MIRO amplitude saturates with increasing MW power (attenuation from -10 to 0 dB). Two plausible arguments can be mentioned. First, the sample is already in a saturated regime due to a high MW electric field where maxima of resistance increase with P^α with $0< \alpha <0.5$ (nonlinear regime) instead of P. Second, it is often discussed that MIRO amplitude is very sensitive to details in the disorder potentials and therefore, one can obtain information about disorder in 2D structures with MIRO measurements which can not be obtained from transport measurements like conventional analysis of SdH oscillations [Dmitriev09]. Having a closer look to SdH oscillations in Figure 2.4, one can easily see that they are damped with increasing MW electric field. SdH oscillations are very sensitive to temperature, see Figure 1.3. The MW electric field leads to an increase of electron temperature T_e. For all microwave experiments this heating effect must be taken into account and one has to distinguish between the lattice temperature $T = T_l$ and electron temperature T_e. In Appendix B, a possibility is mentioned how to estimate the MW electric field by comparing damping of SdH oscillations due to a MW electric field and a dc field (high dc current). Heating effect might also play the dominant role in the non-linear behavior in Figure 2.4(b). An estimation of T_e based on SdH oscillations gives an electron temperature of $T_e \simeq 3.0$ K at B=0 for 0 dB. The periodicity of MIROs with the inverse magnetic field $1/B$ is shown in Figure 2.5 for MW frequencies 170, 140, 110 and 75 GHz at a constant MW electric field of E_ω=2.5 V/cm. It can be recognized that the best pronouced features occur for 170 GHz with integer MIROs up to n=4. For smaller frequencies, the amplitude starts to decrease and for 75 GHz only maxima and minima for MIROs n=1, 2 are visible. The inset in Figure 2.5 presents normalized magnetoresistance $R(B)/R(0)$ exposed to low MW frequencies from 55 GHz down to 32.7 GHz. At 55 GHz, only cyclotron resonance (CR) at $\omega = \omega_c$ occurs whereas all higher integer MIROs vanish. By further decreasing the MW frequency one can see that CR also disappears at 35 and 32.7 GHz. This can be attributed to the strong suppression of the Landau quantization by disorder, i.e. to the experimental smallness of the Dingle factors in the region of the magnetic field where CR occurs. Vanishing MIROs are also reported for high frequencies in Ref. [Studenikin07]. For low-density samples with a mobility of $8.0 \cdot 10^6$ cm^2/V s first a deviation from theory and then a

[3] A discussion about experiments concerning period and phase of microwave-induced resistance oscillations and zero-resistance states in two-dimensional electron systems can be found in Ref. [Zudov04].

[4] For power-dependent measurements in this thesis, we denote each magnetoresistance trace with the attenuation (in dB) corresponding to the value of the attenuator, see Appendix B.

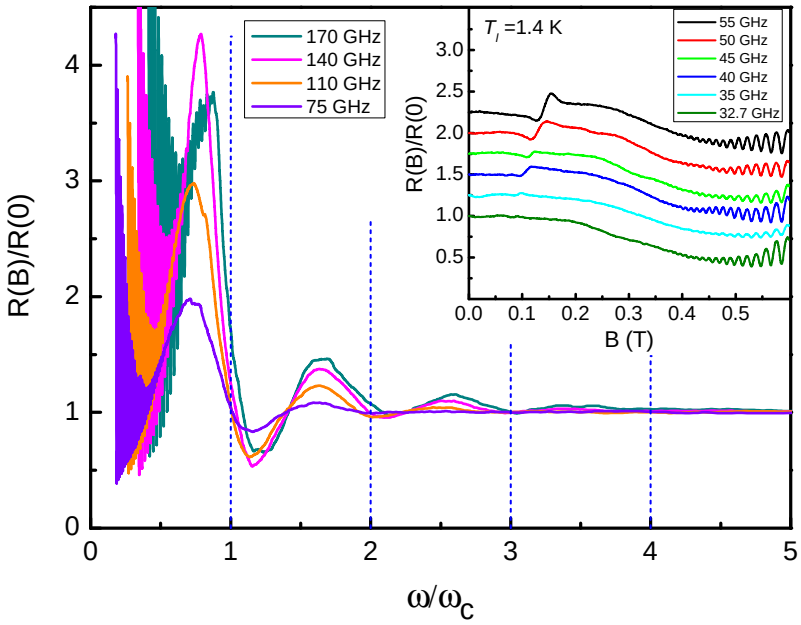

Figure 2.5: Periodicity of MIROs by plotting normalized magnetoresistance as a function of ω/ω_c (the inverse magnetic field) starting from 170 GHz to 75 GHz for a constant electric field of 2.5 V/cm. Amplitude of CR (n=1) starts to decrease for 75 GHz and vanishes for lower frequencies (see inset).

quench of MIROs occurs and all oscillations completely vanish beyond 230 GHz. Only a bolometric-type effect owing to the resonance absorption at $\omega = \omega_c$ remains. This quench cannot be explained by neither displacement nor inelastic mechanism and the authors in Ref. [Studenikin07] give arguments that excited magnetoplasmons may decay through the electron transitions between Landau levels giving rise to MIROs. In contrast to this quench for f >230 GHz, other studies of Mani *et al.* [Mani08] and Smet *et al.* [Smet05] present MIROs in samples with a mobility more than two times larger than in Ref. [Studenikin07]. This might cause the MIRO/ZRS observation at this high frequency.

The last experimental part of integer MIROs focuses on temperature dependent measurements, illustrated in Figure 2.6. Dependence of magnetoresistance has been measured for a constant frequency f=140 GHz and an electric field of $E_\omega \simeq$3.2 V/cm for several lattice temperatures, see Figure 2.6(a). SdH oscillations are visible up to 4.2 K starting at 0.5 T. MIROs n=1 and n=2 are pronounced up to 10 K where SdH oscillations are already damped. This is one characteristic property of MIROs that they persist to much higher temperatures than SdH oscillations. It is interesting to add that the thermal damping factor $\mathcal{T}$ of SdH oscillations is $2\pi^2$ larger than $k_BT/\hbar\omega_c$ [Eq. (1.27)] which arises from the temperature broadening of the Fermi distribution function and the Lorentzian shape of LLs. Figure 2.6(b) shows a zoom at 15 K. Maximum and minimum

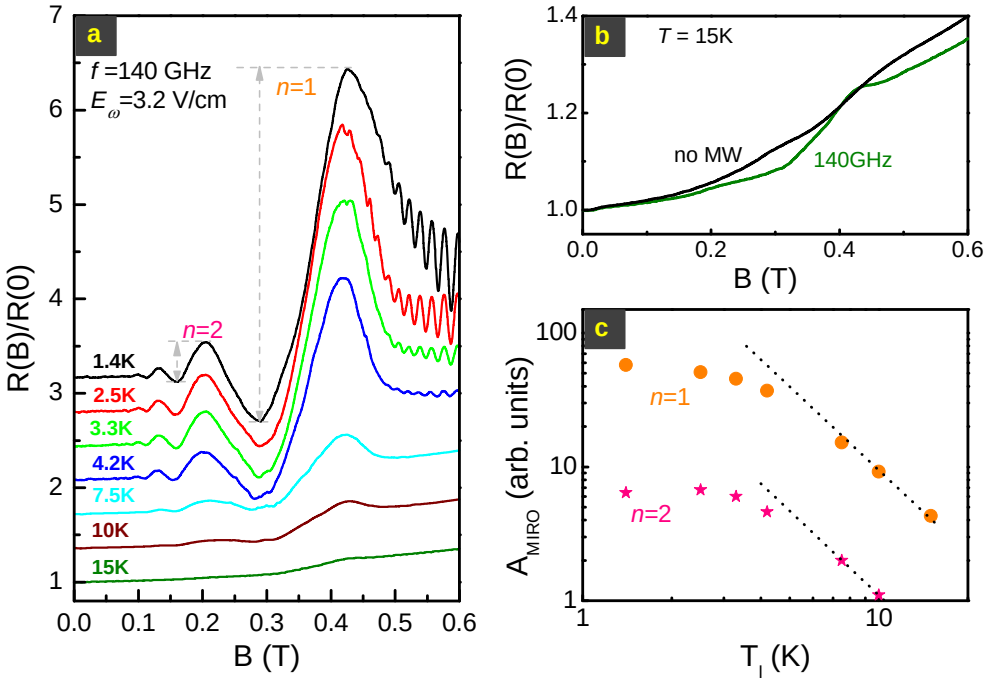

Figure 2.6: Temperature dependence of MIROs at a constant frequency and MW electric field: (a) normalized magnetoresistance under MW irradiation (curves are shifted up for clarity, except the one for 15 K), (b) normalized magnetoresistance for 15 K without (no MW) and exposed to MW irradiation, (c) amplitude of MIROs n=1 and n=2 as a function of T_l, the lattice temperature. The dashed lines indicate T^{-2}-dependence.

of CR can still be observed for this high temperature. In Figure 2.6(c) amplitude [extraction see Figure 2.6(a)] of MIRO n=1 and n=2 are plotted as a function of the lattice temperature T_l. It is obvious to compare now the extracted amplitude of MIROs with the predicted temperature dependence T^{-2} by the inelastic mechanism due to electron-electron scattering [Dmitriev05]. This is indicated by the dashed lines in Figure 2.6(c) for both MIROs. For high T, MIRO amplitude is in agreement with the T^{-2}-behavior but it deviates for low temperatures. This deviation can be explained by heating of the 2DEG. Since T_e is much higher than T_l for a MW electric field of E_ω=3.2 V/cm at 1.4 K, the MIRO amplitude can not fit to the T^{-2}-model. Therefore Figure 2.6(c) was done in purpose in order to illustrate again the heating effect of electrons due to MW irradiation after a discussion about power dependence. In a rough estimation[5] the electron temperature is $T_e \simeq$3.0 K for B=0 and even higher in the region where n=1 and n=2 appear. One can see that even at high MW power amplitude scales with T^{-2}, i.e. inelastic mechanism might still be the dominant contribution. Such a T^{-2}-analysis at

[5] All details about the dependence of electron temperature T_e on radiation frequency, the magnetic field and MW power can be found in Chapter 3-5 assuming energy relaxation of electrons due to their interaction with acoustic phonons.

lower MW power and temperature is also presented in Ref. [Studenikin07]. Note that in displacement mechanism, temperature dependence is only reflected in the τ_q/τ_{tr} which is a slow function of temperature in this temperature range for MIRO experiments.

Since the discovery of MIROs and ZRS, microwave-induced magneto-oscillations have also been reported in the transverse resistance, see Ref. [Mani04a] or Ref. [Studenikin04]. The observed amplitude of ΔR_{xy} is either 5 Ω or 2 Ω, respectively. Hall resistance has also been measured for both wafers studied in this thesis but these two results are not confirmed in samples with high carrier concentration and one occupied 2D subband which might be related to the low mobility. Theory [Dmitriev05] mentions, that a possible origin of the observed oscillatory ρ_{xy} may be a weak variation of the density n_s with ω/ω_c. If n_s was constant, the leading odd-in-B correction $\delta\rho_{yx}^H$ to the Hall conductivity ρ_{yx}^H should be smaller than ρ_{xx} by a factor $1/\omega_c\tau_{tr}$, which is in the order of 10^{-2} under the experimental conditions.

2.4 Fractional MIROs

In addition to MIROs which occur at integer multiples of ω/ω_c, experiments in high mobility samples [Mani04b, Dorozhkin05, Zudov06] have shown features at certain fractional values ω/ω_c=1/2, 3/2, 2/3, 5/2 as well as fractional ZRS. These fractional microwave-induced resistance oscillations (FMIROs) occur with increasing microwave power and appear at

$$\epsilon = \omega/\omega_c = n/m \tag{2.24}$$

where n and m are integers. In a recent experiment [Dorozhkin07], FMIROs have been observed up to ϵ=1/4 in samples with low density ($n_s = 2.7 \cdot 10^{11}$ cm^{-2}) and ultrahigh mobility ($\mu = 17 \cdot 10^6$ cm^2/V s). The authors also report on a m-dependent threshold frequency. No FMIROs appear for f >50 GHz, also observed in Ref. [Zudov03]. Studies of FMIROs are at the beginning and questions about power dependence, the need of high MW electric fields and the quench of FMIROs at high frequencies are still open. In this thesis, FMIRO phenomena have been investigated for the first time in high electron density samples with moderate mobility and high MW electric fields [Wiedmann09a]. Before the analysis of experimental results is presented, a basic introduction in FMIRO theory, also at the beginning of its development, is given. Experimental observations are discussed in connection with both existing theories.

2.4.1 Theoretical models for FMIROs

While all resonances in Eq. (2.24) originate from commensurability of the cyclotron and microwave frequencies, FMIROs corresponding to $m \geq 2$ require multiphoton absorption processes which appear in the strongly nonlinear regime. For these multiphoton processes, two competing models exist. First, a simultaneous absorption of several photons (with intermediate states) [Lei06, Dmitriev07b] and second, a stepwise absorption

of several photons [Pechenezhskii07]. The latter process contributes to the resistance owing to incomplete relaxation of the electron system between absorption events. Both FMIRO theories demonstrate a progressive appearance of oscillations with increasing fractional denominator m as MW power increases which is in agreement with experimental findings [Mani04b, Dorozhkin05, Zudov06, Dorozhkin07].
The first theoretical ansatz (multiphoton absorption) is the multiphoton inelastic mechanism. The approach is again based on the QBE for the semiclassical distribution function $f(\varepsilon, \varphi, t)$. Calculations show that at order E_ω^2, microwaves do not produce any oscillatory structure near fractional values of ω/ω_c whereas a two-photon FMIRO occurs in a narrow interval and at order E_ω^4 which leads to the emergence of FMIROs at half integers of ω/ω_c. As already mentioned for integer MIROs, the inelastic multiphoton contribution dominates over the multiphoton contribution of the FMIROs governed by the displacement mechanism.
The model of stepwise single-photon absorption explains experimental data with a non-equilibrium population of states on disorder-broadened Landau levels due to one photon-processes and its manifestation of commensurability effect between ω_c and ω. The calculation is based on the inelastic mechanism developed in Ref. [Dmitriev05]. In contrast to the regime of overlapping LLs, here the regime of strongly overlapped and well-resolved LLs is analyzed. The result of the calculations exhibits a series of similar features of FMIROs for $\omega < \omega_c$ and $\omega > \omega_c$ in the vicinity of $\omega = \omega_c$ for large $\mathcal{P}_\omega$-factors at B =0. For $\omega > \omega_c$, the FMIROs can only be observed in the crossover from strongly overlapping to well resolved Landau levels. As an example, a FMIRO feature is calculated for various τ_q-values at a constant ω_c-value and is maximal for a certain value of $\omega_c\tau_q$ (point where LLs start to separate) whereas it decreases monotonically to zero for both increasing and decreasing $\omega_c\tau_q$. Interpretation of this example results in constraints in FMIRO experiments. For the observations of commensurability resonances [see Eq. (2.24)] associated with the single-stepwise transitions between adjacent Landau levels (n=1) and in the regime of separated Landau levels [α <2 according to the self-consisting Born approximation (SCBA)] the relation

$$\hbar\omega_c - 2\Gamma < \hbar\omega < \hbar\omega_c + 2\Gamma \tag{2.25}$$

should be satisfied where $\Gamma = \hbar\omega_c[\arccos(1-\alpha) + \sqrt{(2-\alpha)\alpha}]/2\pi$ is the half-width of the Landau levels in the SCBA with $\alpha = \pi/\omega_c\tau_q$. Beyond these intervals, photon transitions are absent and resistance corresponds to the dark value. Once more, it is worth noting that FMIROs are absent in the linear regime of MW power because the manifestation of commensurability effects requires the subsequent absorption of several photons.

2.4.2 FMIROs in high electron density samples

In literature, experimental details about FMIRO studies concerning frequency dependence including a threshold frequency, power dependence of amplitude and the highest FMIRO with denominator m=4 are presented in Ref. [Dorozhkin07]. All FMIRO mea-

surements have been performed until now at the lowest temperature possible. In order to carry out measurements of FMIROs, samples of two wafers with high electron density have been used and exposed to MWs with high intensity. Samples from wafer (A) have a carrier concentration of $n_s = 7.5 \cdot 10^{11}$ cm^{-2} and a mobility of $\mu = 1.2 \cdot 10^6$ cm^2/V s whereas the samples from wafer (B) have a carrier concentration of $n_s = 9.8 \cdot 10^{11}$ cm^{-2} and a mobility of $\mu = 1.6 \cdot 10^6$ cm^2/V s. In Figure 2.7, magnetoresistance for two samples of both wafers is presented. All further studies focus on samples of wafer (A) owing to better pronounced MIROs (deeper minima) at low temperatures. Figure 2.7(a) and

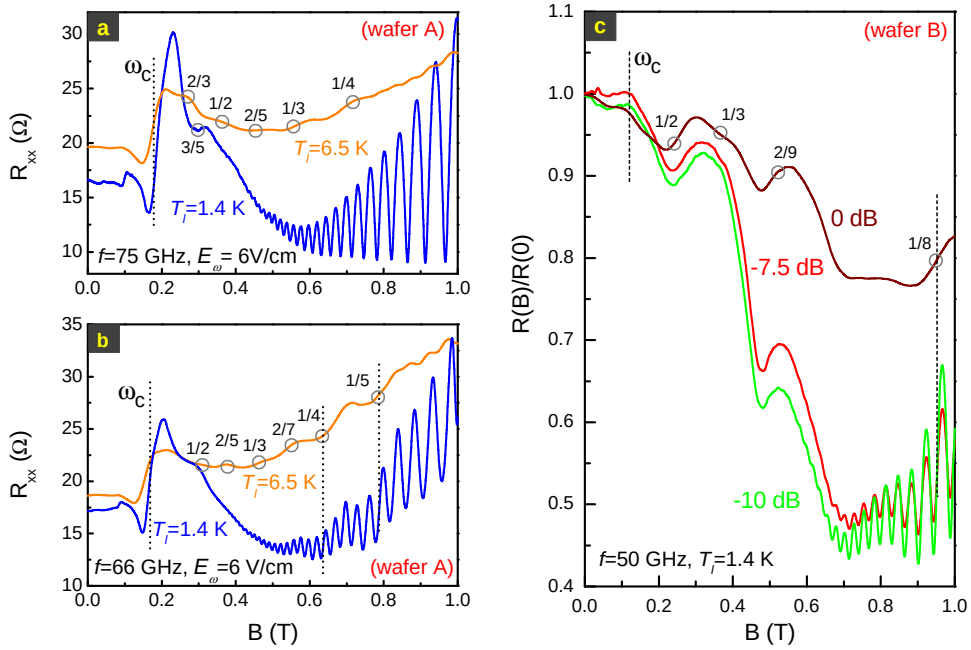

Figure 2.7: (a) FMIROs for 75 GHz at a lattice temperature of 1.4 and 6.5 K and (b) for 66 GHz at the same temperatures and electric field for one sample of wafer A. (c) Power dependence of FMIROs for wafer (B) at 50 GHz and a lattice temperature of 1.4 K. Corresponding FMIROs are indicated by circles and ϵ.

Figure 2.7(b) show magnetoresistance under MW irradiation of 75 GHz and 66 GHz, respectively[6]. The MW electric field is kept constant for both lattice temperatures T_l=1.4 K (blue) and 6.5 K (orange) at E_ω=6 V/cm. For 75 GHz at T_l=1.4 K, FMIRO ϵ=3/5 is clearly visible on the right side of CR and SdH oscillations start to appear at $B \simeq$0.4 T. For 66 GHz at T_l=1.4 K some SdH oscillations are damped[7] around 0.6 and 0.8 T. The damping of these SdH oscillations at both magnetic fields can be connected to FMIROs with $\omega_c/\omega = n/m$. With increasing T_l, SdH oscillations are damped more

[6]Experimental detail: these two frequencies have been chosen because MW power is the highest for the generator within the frequency range 55 to 75 GHz, see Appendix B.

[7]This damping can not be attributed to MPR, because integer multiples of $k = n/W$ do not correspond to the values of magnetic field where oscillations appear.

and more until they vanish at high temperatures due to the thermal damping factor $\mathcal{T}$. Both measurements have been repeated at T_l=6.5 K where FMIROs are no more hindered by SdH oscillations and much more features occur, marked by corresponding $\epsilon = n/m$.

In contrast to low temperatures, clear maxima and minima appear which can be attributed to FMIROs. In addition, the damping of SdH oscillations for 66 GHz at a certain magnetic field corresponds to FMIROs ϵ=1/4 and 1/5. Note that ϵ=1/5 has not yet been observed in experiments until now. To confirm these observations, samples from a second wafer [wafer (B)] have been investigated, see Figure 2.7(c). Here lattice temperature is kept constant at T_l=1.4 K for 50 GHz[8]. MW power is now increased (attenuation from -10 dB to 0 dB). For an attenuation of -10 and -7.5 dB, two features occur on the high-field side of CR. For 0 dB, the sequence of minima and maxima is marked with numbers corresponding to FMIROs. At 0.95 T, the feature is attributed to ϵ=1/8. Note that this feature again is accompanied by a damping of several SdH oscillations for low MW power.

The next step is now a detailed study of frequency dependence at a temperature where FMIROs are not hindered by SdH oscillations or already damped at too high temperatures. A lattice temperature of T=6.5 K satisfies both conditions. Figure 2.8(a) presents frequency dependence of FMIROs from 45 to 90 GHz where all FMIROs with $\epsilon = n/m$ are marked with circles between minima and maxima[9]. The electric field is constant at $E \simeq$4 V/cm, smaller than in Figure 2.7(a,b).

The results of frequency-dependent measurements of magnetoresistance exposed to MW irradiation in Figure 2.8(a) can be summarized as follows:

- High-order FMIROs are observed for 45 and 55 GHz, partially superimposed on SdH oscillations.
- With increasing frequency, f >55 GHz, high-denominator FMIROs vanish.
- A quench of all FMIRO features for frequencies above a threshold frequency of f_{th}=85 GHz.

It should be noticed that no FMIROs are observed for $\omega < \omega_c$ ($m < n$) on the low-field side of $\omega = \omega_c$. Additionally, Figure 2.8(b) demonstrates theoretical calculations, done by Oleg Raichev, including multiphoton displacement and inelastic mechanism where multiphoton inelastic mechanism is still the dominant one (see Figure 2.11) at 6.5 K. For 85 GHz, the theoretical calculation confirms FMIROs at ϵ=2/3 and 1/2 for a MW electric field of $E_\omega \simeq$3 V/cm. Having a closer look at the SdH oscillations, one can see that amplitude for this theoretical trace is slightly higher. FMIRO ϵ=2/5 can not be resolved even at higher MW power. The second calculation is done for 55 GHz, also for

[8] Experimental detail: for 50-55 GHz, generator from 32.7 to 55 GHz, MW electric field has the highest value at our disposal.

[9] exactly speaking, the position of FMIROs with $\epsilon = n/m$ corresponds to a magnetic field where the value of the dark resistance remains unchanged: $\Delta R_{xx} = R_{xx}^{MW} - R_{xx}$=0.

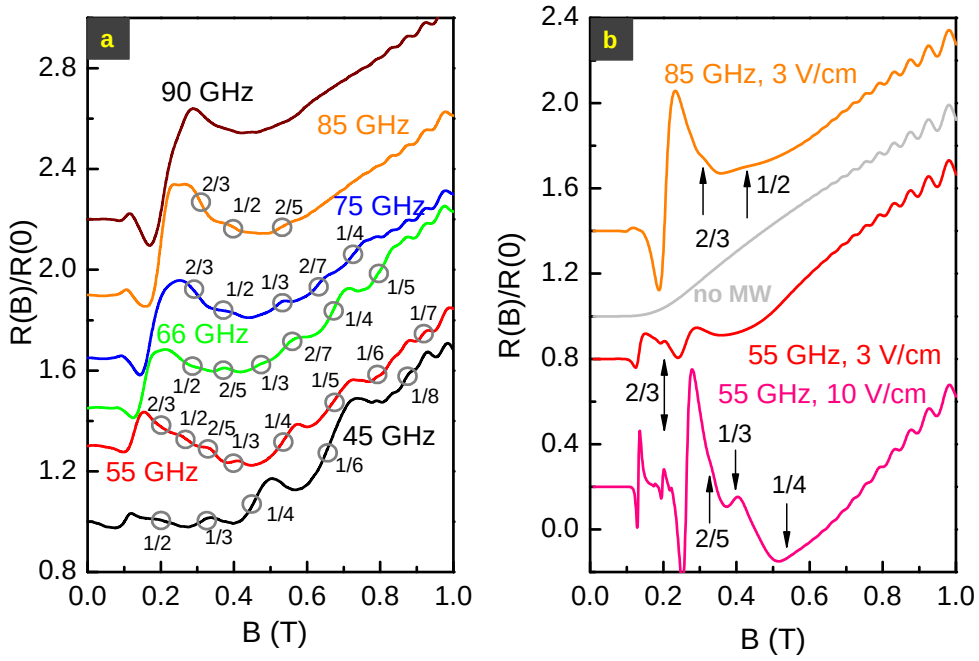

Figure 2.8: (a) Frequency dependence of FMIROs at a constant electric field (E_ω ≃4 V/cm) and temperature from 45 to 90 GHz. For 90 GHz, no more FMIROs can be observed. (b) Theoretical calculations using multiphoton inelastic and displacement mechanism at 55 and 85 GHz for different MW electric fields reveal several FMIRO features which are discussed in the text.

a slightly smaller electric field of E_ω ≃3 V/cm and a high electric field of E_ω ≃10 V/cm. Whereas ϵ=2/3, 1/2 and 1/3 are observed also in our calculation, ϵ=1/4 might be attributed to the "bump" feature at 0.5 T. All high-order FMIROs with m >4 do not appear in the theoretical calculation. Notice, that the MW electric field is fixed at E_ω ≃4 V/cm in Figure 2.8(a). The next step is now to investigate power dependence to obtain information about amplitude of FMIROs since both theoretical models propose a progressive appearance of oscillations with increasing denominator m. This power dependence is first presented for 45 GHz in Figure 2.9 and then for 55 GHz in Figure 2.10. Note that in this frequency range, MWs have the highest intensity. Figure 2.9(a) shows the evolution of FMIROs with increasing MW power up to an attenuation of -5 dB (≃10 V/cm). FMIROs are marked with corresponding numbers. With increasing MW power, the amplitudes of FMIROs with ϵ= 1/3, 1/4 and 1/6 seem to saturate. In order to analyze power dependent FMIRO amplitude of the most pronounced features exactly, we extracted amplitude 2A (peak to peak) from the derivative dR_{xx}/dB in Figure 2.9(b) and plotted it as a function of MW power in 2.9(c). Whereas the high-order FMIROs ϵ= 1/4 and ϵ= 1/6 exhibit similar behavior, FMIRO amplitude of ϵ= 1/3 behaves different with increasing MW power. For ϵ= 1/4 and 1/6, amplitude follows a

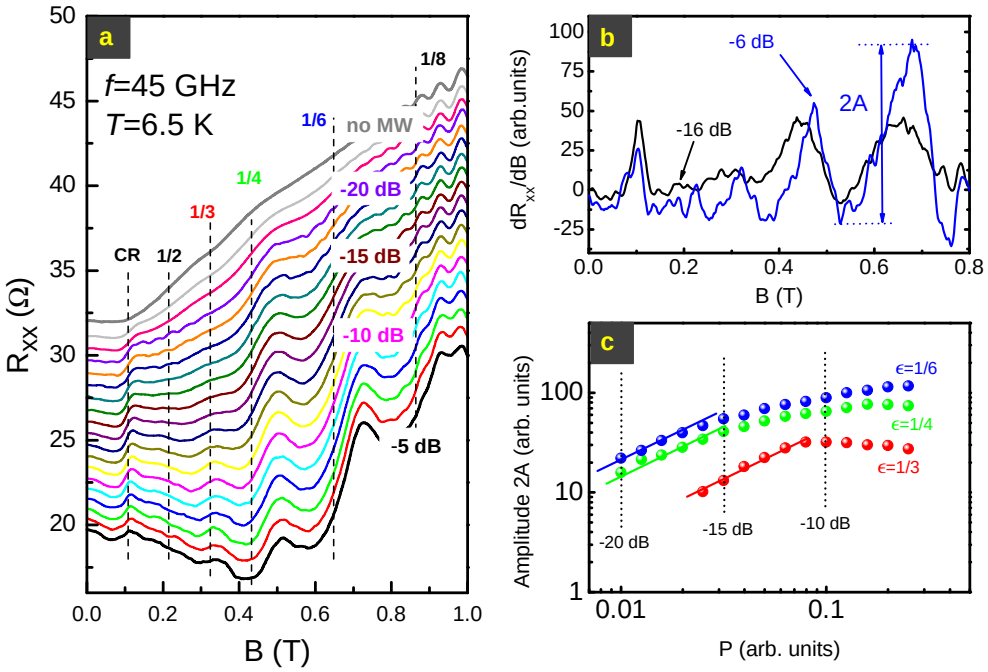

Figure 2.9: (a) Power dependence of magnetoresistance exposed to a MW irradiation of 45 GHz at 6.5 K (traces are shifted up for clarity, except the one for an attenuation of -5 dB) and its analysis of amplitude (b),(c) for FMIROs extracted from dR_{xx}/dB. Thick lines in (c) correspond to linear behavior in P.

linear dependence in the range from -20 to -15 dB, marked with thick lines. For higher MW power, both FMIRO amplitudes start slowly to saturate. FMIRO $\epsilon = 1/3$ has linear behavior from -16 to -12 dB and is already saturated at -10 dB whereas for higher MW power, amplitude starts to decrease. To summarize, FMIRO amplitudes have different sensitivity with increasing MW power for 45 GHz. The same power analysis is now done for the second frequency (55 GHz) in Figure 2.8(a) where MW power is more elevated due to the property of the MW generator. The same extraction of amplitude 2A (peak to peak) in Figure 2.10(a) is presented in Figure 2.10(c). It is already obvious from the waterfall-plot, that FMIRO features are damped at -6 dB ($\simeq$12 V/cm). FMIRO amplitude 2A plotted as a function of MW power reveals damping of all FMIROs at a characteristic MW power. Figure 2.10(c) also presents CR which has its maximum at -17 dB and is strongly damped with increasing MW power. Power dependence at this frequency also confirms a different sensitivity of different FMIROs to MW power and additionally, that CR is also in the saturated regime.

It is predicted in Ref. [Dmitriev07a] that maxima of integer MIROs shift to higher magnetic fields with decreasing MW power. In Figure 2.10(b) the maximum of CR, marked with ω_c in Figure 2.10(a), and FMIRO $\epsilon = 1/4$ are extracted and plotted as a function of P. CR shows a shift of its maximum to higher B whereas maximum $\epsilon = 1/4$ (and all

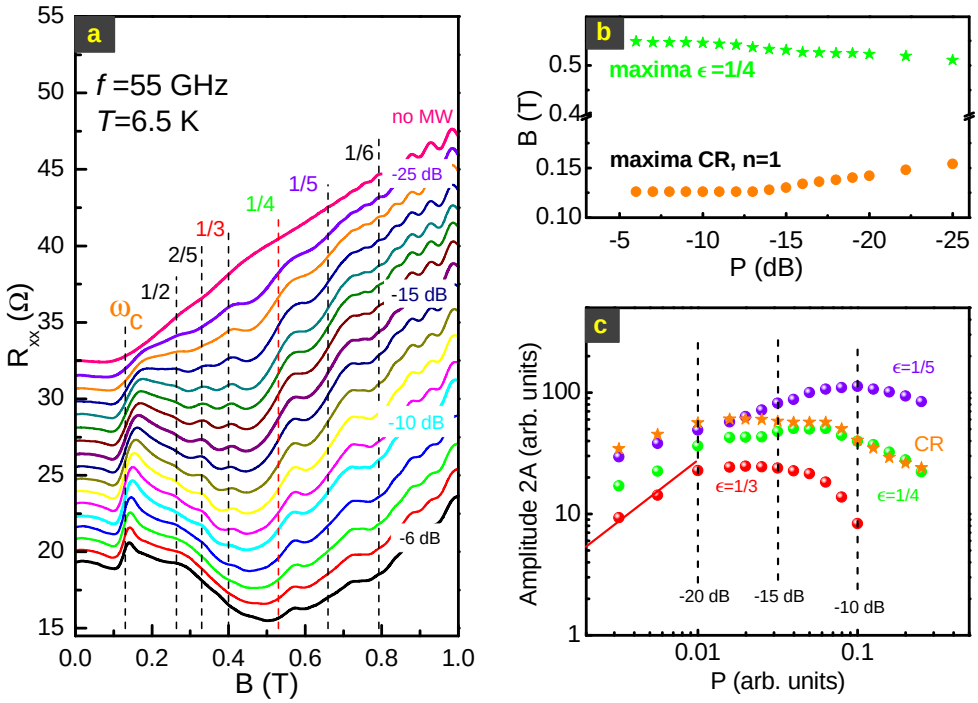

Figure 2.10: Power dependence of magnetoresistance exposed to a MW irradiation of 55 GHz at 6.5 K (traces are shifted up for clarity, except the one for an attenuation of -6 dB) and positions of FMIROs in magnetic field (b) as well as amplitude (c) for FMIROs and CR from dR_{xx}/dB. The thick line in (c) corresponds to linear behavior in P.

other maxima of FMIROs) shift to a lower magnetic field. Both traces, not exposed to MW irradiation (no MW) in Figure 2.9(a) and Figure 2.10(a) exhibit magnetophonon resonance owing to interaction of electrons with acoustic phonons [Zudov01b].

2.4.3 Discussion and comparison of experiments with FMIRO theory

All results mentioned in the previous part of this chapter about power, temperature and frequency dependence need to be discussed and compared to both theoretical models. Theoretical calculations also clarify which contribution for total photoresistance is attributed to either multiphoton inelastic or multiphoton displacement mechanism. The observed high-order FMIROs can distinguish between the stepwise single photon [Pechenezhskii07] and the multiphoton model [Dmitriev07b].

Multiphoton absorption m >2 requires high MW power because the corresponding contributions into the photoresistance [Dmitriev07a, Dmitriev07b] decrease with (W_w^m) where the dimensionless parameters W_w are defined as

$$W_w = \frac{\tau_q}{\tau_{tr}} \left[\frac{eE_\omega v_F}{\hbar\omega(\omega_c \pm \omega)} \right]^2 \tag{2.26}$$

depending on the MW electric field E_ω (here circular polarized), Fermi velocity v_F and the ratio of the quantum lifetime τ_q to the transport time τ_{tr} which is estimated to 1/15 for samples of both wafers. Assuming a MW electric field between 1 V/cm and 12 V/cm, the parameters W_w are vanishingly small for FMIROs, except for the multiphoton process with m=2. Therefore, FMIROs with denominator m=2, e.g. ϵ=1/2, 3/2 observed and reported in previous publications, can be attributed to a two-photon process [Mani04b, Zudov06]. However, other FMIROs ϵ=1/3, 2/3, 1/4 and 2/5 can hardly be ascribed to a multi-photon model. FMIROs due to a stepwiese absorption of several photons seem to be more suitable for these features. In this model, intensity of fractional resonances with denominator m is proportional to the mth power of the squared Dingle-factor $d = \exp(-2m\alpha)$ with $\alpha = \pi/\omega_c\tau_q$. Similar to the disappearance of CR for low MW frequencies (see inset of Figure 2.5), this proportionality explains why FMIROs are absent on the low-field side of CR. With increasing temperature, FMIRO amplitude should damp exponentially faster than for integer MIROs due to the decrease of τ_q in the squared Dingle factor, studied in single- and multilayer electron systems [Mamani08, Goran09, Wiedmann09b]. In the stepwise absorption model, fractional features are in any case more sensitive to broadening of LLs or damping factors than integer features but in all studies presented here, FMIROs weaken at the same temperatures as MIROs.

The power dependence observed for both frequencies (Figure 2.9 and Figure 2.10) is linear in a certain range of MW power but different for each feature. With increasing power, the amplitude is sublinear and weakly dependent on MW power until a saturation occurs. This behavior is similar to integer MIRO and consistent with the stepwise absorption model. For 55 GHz, at elevated MW power, FMIRO amplitudes even start to decrease. It is worth noting that for this MW power CR amplitude (peak to peak) at $\omega = \omega_c$ is already sublinear (for lower power $P^{0.3}$) and damping occurs earlier compared to FMIROs, in agreement with theory [Dmitriev05]. The transition to a weaker power dependence (e.g. from linear to sublinear) is attributed to the saturation effect of MWs on the electron distribution function, which is the basic feature of the inelastic mechanism. In order to get an impression about the strength of either inelastic or displacement mechanism under both simultaneous and stepwise multiphoton processes and their contribution to photoresistance at T=6.5 K, calculations have been carried out [Raichev09], shown in Figure 2.11 for magnetoresistance exposed to a MW frequency of 55 GHz for two different MW electric fields. The calculation is done using the SCBA with τ_q=3 ps and τ_{in}/τ_{tr}=2, extracted from experimental data at 6.5 K. It is obvious from both MW electric fields of either E_ω=3 V/cm or E_ω=10 V/cm that displacement contribution to resistance is very small and only exhibits CR for E_ω=3 V/cm and FMIROs ϵ=1/2, and 2/3 for E_ω=10 V/cm whereas inelastic contribution dominates and reveals all observed FMIRO features in experiments up to ϵ=1/4 for 55 GHz, even more than experimentally observed in the region between CR and ϵ=1/2. On the high-field side of ϵ=1/2, inelastic contribution also depicts ϵ=1/3 and shows a "bump" feature at B=0.5 T which might

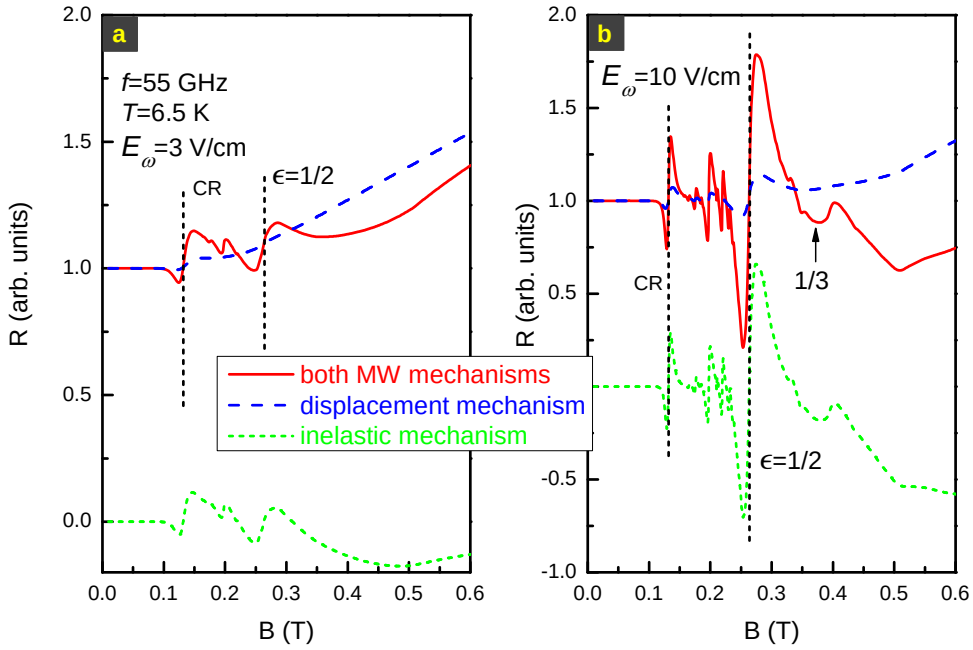

Figure 2.11: Theoretical calculations of resistance exposed to MW irradiation for multiphoton displacement (blue, dashed) and multiphoton inelastic contribution (green, short dashed) and their sum (red solid) for (a) 85 GHz and (b) 55 GHz. Strength of MW electric fields are labeled. The bump feature in (b) might be related to $\epsilon = 1/4$.

be attributed to ϵ=1/4.

Next, we discuss frequency dependence of FMIROs as well as the observed threshold frequency f_{th} in connection to the stepwise absorption model which actually predicts a threshold frequency. Figure 2.12 illustrates experimentally observed FMIROs and theory of the stepwise absorption model. In the theoretical introduction of FMIROs, the "limits" of single-photon transitions in the regime of adjacent Landau levels (n=1) are given in Eq. (2.25). First, the horizontal lines in Figure 2.12 belong to the investigated frequency range from 45 to 85 GHz and the corresponding FMIROs observed in experiments are presented with different symbols for each frequency. The intersection of photon energy $\hbar\omega$ with the dashed lines mark the position of FMIRO ϵ=1/m while the intersection of the dashed lines with the border line $\hbar\omega_c$-2Γ shows the threshold frequency for the corresponding FMIROs owing to the stepwise absorption model. While the upper limit for ω in Eq. (2.25) is not essential in the range of frequencies and magnetic fields studied in the experiments, the lower limit imposes severe constraints for high-order FMIROs. It is obvious from the theoretical calculations that FMIROs appear below this threshold while at the border $\hbar\omega_c$-2Γ, photoresistance exhibits a bump-like feature at high MW power, see Figure 2.11. This quenching effect is also observed for MIROs, already mentioned earlier in the report of Studenikin *et al.* [Studenikin07].

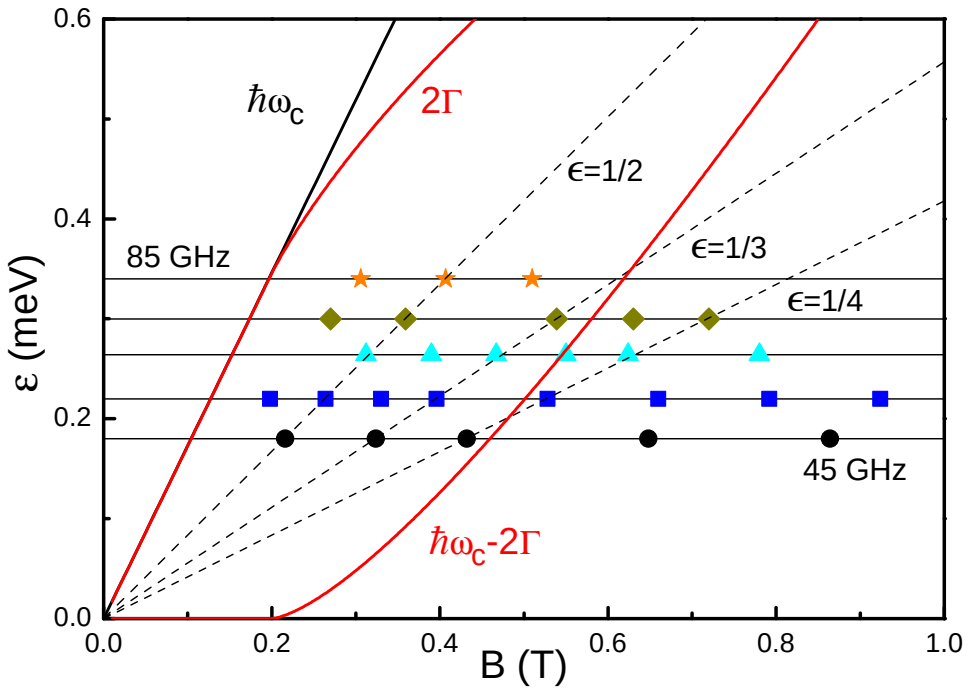

Figure 2.12: Fractional MIROs (different symbols) observed between 45 and 85 GHz, photon energies and the threshold energy $\hbar\omega_c - 2\Gamma$ as functions of the magnetic field. FMIRO features which are beyond the right border line cannot be described within the model of stepwise multiphoton absorption.

The mechanism of MIRO quenching is still not understood and more studies are necessary for different parameters (carrier concentration and mobility) since different reports, [Studenikin07] and [Smet05, Mani08], observe different results. The same conclusion can be made for FMIROs where, e.g. Ref. [Dorozhkin07] presents a threshold frequency which is two times smaller than f_{th} for the investigated samples here. A common theoretical approach is necessary to explain first the damping effect and then the quench of both integer and fractional MIROs.

The last part addresses temperature dependence of FMIROs at a fixed frequency and power, presented in Figure 2.13 at 45 GHz. The chosen temperature range starts from 6.5 K up to 15 K and resistance is plotted as a function of ω_c/ω. The magnetic field range is extended to 2.0 T compared to previous figures. First, increasing T damps CR which is no more visible at 15 K. Contrary to this observation, amplitude for both high-order FMIROs starts to decrease whereas the FMIRO attributed to ϵ=1/4 still exists. A closer look to the position for FMIRO maxima reveals a shift to lower magnetic fields. In contrast to this behavior, MIROs and CR at $\omega = \omega_c$ shift slightly to higher magnetic fields (see Figure 2.6). The difference of the field-shift to the other direction in magnetic field has already been observed in power-dependent measurements. In this temperature range, it is obvious and reasonable to discuss

also a connection of FMIROs, especially of high order, to phonon-induced resistance oscillations (PIROs) which have been introduced in Chapter 1. Generally speaking, the distribution function of electrons is modified in the presence of MW irradiation and this changes both electron and phonon contributions. Figure 2.14(a) presents theoretical calculations taking into account electron and phonon contributions to resistivity [Raichev09]. The frequency is fixed for 55 GHz at 6.5 K and the MW electric field is increased from 0 to 5 V/cm. The parameters for transport time, quantum lifetime and inelastic scattering time are extracted from the experiment and corresponding PIROs from n=2 to n=4 are marked with arrows as wells as FMIROs for E_ω =5 V/cm. Even for a moderate electric field of 1.5 V/cm, PIRO n=2 shifts slightly to a lower magnetic field and by further increasing the MW electric field, an additional peak at $B \simeq$0.35 T appears, marked by a blue arrow and an asterisk. In magnetoresistance, CR and FMIRO features can be identified as 2/3, 1/2 and 1/3. With increasing MW electric field, the additional peak at $B \simeq$0.35 T first increases its amplitude and vanishes for E_ω =5 V/cm. This peak corresponds also to n/m=2/5 which has been interpreted as an FMIRO feature. The phonon contribution due to the change of the electron distribution function by microwaves is presented in Figure 2.14(b). From this point of view, it is possible to describe, e.g. the peak at n/m=2/5 as a result of MIRO/PIRO interference. The second peak, marked with (∗∗) has a smaller amplitude and is damped with increasing MW electric field.

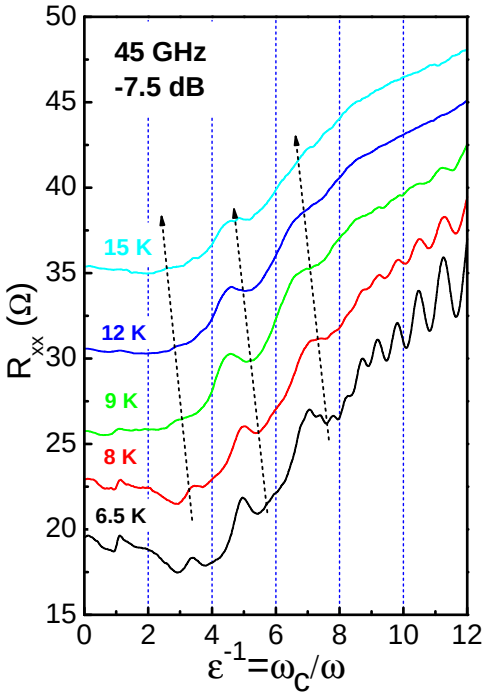

Figure 2.13: Temperature dependence for FMIROs at 45 GHz for -7.5 dB.

The main problem concerning phonon-induced peaks and thus a confirmation for interference of MIROs and PIROs is the magnitude which is, according to the calculations, considerably smaller than experimentally observed, especially for the features at 0.6 and 0.8 T at 55 GHz, see Figure 2.8(a). Note that for the calculations only the quasielastic approximation has been used assuming that energies transferred in electron-phonon scattering are smaller than the temperature [Raichev09]. Calculations beyond that approximation have also not shown the oscillations at 0.6 and 0.8 T for 55 GHz [Raichev09]

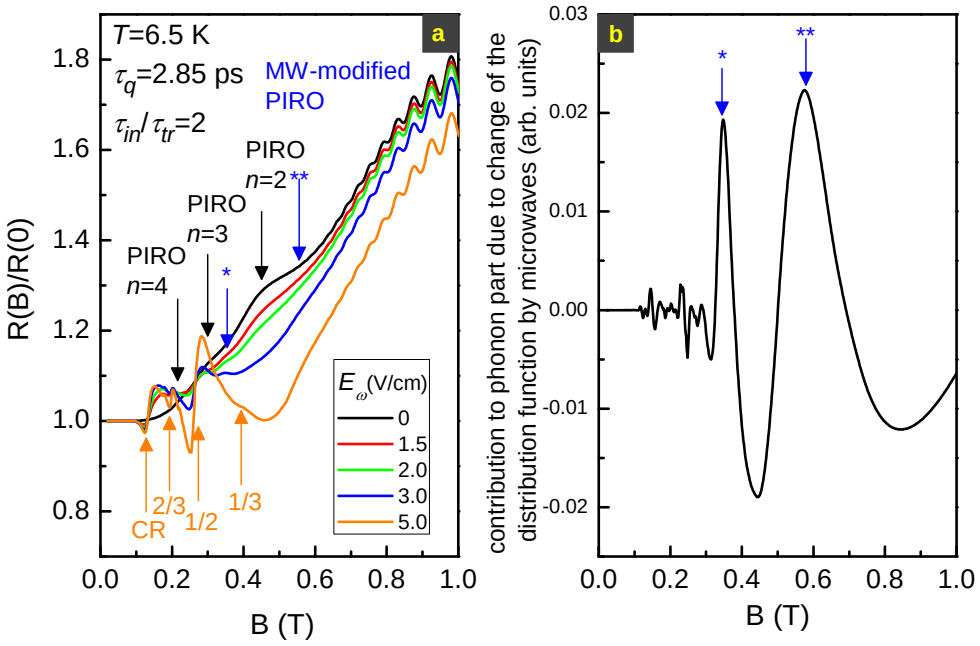

Figure 2.14: (a) Normalized theoretical magnetoresistance for 6.5 K exposed to a MW irradiation of 55 GHz reveals two additional peaks owing to phonons. (b) Contribution of phonons due to the change of electron distribution function.

which are attributed to high-order FMIROs. The remaining high-order features in Figure 2.13 can therefore also not arise owing to MIRO/PIRO interference.

Summary

This chapter presented first the experimental discoveries of microwave-induced resistance oscillations (MIROs) and zero-resistance (ZRS) if a two-dimensional (2D) electron system is exposed to a continuous microwave (MW) irradiation. Two theoretical models, displacement and inelastic mechanism, have been introduced and a general theoretical description, based on a microwave-generated non-equilibrium oscillatory component of the electron distribution function and its harmonics, has been given. Inelastic mechanism is the dominant contribution to photoresistance at low temperatures due to the proportionality $\tau_{in} \propto T^{-2}$. The whole theory can be applied for a 2D system with one occupied subband.

Experimental analysis based on studies of 2D systems with high electron density and moderate mobility, have shown power, frequency and temperature dependence of the MIRO phenomenon. In experiments, it is important to take into account the heating of electrons due to MW irradiation which is reflected in the electron temperature T_e.

The last part first introduced the FMIRO phenomenon in experiment and theory, where MW-induced oscillations occur on the high-field side of the cyclotron resonance. Studies

in our samples at high temperatures and electric fields exhibited high-order fractional microwave-induced resistance oscillations (FMIROs) up to denominator m=8, which have not been observed in previous studies of other groups. It has been found that FMIROs and MIROs have a similar temperature dependence which may indicate that the inelastic mechanism under multiphoton absorption is the dominant one. Furthermore, we have observed a transition to sublinear power dependence of FMIRO amplitude and to a saturation with increasing MW power, attributed to the saturation effect which also favors the inelastic mechanism. The mechanism of multiphoton absorption fails to explain the experimental results. Concerning the stepwise absorption mechanism, both the existence of high-order FMIROs and the independence of the threshold frequency for FMIRO quenching of the number of fraction disagrees with its predictions. Including effects of phonon-induced resistance oscillations (PIROs) which interfere with MIROs can also not account for the high-order features and require another explanation. MIRO/PIRO interference might explain features like n/m=2/5 and their special power dependence.

Chapter 3

Bilayer systems exposed to MW irradiation - double quantum wells

This thesis presents the first experimental and theoretical studies of magnetoresistance exposed to a continuous microwave (MW) irradiation in bilayer electron systems. The aim is to gain fundamental knowledge about the influence of MWs on magnetotransport, i.e. on magneto-intersubband (MIS) oscillations which are present due to the additional quantum degree of freedom.

In the previous chapter the phenomena of microwave-induced resistance oscillations (MIROs) and fractional microwave-induced resistance oscillations (FMIROs) have been discussed in single-layer systems. In contrast to these results, double quantum wells (DQWs) exhibit new and peculiar oscillations of magnetoresistance that are strongly correlated with MW frequency: MIS oscillations are enhanced/damped or even inverted (peak flip). After an overview of preliminary results of photoresistance in DQWs, this chapter introduces the theoretical model for photoresistivity, see Ref. [Wiedmann08].

We explain our results by an interference of MIRO and MIS oscillations. For low temperatures and not too elevated MW power, the inelastic mechanism, developed in Ref. [Dmitriev05], is generalized to the two-subband case and enables us to explain all observed features. Electrodynamic effects are also included in this model. The theoretical calculation of magnetoresistance exposed to MW irradiation can be used for data analysis and extraction of different parameters.

Within this model, a detailed analysis of temperature dependent photoresistance is possible and gives an opportunity to distinguish between MW mechanisms, which obey different sensitivity to temperature. We demonstrate that the inelastic mechanism fails to explain all features of photoresistance above a critical temperature T^* which implies a crossover between two (or more) distinct microwave mechanisms. Additionally, and for high temperatures, a superposition of magneto-intersubband oscillations with fractional MIROs is observed in a small range of frequency, power and temperature.

3.1 Preliminary results

The first section in this chapter gives a brief introduction into experimental studies on DQWs exposed to MW irradiation with a barrier width[1] of 14 Å . First, magnetoresistance without microwaves and exposed to a continuous MW irradiation of 170 GHz in a QW and a DQW is presented in Figure 3.1. Without microwaves, the QW shows well-developed SdH oscillations whereas the DQW exhibits MIS oscillations, superimposed on low-field SdH oscillations starting at $B \simeq 0.3$ T. A QW exposed to MW irradiation exhibits MIROs up to n=3 if one subband is occupied whereas the DQW presents enhanced MIS oscillations for 0.25 or 0.5 T, a damped MIS oscillation feature at 0.4 T and even an inverted MIS oscillation for 0.32 T. Damping of SdH oscillations is observed for

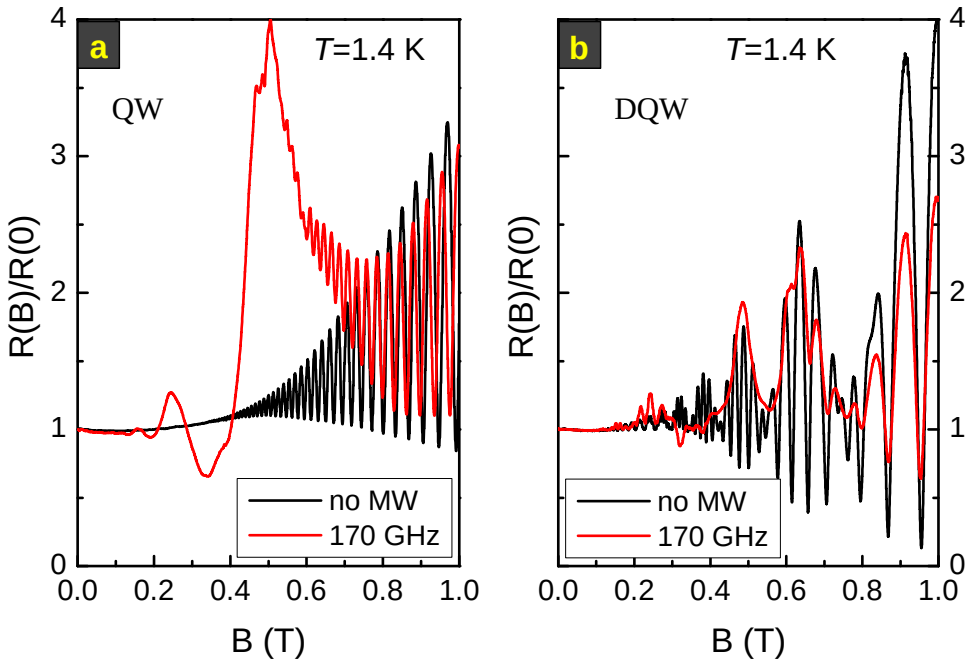

Figure 3.1: Comparison of a QW (a) and a DQW (b) with/without a continuous MW irradiation of 170 GHz at 1.4 K. The MIS oscillation picture is dramatically changed and no cyclotron resonance ($\omega = \omega_c$) or MIROs as in a single QW are observed.

both systems due to electron heating of the 2DEG ($T_e > T_l$). In order to obtain more information about MIS oscillations exposed to MW irradiation, frequency-dependent measurements have been performed in the range between 35 and 170 GHz, presented in Figure 3.2. The MW electric field is constant, extracted to E_ω=2.5 V/cm by fitting experimental traces to theory[2]. Note that in experiments, we ensure a constant electric field by comparing amplitude of SdH oscillations. In Figure 3.2, magnetoresistance is

[1] Samples with thicker barriers have also been investigated, but the MIS oscillations are weaker, see MIS oscillations without MW irradiation in Ref. [Mamani08].

[2] See fitting procedure and the extraction of E_ω in this chapter and in Appendix B.

exposed to MW excitation for frequencies 170, 128, 100, 68 and 35 GHz. Some MIS oscillation have been chosen and denoted by roman numbers (I) to (IV). Starting from 170 GHz, MIS oscillation for B <0.3 T and B >0.45 T are enhanced whereas MIS oscillation (II) is inverted and oscillation (III) is suppressed. With decreasing MW frequency, at 128 GHz, MIS oscillation for B <0.2 T are enhanced while oscillation (I) exhibits a peak flip. All other MIS oscillations for B >0.3 T are enhanced. At 100 GHz MIS

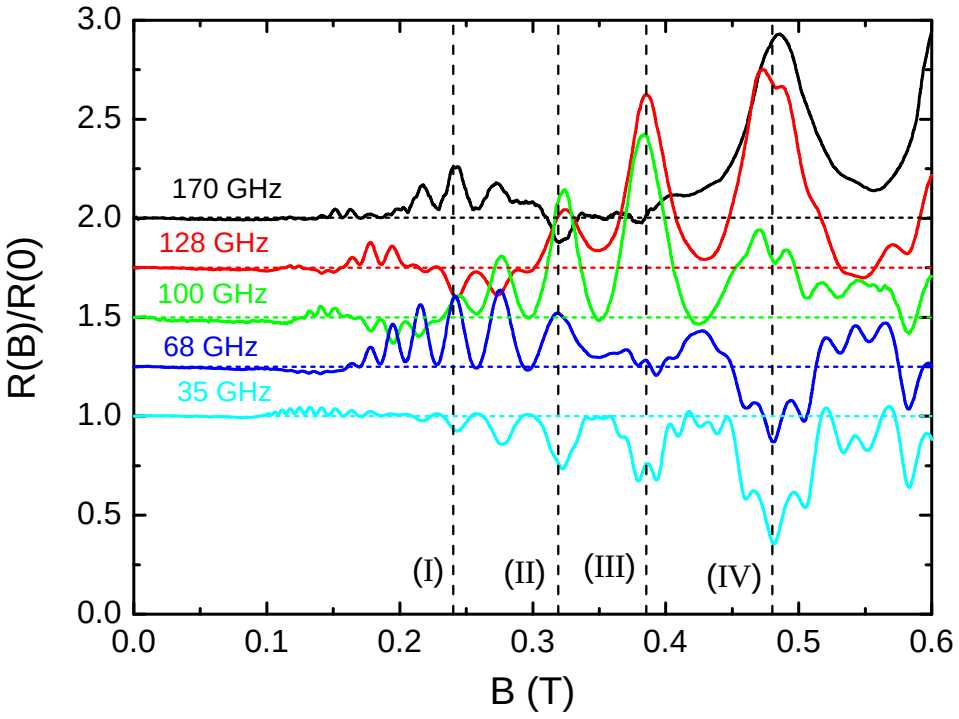

Figure 3.2: Normalized resistance for frequency-dependent measurements in a DQW exposed to MW irradiation for a constant electric field E_ω = 2.5 V/cm at 1.4 K. The MIS oscillation picture is correlated with MW frequency. The roman numbers (I) to (IV) correspond to MIS peaks discussed in the text. Curves are shifted up for clarity, except the one for 35 GHz.

peaks (I) to (III) are enhanced, also peak (IV) but compared to higher frequency its amplitude is smaller. The MIS features around B=0.2 T are all inverted in contrast to higher frequencies. For the first time low-field MIS oscillations around B = 0.15 T are enhanced. By further decreasing MW frequency, at 68 GHz, MIS peaks are enhanced for 0.15 T< B < 0.35 T whereas MIS peaks (III) and (IV) have already changed their sign (peak flip). For the lowest frequency (35 GHz), all MIS peaks are flipped and only the low-field MIS oscillations around B=0.15 T are slightly enhanced. In more detail, it can be seen in Figure 3.2 that that we are able to assign MIS peaks to groups which behave similar by changing MW frequency. At 100 GHz, e.g. all MIS oscillations are enhanced around B=0.15 T while contrary at B=0.2 T, all MIS peaks are inverted.

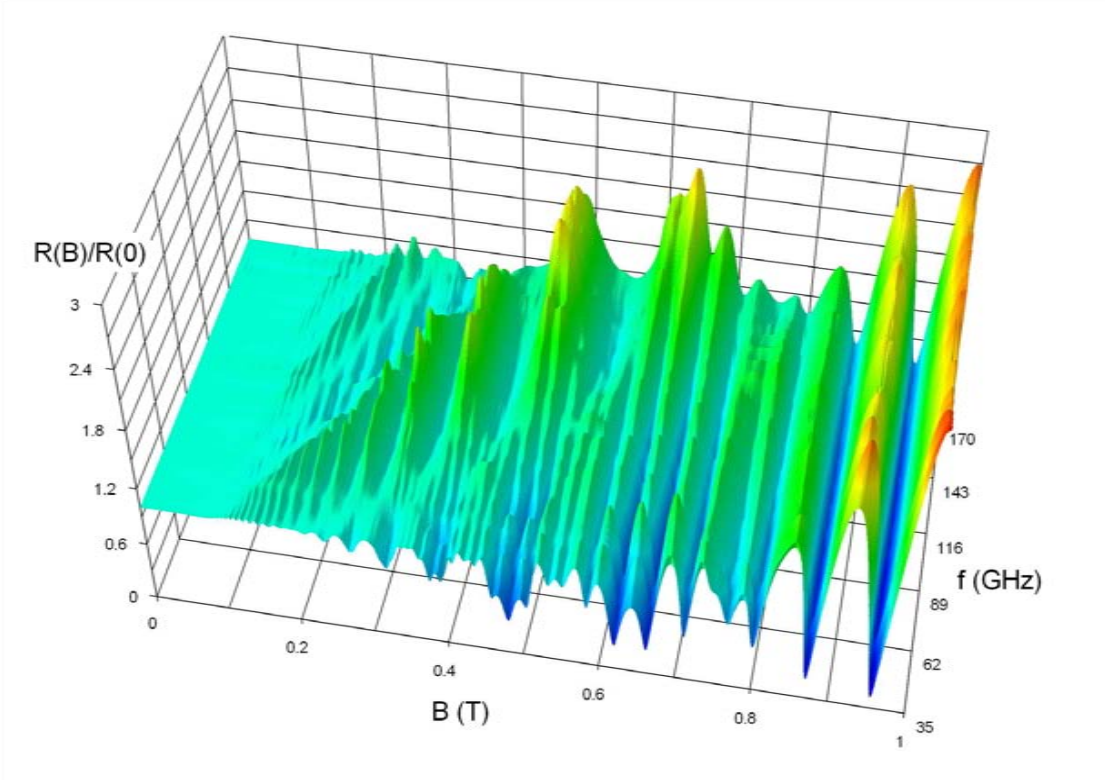

Figure 3.3: 3D-plot of frequency dependence from 170 to 35 GHz in a DQW for a MW electric field of $E_\omega \simeq$2.5 V/cm and at a temperature of 1.4 K.

To get an overview how MIS oscillations behave within the whole frequency range between 35 and 170 GHz, Figure 3.3 presents a 3 D-plot for a constant lattice temperature T=1.4 K and a constant MW electric field of E_ω=2.5 V/cm. Normalized magnetoresistance is plotted as a function of the magnetic field up to 1 T. It should be noted that the constant electric field can be verified again in the constant amplitude of SdH oscillations for $B >$0.8 T. Generally speaking, the enhanced MIS oscillations shift to lower magnetic fields with decreasing MW frequency until for 35 GHz, enhanced MIS oscillations occur only around 0.15 T and all other MIS oscillations are inverted. For a high dc current, MIS oscillations are also inverted, see Ref. [Mamani09b]. Measurements for linear polarization with different orientations of the MW electric field have also been carried out but no polarization dependence has been found.

The next step is now to investigate the evaluation of MIS oscillations from dark magnetoresistance to their peculiar oscillations picture if samples are exposed to highest MW intensity (attenuation 0 dB) for each corresponding frequency. First, Figure 3.4 shows qualitative dependence with increasing MW intensity for frequencies 170, 130, 110 and 90 GHz. The top (bottom) trace corresponds to normalized dark magnetoresistance (attenuation 0 dB). The same evolution with increasing MW power is also presented for 35 and 50 GHz with an attenuation of 0 dB (highest intensity) to an attenuation of -20 dB as well as dark magnetoresistance in Figure 3.5. Note that for both frequencies, amplitude of inverted MIS oscillations first increases, is saturated for an attenuation of

≃-10 dB and decreases for -5 and 0 dB.

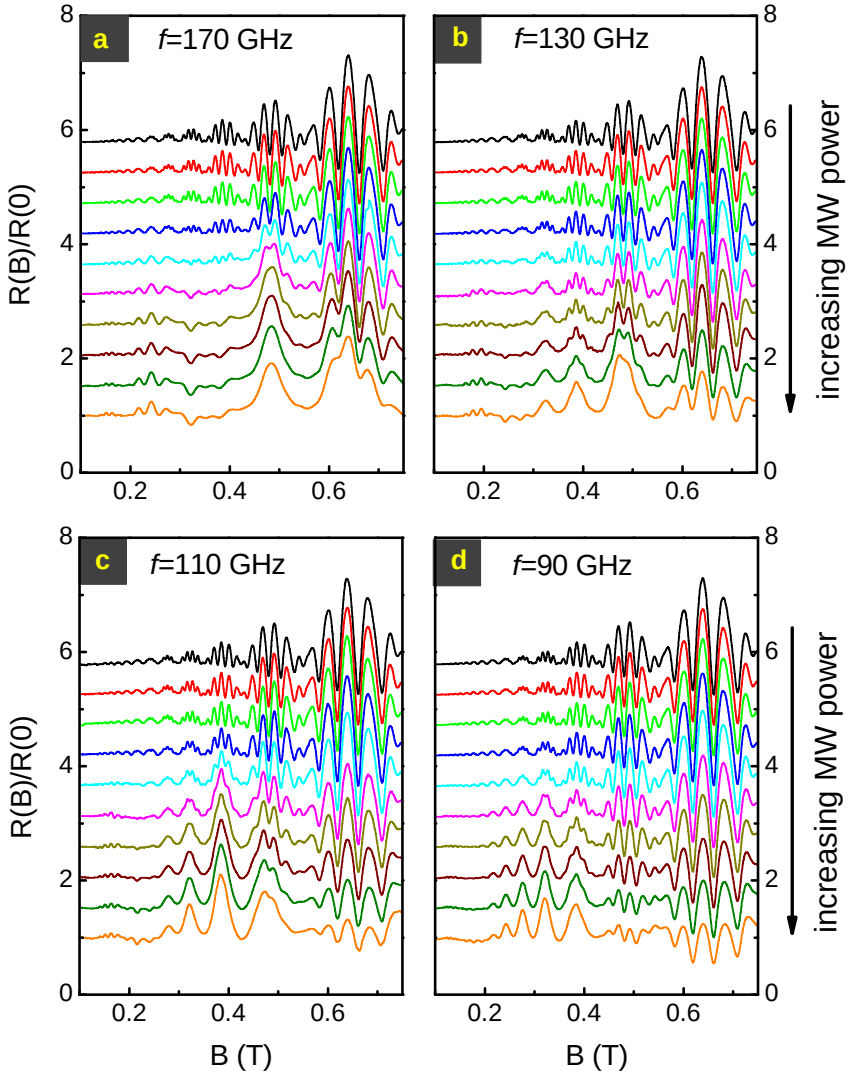

Figure 3.4: Power-dependent normalized magnetoresistance exposed to MW irradiation with frequencies 170, 130, 90 and 70 GHz. The traces show qualitatively the MW effect on MIS oscillations with an increasing electric field [top/black (not exposed to MW irradiation) to bottom/orange (attenuation 0 dB)]. Traces are shifted up for clarity.

3.2 Theoretical model: inelastic mechanism

MIS oscillations exposed to MW irradiation are strongly correlated with the radiation frequency, follow the periodicity ω/ω_c and can thus be attributed to a MIRO-related phenomenon. However, the peculiar or special oscillation picture can not be explained by a simple superposition of the factors $-\sin(2\pi\omega/\omega_c)$ and $\cos(2\pi\Delta_{12}/\hbar\omega_c)$ describing MIROs and MIS oscillations, respectively. In this section, the experimental results are explained by the physical model of Dmitriev *et al.* [Dmitriev05] (inelastic mechanism)

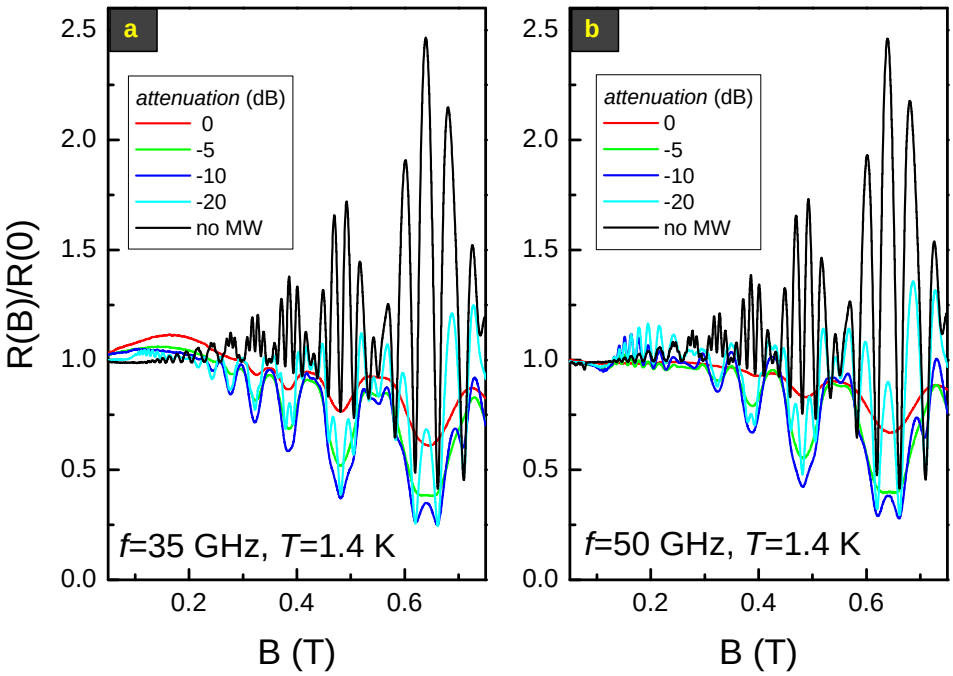

Figure 3.5: Power-dependent normalized magnetoresistance exposed to a MW irradiation of (a) 35 GHz and (b) 50 GHz with attenuations of 0, -5, -10 and -20 dB as well as dark magnetoresistance (no MW).

which is generalized to the two-subband case and improved by taking into account electrodynamic effects in the absorption of radiation by 2D layers [Chiu76, Mikhailov04, Studenikin05] valid for low temperatures[3]. Furthermore it is assumed that the elastic scattering of electrons, including intersubband scattering, is much stronger than the inelastic one, so the electron distribution function (averaged over the time period $2\pi/\omega$) under microwave excitation remains quasi-isotropic and common for both subbands, though essentially non-equilibrium.

3.2.1 General formalism

The energy distribution function, f_ε, is found from the kinetic equation (Quantum Boltzmann equation - QBE) $G_\varepsilon(f) = -J_\varepsilon(f)$, where G_ε is the generation term, and J_ε is the inelastic collision integral[4]. Excitation by a linearly polarized high-frequency electric field $\mathbf{E}_t = \mathbf{E}\cos(\omega t)$ which is weak enough to neglect multi-photon processes, the gen-

[3]This model (general formalism) was formulated by Oleg Raichev.

[4]See Eq. (2.8) where the inelastic mechanism is introduced. Note that starting from this chapter a different notation has been chosen, i.e. f_ε instead of $f(\varepsilon)$.

eration term is written as

$$G_\varepsilon = \frac{1}{\mathcal{D}_\varepsilon}\frac{e^2}{8\pi m^*\omega^2}\sum_{\pm}|E_\omega^{(\pm)}|^2\Big[\Phi_\varepsilon^{(\pm)}(\omega)(f_{\varepsilon+\hbar\omega}-f_\varepsilon) + \Phi_{\varepsilon-\hbar\omega}^{(\pm)}(\omega)(f_{\varepsilon-\hbar\omega}-f_\varepsilon)\Big]. \tag{3.1}$$

where $\mathcal{D}_\varepsilon$ is the density of states, e is the electron charge, and m^* is the effective mass of electrons. Next, $E_\omega^{(\pm)} = E\lambda_\omega^{(\pm)}$, where $\lambda_\omega^{(\pm)} = [1+2\pi\sigma_\pm(\omega)/c\sqrt{\epsilon^*}]^{-1}$ are the amplitudes of the circular polarized components of the electric field in the 2D plane, found from the Maxwell equations [Chiu76, Mikhailov04]. Here, $\sigma_\pm(\omega)$ are the complex conductivities describing response of the electron system to the circular polarized fields, c is the velocity of light, and ϵ^* is the dielectric permittivity of the medium which surrounds the 2D system. The functions $\Phi_\varepsilon^{(\pm)}(\omega)$, which describe the probability of electron transitions between the states with energies ε and $\varepsilon+\hbar\omega$, are written here in terms of Green's functions as $\Phi_\varepsilon^{(\pm)}(\omega) = \mathrm{Re}(Q_{\varepsilon,\omega}^{AR(\pm)} - Q_{\varepsilon,\omega}^{AA(\pm)})$, where

$$Q_{\varepsilon,\omega}^{ss'(+)} = \frac{2\omega_c}{L^2}\sum_{nn'}\sum_{jj'}\sqrt{(n+1)(n'+1)}\sum_{p_yp_y'} \times\Big\langle\Big\langle G_\varepsilon^{jj',s}(n+1p_y,n'+1p_y')G_{\varepsilon+\hbar\omega}^{j'j,s'}(n'p_y',np_y)\Big\rangle\Big\rangle, \tag{3.2}$$

and $Q_{\varepsilon,\omega}^{ss'(-)}$ is given by the permutation of the indices, $n+1\leftrightarrow n$ and $n'+1\leftrightarrow n'$, in the arguments of Green's functions in Eq. (3.2). The Green's functions G, retarded (R) and advanced (A), are determined by interaction of electrons with static disorder potential in the presence of a magnetic field. They are written in the representation given by the product of the ket-vectors $|j\rangle$ and $|np_y\rangle$, describing the 2D subbands and the Landau eigenstates, respectively. Here $j=1,2$ are the electron subbands of the quantum well, n is the Landau level number, and p_y is the continuous momentum, where the Landau gauge is used. The double angular brackets in Eq. (3.2) denote random potential averaging. The conductivities $\sigma_\pm(\omega)$ are expressed in terms of the functions, see Eq. (3.2), as

$$\sigma_\pm(\omega) = i\frac{e^2n_s}{m\omega} + \frac{e^2}{2\pi m\omega}\int d\varepsilon\Big[(f_\varepsilon - f_{\varepsilon+\hbar\omega})Q_{\varepsilon,\omega}^{AR(\pm)} + f_{\varepsilon+\hbar\omega}Q_{\varepsilon,\omega}^{AA(\pm)} - f_\varepsilon Q_{\varepsilon,\omega}^{RR(\pm)}\Big]. \tag{3.3}$$

In the limit $\omega\to 0$, Eq. (3.3) gives the dc conductivity components $\sigma_d = \mathrm{Re}(\sigma_+ + \sigma_-)/2$ and $\sigma_\perp = \mathrm{Im}(\sigma_+ - \sigma_-)/2$.

Using the self-consistent Born approximation (SCBA) and expanding the Green's functions in powers of small Dingle factors, an analytical evaluation of the correlation functions in Eq. (3.2) can be done in the case of relatively weak magnetic fields. The investigated samples are all balanced DQWs where the subband energy separation is typically small compared to the Fermi energy ε_F, thus one can assume that the difference in subband populations is small compared to n_s. This is justified and reasonable for our samples where $\varepsilon_F = \hbar^2\pi(n_s/2)/m^*$=17 meV is much larger than $\Delta_{12}/2$=1.8 meV. The

difference between quantum lifetimes of electrons in the two subbands, τ_1 and τ_2, (and between the corresponding transport times) is also small and neglected everywhere except in the Dingle exponents. In the first order in the Dingle factors $d_j = \exp(-\pi/\omega_c\tau_j)$, the generation term acquires the following form:

$$G_\varepsilon = \mathcal{G}_\omega[r_\omega^{(0)} + (r_\omega^{(0)} - r_\omega^{(1)})g_\varepsilon - r_\omega^{(1)} g_{\varepsilon+\hbar\omega}] \times(f_{\varepsilon+\hbar\omega} - f_\varepsilon) + \{\omega \to -\omega\}, \tag{3.4}$$

where

$$\mathcal{G}_\omega = \frac{\pi e^2 E_\omega^2 n_s \tau_{tr}}{8m^* 2\omega^2}, \quad g_\varepsilon = \sum_{j=1,2} d_j \cos\frac{2\pi(\varepsilon - \varepsilon_j)}{\hbar\omega_c}, \tag{3.5}$$

$$r_\omega^{(0)} = \sum_\pm \frac{|\lambda_\omega^{(\pm)}|^2}{1+s_\pm}, \quad r_\omega^{(1)} = \sum_\pm \frac{|\lambda_\omega^{(\pm)}|^2 s_\pm}{(1+s_\pm)^2}, \tag{3.6}$$

$s_\pm = (\omega \pm \omega_c)^2\tau_{tr}^2$, and τ_{tr} is the transport time, common for both subbands in this approximation.

The kinetic equation is solved now by representing the distribution function as a sum $f_\varepsilon^0 + \delta f_\varepsilon$, where the first term slowly varies on the scale of cyclotron energy, while the second term rapidly oscillates with energy. The first term satisfies the equation $\mathcal{G}_\omega r_\omega^{(0)}(f_{\varepsilon+\hbar\omega}^0 + f_{\varepsilon-\hbar\omega}^0 - 2f_\varepsilon^0) = -J_\varepsilon(f^0)$. Under the assumption that electron-electron scattering controls the electron distribution, one can approximate f_ε^0 by a heated Fermi distribution, $f_\varepsilon^0 = \{1+\exp[(\varepsilon-\varepsilon_F)/T_e]\}^{-1}$. The electron temperature T_e is found from the balance equation $P_\omega = P_{ph}$, where $P_\omega = \int d\varepsilon\, \varepsilon D_\varepsilon G_\varepsilon(f^0) = \mathrm{Re}[|\lambda_\omega^{(+)}|^2\sigma_+(\omega) + |\lambda_\omega^{(-)}|^2\sigma_-(\omega)]E^2/4$ is the power absorbed by the electron system and $P_{ph} = -\int d\varepsilon\, \varepsilon D_\varepsilon J_\varepsilon(f^0)$ is the power lost to phonons (more details, see next section or Ref. [Ma91] and Ref. [Fletcher00]). The second term satisfies the equation

$$r_\omega^{(0)}[\delta f_{\varepsilon+\hbar\omega} + \delta f_{\varepsilon-\hbar\omega} - 2\delta f_\varepsilon] - \frac{\delta f_\varepsilon}{\tau_{in}\mathcal{G}_\omega} = r_\omega^{(1)}[g_{\varepsilon+\hbar\omega}(f_{\varepsilon+\hbar\omega}^0 - f_\varepsilon^0) + g_{\varepsilon-\hbar\omega}(f_{\varepsilon-\hbar\omega}^0 - f_\varepsilon^0)], \tag{3.7}$$

where the relaxation time approximation for the collision integral, $J_\varepsilon(\delta f) \simeq -\delta f_\varepsilon/\tau_{in}$ is used, with the inelastic relaxation time τ_{in}. The solution of this equation is

$$\delta f_\varepsilon \simeq \frac{\hbar\omega_c}{2\pi}\frac{\partial f_\varepsilon^0}{\partial\varepsilon}\frac{A_\omega}{2}\sum_{j=1,2} d_j \sin\frac{2\pi(\varepsilon-\varepsilon_j)}{\hbar\omega_c}, \tag{3.8}$$

$$A_\omega = \frac{\mathcal{P}_\omega(2\pi\omega/\omega_c)\sin(2\pi\omega/\omega_c)}{1+\mathcal{P}_\omega\sin^2(\pi\omega/\omega_c)}\frac{r_\omega^{(1)}}{r_\omega^{(0)}}, \tag{3.9}$$

where $\mathcal{P}_\omega = 4\mathcal{G}_\omega r_\omega^{(0)}\tau_{in}$.

Using the energy distribution function found above, one can calculate the dc resistivity $\rho_{xx} = \sigma_d/(\sigma_d^2 + \sigma_\perp^2)$:

$$\frac{\rho_d}{\rho_0} = 1 - 2\mathcal{T} g_{\varepsilon_F} + \frac{\tau_{tr}}{\tau_{11}^{tr}}(d_1^2 + d_2^2) + 2\frac{\tau_{tr}}{\tau_{12}^{tr}} d_1 d_2 \times\cos\frac{2\pi\Delta_{12}}{\hbar\omega_c} - \frac{A_\omega}{2}\left(d_1^2 + d_2^2 + 2d_1 d_2\cos\frac{2\pi\Delta_{12}}{\hbar\omega_c}\right), \tag{3.10}$$

where $\rho_0 = m^*/e^2 n_s \tau_{tr}$ is the zero-field Drude resistivity and $\Delta_{12} = |\varepsilon_2 - \varepsilon_1|$ is the subband separation. The second term, proportional to g_{ε_F}, describes the SdH oscillations. The third and the fourth terms describe positive magnetoresistance and the MIS oscillations, respectively. Note that these terms are written under condition of classically strong magnetic fields, $\omega_c \tau_{tr} \gg 1$. Here, $\tau_{11}^{tr} = \tau_{22}^{tr}$ and τ_{12}^{tr} are the intrasubband and intersubband transport scattering times, which contribute to the total transport time according to $1/\tau_{tr} = 1/\tau_{11}^{tr} + 1/\tau_{12}^{tr}$. The term proportional to the oscillating factor A_ω describes modification of the oscillatory resistivity under photoexcitation. Another effect of MW irradiation is the electron heating observed in experiments, which increases thermal suppression of the SdH oscillations, described by the factor $\mathcal{T} = (2\pi^2 T_e/\hbar\omega_c)/\sinh(2\pi^2 T_e/\hbar\omega_c)$.

The most essential feature of the resistivity given by Eq. (3.10) is the presence of the product of the oscillating factors $\cos(2\pi\Delta_{12}/\hbar\omega_c)$ and $\sin(2\pi\omega/\omega_c)$, which corresponds to an interference of the MIS oscillations with the MIROs. The interference takes place because the photoexcitation involves both subbands, so the scattering-induced coupling between the subbands, which oscillates as $\cos(2\pi\Delta_{12}/\hbar\omega_c)$, modifies the amplitude of the oscillating photocurrent. Usually, the microwave quantum energy is smaller than the subband separation and the magnetoresistance shows fast MIS oscillations modulated by a slow MIRO component $\propto -\sin(2\pi\omega/\omega_c)$. In all further fitting procedures and analysis, Eq. (3.10) with $d_1 = d_2 = \exp(-\pi/\omega_c\tau_q)$ and $\tau_{12}^{tr} = \tau_{11}^{tr} = 2\tau_{tr}$ is used, which is a good approximation for balanced DQWs[5] [Mamani08]. Then the theoretical result on the dc resistivity is given by

$$\frac{\rho_d}{\rho_0} = 1 - 2d\mathcal{T} \sum_{j=1,2} \cos\frac{2\pi(\varepsilon_F - \varepsilon_j)}{\hbar\omega_c} + d^2(1 - A_\omega)\left[1 + \cos\frac{2\pi\Delta_{12}}{\hbar\omega_c}\right]. \tag{3.11}$$

Based on Eq. (3.11), all experimental data can be analyzed and parameters like MW electric field, electron temperature T_e or scattering times can be extracted. Notice that in the theoretical model of dc resistivity for bilayer systems, the second-order quantum contribution containing MIS oscillations ($\propto d^2$) in Eq. (1.35) is multiplied by the factor $(1 - A_\omega)$ to obtain Eq. (3.11) if such a bilayer system is exposed to MW irradiation.

3.2.2 Heating effect due to MW irradiation

As it was already shown in the previous chapter for 2D systems with one occupied subband, elevated MW power can heat the 2DEG which is first visible in the damping of SdH oscillations. In the last section it has been mentioned that the electron temperature T_e is found from the balance equation $P_\omega = P_{ph}$, with P_ω the power absorbed by the electron system and P_{ph} is the power lost to phonons. In fact, T_e is determined by the power lost to acoustic phonons. If $T_e \ll 10$ K, electron-phonon scattering is small-angle scattering and the lost power owing to piezoacoustic (PA) and deformation-acoustic (DA) interactions can be written as $P_{ph} = P_{PA} + P_{DA}$ with the contributions

[5] See also approximations in Chapter 1 how Eq. (1.35) is obtained for balanced DQWs.

of piezoacoustic interaction

$$P_{PA}(T_e) = \frac{7\zeta(3)(eh_{14})^2 m^{*2}}{4\pi^2 \rho k_F s_l^2 \hbar^5} \left(\frac{9}{16} + \frac{13 s_l^2}{16 s_t^2} \right) T_e^3, \tag{3.12}$$

and the contribution of deformation-acoustic interaction

$$P_{DA}(T_e) = \frac{186\zeta(5) D^2 m^{*2}}{\pi^2 \rho k_F s_l^4 \hbar^7} T_e^5. \tag{3.13}$$

In both contributions $\zeta(n)$ is Rieman's zeta-function, k_F the Fermi wavevector, ρ the material density and $s_{l(t)}$ the longitudinal (transverse) sound velocity. D is the deformation potential (D=7.2 eV for GaAs) and h_{14} is the piezoacoustic module (h_{14}=1.2 V/nm for GaAs). Both expressions for P_{PA} and P_{DA} are written under the condition of strong heating ($T_e^3 \ll T^3$) [Raichev09]. Detailed experiments, estimations and calculations of electron temperature can be found in Refs. [Ma91, Fletcher00]. Both contributions are now equated to the power absorbed by the electron gas which is given by

$$P_\omega = \sigma_\omega \frac{E_\omega^2}{2} \simeq \frac{e^2 E_\omega^2 n_s}{2m^* \tau_{tr}} \frac{(\omega^2 + \omega_c^2)}{(\omega^2 - \omega_c^2)^2}. \tag{3.14}$$

One can see that P_ω depends on both ω and ω_c, so T_e also depends on these two parameters. The balance equation is now summarized to

$$P_\omega = P_{DA} + P_{PA}. \tag{3.15}$$

This balance equation can be solved analytically for B=0 and has to be solved numerically for $B \neq 0$. Note that the inelastic scattering time τ_{in}, quantum lifetime τ_q and transport time τ_{tr} depend also on temperature and therefore heating should also be taken into account, especially for the additional dependence of $\mathcal{P}_\omega$ on ω_c through τ_{in}=$\tau_{in}(T_e)$. The heating of electrons is presented in Figure 3.6 for 170 GHz (0 dB) which corresponds to a MW electric field of 2.5 V/cm and three different lattice temperatures. The maximal heating appears at $\omega \simeq \omega_c$ but this heating effect is not too strong because of the radiative broadening of the cyclotron resonance [Mikhailov04, Studenikin05].

3.2.3 Experimental results and theoretical analysis - fitting procedure

The application of basic principles of the inelastic mechanism generalized to 2D systems with two occupied subbands allows now a broad comparison of theory and experiment for various (low) temperatures, frequencies and intensities of microwave irradiation. To carry out such a comparison, one has first to take into account the heating of electrons by the electric field and the dependence of the characteristic times τ_q, τ_{tr}, and τ_{in} on the electron temperature T_e. According to theory [Dmitriev05], based on the consideration of electron-electron scattering, τ_{in} scales as

$$\frac{\hbar}{\tau_{in}} \simeq \lambda_{in} \frac{T_e^2}{\varepsilon_F}, \tag{3.16}$$

where λ_{in} is a numerical constant in the order of unity[6]. Here we use λ_{in}=1 and obtain

[6]Please notice that λ_{in} and λ are in general not equal. Theoretically, the first quantity characterizes the inelastic relaxation time obtained from the linearized electron-electron collision integral in the kinetic

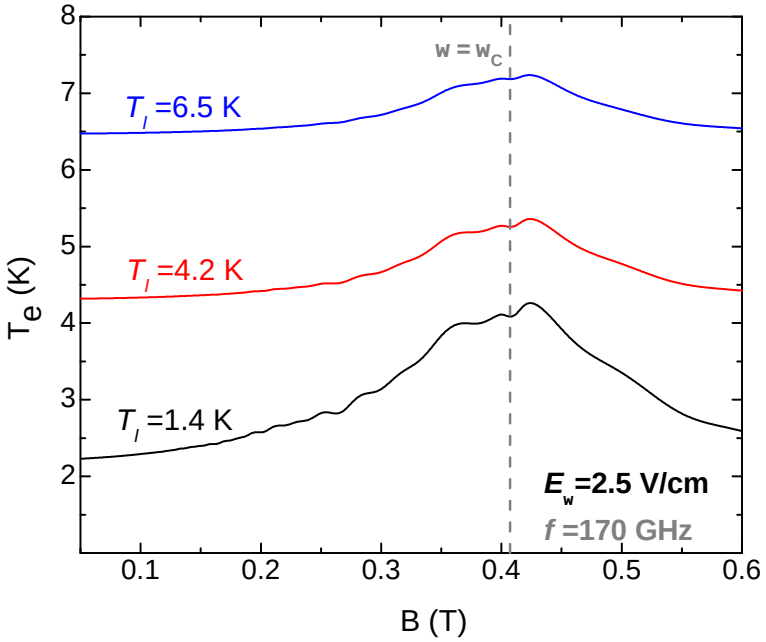

Figure 3.6: Electron temperature T_e as a function of the magnetic field under a continuous MW irradiation of 170 GHz for lattice temperatures of 1.4, 4.2 and 6.5 K.

$\hbar/\tau_{in}$ = 4 mK at T_e=1 K for our DQW system. The temperature dependence of the transport time τ_{tr} and quantum lifetime τ_q of electrons in our samples have been empirically determined by analyzing temperature dependence of zero-field resistance and MIS oscillation amplitudes. The fitting procedure starts by comparing first amplitude of SdH oscillations of dark magnetoresistance (T_e) with magnetoresistance exposed to MW irradiation in order to extract electron temperature. In addition, MIS peaks are still superimposed on low-field SdH oscillations for low temperatures even in the presence of a MW electric field (not too strong) which can also be used as a tool to obtain T_e. Both procedures are in accordance with the theoretical calculation of the electron temperature due to the interaction of electrons with acoustic phonons. Now, both transport time τ_{tr} and quantum lifetime τ_q can be extracted from dark magnetoresistance. The inelastic time τ_{in} is then calculated by Eq. (3.16). Now, there is only one free parameter: the corresponding microwave electric field E_ω which is estimated by fitting calculated amplitudes of magnetoresistance oscillations to experimental data. Examples for the whole frequency range (170 to 36 GHz) at T=1.4 K are presented in Figure 3.7 with $E_\omega \simeq$2.5 V/cm, except for 48 and 36 GHz, where an electric field of $E_\omega \simeq$3.2 V/cm has been used. The same fitting has been done for power dependent measurements, see Figure 3.8. The results of the calculations are in good agreement with the experiment

equation, while the second one characterizes the electron-electron scattering-induced contribution to quantum lifetime which enters the self-energy in the Green's function of electrons [Giuliani82]. Therefore, although these times both scale with temperature as $1/T^2$, they are different quantities.

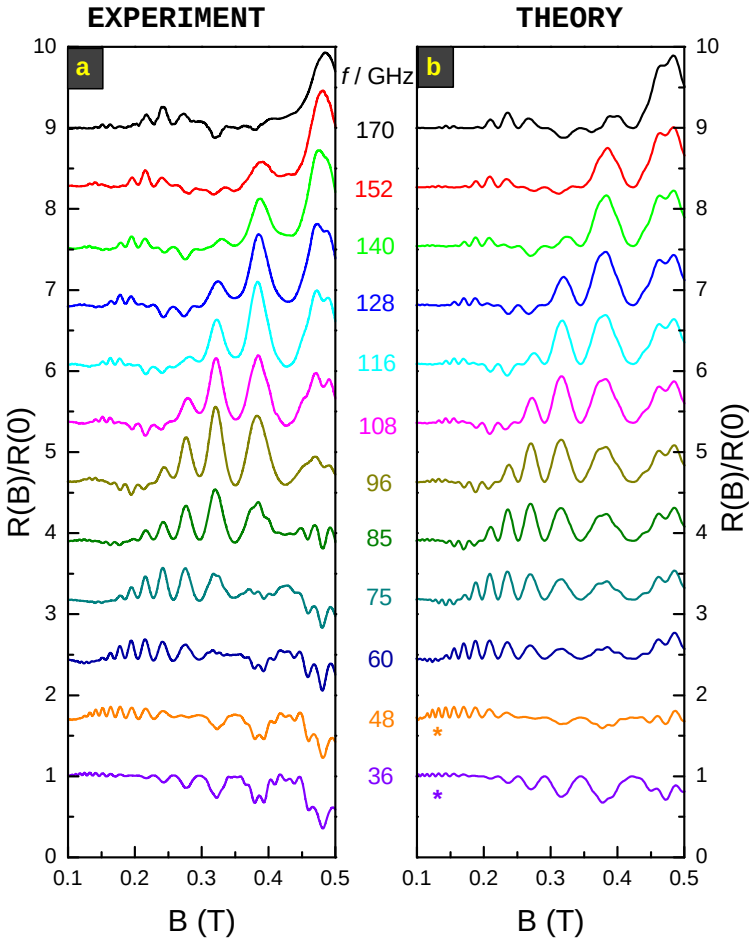

Figure 3.7: Measured (a) and calculated (b) magnetoresistance of DQWs (d_b =1.4 nm) for different frequencies from 170 to 36 GHz under MW excitation at 1.4 K. The calculations have been done using a constant MW electric field of 2.5 V/cm, except for 48 and 36 GHz where E_ω=3.2 V/cm (marked with an asterisk). The traces are shifted up for clarity, except the ones for f=36 GHz.

and capture all features of photoresistance depending on frequency, radiation power, temperature and magnetic field[7].

To understand the MIRO phenomenon requires a comparison of measured photoresistance with the results provided by existing theories. Among the physical mechanisms responsible for the MIROs, this section has shown that the inelastic mechanism which describes the oscillations as a result of microwave-induced change of the isotropic part of electron distribution function dominates at moderate radiation power, owing to a large ratio of τ_{in}/τ_q, which is in the order of 10^2 under typical experimental conditions. The observed insensitivity of the MIROs to polarization of incident radiation and T^{-2} scaling of the oscillatory photoresistance amplitude are also in favor of the inelastic mechanism.

[7]This procedure can only be applied if amplitude of MIS oscillations is not yet saturated for a chosen attenuation, see next section and Appendix B.

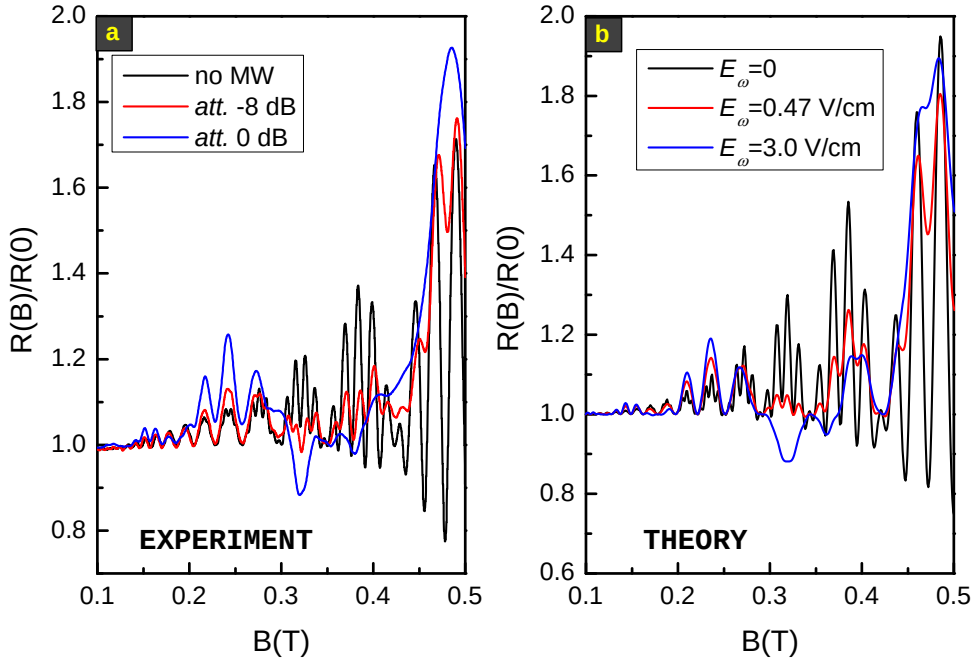

Figure 3.8: Measured (a) and calculated (b) magnetoresistance of a DQW for different MW power (attenuation) for 170 GHz at 1.4 K. The attenuation in experiments in decibels can be translated in a MW electric field.

To summarize, our model confirms the reliability of theoretical estimates for the inelastic relaxation time and leads to a satisfactory explanation of photoresistance in bilayer electron systems.

3.3 Crossover between distinct mechanisms of microwave photoresistance

For low temperatures the inelastic mechanism plays the dominant role because the relaxation of the microwave-induced oscillatory part of the electron distribution is slow. Its application to bilayer electron systems captures all features of photoresistance. Nevertheless, a recent experimental study in a quantum well with one occupied 2D subband on high-mobility samples suggests that the displacement mechanism cannot be ignored and becomes important with increasing temperature when the relative contribution of the inelastic mechanism decreases [Hatke09a]. The crossover between these two mechanisms was observed at $T^* \simeq 2$ K assuming $\tau_{in} \simeq \tau_q^{ee}$. The conclusion that displacement contribution in this work is responsible for the observed crossover, is based on the assumption of small-angle scattering caused by remote impurities (smooth disorder). It should be mentioned that, since these mechanisms produce nearly the same frequency dependence of MIROs, the only way to distinguish between them is to measure tem-

perature dependence of the oscillation amplitudes. Although the magnetoresistance is more complicated in a two-subband system than that for single-subband electron systems, it offers certain advantages in analyzing the effect of microwaves. The reason is that the quantum component of magnetoresistance, which is affected by the microwaves, is "visualized" in DQWs by the MIS oscillations whose period is typically smaller than the period of the MIROs. As a result, the changes in MIRO amplitudes caused by a variation of temperature or microwave intensity are visible in the behavior of single or groups of MIS peaks.

3.3.1 Experimental and theoretical basics

Experiments have been carried out using balanced DQWs with d_b=14 Å and a subband separation of Δ_{12}=3.05 meV. This value is again extracted from the periodicity of low-field MIS oscillations. Photoresistance under a continuous microwave irradiation between 55 GHz and 140 GHz is investigated here. Figure 3.9 presents the basis of experimental analysis for further temperature dependent measurements for 85 GHz. Without microwaves (no MW), MIS oscillations are superimposed on low-field SdH oscillations at 1.4 K. With increasing MW power (at a fixed microwave frequency f=85 GHz), the MIS oscillation picture is modified by the MIRO contribution. Note that the experimental analysis has to be performed for low microwave intensity to ensure that the amplitude of MIS peaks is not yet saturated. Figure 3.9 illustrates power-dependent measurements for several chosen attenuations: 0, -1, -2.5, -5, -7.5, -10 and -15 dB. The inset to Figure 3.9 shows MIS peak amplitude at $B = 0.3$ T (marked by an asterisk) where saturation occurs between -2.5 and -5 dB. Consequently, experimental data with lower microwave intensity (attenuation $\leq$-7.5 dB) has to be used for analysis. The heating of 2D electrons by microwaves is still observable by a suppression of SdH oscillations but is not strong and does not lead to the bolometric effect at $\omega_c \simeq \omega$ because of the radiative broadening of the cyclotron resonance. For temperatures below T=10 K the phonon-induced contribution to electron mobility in these samples is weak, so the transport is controlled by electron-impurity scattering.

The theoretical model takes now into account both inelastic and displacement mechanisms of photoresistance generalized to the two-subband case. In the regime of classically strong magnetic fields, the symmetric part of the diagonal resistivity ρ_d in the presence of microwaves is given by the expression

$$\begin{aligned}\frac{\rho_d}{\rho_0} &= 1 - 2\mathcal{T}\tau_{tr}\sum_{j=1,2}\nu_j^{tr}d_j\cos\frac{2\pi(\varepsilon_F-\varepsilon_j)}{\hbar\omega_c} \\ &+\tau_{tr}\left[\sum_{j=1,2}\frac{2n_j}{n_s}\nu_{jj}^{tr}d_j^2 + 2\nu_{12}^{tr}d_1d_2\cos\frac{2\pi\Delta_{12}}{\hbar\omega_c}\right] \\ &-\frac{1}{2}\tau_{tr}^2A_\omega\left[\sum_{j=1,2}(\nu_j^{tr}d_j)^2 + 2\nu_1^{tr}\nu_2^{tr}d_1d_2\cos\frac{2\pi\Delta_{12}}{\hbar\omega_c}\right] \\ &-\tau^*B_\omega\left[\sum_{j=1,2}\left(\frac{2n_j}{n_s}\right)^2\nu_{jj}^{*}d_j^2 + 2\nu_{12}^{*}d_1d_2\cos\frac{2\pi\Delta_{12}}{\hbar\omega_c}\right], \qquad (3.17)\end{aligned}$$

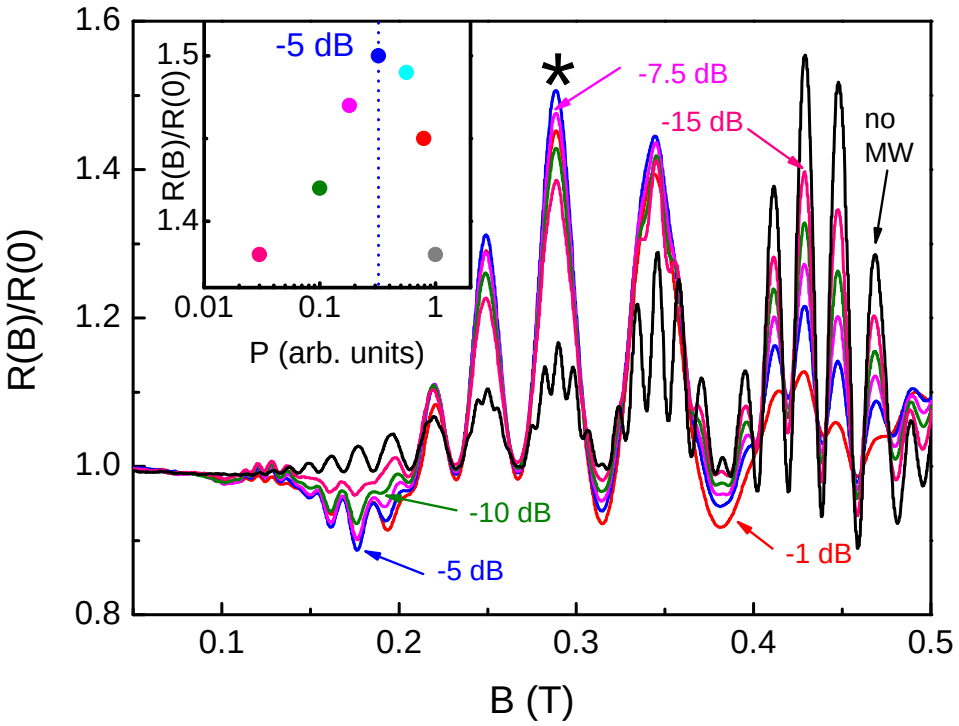

Figure 3.9: Normalized power-dependent magnetoresistance for 85 GHz at 1.4 K as a function of the magnetic field. An increase in MW intensity leads to an enhancement, damping or flip of MIS peaks. Saturation of MIS oscillations appears between attenuations of -2.5 dB and -5 dB. Inset shows this effect for the MIS peak marked with an asterisk.

where the sums are taken over the subbands $j = 1, 2$ with energies ε_j separated by $\Delta_{12} = |\varepsilon_2 - \varepsilon_1|$. Again, the second term is the first-order quantum correction describing the SdH oscillations ($\varepsilon_F = \hbar^2 \pi n_s / 2m^*$ is the Fermi energy), and the third term is the equilibrium second-order quantum correction containing the MIS oscillations. The fourth and the fifth terms are non-equilibrium second-order quantum corrections describing the influence of microwaves owing to inelastic and displacement mechanisms, respectively. In Eq. (3.17), $\rho_0 = m^*/e^2 n_s \tau_{tr}$, τ_{tr} is the averaged transport time defined as $1/\tau_{tr} = (\nu_1^{tr} + \nu_2^{tr})/2$, $1/\tau^* = (\nu_1^* + \nu_2^*)/2$, $d_j = \exp(-\pi \nu_j / \omega_c)$ are the Dingle factors, $\mathcal{T} = X/\sinh X$ with $X = 2\pi^2 T/\hbar\omega_c$ is the thermal suppression factor, and n_j are the partial densities in the subbands ($n_1 + n_2 = n_s$). The subband-dependent quantum relaxation rates ν_j and $\nu_{jj'}$, as well as the scattering rates ν_j^{tr}, ν_j^*, $\nu_{jj'}^{tr}$, and $\nu_{jj'}^*$ are defined in Eq. (1.33) and Eq. (1.34). Applying the approximations for the DQWs to Eq. (3.17), see Chapter 1, one can rewrite it in the form

$$\frac{\rho_d}{\rho_0} \simeq 1 - 2\mathcal{T} d \sum_{j=1,2} \cos \frac{2\pi(\varepsilon_F - \varepsilon_j)}{\hbar\omega_c} + d^2 \left[1 - A_\omega - B_\omega\right] \left(1 + \cos \frac{2\pi\Delta_{12}}{\hbar\omega_c}\right). \quad (3.18)$$

The factors A_ω and B_ω are dimensionless oscillating functions describing MIROs owing to inelastic and displacement mechanism, respectively, and defined [see Eq. (3.9)] as

$$A_\omega \simeq \frac{\mathcal{P}_\omega(2\pi\omega/\omega_c)\sin(2\pi\omega/\omega_c)}{1+\mathcal{P}_\omega\sin^2(\pi\omega/\omega_c)} \tag{3.19}$$

and

$$B_\omega \simeq \frac{\tau_{tr}}{\tau^*}P_\omega\left[\frac{\pi\omega}{\omega_c}\sin\frac{2\pi\omega}{\omega_c}+\sin^2\frac{\pi\omega}{\omega_c}\right] \tag{3.20}$$

The denominator of A_ω also accounts for the saturation effect at high enough microwave intensity. Finally,

$$\mathcal{P}_\omega = \frac{\tau_{in}}{\tau_{tr}}P_\omega, \quad P_\omega = \left(\frac{eE_\omega}{\hbar\omega}\right)^2\overline{v_F^2}\frac{\omega_c^2+\omega^2}{(\omega^2-\omega_c^2)^2}. \tag{3.21}$$

The dimensionless factor P_ω is proportional to the absorbed microwave power. $\overline{v_F^2} = (v_1^2+v_2^2)/2$ is the averaged Fermi velocity (the Fermi velocities in the subbands are defined as $v_j = \hbar k_j/m^*$), and τ_{in} is the inelastic relaxation time. This expression for P_ω assumes again linear polarization of microwaves and is valid away from the cyclotron resonance. The MIROs are given now by the term $-A_\omega - B_\omega$ in Eq. (3.18) representing a combined action of the inelastic and displacement mechanisms. Since the factor $2\pi\omega/\omega_c$ is large compared to unity in the region of integer MIROs ($\omega > \omega_c$), the functions A_ω and B_ω have nearly the same frequency dependence (if far from the saturation regime) and differ only by magnitude and by different sensitivity to temperature.

As mentioned above, the dependence of all characteristic scattering times on the effective electron temperature T_e has to be taken into account. Taking into account Landau level broadening due to electron-electron scattering, a similar contribution should be added to the inverse quantum lifetime, so $1/\tau_q$ is replaced with $1/\tau_q + 1/\tau_q^{ee} \equiv 1/\tau_q(T_e)$, where $\hbar/\tau_q^{ee} \simeq \lambda T_e^2/\varepsilon_F$. As a result, the Dingle factor becomes temperature-dependent: $d \to d(T_e) = \exp[-\pi/\omega_c\tau_q(T_e)]$.

For weak microwave power (far from the saturation regime), Eq. (3.18) can be rewritten in the form

$$\frac{\rho_d}{\rho_0} \simeq 1 - 2\mathcal{T}d\sum_{j=1,2}\cos\frac{2\pi(\varepsilon_F-\varepsilon_j)}{\hbar\omega_c} + d^2(T_e)\left(1+\cos\frac{2\pi\Delta_{12}}{\hbar\omega_c}\right)\left\{1-P_\omega \times\left[\left((T_0/T_e)^2+\beta\right)\frac{2\pi\omega}{\omega_c}\sin\frac{2\pi\omega}{\omega_c}+2\beta\sin^2\frac{\pi\omega}{\omega_c}\right]\right\}. \tag{3.22}$$

In this expression the dependence $\tau_{in} \propto T_e^{-2}$ is applied and T_0 is denoted as the temperature when $\tau_{in} = \tau_{tr}$. Next, $\beta = \tau_{tr}/2\tau^*$. The contributions which are proportional to β result from the displacement mechanism. Since the first term in the square brackets is considerably larger than the second one, it dominates the frequency dependence of MIROs. Therefore, the combined action of both inelastic and displacement mechanism on the magnetoresistance can be approximately described by using the expression for the contribution of inelastic mechanism with an effective (enhanced owing to the displacement mechanism) relaxation time τ_{in}^*:

$$\tau_{in}^* \equiv \tau_{in} + \frac{\tau_{tr}^2}{2\tau^*} = \tau_{tr}\left[(T_0/T_e)^2+\beta\right]. \tag{3.23}$$

The crossover between inelastic and displacement mechanisms should take place at a characteristic temperature $T_C = T_0/\sqrt{\beta}$. Note also, that the consideration presented above neglects the contribution of the photovoltaic mechanism, which, according to theory, should give a different frequency dependence leading, in particular, to a different phase of MIROs. This contribution decreases with increasing ω. According to our theoretical estimates, the contribution of photovoltaic mechanism in our samples can be neglected in comparison to contributions of both inelastic and displacement mechanisms at the frequencies we use, while in samples with higher mobilities its relative contribution is even smaller. Taking also into account that the phase shift of MIROs specific for the photovoltaic mechanism has not been detected in experiments, the neglect of this mechanism is reasonably justified [Wiedmann10a].

3.3.2 Extraction of the relaxation time τ_{in}^*

The procedure how to extract the relaxation time τ_{in}^* is demonstrated at f=85 GHz (attenuation -7.5 dB) for several temperatures in Figure 3.10. The electric field is kept constant and estimated to $E_\omega = 2$ V/cm for low temperature, and the corresponding (B-dependent) electron temperatures T_e were estimated by comparing the effect of heating-induced suppression of SdH oscillations for low temperatures. Low-temperature magnetoresistance exposed to MW irradiation can be satisfactorily described by the inelastic mechanism, see Figure 3.10(a)-(c), with τ_{in} in Eq. (3.16) and a comparison of experimental and theoretical results allows one to determine $\lambda_{in} \simeq 0.94$ in this dependence. However, with increasing temperature, the inelastic mechanism alone fails to describe the experimental magnetoresistance, and we introduce now the effective relaxation time τ_{in}^*, see Eq. (3.23). Both theorectial models with τ_{in} and τ_{in}^* are presented in Figure 3.10(c)-(h) where normalized magnetoresistance is plotted as a function of B for the inelastic model with corresponding τ_{in} (red), combined action of inelastic and displacement mechanisms with an effective τ_{in}^* (blue), and experimental trace (black) for several chosen temperatures. The heating due to microwaves can be neglected for $T \geq$2.8 K, thus $T \simeq T_e$. With increasing temperature, the theoretical model does not fit magnetoresistance for 0.1 T$< B <$0.3 T. Neither the flipped MIS oscillations around B=0.17 T nor the slightly enhanced MIS oscillations at B=0.13 T occur if only the contribution of the inelastic model is used. With an effective relaxation time τ_{in}^*, e.g. in Figure 3.10(f), with $\tau_{in}^* = 3.5\tau_{in}$, both features appear at the corresponding magnetic field. This deviation is also clear in Figure 3.10(g) at $T = 8$ K where an effective relaxation time $\tau_{in}^* = 6.7\tau_{in}$ has to be used in order to obtain the closest fit to the experimental result. This fitting procedure has been applied for various frequencies between 55 and 140 GHz for different attenuations and MW electric fields (Figure 3.11), but always far away from the saturation regime. Figure 3.11 presents the effective relaxation time τ_{in}^* as a function of electron temperature T_e. Note that also a measurement at 85 GHz with -15 dB attenuation has been added where the estimated electric field is E_ω=0.8 V/cm to demonstrate that inelastic mechanism explains photoresistance for low temperatures.

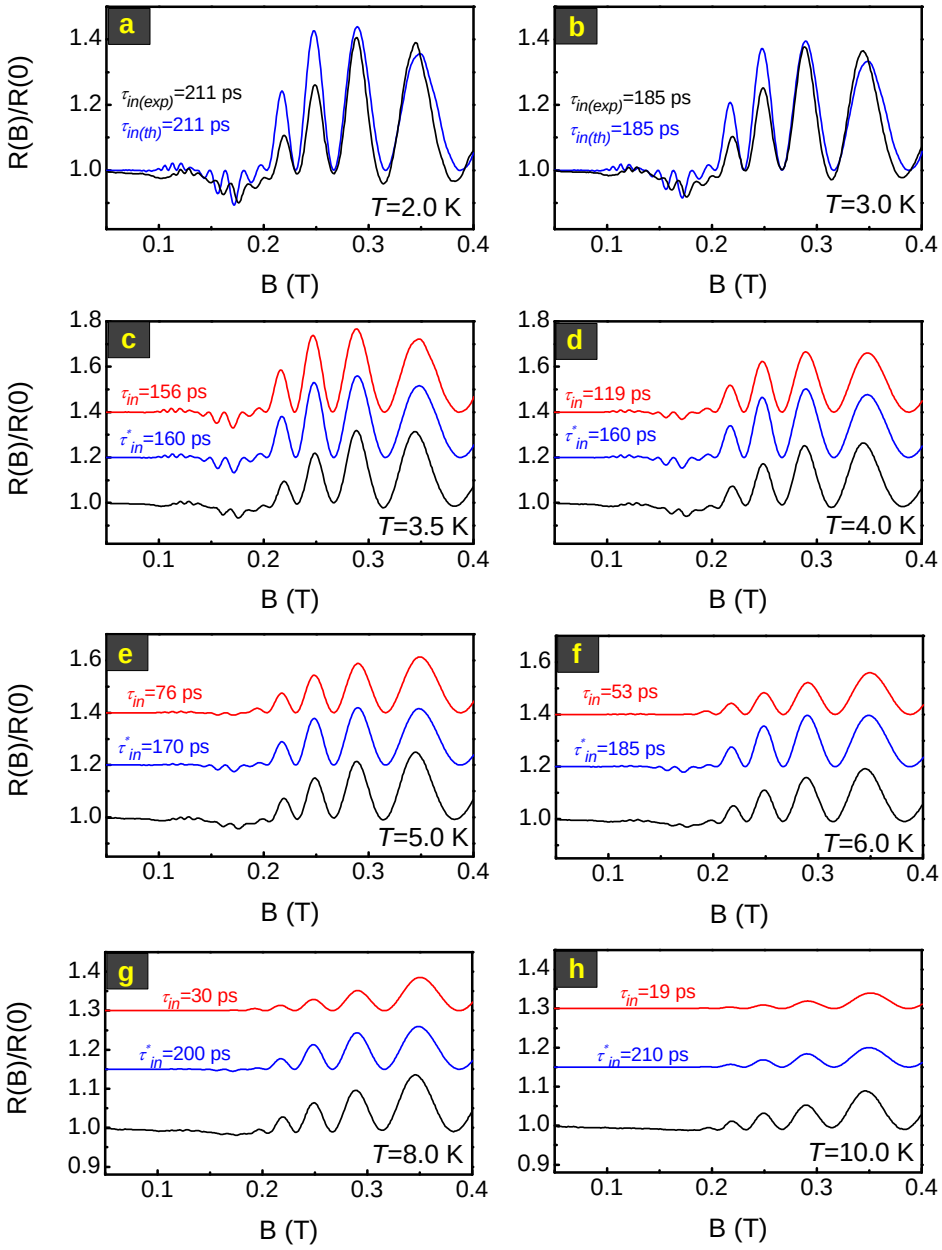

Figure 3.10: Examples of measured (bottom traces, black) and calculated (top traces, red) magnetoresistance for 85 GHz and 2.0 V/cm (-7.5 dB) for various temperatures (a)-(h) denoted by $T = T_e$ except the one for T=2.0 K. Theoretical magnetoresistance (c)-(h) with an effective relaxation time τ^*_{in} (middle traces, blue) fit the experimental data.

It is clearly seen that τ^*_{in} is very close to $\tau_{in} \propto T_e^{-2}$ for $T_e \leq T^*$, which strongly confirms the relevance of the inelastic mechanism of photoresistance in this temperature region. The deviation from this mechanism starts at $T^* \simeq 4$ K, which is denoted by a "critical" temperature T^*. For $T_e > T^*$, a nearly temperature-independent (constant) τ^*_{in} is obtained in the whole frequency and temperature range. Note that the dispersion

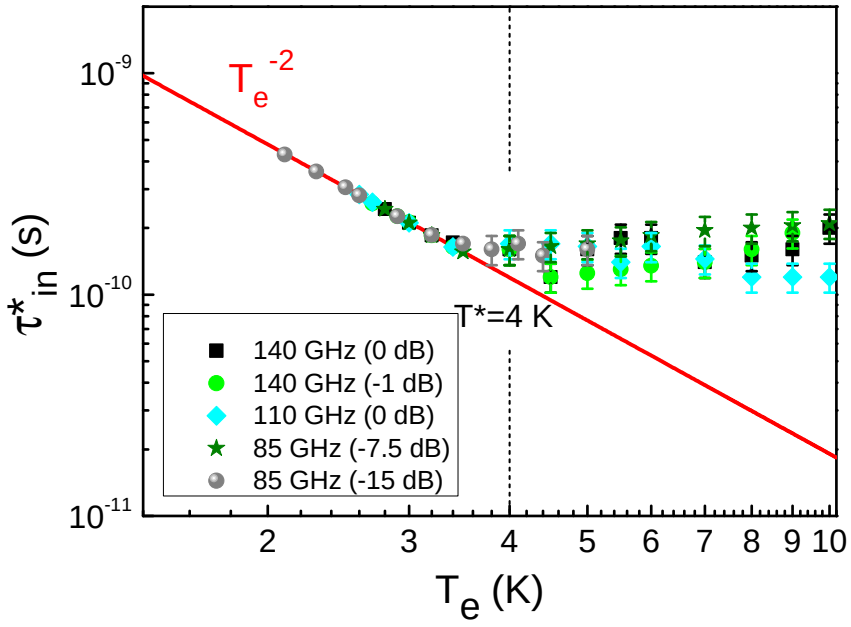

Figure 3.11: Temperature dependence of the effective relaxation time τ^*_{in} extracted for different microwave frequencies and intensities (different symbols), and theoretically predicted inelastic relaxation time $\tau_{in} \propto T_e^{-2}$ of Eq. (3.16) (red thick line). Deviation from the inelastic model starts at a critical temperature $T^* \simeq 4$ K. For higher T_e we observe an almost temperature-independent behavior until the effect of microwaves on the DQW systems vanishes depending on the strength of the electric field E_ω.

of the experimental points is attributed to a limited accuracy of our analysis (mostly by temperature dependence of the Dingle factor), expressed by error bars for T >3.5 K. Owing to the T^{-2}-dependence, this error becomes larger with increasing temperature.

3.3.3 Analysis based on both inelastic and displacement mechanism

It is now tempting to attribute this observed crossover to the theoretically predicted crossover between the inelastic and displacement mechanisms. A recent theoretical work [Dmitriev09] contains a comprehensive analysis of photoresponse taking into account all four contributions to the MIROs (inelastic, displacement, photovoltaic and quadrupole mechanism) and uses a generic-disorder model. The results are analyzed for a realistic model of mixed disorder formed by a superposition of a smooth random potential (previous studies in [Dmitriev05]) and short range scatterers. Whereas the smooth component of disorder is produced by remote impurities from the 2DEG by a wide spacer, the short-range component is produced by residual impurities sitting near or at the interface.
In order to check the reliability of this model, the experimental critical temperature T^* is compared with the theoretical crossover temperature. Based on experimental data, we find $T_0 \simeq$6.0 K where $\tau_{in} = \tau_{tr}$. To find the parameter β, an additional consid-

eration is required, because τ^* is not directly determined from the experiment. This time is expressed through the angular harmonics of the scattering rate, see [Khodas08, Dmitriev09], as

$$\frac{1}{\tau^*} = \frac{3}{2\tau_0} - \frac{2}{\tau_1} + \frac{1}{2\tau_2}, \tag{3.24}$$

with $1/\tau_q = 1/\tau_0$ and $1/\tau_{tr} = 1/\tau_0 - 1/\tau_1$. A large ratio of τ_{tr}/τ_q (τ_{tr}/τ_q=15 in our samples), which is typical for modulation-doped structures, suggests that the scattering is caused mostly by the long-range random potential (smooth disorder, see Chapter 2). If a model of exponential correlation is used [$w(q) \propto \exp(-l_c q)$, where l_c is the correlation length of the random potential], each harmonic is given by the following expression:

$$\frac{1}{\tau_k} = \frac{1}{\tau_{sm}} \frac{1}{1+\chi k^2}, \quad \chi = (k_F l_c)^{-2} \ll 1. \tag{3.25}$$

Here $1/\tau_{sm}$ is the total quantum rate. Since the parameter χ can be determined from the known ratio τ_{tr}/τ_q, which is equal to $1+\chi^{-1}$ in this model, the time τ^* and, hence, β can be found. The crossover temperature for our samples is found to be $T_C \simeq$15.3 K, which is considerably larger than T^*. Therefore, the contribution of displacement mechanism is not strong enough to explain the observed temperature behavior.

The presence of a small amount of short-range scatterers (such as point defects whose radius is much smaller than the inverse Fermi wavenumber $1/k_F$) increases the contribution of the displacement mechanism. For this two-component disorder model, Eq. (3.25) should be replaced with [Khodas08, Dmitriev09]

$$\frac{1}{\tau_k} = \frac{\delta_{k,0}}{\tau_{sh}} + \frac{1}{\tau_{sm}} \frac{1}{1+\chi k^2}, \tag{3.26}$$

where τ_{sh} is the isotropic scattering rate. The relative content of the short-range scatterers can be characterized by the ratio τ_{sm}/τ_{sh}. The crossover temperature T_C, indeed, decreases with increasing τ_{sm}/τ_{sh}. However, to keep a constant τ_{tr}/τ_q which is determined experimentally, the ratio τ_{sm}/τ_{sh} can not be made too large. In Figure 3.12(a) the dependence of T_C/T_0 on the content of the short-range scatterers for several ratios of τ_{tr}/τ_q is illustrated. Each curve stops at the point when the given ratio cannot be reached if we add more short-range scatterers; this point corresponds to $\beta = 3/4$. Therefore, for two-component disorder we can reduce T_C down to $(2/\sqrt{3})T_0$, which in our case gives the lower limit $T_C \simeq$7 K. Again, the displacement mechanism contribution is still too weak to produce the crossover at $T \simeq$4 K. In order to demonstrate the temperature dependence of the expected τ_{in}^*, theoretical plots based on Eq. (3.23) with T_C=15.3 K and T_C=7 K are added to the extrated experimental values for τ_{in}^*, see Figure 3.12(b). It is clear that the smooth disorder model cannot fit the experimental data above $T^* = 4$ K. The mixed disorder model produces a better but still not sufficient agreement with the experimental observations in this region. Nevertheless it leads to a noticeable deviation from the $\tau_{in}^* \propto T^{-2}$ dependence in the region $T < T^*$. This essential observation shows that the behavior of τ_{in}^* can hardly be explained within a model that adds a temperature-independent or weakly temperature-dependent term to τ_{in}. Such

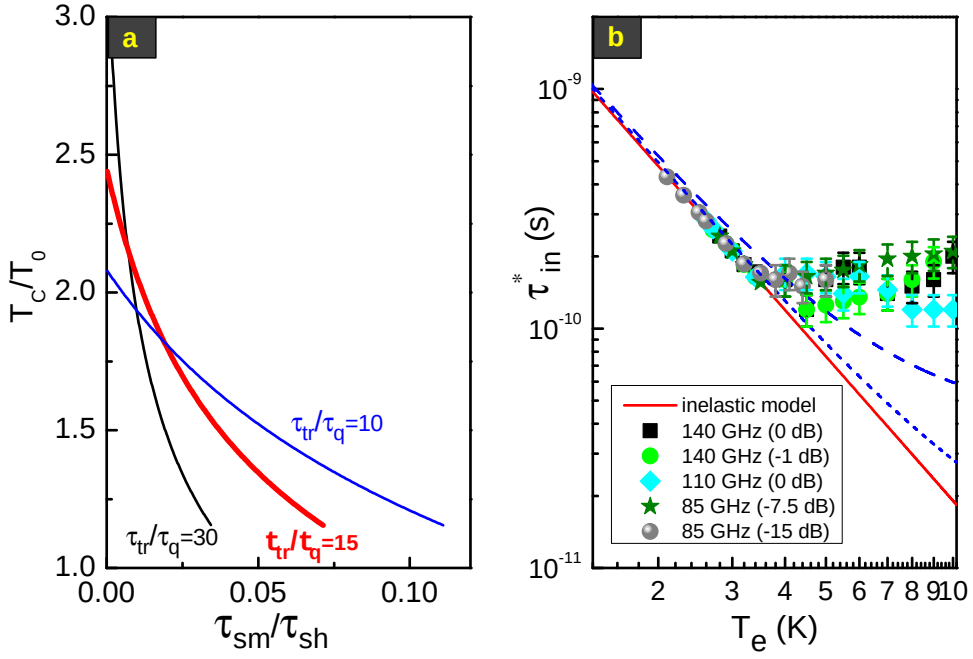

Figure 3.12: (a) Theoretical dependence of the crossover temperature on the content of short-range scatterers for several given ratios τ_{tr}/τ_q (for our samples τ_{tr}/τ_q=15). T_0 is the temperature when τ_{in} equals τ_{tr}. (b) Theoretical dependence of τ^*_{in} under approximations of smooth scattering potential (short dashed) and of mixed disorder at maximal possible content of short-range scatterers (dashed) as well as extracted experimental data of Figure 3.11.

a term cannot lead to a distinct change of the slope of the T-dependence around T^*. Indeed we can attribute the observed magnetoresistance exposed to MW irradiation to a superposition of inelastic and displacement mechanism but it might also be suggested now that another, previously unaccounted mechanism of photoconductivity, which turns on at $T \simeq T^*$ more abruptly than the displacement mechanism, should be important.

3.4 Interference of FMIROs and MIS oscillations in a bilayer electron system

With increasing temperature, MIS oscillations interfere with fractional microwave induced resistance oscillations. This section presents this interference in a small range of temperature, frequency and microwave power. Since the barrier width d_b is related to the strength of MIS oscillations, we focus on two wafers with d_b=14 Å where we extracted a subband separation from the periodicity of low-field MIS oscillations $\Delta_{12} = 3.35$ meV (wafer A) and $\Delta_{12} = 3.05$ meV (wafer B), respectively.

3.4.1 MIS and FMIRO interference at high temperatures

With increasing microwave power, FMIROs are observed which can be described by $\epsilon = \omega/\omega_c = n/m$ with integer n and m and $m \geq 2$, see Chapter 2. If a bilayer system is now exposed to microwave irradiation, photoresistance differs from the single-subband case because of the additional intersubband scattering.

The observation of FMIRO/MIS-interference is based on three conditions found in experimental studies: (i) enhanced MIS oscillations due to MW irradiation, (ii) an elevated MW power where FMIROs can occur and (iii) high temperature. The first condition is connected to frequency and satisfied in the frequency range between 62 and 75 GHz. The second condition requires high MW power and this interference appears for an electric field of $E \simeq 4$ V/cm. The last condition is satisfied for a temperature range 8 K$<T<$12 K, where MIS oscillations exhibit a "modulation" for several MIS peaks for $\omega > \omega_c$. Temperature and power dependence are illustrated in Figure 3.13 for 66 GHz for both wafers. It has been already discussed in this chapter, that MIS oscillations can be arranged in groups of enhanced MIS oscillations, but now, one MIS peak at B=0.3 T is slightly damped for 8 and 10 K, see Figure 3.13(a). This behavior is not observed for lower or higher temperature. Power dependence reveals the interference phenomenon for 0 and -1 dB, but this effect disappears for lower MW power, see Figure 3.13(b). It has to be pointed out that SdH oscillations are already suppressed for these temperatures and low magnetic fields.

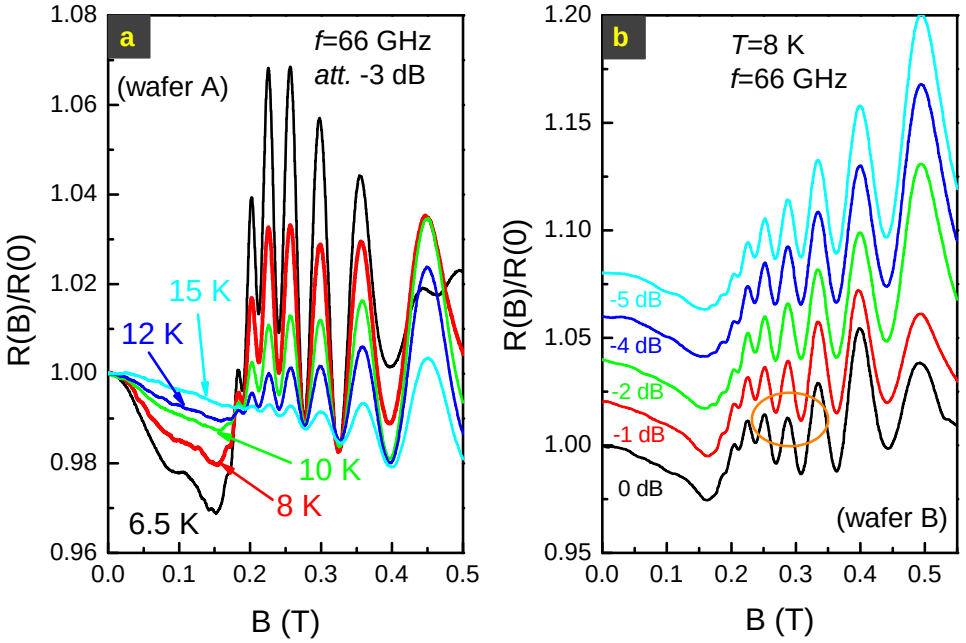

Figure 3.13: (a) Temperature and (b) power dependence of magnetoresistance exposed to a MW irradiation of 66 GHz. This interference appears in a small range of temperature, power and frequency.

It is worth noting that MIS oscillations are superimposed on cyclotron resonance at $\omega = \omega_c$ for different temperatures and attenuations (MW power) in Figure 3.13.

3.4.2 Extension to high MW electric fields

Finally, the MW power has been increased further which is only possible within the frequency range of 35 to 55 GHz (wafer B). The temperature is kept constant at 8 K, and Figure 3.14(a) shows magnetoresistance exposed to MWs at a frequency of 55 GHz for -10 and 0 dB. The attenuation of -10 dB corresponds to the electric field at 66 GHz with 0 dB, approximately 4 V/cm, which is plotted in Figure 3.14(b). The dashed-dotted lines mark ω_c and $\omega_c/2$ for both frequencies. For an attenuation of 0 dB, all MIS oscillations are damped due to the strength of the MW electric field. The feature at $\omega_c/3$ might be attributed to an FMIRO or is "simply" an inverted MIS oscillation. Theoretical calculations based on a general description of the MIRO and FMIRO phenomenon are currently under study. The first results confirm the interference of FMIROs with MIS oscillations at high temperatures.

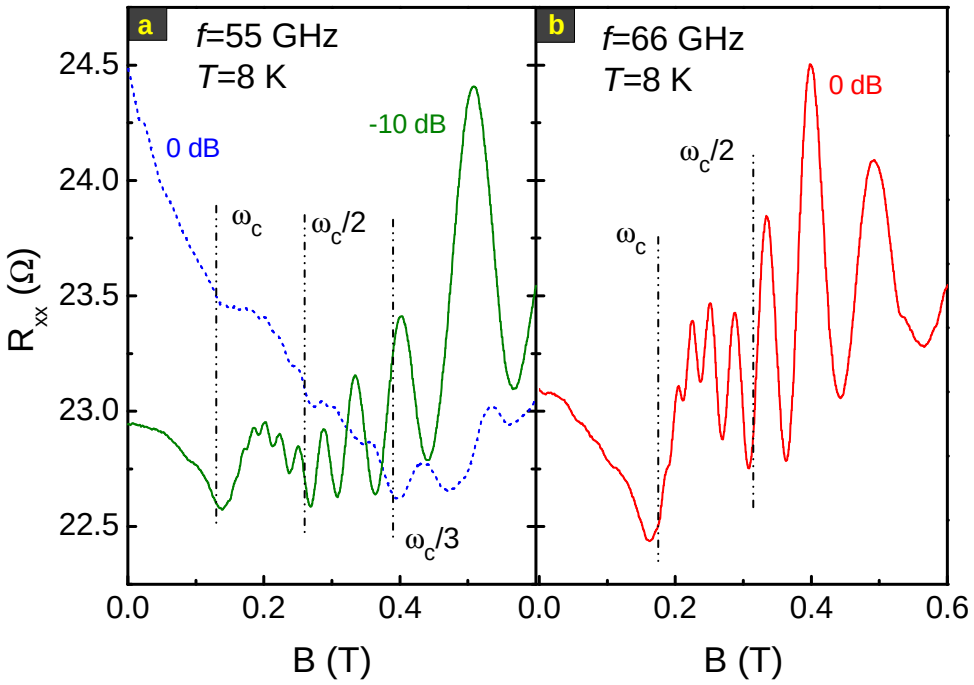

Figure 3.14: Magnetoresistance exposed to MW irradiation at 8 K: (a) from moderate to very high power (attenuation of -10 and 0 dB) at 55 GHz where MIS oscillations experience a strong damping. (b) Corresponding magnetoresistance exposed to a MW irradiation of f=66 GHz (0 dB, 4 V/cm) which corresponds to the same electric field for 55 GHz with an attenuation of -10 dB.

Summary

This chapter presented the first photoresistance studies in low dimensional bilayer electron systems which are different from pure single-layer system. If such a bilayer electron system is exposed to a continuous microwave (MW) irradiation, magneto-intersubband (MIS) oscillations are enhanced, damped or inverted, strongly correlated with MW frequency. For bilayer systems formed by double quantum wells, no zero-resistance states (ZRS) have been observed. The physical mechanism responsible for the microwave-induced resistance oscillations (MIROs), is the inelastic mechanism which describes well the oscillations as a result of microwave-induced change of the isotropic part of electron distribution function and dominates at moderate radiation power and low temperatures. The presence of the product of the oscillating factors $\cos(2\pi\Delta_{12}/\hbar\omega_c)$ and $\sin(2\pi\omega/\omega_c)$, which corresponds to the MIS oscillations and to the microwave part, respectively, leads to an interference of the MIS oscillations with the MIROs.

In addition, temperature dependent experiments have shown that the inelastic mechanism alone fails to explain magnetoresistance exposed to MW irradiation for high temperature ($T >$4 K). Despite the limited accuracy of our analysis, the observed deviation cannot be fully explained by the contribution of the displacement mechanism, and, therefore, requires another explanation. At high temperature, an interference of fractional microwave-induced resistance oscillations (FMIROs) with MIS oscillations in a small range of parameters (temperature, power and frequency) has been observed. The discovery of MW photoresistance in bilayer electron systems presented in this chapter should stimulate further theoretical and experimental work on the transport properties of 2D electron systems.

Chapter 4

Zero-resistance states in bilayer electron systems - wide quantum wells

Beside double quantum wells, high-quality bilayer electron systems can also be formed by wide quantum wells (WQWs). If the electron density is high enough, the WQW can be considered to be an effective bilayer system where electrons occupy two two-dimensional (2D) subbands. The advantage of this bilayer electron system compared to double quantum wells is a higher mobility.

Zero-resistance states (ZRS) which appear if a 2D-system is exposed to microwave (MW) irradiation have created much experimental and theoretical attention, and this phenomenon became an interestring topic in general physics [Mani02, Zudov03, Durst03, Andreev03, Willett04, Dmitriev05]. So far, experiments of ZRS have been carried out only in high-mobility 2D systems (single quantum wells or heterojunctions) with one populated subband including studies on temperature, power and MW frequency, and all experimental and theoretical works focus on such systems.

This rises the question wheater such ZRS with vanishing dissipative resistance appear only in a one-subband system or might occur in multilayer electron systems or even in quasi three-dimensional (3D) systems.

In this chapter we present the first results for a system which is different from single-layers. ZRS are observed in a bilayer electron system formed by WQWs exposed to microwave irradiation even in the presence of additional magneto-intersubband scattering due to two populated subbands. We show that the phenomenon of ZRS in bilayers is distinct from single-layer systems and the vanishing resistance develops for inverted magneto-intersubband (MIS) oscillations. MIS oscillations are inverted and approach zero-resistance.

After introducing the samples which have been investigated, results of magnetoresistance are presented which exhibit ZRS for different frequencies. The appearance of ZRS is analyzed for different MW power and temperature. We compare the experimental results quantitatively to theory and we show that the strength of MW electric field where absolute negative photoresistance occurs is coincident with the appearance of ZRS based on the inelastic mechanism of photoresistance.

4.1 Wide quantum wells: samples and properties

If electrons are confined to a WQW with very low density n_s, they occupy the lowest electric subband and have a single-layer-like charge distribution. If more electrons are added, density increases and owing to charge redistribution, WQWs form a double-well configuration where electrons occupy two 2D subbands as a result of tunnel hybridization of electron states. The two wells formed near the interfaces are separated by an electrostatic potential barrier. The samples used in this thesis have a well width of w=45 nm with a total density $n_s = 9.1 \cdot 10^{11}$ cm^{-2}, extracted from the periodicity of Shubnikov-de Haas (SdH) oscillations. The mobility is $\mu \simeq 1.9 \cdot 10^6$ cm^2/V s at 1.4 K. In Figure 4.1(a) the wide quantum well with corresponding wavefunctions, symmetric (S) and antisymmetric (AS), is sketched. Theoretical results based on a Hartree-Fock calculation are shown in Figure 4.1(b) where subband separation is plotted as a function of electron density. For a density of $n_s = 9.1 \cdot 10^{11}$ cm^{-2}, we obtain a subband separation of Δ_{SAS}=1.4 meV. Figure 4.1(c) demonstrates both experimental and calculated magnetoresistance. The subband separation Δ_{SAS} is extracted to Δ_{SAS}=1.4 meV (periodicity of MIS oscillations) and the quantum lifetime to τ_q=7.1 ps (Dingle factor) from the experiment using Eq. 3.11. Both are in agreement with theory. It is also worth noting that the appearance of MIS oscillations confirms that electrons occupy the two lowest subbands.

In addition to MIS oscillations, short-period oscillations appear in a temperature range from 10 to 35 K in WQWs (not shown in this thesis). They have the periodicity of SdH oscillations but, surprisingly, are not damped by temperature. The occurrence might be based on the existence of quasi-localized states, with a resonant level characterized by a peak of the density of states not far from the Fermi level and not sensitive (or weakly sensitive) to the magnetic field, but most likely, those oscillations occur due to the population of the third subband with increasing temperature which is slightly above ε_F. Studies are currently performed [Wiedmann10c].

4.2 Zero-resistance states

Zero-resistance states have been experimentally discovered by Mani *et al.* [Mani02] and Zudov *et al.* [Zudov03] in a one-subband system. The previous section has demonstrated that due to high electron density, two subbands are occupied in our WQWs, thus we have additional intersubband scattering which occurs owing to the sequential passage of Landau levels through the Fermi energy ε_F with increasing magnetic field. The interference of MIS oscillations and MIROs has been extensivly discussed in the previous chapter but a transition from MIROs to ZRS with increasing MW power has not been observed due to the lower quality of the bilayer systems, formed by double quantum wells.

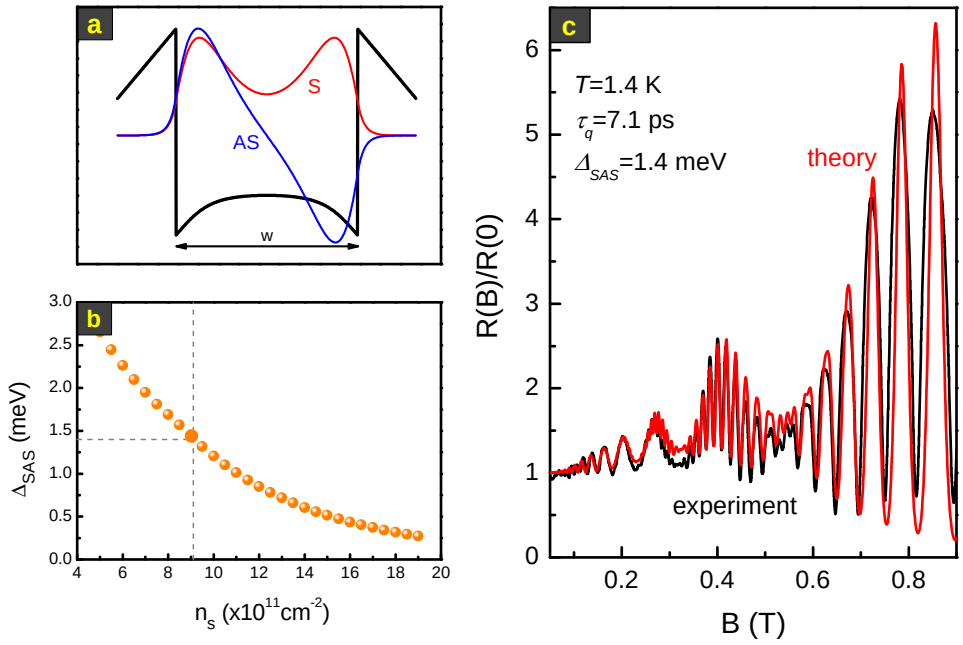

Figure 4.1: (a) Sketch of a wide quantum well with a width w=45 nm and corresponding symmetric (S) and antisymmetric (AS) wavefunctions. (b) Theoretical calculation of subband separation as a function of electron density n_s (dashed line indicates the density of our samples). (c) Measured and calculated magnetoresistance at 1.4 K.

4.2.1 Experimental observation

If a bilayer system is exposed to MW irradiation, MIS peaks are enhanced, damped or inverted depending strongly on frequency. Figure 4.2 shows longitudinal resistance R_{xx} and Hall resistance R_{xy} up to a magnetic field of 11 T at a temperature of 1.4 K. Notably, R_{xx} exposed to MW irradiation with a frequency of 143.2 GHz (attenuation 0 dB) exhibits a strongly enhanced and an inverted MIS oscillation with zero-resistance for B <0.5 T, see inset of Figure 4.2. High-field SdH oscillations exposed to MW irradiation are slightly damped due to heating of the electron system and no change in Hall resistance is visible. The SdH oscillations are damped due to electron heating by microwaves except two features at B=1.2 T which are enhanced and marked with an asterisk. Figure 4.2 exhibits also a minimum at 0.55 T and weak minima at 0.22 and 0.32 T which are not attributed to MIS oscillations. They occur in the region of transitions from inverted to enhanced MIS oscillations.

Figure 4.3 illustrates resistance for positive and negative magnetic field in the frequency range from 68.5 GHz to 143.2 GHz with four chosen frequencies at 68.5 GHz, 87.2 GHz, 100 GHz and 143.2 GHz (from top to bottom). For all four traces, we show the highest MW intensity (attenuation 0 dB) at a temperature of 1.4 K. We observe ZRS at B = 0.27 T for 143.2 GHz and denote this ZRS as peak (I), ZRS at B = 0.2 T for 100 GHz

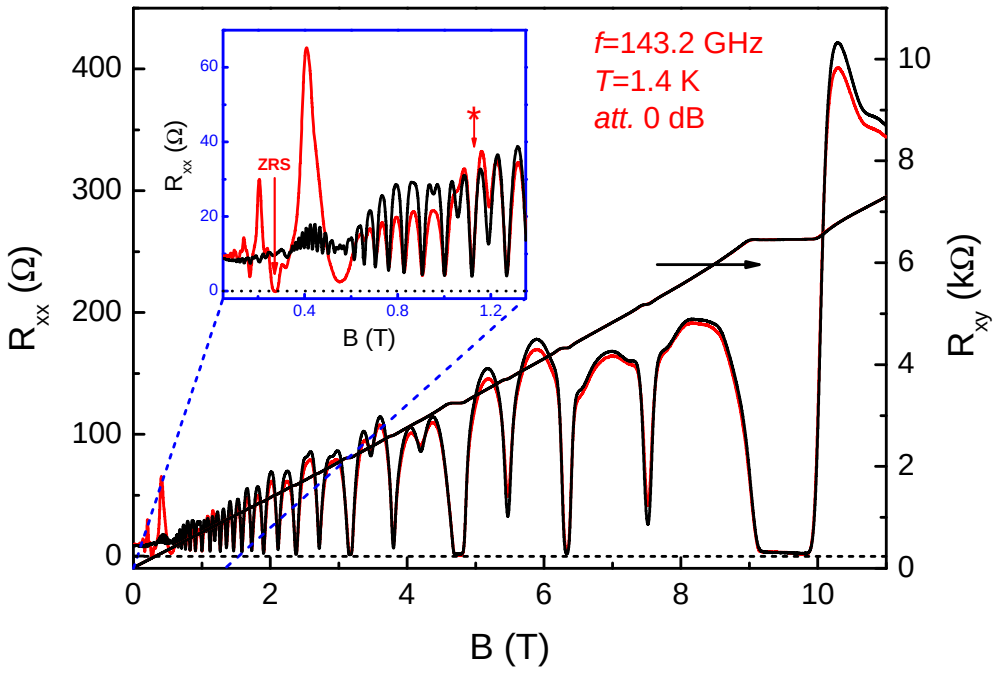

Figure 4.2: The Hall effect and the magnetoresistance in a high-mobility bilayer system, with and without MW excitation. For 143.2 GHz at a temperature of 1.4 K, one inverted MIS oscillation exhibits zero-resistance at B=0.27 T. Quantum Hall effect occurs at high B as well as SdH oscillations. Inset illustrates an expanded view of the low-field data showing $R_{xx} \rightarrow 0$ in the vicinity of 0.27 T.

as peak (II), ZRS at $B = 0.16$ T for 87.2 GHz as peak (III), and ZRS at $B = 0.125$ T for 68.5 GHz as peak (IV)[1]. It is worth noting that other MIS oscillations also show an enhancement or a peak flip correlated with MW frequency but no ZRS, e.g. amplitude of MIS peak at $B \simeq 0.4$ T becomes smaller with decreasing frequency and starts to be inverted for 68.5 GHz. All four chosen frequencies exhibit an almost perfect symmetry under field inversion, except the one for 68.5 GHz. The ZRS for positive magnetic field at 68.5 GHz is also very narrow.

MIS oscillation	frequency range (GHz)	widest ZRS (GHz)
Peak (I)	130 - 158	143
Peak (II)	98 - 111	103
Peak (III)	87 - 90	88.6
Peak (IV)	68.5	68.5

Table 4.1: Regions where ZRS occur for corresponding inverted MIS oscillations.

[1]The notation "peak" for a ZRS (inverted MIS oscillation) refers to the corresponding MIS oscillation without MW irradiation.

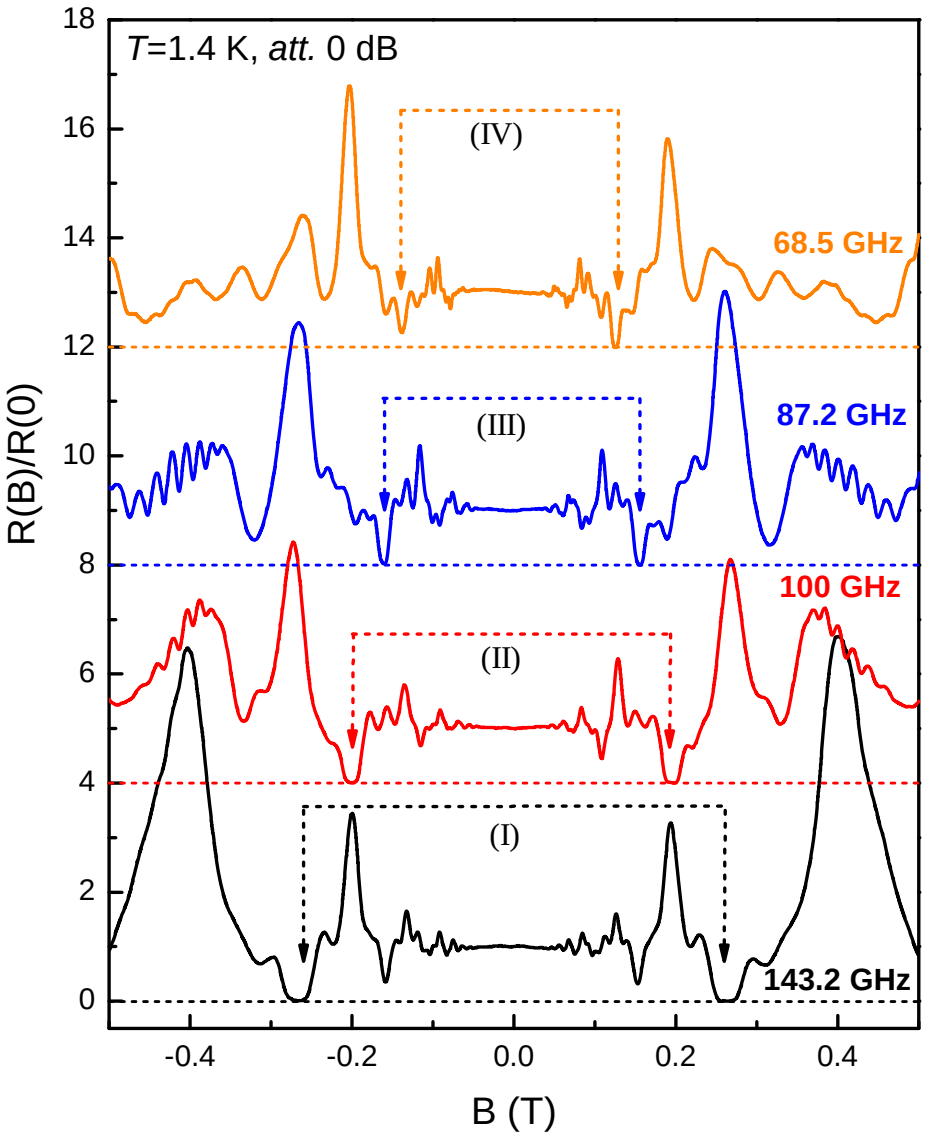

Figure 4.3: Normalized magnetoresistance for positive and negative magnetic field exposed to MW irradiation from 68.5 to 143.2 GHz for highest intensity (attenuation 0 dB). ZRS can be observed for four inverted MIS oscillations, denoted with peak (I) to peak (IV). Traces are shifted up for clarity except the one for 143.2 GHz and dashed lines mark R_{xx}=0.

The transition of ZRS from peak (I) to peak (IV) with decreasing MW frequency has been investigated and is presented in Figure 4.4. For each inverted MIS oscillation, three frequencies (with comparable MW power) are presented giving rise to the low and high frequency limit, and the widest region (R_{xx}=0) where ZRS can be observed for each corresponding inverted MIS oscillation. The results are also summarized in Table 4.1. The regions where ZRS occur, depend strongly on the "width" of the corresponding MIS oscillation, see Figure 4.4(a)-(d). Wheras the frequency range is almost 30 GHz where

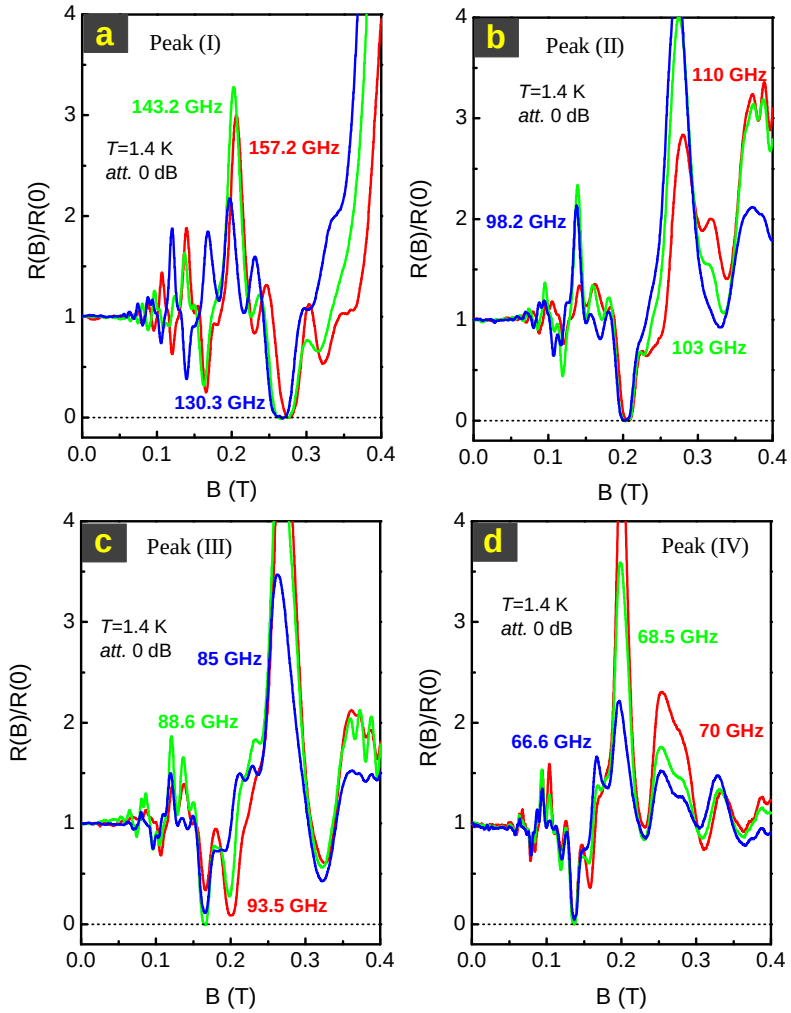

Figure 4.4: Normalized magnetoresistance exposed to MW irradiation in all frequency ranges where ZRS can be observed: (a) ZRS for peak (I), (b) ZRS for peak (II), (c) ZRS for peak (III) and ZRS for peak (IV) at maximum electric field (attenuation 0 dB) and a temperature of 1.4 K.

a ZRS for peak (I) can be observed, the window for other peaks becomes more narrow until for peak (IV), a small deviation from 68.5 GHz does not reveal a ZRS for the corresponding inverted MIS oscillation any more[2]. It is worth noting that, e.g. peak (I) which exhibits zero-resistance for 143.2 GHz is strongly enhanced for 100 and 87.2 GHz, and amplitude of this MIS oscillation decreases again for 68.5 GHz. Other MIS peaks which are transformed into ZRS obey a similar behavior.

In addition, we present the whole frequency range to our disposal (32.7 to 170 GHz) in Figure 4.5 from (a) 170 GHz to (h) 35 GHz. The temperature is kept constant at 1.4 K and the MW electric field is slightly varried around $E_\omega \simeq 4.0$ V/cm. Figure 4.5(c)

[2]MW electric field is comparable ($E_\omega \simeq 4.0$ V/cm) for all measured traces in Figure 4.4 which is ensured by a suppression of SdH oscillations for $B > 0.6$ T.

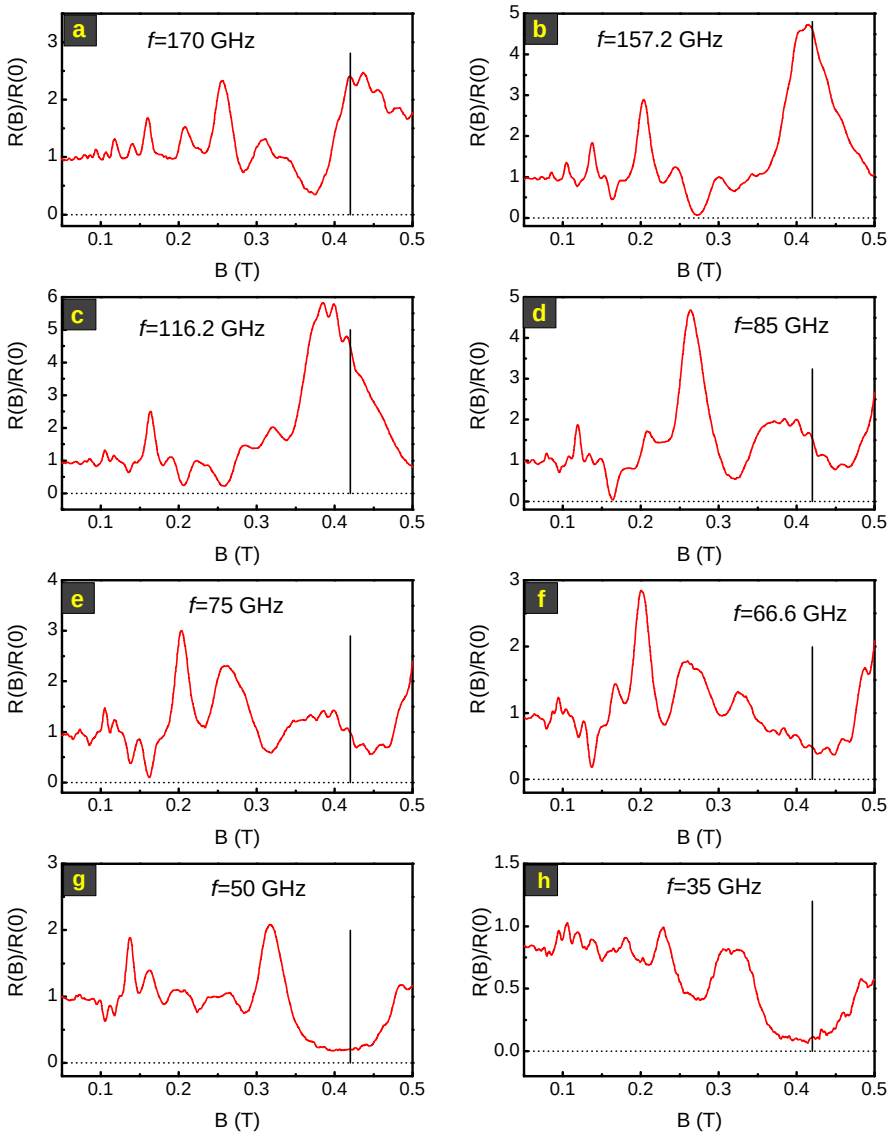

Figure 4.5: Frequency-dependent normalized magnetoresistance from (a) 170 GHz to (h) 35 GHz. For low frequencies (g,h), MIS oscillation at B =0.42 T is inverted but a ZRS does not appear. All traces are measured at 1.4 K and with an electric field of E_ω ≃4 V/cm.

illustrates the passage of the ZRS [peak (I)] for higher frequencies to MIS peak (II). The same passage is presented in Figure 4.5(e) where ZRS is no more observed for peak (III). For lower frequencies, see Figure 4.5(g) and (h), the enhanced MIS oscillation at B ≃0.42 T, marked by a solid line from 170 to 35 GHz, is inverted but does not reach zero-resistance.

In single-layer systems, two reports have studied the influence of a parallel magnetic field on ZRS [Mani05, Yang06]. In bilayer systems, MIS oscillations are sensitive to $B_\parallel$ owing to Aharonov-Bohm effect [Gusev08]. Consequently, the MIS oscillation picture changes with increasing parallel magnetic field.

Figure 4.6 presents magnetoresistance exposed to MW irradiation for 87.2 and 123.7 GHz as a function of the perpendicular magnetic field. The change in the MIS oscillation picture (dark magnetoresistance) for $\Theta = 60°$ and $\Theta = 80°$ is shown in the inset of Figure 4.6(a). The sample is fixed for different tilt angles on a special sample holder (see details in Appendix B). Inversion of MIS oscillations for B <0.2 T occurs due to high current [Mamani09b][3]. ZRS can be observed at 87.2 GHz for $\Theta = 0°$ and $\Theta = 60°$ although the MIS oscillation picture is changed. In Figure 4.6(b) the sample is exposed to a MW irradiation of 123.7 GHz for $\Theta = 60°$ and $\Theta = 80°$. Whereas for a perpendicular magnetic field ($\Theta = 0°$) no ZRS appears, a feature with zero-resistance occurs at B=0.22 T. In addition, a measurement at $\Theta = 80°$ has been performed but the effect of microwaves is decreased with increasing tilt angle due to the MW setup, see Figure B.7 in Appendix B. The appearance of ZRS in bilayer electron systems with a parallel magnetic field component warrants further studies since the position of ZRS depends on frequency and on the MIS oscillation picture.

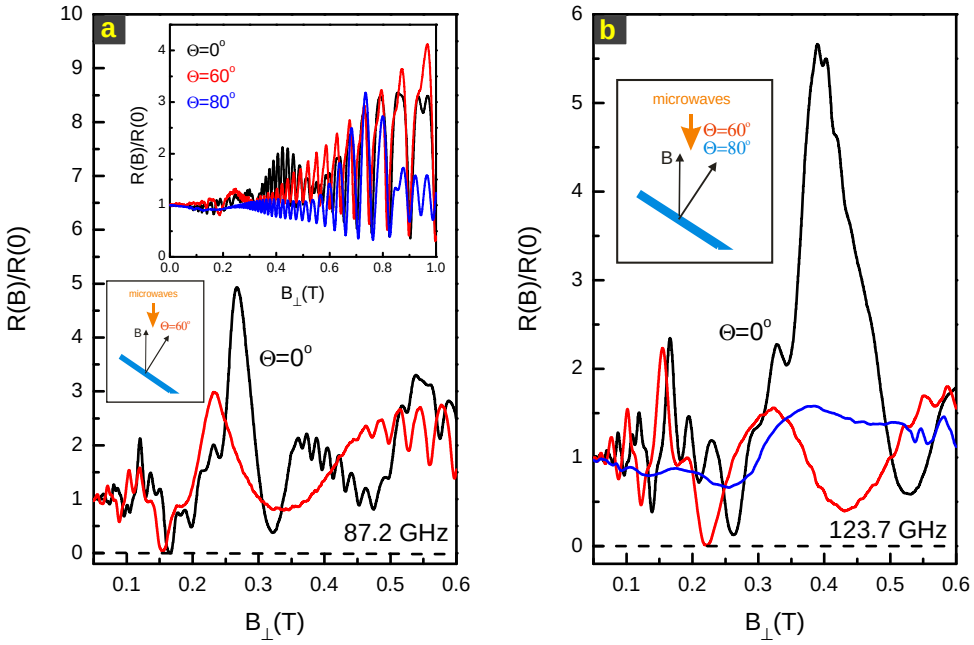

Figure 4.6: ZRS in tilted magnetic fields for (a) 87.2 GHz and (b) 123.7 GHz. A parallel magnetic field changes MIS oscillations [inset in (a)] and ZRS appear now at different positions. For $\Theta = 80°$, the strength of the MW electric field is much smaller than for smaller tilt angles due to the MW setup (see sketches).

[3]We use a current of 1 μA.

4.2.2 Theoretical model

The results in Figure 4.2 and Figure 4.3 demonstrate the striking difference of ZRS in our bilayer system compared to single-subband systems. In the single-subband systems, MIRO minima evolving into ZRS are placed at $\omega/\omega_c = j + 1/4$ (j is integer) and ZRS are observed in a wide frequency range from 7.5 GHz [Willett04] to 240 GHz [Smet05, Mani08], while in bilayer systems ZRS develop from the strongest minima of combined MIS-MIRO oscillations and their location depends also on subband splitting. We now discuss the appearance of ZRS in our bilayer systems. The origin of ZRS is conventionally described in terms of the formation of a domain structure when the resistivity becomes absolutely negative. According to theory [Ryzhii70, Durst03, Vavilov04a, Dmitriev05], displacement and inelastic mechanism can lead to negative dissipative resistivity in the MIRO minima with increasing MW power.
A direct consequence of negative resistivity (regardless of its microscopic mechanism) is the instability of homogeneous current flow and spontaneous breaking of the sample into a pattern of domains [Andreev03]. The simplest domain structure consists of two domains with opposite directions of currents and Hall fields [Andreev03, Vavilov04a]. Each domain is characterized by zero dissipative resistance and classical Hall resistance. A change of the current in this regime is accommodated by a shift of the domain wall without any voltage drop, so the resistivity becomes zero.

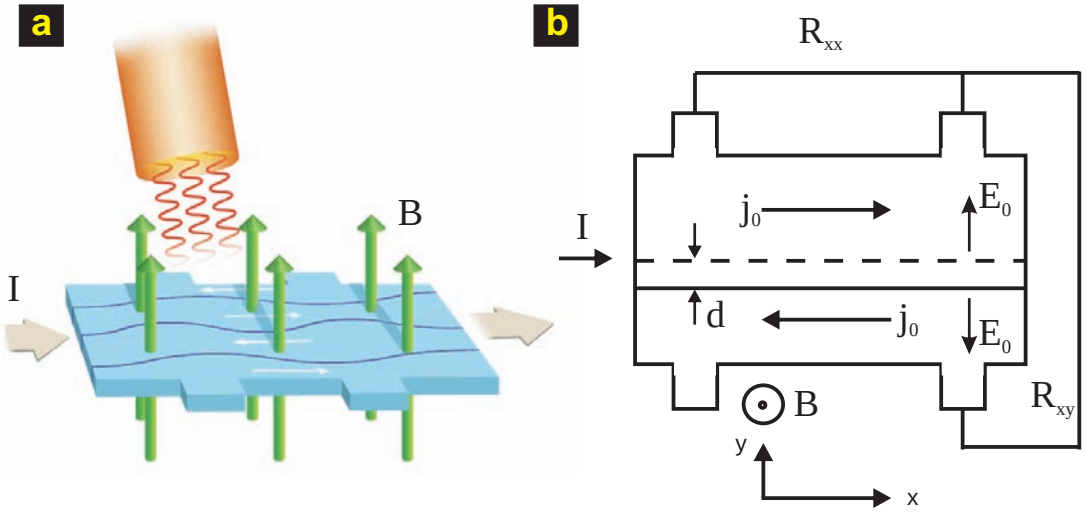

Figure 4.7: Domain structure for ZRS. (a) Image of a domain structure for a sample exposed to MW irradiation which exhibit ZRS. Here, four domains are sketched. Figure taken from Ref. [Durst04]. (b) Sketch of the simplest possible domain structure (explanation, see text). Figure adapted from Ref. [Andreev03].

Figure 4.7 illustrates the occurrence of domains if the sample exhibits zero-resistance exposed to MW irradiation. In Figure 4.7(a), an image drafts the domain structure with four domains. The simplest possible pattern is shown in Figure 4.7(b), adapted from Ref. [Andreev03]. The suggestion by Andreev *et al.* is that the ZRS should directly result from absolute negative conductivity whose instability causes a development of lo-

cal current density with specific magnitude circulating almost everywhere in the system, except in some small volume singular regions (such as domains, or vortices of current). The component of electric field parallel to local current vanishes. If we consider the simple sketch in Figure 4.7(b) which shows a magnetoresistance measurement in Hall-bar geometry, the current I passes along x-direction. We measure now longitudinal and Hall-resistance R_{xx} and R_{xy}. Two current domains are separated by a domain wall which is located at position d relative to the center of the Hall-bar. Thus, we obtain a net current of $I = 2j_0d$ and under the condition of formation of current domains, V_{xx}=0 and $V_{xy} = -\rho_h I$, which is the classical Hall voltage [Andreev03]. Recently more complicated domain structures have been proposed [Finkler09].
An alternative mechanism of ZRS, based on the MW stabilization of the edge-state transport predicting exponentially vanishing dissipative resistivity has also been proposed [Chepelianskii09]. Measurements which have been carried out in "ballistic microbars" might confirm this model [Bykov09]. This experimental result indicates that the mechanisms of MW photoresistance of a 2D electron gas might be different for macroscopic and microscopic bars since we were not able to confirm these results in our macroscopic samples by non-local measurements (not shown here).

To confirm whether a negative resistivity can be reached in our bilayer system under MW excitation, a microscopic calculation of magnetoresistance is necessary which has been carried out including both displacement and inelastic mechanism of microwave photoresistance. These calculations have revealed that the inelastic mechanism is the dominant contribution (see Figure 4.11). The following theoretical expressions are presented in a shortened form based on the calculations which have been shown in detail in Chapter 3. In the regime of classically strong magnetic fields $\omega_c\tau_{tr} \gg 1$, where τ_{tr} is the transport time, and under a valid condition $\varepsilon_F \gg \Delta_{12}/2$, where $\varepsilon_F = \hbar^2\pi n_s/2m^*$ is the Fermi energy ($\varepsilon_F \simeq 16.3$ meV for our sample), magnetoresistance of the balanced double-layer system is expressed as

$$\frac{R(B)}{R(0)} = \int d\varepsilon \left(-\frac{\partial f_\varepsilon}{\partial \varepsilon}\right) \mathcal{D}_\varepsilon^2, \tag{4.1}$$

where f_ε is the distribution function of electrons and $\mathcal{D}_\varepsilon$ is the dimensionless density of states. The influence of microwaves on the distribution function is described by the kinetic equation [Dmitriev05]

$$\frac{P_\omega}{4\tau_{tr}} \sum_{\pm} \mathcal{D}_{\varepsilon\pm\hbar\omega}(f_\varepsilon - f_{\varepsilon\pm\hbar\omega}) = -\frac{f_\varepsilon - f_\varepsilon^e}{\tau_{in}}, \tag{4.2}$$

where the generation term (left-hand side) accounts for single-photon absorption of electromagnetic waves, and the electron-electron collision integral (right-hand side) is written through the inelastic relaxation time τ_{in}. f_ε^e is the Fermi-Dirac distribution with an effective electron temperature T_e due to heating of the electron gas by microwaves and $P_\omega \propto E_\omega^2$ is the dimensionless MW power. The density of states $\mathcal{D}_\varepsilon$ for a two-subband system has been calculated numerically by using the self-consistent Born approximation.

The quantum lifetime $\tau_q \simeq 7.1$ ps at 1.4 K ($\tau_{tr}/\tau_q \simeq 10$) is extracted from the amplitudes of MIS oscillations in dark magnetoresistance measurements, see Figure 4.1(c). The temperature dependence of the inelastic relaxation time is taken in the usual form of Eq. (3.16) [Dmitriev05]. The electron temperature T_e, which depends on MW power, frequency and magnetic field, is determined from the energy balance consideration assuming energy relaxation of electrons due to their interaction with acoustic phonons. The calculations based on both equations given above are shown in Figure 4.8 for f=143 GHz (attenuation 0 dB) and the corresponding MW electric field is extracted to $E_\omega = 4.2$ V/cm with $\lambda_{in} = 0.5$. This theoretical calculation reproduces all experimentally observed features and shows the principal possibility to obtain the negative resistivity around $B = 0.27$ T. Dependence of electron temperature T_e for these parameters is presented as a function of magnetic field in Figure 4.8(b) with a maximum close to ω=ω_c. The corresponding (modified) oscillating Fermi-Dirac distribution function f^e_ε (red trace) as well as the density of states $\mathcal{D}_\varepsilon$ are illustrated in Figure 4.8(c) with corresponding Fermi energy ε_F for the ZRS which appears at B=0.27 T.

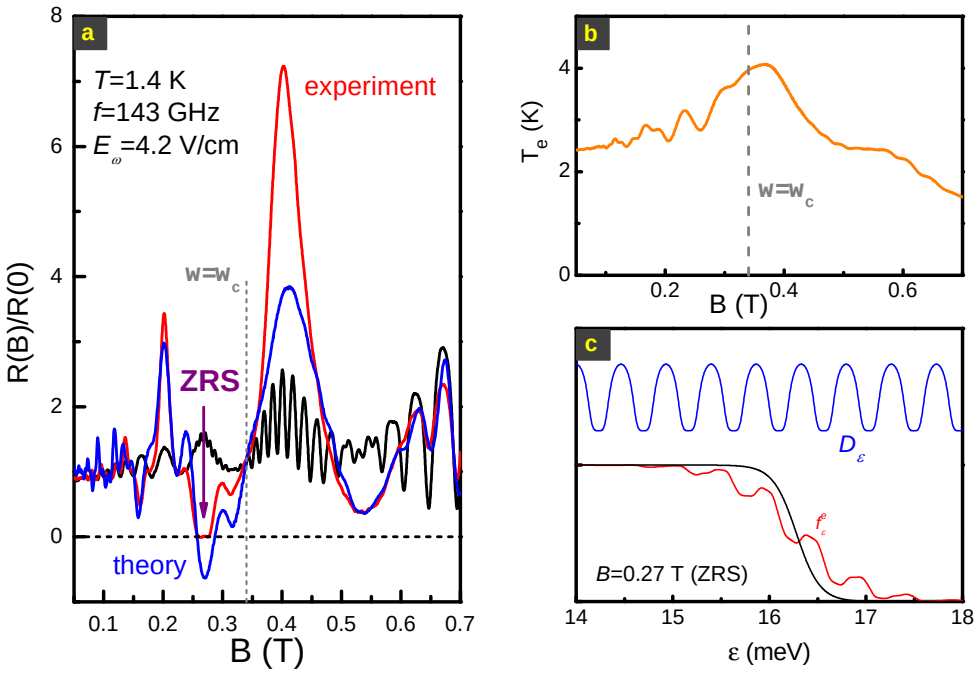

Figure 4.8: (a) Measured and calculated magnetoresistance exhibit ZRS at 0.27 T under a MW excitation of 143 GHz at 1.4 K with an electric field of E_ω=4.2 V/cm. The black trace is measured dark magnetoresistance at 1.4 K. (b) Electron temperature for these parameters as a function of B, (c) DOS D_ε and electron distribution function f^e_ε for corresponding parameters [ZRS, peak (I)].

4.3 Analysis and discussion

The appearance of vanishing longitudinal resistance is now investigated for different MW power (electric field) and temperature. In Figure 4.9 both power and temperature dependence of magnetoresistance at 143 GHz, when ZRS develops around B=0.27 T with the largest width, is presented. The temperature dependence in Figure 4.9(a),(b) is carried out at the highest MW intensity (attenuation 0 dB), which corresponds to a MW electric field of $E_\omega = 4.2$ V/cm. The ZRS starts to narrow at $T = 2.1$ K and disappears at $T \simeq 2.5$ K. Figures 4.9(c),(d) show power dependence at 1.4 K starting from an attenuation of 0 dB (highest intensity) to -10 dB, as well as dark magnetoresistance (no MW). With decreasing MW power, the amplitudes of all enhanced and inverted MIS oscillations decrease while ZRS [peak (I)] first narrows at -4 dB and then disappears with decreasing MW power.

Now, power and temperature dependence of normalized magnetoresistance $R(B)/R(0)$ for both MIS peaks (I) and (II) which evolve into ZRS states is analyzed. In Figure 4.10(a), magnitudes of the enhanced peak (II) and of the inverted peak which evolves into the ZRS at 143 GHz are plotted as functions of MW power. For the enhanced peak (II), R_{xx} exhibits sublinear power dependence before saturation occurs. For the inverted MIS peak (I), R_{xx} decreases very fast in a narrow power range over more than one decade. The amplitude of the inverted peak [i.e. $1 - R(B)/R(0)$] scales similar to the peak (II), i.e. peak (II) reveals also a sublinear power dependence. Concerning temperature dependence, we observe a strong decrease of $R(B)/R(0)$ in the low-temperature region, when we approach the ZRS. Therefore, one can construct an Arrhenius plot which is presented in Figure 4.10(b) for 143 GHz [ZRS for peak (I)] and 100 GHz [ZRS for peak (II)]. Applying the expression $R_{xx} \propto \exp(-E_{ZRS}/T)$, an activation energy of E_{ZRS}=7 K is obtained, which is in the same order as in single-layer systems [Zudov03]. Notice that in the region where the resistivity is not very low [$R(B)/R(0) >$0.2], the relative changes of $R(B)/R(0)$ with temperature can also be fitted by the dependence $\propto -T^{-2}$, for both inverted peaks.

The evolution from inverted MIS peak to ZRS at -4 dB [see Figure 4.9(d)] enables us to define a MW electric field E^*_ω=2.65 V/cm where the resistance becomes negative (see below). Although the generation term responsible for the oscillatory behavior of the distribution function in Eq. (4.2) is linear in MW power, the changes in the MIS oscillation amplitudes under MW excitation should occur sublinear in MW power, because of inelastic relaxation enhancement under MW heating and of other nonlinear effects (e.g. saturation [Dmitriev05]). The experimental data [Figure 4.10(a)] are in agreement with this conclusion. Also, the dependence of the amplitudes of MW-modified MIS peaks on the electron temperature T_e correlates with temperature dependence of the inelastic relaxation time $\tau_{in} \propto T_e^{-2}$. However, when approaching ZRS, the temperature dependence of R_{xx} apparently changes to an activation law similar to that observed in high-mobility single-layer systems and still lacking a clear theoretical explanation. In Figure 4.11(a) and (b) experiment is again compared to theoretical cal-

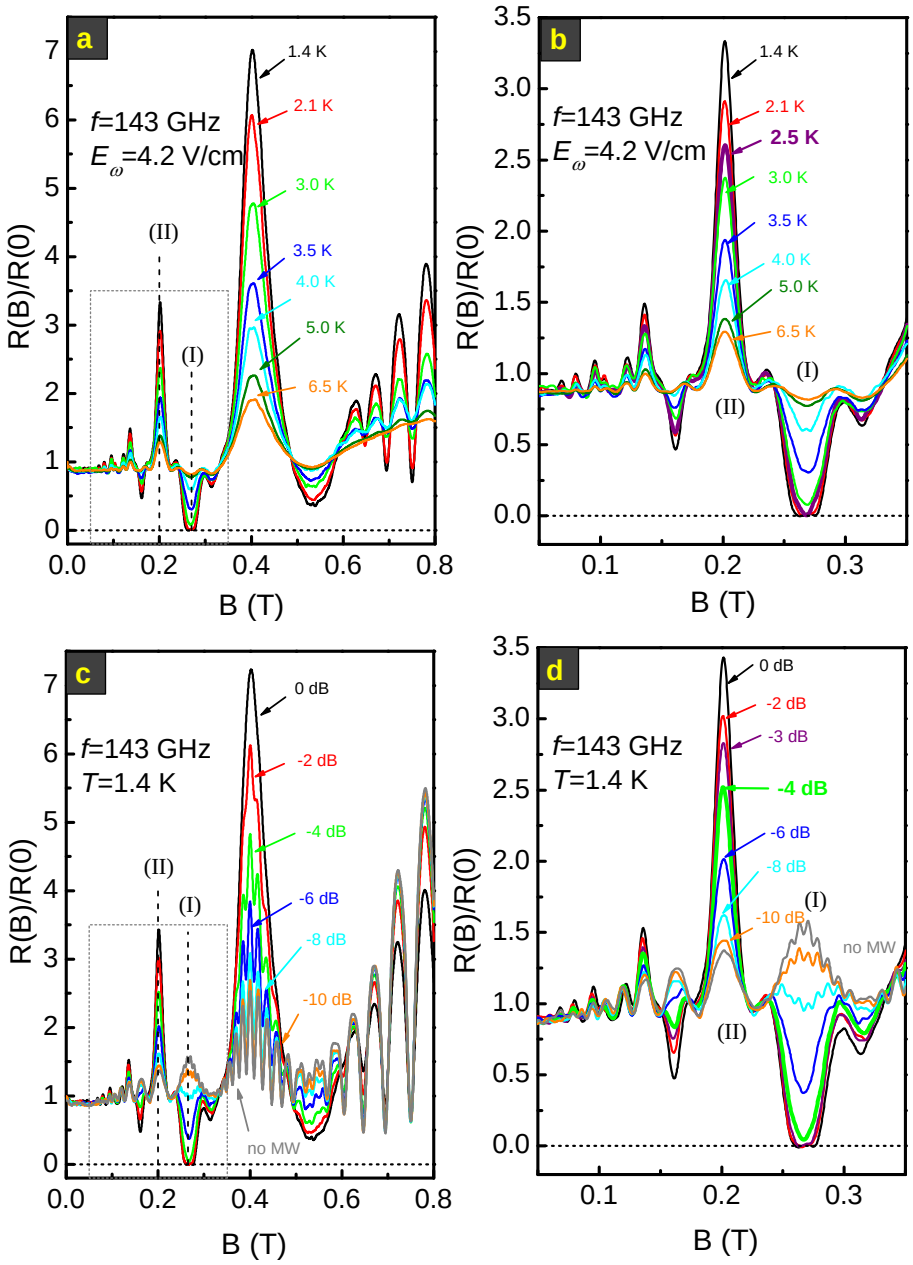

Figure 4.9: (a) Temperature and (c) power dependence for the ZRS which occurs for MIS peak (I) at f=143 GHz. (b) and (d) enlarge the dotted boxes in (a) and (c). This ZRS first narrows at 2.1 K and vanishes for T >2.5 K. With decreasing MW power, ZRS disappears for an attenuation of -4 dB which corresponds to an electric field of E^*_ω=2.65 V/cm.

culations based on inelastic mechanism and on a sum of displacement and inelastic mechanism. Displacement contribution is very small and amplitude of inverted MIS peaks is only slightly increased. Displacement contribution becomes essential only for higher electric fields (6-7 V/cm) [Raichev09]. The disappearance of ZRS at -4 dB (E_ω = 2.65 V/cm) shown in Fig. 4.11(b) correlates with the results of theoretical cal-

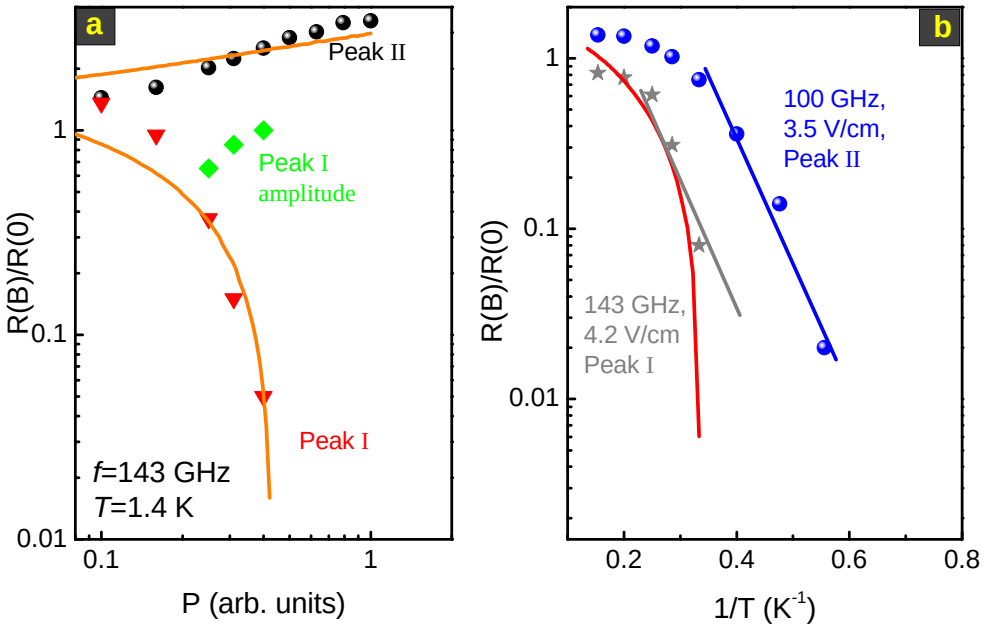

Figure 4.10: Analysis for (a) power and (b) temperature dependent magnetoresistance exposed to MW irradiation based on the measurements of Figure 4.9. (a) Peak (II) and the amplitude of peak (I) exhibit sublinear power-dependence whereas the inverted peak [peak (I)] strongly decreases with increasing MW power. (b) R(B)/R(0) for 100 GHz [ZRS, peak (II)] and 143 GHz [ZRS, peak (I)]. The solid lines are fits to $R \propto \exp(-E_{ZRS}/T)$.

culations. The deviation of theory from experimental data (MW-enhanced MIS peaks at 0.2 and 0.4 T) is mostly related to a limited applicability of the relaxation-time approximation [Dmitriev09] in Eq. (4.2) and to a neglect of effects of finite sample size on MW absorption [Fedorych09]. Nevertheless, theoretical plots reproduce all experimentally observed features and show the negative resistivity around $B = 0.27$ T [peak (I)]. Calculations for 100 GHz ($E_\omega = 3.5$ V/cm) also show negative resistivity around $B = 0.2$ T [peak (II)].

Another source of deviation may be the assumption of a homogeneous distribution of the MW electric field inside the sample and a neglect of the role of contacts or edges. Recently observed insensitivity of MIROs to the sense of circular polarization [Smet05], the absence of MIROs in contactless measurements [Andreev08], and theoretical calculations of the MW-field distribution in 2D electron systems with metallic contacts [Mikhailov06] indicate probably a near-contact origin of the phenomena of MIRO and ZRS in high-mobility layers. Our studies based on linear and indeterminate polarization and on the bulk properties of 2D electrons cannot definitely say or rule out whether a strong MW-field gradient near the contacts is important for photoresistance in our bilayer systems. We can not definitively solve this controversy, but it should also be pointed out that the presence of the microwave field inhomogeneity with strong field

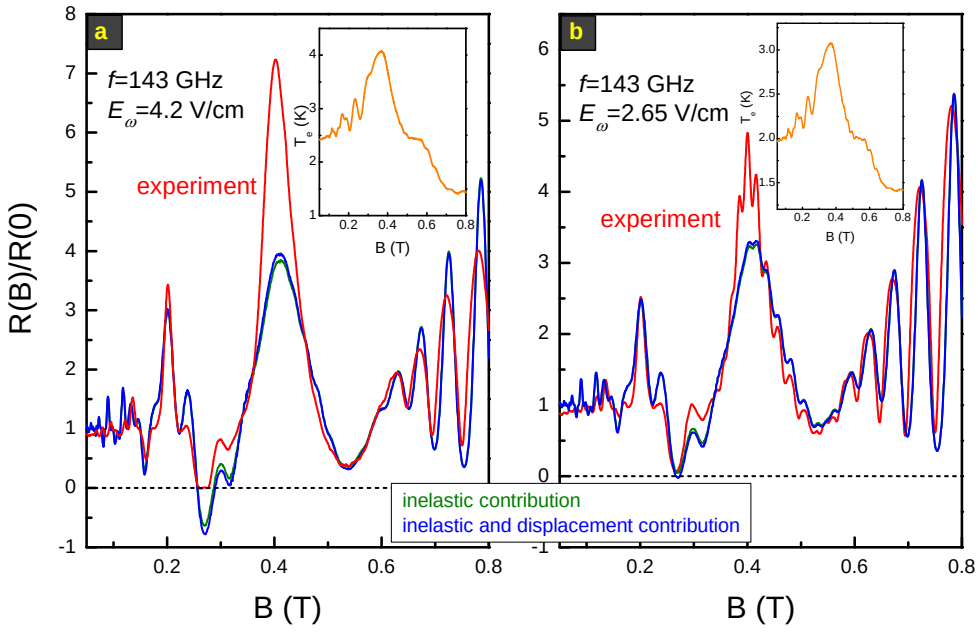

Figure 4.11: Experimental traces together with calculated magnetoresistance based on inelastic (wine) as well as inelastic and displacement (blue) contributions for (a) 4.2 V/cm and (b) 2.65 V/cm where ZRS disappears. Theoretical calculations of electron temperature are presented in the inset for both field strengths.

gradients near the edges or contacts does not cancel the role of electron transitions between Landau levels as a source of $1/B$-periodic oscillations and hence the validity of microscopic mechanisms of MIROs.

To summarize, this controversy between bulk and near-contact oscillating contribution to resistivity [Mikhailov06] does not allow to discuss this problem in more detail, on the quantitative level, owing to the absence of clear knowledge about the specific nature of these near-contact effects.

Summary

Zero-resistance states (ZRS) have been observed in a bilayer electron system exposed to microwave irradiation for the first time even in the presence of additional magneto-intersubband scattering due to two populated subbands. ZRS in bilayers are distinct from single-layer systems and the vanishing resistance develops for inverted magneto-intersubband (MIS) oscillations. Intervals of zero-resistance are narrow and very sensitive to microwave frequency. Experimental results are compared to theory and we have found that under conditions for absolute negative resistivity, our calculations based on one theoretically proposed microwave mechanism (inelastic mechanism) correlate with the appearance of ZRS. This is the first quantitative comparison of experiment and the-

ory. The observed ZRS can be described as a consequence of current instability under absolute negative resistivity. A proof of the existence of current domains is still missing but the knowledge of the current distribution in a sample which exhibits ZRS is the key to provide a complete understanding of this phenomenon.
To summarize, this result is the first step to a generalization of ZRS for systems beyond the single-subband case and opens the possibility for experimental and theoretical studies of ZRS in quasi three-dimensional systems since we have shown that additional scattering is not a hindrance for the observation of ZRS [Wiedmann10b].

Chapter 5

Magnetotransport and microwave studies in multilayer electron systems

Previous studies of magneto-intersubband (MIS) oscillations and their interference with microwave-induced resistance oscillations (MIROs) have been restricted to two-subband systems formed by either double quantum wells (DQWs) or wide quantum wells. In this chapter, we present and develop a theoretical model for these phenomena in systems with multiple subbands which have also been tested in experiments with three occupied 2D subbands formed in triple quantum wells (TQWs). In the presence of microwave (MW) irradiation, we show that TQWs exhibit also a special photoresistance picture where single MIS oscillations are enhanced, damped or inverted. Theoretical analysis has been done involving the inelastic mechanism of photoresistance for low temperatures and all experimental results are in agreement with theoretical calculations. Our theory can be applied for experimental studies with an arbitrary (multiple) number of subbands.

5.1 Generalization of magnetotransport for N layers

Multilayer electron systems can be in general described by a 2DEG confined in N single quantum wells which are separated by thin barriers and coupled by tunneling. To understand first magnetoresistance with additional intersubband scattering, theory of magnetoresistance has to be generalized to the case of N subbands. As for bilayer systems, elastic scattering of electrons in the presence of a magnetic field under the condition of large filling factors (Fermi energy ε_F is much larger than $\hbar\omega_c$) is considered and the self-consistent Born approximation is applied to describe the density of states and the linear response. The expression for magnetoresistance is conveniently presented in the form

$$\rho_d = \rho_d^{(0)} + \rho_d^{(1)} + \rho_d^{(2)}, \tag{5.1}$$

where $\rho_d^{(0)}$ is the classical resistivity, $\rho_d^{(1)}$ is the first-order (linear in Dingle factors) quantum contribution describing the SdH oscillations, and $\rho_d^{(2)}$ is the second-order (quadratic in Dingle factors) quantum contribution containing the MIS oscillations. In the regime of classically strong magnetic fields, classical resistivity is given by

$$\rho_d^{(0)} = \frac{m^*}{e^2 n_s \tau_{tr}}, \quad \frac{1}{\tau_{tr}} = \frac{1}{N}\sum_j \nu_j^{tr}, \tag{5.2}$$

the first-order quantum contribution by

$$\rho_d^{(1)} = -\mathcal{T}\frac{4m^*}{e^2 n_s}\frac{1}{N}\sum_j \nu_j^{tr} d_j \cos\frac{2\pi(\varepsilon_F - \varepsilon_j)}{\hbar\omega_c}, \tag{5.3}$$

and the second-order quantum contribution by

$$\rho_d^{(2)} = \frac{m^*}{e^2 n_s}\sum_{jj'}\frac{n_j + n_{j'}}{n_s}\nu_{jj'}^{tr} d_j d_{j'} \cos\frac{2\pi\Delta_{jj'}}{\hbar\omega_c}, \tag{5.4}$$

where m^* is the effective mass of electrons, $d_j = \exp(-\pi\nu_j/\omega_c)$ are the Dingle factors, $\mathcal{T} = X/\sinh X$ with $X = 2\pi^2 T/\hbar\omega_c$ is the thermal suppression factor, and n_j are the partial densities in the subbands ($\sum_j n_j = n_s$). The sums are taken over all subbands, and since for the terms with $j = j'$ one has $\Delta_{jj'} = 0$, the corresponding cosines in Eq. (5.4) are equal to 1. The subband-dependent quantum relaxation rates ν_j and $\nu_{jj'}$, as well as the transport scattering rates ν_j^{tr} and $\nu_{jj'}^{tr}$ entering Eqs. (5.2)-(5.4) are defined already in Chapter 1 according to Eq. (1.33) and Eq. (1.34). In addition one can introduce an averaged quantum lifetime $1/\tau_q = N^{-1}\sum_j \nu_j$. The application of all equations presented above to the particular case of three subbands for our TQWs ($N = 3$, $j = 1, 2, 3$) is now straightforward.

5.2 Magneto-intersubband oscillations for a trilayer electron system

This section introduces now magnetotransport and demonstrates the applicability of the generalized theory for N layers for triple quantum wells with three occupied 2D subbands. The samples are symmetrically doped GaAs TQWs with a total electron sheet density $n_s = 9 \cdot 10^{11}$ cm^{-2} and mobilities of $5 \cdot 10^5$ cm^2/V s (wafer A) and $4 \cdot 10^5$ cm^2/V s (wafer B). The central well width is about 230 Å and both side wells have equal well widths of 100 Å. The barrier thickness d_b is 14 Å (wafer A) and 20 Å (wafer B). The symmetric triple-well structure under investigation is depicted in Figure 5.1.

The barriers dividing the wells are thin enough to have a strong tunnel hybridization of electron states in different wells. As a result, there exist three subbands with different quantization energies ε_j ($j = 1, 2, 3$). All three subbands are occupied by electrons due to the high electron density in all investigated samples. Magnetoresistance of such systems exhibits MIS oscillations with several periods determined by the subband separation energies $\Delta_{jj'} = |\varepsilon_j - \varepsilon_{j'}|$, see Table 5.1. These energies can be either extracted from a simple Fast Fourier Transform (FFT) analysis or by comparing experimental with theoretical magnetoresistance given in Eq. (5.9).

In order to describe the scattering rates, wavefunctions and electron energies in the subbands found from the tight-binding Hamiltonian are employed [Hanna96] using the expansion of the wavefunction $\psi(z) = \sum_i \varphi_i F_i(z)$ in the basis of single-well orbitals $F_i(z)$ (here, $i = 1, 2, 3$ numbers the left, central, and right well, respectively). This leads

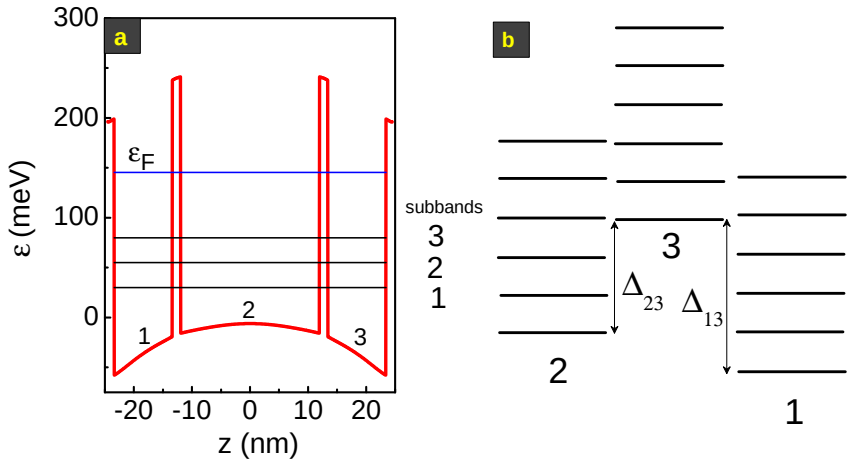

Figure 5.1: (a) TQW configuration for all samples used in this thesis with three 2D occupied subbands and (b) Landau level staircase with corresponding gaps Δ_{13} and Δ_{23}.

wafer	Δ_{12} (meV)	Δ_{23} (meV)	Δ_{13} (meV)
A	1.4	3.9	5.3
B	1.0	2.4	3.4

Table 5.1: Subband separation energies for wafer (A) and (B), extracted from Fourier analysis of magnetoresistance.

to the matrix equation for the coefficients φ_i:

$$\begin{pmatrix} \varepsilon_1^{(0)} - \varepsilon & -t_{12} & 0 \\ -t_{12} & \varepsilon_2^{(0)} - \varepsilon & -t_{23} \\ 0 & -t_{23} & \varepsilon_3^{(0)} - \varepsilon \end{pmatrix} \begin{pmatrix} \varphi_1 \\ \varphi_2 \\ \varphi_3 \end{pmatrix} = 0, \tag{5.5}$$

where $\varepsilon_i^{(0)}$ are the single-well quantization energies and $t_{ii'}$ are the tunneling amplitudes. For the case of symmetric TQWs ($\varepsilon_1^{(0)} = \varepsilon_3^{(0)} \equiv \varepsilon_s$, $\varepsilon_2^{(0)} \equiv \varepsilon_c$, $t_{12} = t_{23} \equiv t$) the energies of the three subbands, ε_j, are [Hanna96]

$$\begin{aligned} \varepsilon_1 &= \frac{\varepsilon_c + \varepsilon_s}{2} - \sqrt{\left(\frac{\varepsilon_c - \varepsilon_s}{2}\right)^2 + 2t^2}, \\ \varepsilon_2 &= \varepsilon_s, \\ \varepsilon_3 &= \frac{\varepsilon_c + \varepsilon_s}{2} + \sqrt{\left(\frac{\varepsilon_c - \varepsilon_s}{2}\right)^2 + 2t^2}, \end{aligned} \tag{5.6}$$

The corresponding eigenstates are expressed through the single-well orbitals as $\psi_j(z) = \sum_i \chi_{ij} F_i(z)$. The matrix χ_{ij} is given by

$$\chi_{ij} = \begin{pmatrix} C_1 t/(\varepsilon_s - \varepsilon_1) & 1/\sqrt{2} & C_3 t/(\varepsilon_s - \varepsilon_3) \\ C_1 & 0 & C_3 \\ C_1 t/(\varepsilon_s - \varepsilon_1) & -1/\sqrt{2} & C_3 t/(\varepsilon_s - \varepsilon_3) \end{pmatrix}, \tag{5.7}$$

where $C_{1,3} = \left[1 + 2t^2/(\varepsilon_s - \varepsilon_{1,3})^2\right]^{-1/2}$. This matrix consists of the three columns of φ_i for the states $j = 1, 2, 3$. The parameters of the tight-binding model can be extracted from the subband gaps found experimentally. By setting ε_s as the reference energy, one has:

$$\varepsilon_c = \Delta_{23} - \Delta_{12}, \quad t = \sqrt{\frac{\Delta_{23}\Delta_{12}}{2}}. \tag{5.8}$$

For the samples with d_b=14 Å (wafer A) one obtains $\varepsilon_c = 2.5$ meV and $2t = 3.35$ meV. Using the total density $n_s = 9 \times 10^{11}$ cm^{-2}, subband densities $n_1 = 3.62 \times 10^{11}$ cm^{-2}, $n_2 = 3.23 \times 10^{11}$ cm^{-2}, and $n_3 = 2.14 \times 10^{11}$ cm^{-2} are found. The electron density in each side well is $n_{side} = \sum_j \chi_{1j}^2 n_j = \sum_j \chi_{3j}^2 n_j = 3.23 \times 10^{11}$ cm^{-2}, and the electron density in the central well is $n_{cent} = \sum_j \chi_{2j}^2 n_j = 2.53 \times 10^{11}$ cm^{-2}.

Due to three populated subbands, the MIS oscillation picture is distinct from the one observed in DQWs where only one MIS period exists. Note that these features have not been mentioned in previous studies of TQWs by other groups [Jo92, Shukla98]. These works focus on the regime of high magnetic fields and integer or fractional quantum Hall effect. MIS oscillations are presented in Figure 5.2(a) first for d_b=14 Å with increasing temperature from 1.4 to 4.2 K. At T=1.4 K, MIS oscillations are superimposed on SdH oscillations starting at 0.25 T. With increasing temperature and in this magnetic field range (0 to 0.6 T), SdH oscillations are damped until we observe at 4.2 K only MIS oscillations characteristic for the parameters of this wafer. Additionally, the inset in Figure 5.2(a) shows a low-temperature measurement at T=50 mK. In Figure 5.2(b) MIS oscillations in TQWs with two distinct barrier thicknesses d_b=14 Å and d_b=20 Å depict the difference of MIS oscillations at 4.2 K. Owing to a smaller coupling for d_b=20 Å, MIS amplitude is smaller and periodicity is also different, see Table 5.1. All further analysis will now focus on samples with d_b=14 Å. The theoretical model for magnetoresistance in TQWs ($N = 3$, $j = 1, 2, 3$) can now be illustrated within a simple model using equal electron densities $n_j = n_s/N$ and assuming that all $\nu_{jj'}^{tr}$ and d_j are equal to each other, in particular, $d_j = d = \exp(-\pi/\omega_c\tau_q)$. By neglecting the SdH oscillations, one obtains

$$\frac{\rho_d(B)}{\rho_d(0)} \simeq 1 + \frac{2}{3}d^2\left[1 + \frac{2}{3}\cos\left(\frac{2\pi\Delta_{12}}{\hbar\omega_c}\right) + \frac{2}{3}\cos\left(\frac{2\pi\Delta_{13}}{\hbar\omega_c}\right) + \frac{2}{3}\cos\left(\frac{2\pi\Delta_{23}}{\hbar\omega_c}\right)\right]. \tag{5.9}$$

The MIS oscillations are represented as a superposition of three oscillating terms determined by the relative positions of subband energies. It should be added that Eq. (5.9) does not depend on transport rates except the one standing in the Dingle factor d. This approximation, in principle, can be applied for estimates to our systems owing to a high total electron-sheet density and a strong tunnel coupling. Magnetoresistance of our TQW system is also calculated under a simplified assumption that the scattering potential is essential only in the side (s) wells, since the growth technology implies that most of the scatterers reside in the outer barriers. The correlation length l_c=18.3 nm entering the scattering potential correlator $w_{jj'}(q) \propto w_s(q)$ is determined by comparing the results of calculations to low-temperature magnetoresistance data for the samples of wafer A (see for more details Ref. [Wiedmann09b]). In Figure 5.3 measured and

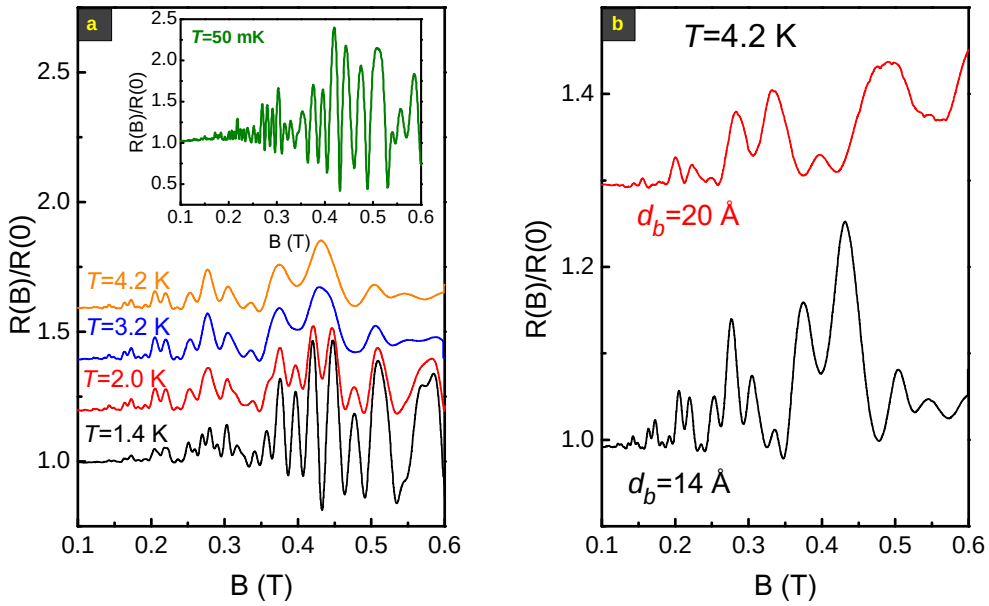

Figure 5.2: (a) MIS oscillations for a sample with a barrier thickness of d_b=14 Å from 1.4 to 4.2 K (inset for 50 mK). MIS oscillations are superimposed on SdH oscillations for T <3.2 K. (b) Comparison of MIS oscillations for two different barrier widths at 4.2 K.

calculated magentoresistance are presented for $T = 6$ K and $T = 10$ K. The averaged quantum lifetime estimated in this way is $\tau_q \simeq 3.8$ ps. The experiment shows a slow suppression of the MIS oscillation amplitude with temperature, which occurs owing to the contribution of electron-electron scattering into Landau level broadening. Though the theory presented above does not take this effect into account explicitly, it can be improved by replacing the quantum relaxation rates according to

$$\nu_j \;\rightarrow\; \nu_j + \nu_{ee}, \quad \nu_{ee} = \lambda \frac{T_e^2}{\hbar \varepsilon_F} \tag{5.10}$$

where ν_{ee} is the electron-electron scattering rate [Giuliani82, Berk95], the Fermi energy is expressed through the averaged electron density as $\varepsilon_F = \hbar^2 \pi (n_s/3)/m^*$, and λ is a numerical constant in the order of unity. Using $\varepsilon_F \simeq 10.5$ meV, we find $\lambda = 2.2$. This fitting procedure has been carried out for many temperatures from $T = 1$ K up to 30 K, and the estimated ν_{ee} by fitting the amplitudes of theoretical and experimental magnetoresistance traces, is presented in Figure 5.3(c). The effect of electron-electron scattering becomes essential for T >2 K and strongly reduces the amplitude of the MIS oscillations at $T \sim 10$ K. Note, that in the log-log plot in Figure 5.3(c), the extracted scattering rate ν_{ee} follows the T^2-dependence, in accordance with Eq. (5.10). This behavior is similar to that observed in DQWs in Figure 1.12 [inset (2)] and in Ref. [Mamani08].

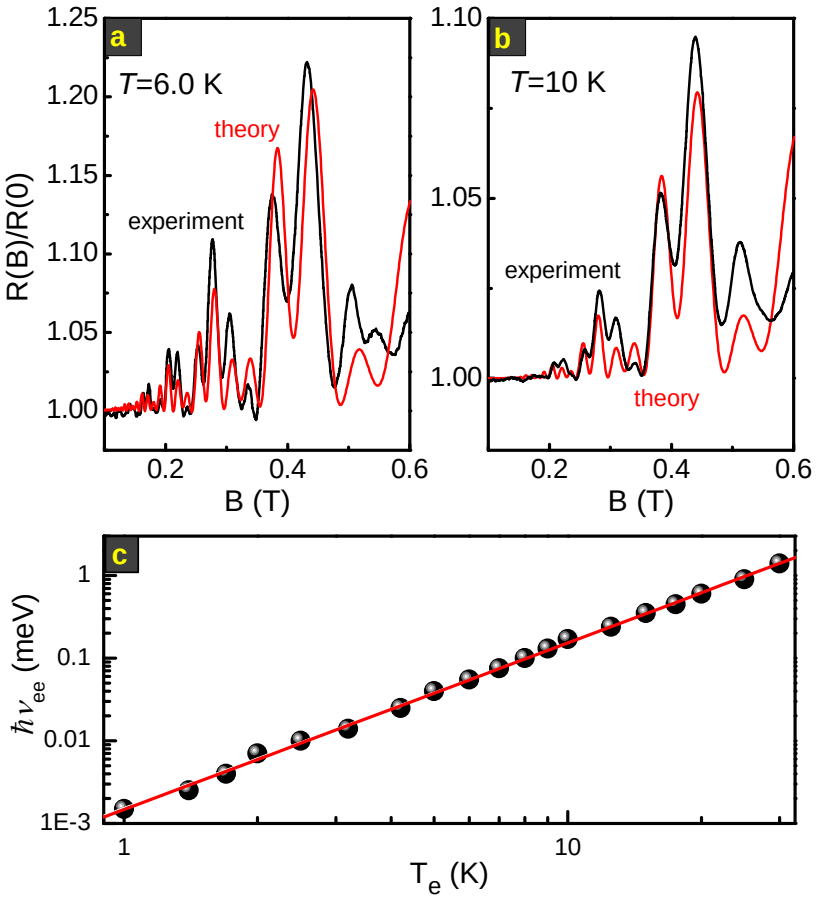

Figure 5.3: Measured and calculated magnetoresistance for (a) 6 K and (b) 10 K. (c) By fitting MIS oscillation amplitude, the relaxation rates can be extracted from Eq. (5.10) with λ=2.2.

5.3 Multilayer electron systems exposed to microwave irradiation

Influence of microwaves on bilayer electron systems has been successfully explained in the previous chapters and now it is also desirable to find a general theory which explains microwave-induced oscillations of a many-subband system. In this section, we present the generalized theory formulated by Oleg Raichev which will be applied in the second part for triple quantum wells. A comparison of measured and calculated magnetoresistance exposed to microwave irradiation which reveals a good agreement between experiment and theory for N=3 is presented.

5.3.1 Theoretical model

In the presence of electromagnetic radiation (here microwaves) with a frequency ω and for dc excitation, one can derive the quantum Boltzmann equation for electrons in a

magnetic field by using a transition to the moving coordinate frame, in a similar way as for the single-subband system (see e.g. [Dmitriev07a] and references therein). In this section $\hbar = 1$. This transition leads to the kinetic equation for the Wigner distribution function $f_{j\varepsilon\varphi}$, which depends on the subband index j, energy ε, and angle φ of the electron momentum:

$$\omega_c \frac{\partial f_{j\varepsilon\varphi}}{\partial \varphi} = \sum_{j'} \int_0^{2\pi} \frac{d\varphi'}{2\pi} \nu_{jj'}(\varphi - \varphi') \sum_n [J_n(\beta_{jj'})]^2 \times \mathcal{D}_{j'}(\varepsilon + n\omega + \gamma_{jj'})[f_{j',\varepsilon+n\omega+\gamma_{jj'},\varphi'} - f_{j\varepsilon\varphi}] + J_{in}. \tag{5.11}$$

In the kinetic equation, the dimensionless density of states $\mathcal{D}_j(\varepsilon)$ (normalized to its zero field value) is introduced. Next, $J_n(x)$ is the Bessel function, J_{in} is the collision integral describing inelastic scattering, and $\nu_{jj'}$ are the scattering rates. The other quantities standing in Eq. (5.11) are

$$\beta_{jj'}(\varphi, \varphi') = \frac{eE_\omega}{\sqrt{2}\omega} \left| s_-(v_j e^{i\varphi} - v_{j'} e^{i\varphi'}) + s_+(v_j e^{-i\varphi} - v_{j'} e^{-i\varphi'}) \right|, \tag{5.12}$$

and

$$\gamma_{jj'}(\varphi, \varphi') = \frac{e}{2i\omega_c}[E_-(v_j e^{i\varphi} - v_{j'} e^{i\varphi'}) - E_+(v_j e^{-i\varphi} - v_{j'} e^{-i\varphi'})], \tag{5.13}$$

where $E_\pm = E_x \pm iE_y$, $\vec{E} = (E_x, E_y)$ is the dc field strength, E_ω is the strength of the microwave electric field (related to the incident microwave field strength E_i in vacuum as $E_\omega = E_i/\sqrt{\epsilon^*}$, see below), and $v_j = p_j/m^*$ are the subband-dependent Fermi velocities. The factors $s_\pm$ describe polarization of the radiation and account for electrodynamic effects [Chiu76, Mikhailov04]. For linear polarization,

$$s_\pm = \frac{1}{\sqrt{2}} \frac{1}{\omega \pm \omega_c + i\omega_p}, \tag{5.14}$$

where $\omega_p = 2\pi e^2 n_s/m^* c\sqrt{\epsilon^*}$, $\sqrt{\epsilon^*} = (\sqrt{\epsilon_{vac}} + \sqrt{\epsilon_d})/2$, $\epsilon_{vac} = 1$ is the dielectric permittivity of vacuum, and ϵ_d is the dielectric permittivity of the medium surrounding the quantum wells. The distribution function can be expanded in the angular harmonics [see Eq. (2.19)]: $f_{j\varepsilon\varphi} = \sum_l f_{j\varepsilon l} e^{il\varphi}$. The density of dissipative electric current in the 2D plane, $\mathbf{j} = (j_x, j_y)$, is determined by the $l = 1$ harmonic:

$$j_- \equiv j_x - ij_y = \frac{e}{\pi} \sum_j p_j \int d\varepsilon \mathcal{D}_j(\varepsilon) f_{j\varepsilon 1}. \tag{5.15}$$

In the regime of classically strong magnetic fields, the anisotropic part of the distribution function is expressed through the isotropic (angular-independent) part $f_{j\varepsilon} \equiv f_{j\varepsilon l}$ for $l = 0$. This leads to the expression for the current in the form

$$j_- = \frac{e}{i\pi\omega_c} \sum_{jj'} p_j \int d\varepsilon \mathcal{D}_j(\varepsilon) \int_0^{2\pi} \frac{d\varphi}{2\pi} e^{-i\varphi} \int_0^{2\pi} \frac{d\varphi'}{2\pi} \times \nu_{jj'}(\varphi - \varphi') \sum_n [J_n(\beta_{jj'})]^2 \mathcal{D}_{j'}(\varepsilon + n\omega + \gamma_{jj'}) \times [f_{j'\varepsilon+n\omega+\gamma_{jj'}} - f_{j\varepsilon}]. \tag{5.16}$$

The response to E_- [$j_- = \sigma_d E_-$] gives the symmetric part of dissipative conductivity considered below. The resistivity is then given by $\rho_d^{MW} = \sigma_d/\sigma_\perp^2$, where $\sigma_\perp = e^2 n_s/m^*\omega_c$ is the classical Hall conductivity.

The isotropic part of the distribution function can be represented in the form

$$f_{j\varepsilon} = f_\varepsilon^{(0)} - i\omega \frac{\partial f_\varepsilon^{(0)}}{\partial \varepsilon} g_{j\varepsilon}. \tag{5.17}$$

where $f_\varepsilon^{(0)}$ is a slowly varying function of energy, which is close to a quasi-equilibrium (heated Fermi) distribution, while $g_{j\varepsilon}$ is a rapidly oscillating (periodic in $\hbar\omega_c$) function, which is also represented as $g_{j\varepsilon} = \sum_k g_{jk} \exp(2\pi i k\varepsilon/\omega_c)$. After a substitution of expression (5.17) into Eq. (5.16), the contribution coming from $f_\varepsilon^{(0)}$ produces the "dark" resistivity and its modification by microwaves due to the displacement mechanism. The microwave modification of the resistivity due to the inelastic mechanism originates from the term proportional to $g_{j\varepsilon}$. In the following, we search for the response linear in the dc field and quadratic in the microwave field. This is done by expanding the Bessel functions in powers of $\beta_{jj'}$ and retaining only the lowest-order terms. Also, we use the lowest-order expansion of the density of states in the Dingle factors, $\mathcal{D}_j(\varepsilon) \simeq 1 - 2d_j \cos[2\pi(\varepsilon - \varepsilon_j)/\omega_c]$, so only the lowest oscillatory harmonics ($k = \pm 1$) are relevant. The angular and energy averaging in Eq. (5.16) in this case are carried out analytically, and one obtains the expression for the dark resistivity ρ_d [see Eq. (5.9)], as well as the microwave-induced contributions ρ_{di} and ρ_{in}:

$$\begin{aligned}\rho_{di} = &-\frac{m^*}{e^2 n_s} P_\omega \left[\sin^2 \frac{\pi\omega}{\omega_c} + \frac{\pi\omega}{\omega_c} \sin \frac{2\pi\omega}{\omega_c}\right] \\ &\times \frac{N}{2} \sum_{jj'} \left(\frac{n_j + n_{j'}}{n_s}\right)^2 \nu_{jj'}^* d_j d_{j'} \cos \frac{2\pi\Delta_{jj'}}{\omega_c},\end{aligned} \tag{5.18}$$

where P_ω is defined by Eq. (5.25),

$$\nu_{jj'}^* = \int_0^{2\pi} \frac{d\theta}{2\pi} \nu_{jj'}(\theta) [F_{jj'}(\theta)]^2, \tag{5.19}$$

and

$$\rho_{in} = -\frac{m^*}{e^2 n_s} \frac{2\pi\omega}{\omega_c} \sum_{jj'} \frac{n_j + n_{j'}}{n_s} \nu_{jj'}^{tr} \times \left[g_{j'1} d_j \exp\left(\frac{2\pi i \varepsilon_j}{\omega_c}\right) + \text{c.c.}\right]. \tag{5.20}$$

One can find $g_{j\varepsilon}$ from the isotropic part of Eq. (5.11) by using the relaxation time approximation for the isotropic part of the inelastic collision integral:

$$J_{in} = -\frac{f_{j\varepsilon} - f_\varepsilon^{(0)}}{\tau_j^{in}}. \tag{5.21}$$

This approximation is valid for small deviations $f_{j\varepsilon} - f_\varepsilon^{(0)}$, and is justified in a similar way as for the single-subband systems, based on a linearization of the collision integral for electron-electron scattering [Dmitriev05]. After substitution of expression (5.21) into Eq. (5.11), one can obtain a system of linear equations for g_{jk}, which is easily

solved under a reasonable condition that the intersubband scattering dominates over the inelastic one: $\nu_{jj'} \gg 1/\tau_j^{in}$ $(j \neq j')$. This gives subband-independent harmonics $g_{jk} = g_k$, in particular,

$$g_1 = \frac{P_\omega \tau_{in} \sin(2\pi\omega/\omega_c)}{1 + P_\omega(\tau_{in}/\tau_{tr}) \sin^2(\pi\omega/\omega_c)} \times \frac{1}{2N} \sum_j \nu_j^{tr} d_j \exp\left(-\frac{2\pi i \varepsilon_j}{\omega_c}\right), \tag{5.22}$$

where the averaged inelastic relaxation time is defined according to $1/\tau_{in} = N^{-1} \sum_j 1/\tau_j^{in}$. The denominator in Eq. (5.22) describes the effect of saturation. A substitution of the result Eq. (5.22) into Eq. (5.20) leads to Eq. (5.24).

5.3.2 Application for triple quantum wells

The next step is now to apply the generalized theory for TQWs exposed to microwave irradiation. As for bilayer electron systems, power, temperature and frequency dependence of magnetoresistance have been studied for both wafers. The focus is again on samples with $d_b = 14$ Å . In Figure 5.4, magnetoresistance for different MW intensities at a temperature of $T = 4.2$ K and a frequency of 55 GHz are compared with theory. Without microwave irradiation (no MW), only MIS oscillations are visible. A small microwave power (attenuation -10 dB) leads to an enhancement of all MIS features for B <0.25 T and to a damping of all features for B >0.35 T whereas the MIS oscillations around B =0.3 T are almost unchanged. A further increase in MW power (attenuation -2 dB) leads to a damping of the MIS oscillation amplitude for B <0.25 T, slightly increased compared to the MIS oscillation amplitude without microwave irradiation. The MIS features around B =0.3 T are considerably damped, while for 0.35 T< B <0.5 T the MIS peaks are inverted. Again, no polarization dependence of magnetoresistance has been found. In the range between 35 GHz and 170 GHz, as shown in Figure 5.5, a strongly modified picture of the MIS oscillations appears which correlates with the microwave frequency. Enhancement, suppression or inversion of MIS oscillations occurs in the whole frequency range. Again, inversion of MIS peaks appears for low frequency (35 GHz). The features which are most affected by MW irradiation, strongly sensitive to its frequency, occur at B=0.27 T and B=0.43 T. The plots for 110 GHz and 170 GHz definitely show several regions of enhanced peaks and two regions of suppressed or inverted peaks (for example, the regions around 0.18 T and 0.34 T for 170 GHz). For 35 GHz, all the MIS oscillations above 0.2 T are inverted. For 35 GHz and 70 GHz, some SdH oscillations are visible in the region above 0.4 T. For 110 GHz and 170 GHz, when the absorption of microwave radiation in this region is higher, the SdH oscillations are suppressed because of the heating of the electron gas by microwaves.

The peculiar features of the microwave-modified magnetoresistance in TQWs and, generally, in multi-subband systems can be understood in terms of interference of the MIS oscillations with MIROs. The dissipative resistivity in the presence of microwaves is given by

$$\rho_d^{MW} = \rho_d + \rho_{in} + \rho_{di}, \tag{5.23}$$

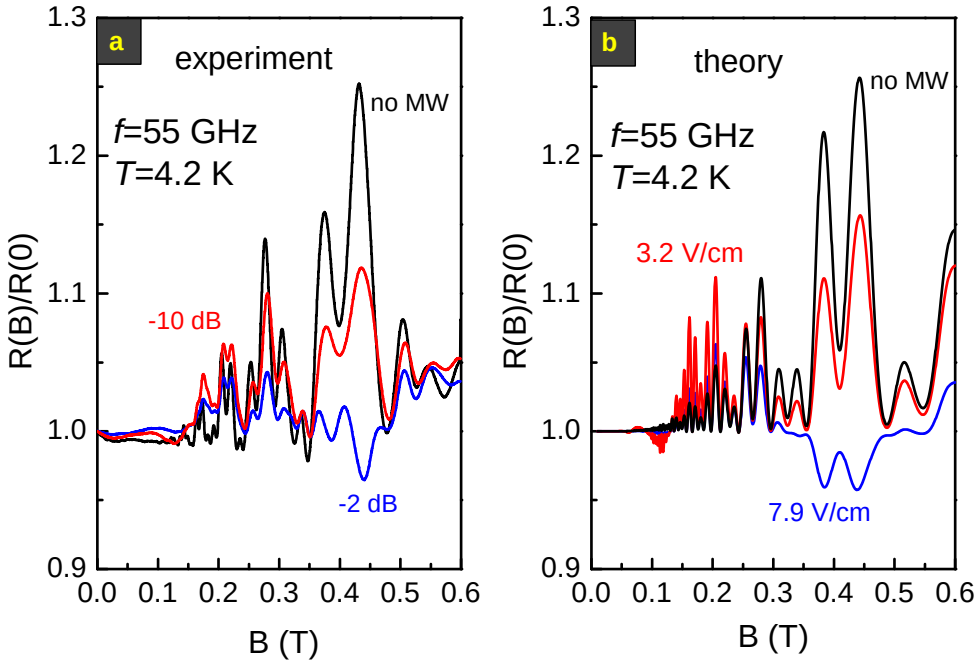

Figure 5.4: (a) Measured and (b) calculated power dependence of magnetoresistance exposed to MW irradiation at a fixed frequency of 55 GHz at 4.2 K where SdH oscillations are already suppressed. Corresponding MW electric field is in good agreement with attenuation in dB.

where the dark resistivity ρ_d is described in the first part of this chapter, while ρ_{in} and ρ_{di} are the microwave-induced contributions due to inelastic and displacement mechanisms, respectively. At low temperatures, ρ_{in} is the main contribution given by

$$\rho_{in} = -\frac{m^*}{e^2 n_s}\frac{2\tau_{tr}A_\omega}{N^2}\sum_{jj'}\nu_j^{tr}\nu_{j'}^{tr}d_j d_{j'}\cos\frac{2\pi\Delta_{jj'}}{\hbar\omega_c}, \tag{5.24}$$

with A_ω defined in Eq. (3.19) which is an oscillating function describing MIROs, and

$$\mathcal{P}_\omega = \frac{\tau_{in}}{\tau_{tr}}P_\omega, \quad P_\omega = \left(\frac{eE_\omega}{\hbar\omega}\right)^2\overline{v_F^2}(|s_+|^2+|s_-|^2) \tag{5.25}$$

is the dimensionless function proportional to the microwave power. In this expression, $\overline{v_F^2} = N^{-1}\sum_j v_j^2$ is the averaged Fermi velocity, and τ_{in} is the averaged inelastic relaxation time. Notice that in the case of linear polarization of radiation, and away from the cyclotron resonance, $|s_+|^2+|s_-|^2 \simeq (\omega^2+\omega_c^2)/(\omega^2-\omega_c^2)^2$. Since ρ_{di} is much smaller than ρ_{in}, it is not taken into account in our consideration. The influence of microwave radiation on the SdH oscillations can also be neglected at weak radiation power.

To get a visual description of the influence of radiation on magnetoresistance, we again use a simple model assuming equal partial densities $n_j = n_s/N$, equal transport scattering rates $\nu_{jj'}^{tr}$ and Dingle factors $d_j = d$. The magnetoresistance of a three-subband

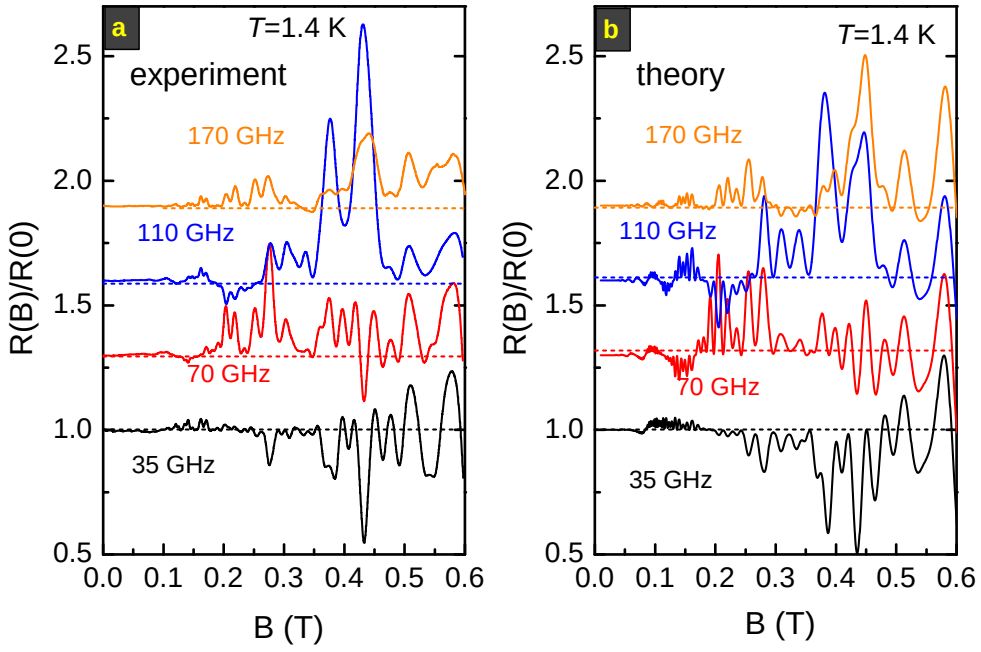

Figure 5.5: (a) Measured and (b) calculated frequency dependence of magnetoresistance exposed to MW irradiation for frequencies of 170, 110, 70 and 35 GHz for MW electric fields between 2.2 and 4.0 V/cm (see text) at T=1.4 K. Curves are shifted up for clarity, except the ones for 35 GHz.

system ($N = 3$) then takes the form

$$\frac{\rho_d^{MW}(B)}{\rho_d(0)} \simeq 1 + \frac{2}{3}(1 - A_\omega)d^2 \left[1 + \frac{2}{3}\cos\left(\frac{2\pi\Delta_{12}}{\hbar\omega_c}\right) + \frac{2}{3}\cos\left(\frac{2\pi\Delta_{13}}{\hbar\omega_c}\right) + \frac{2}{3}\cos\left(\frac{2\pi\Delta_{23}}{\hbar\omega_c}\right)\right], \tag{5.26}$$

which differs from Eq. (5.9) only by the presence of the factor $(1 - A_\omega)$. The products of A_ω with the MIS oscillation factors $\cos(2\pi\Delta_{jj'}/\hbar\omega_c)$ lead to interference oscillations of the magnetoresistance. In the frequency regions where A_ω is negative, one expects an enhancement of the MIS peaks. If A_ω is positive, the peaks are suppressed and inverted with increasing microwave power. This is the main feature of the behavior experimentally observed in Figure 5.4(a) and Figure 5.5(a). The comparison of experimental results with theory based on Eqs. (5.24)-(5.26) is demonstrated in Figure 5.4(b) and Figure 5.5(b). Apart from the known parameters, the estimate for the inelastic relaxation time based on Eq. (3.16) is applied, assuming that the relaxation is governed by the electron-electron interaction. To explain the experimental data, it is important to take into account microwave heating of the electron gas. This effect is directly visible in our experiment in TQWs and results also in a suppression of the SdH oscillations under microwave irradiation. The increase of the effective electron temperature over the lattice

temperature also leads to a decrease of the inelastic relaxation time and quantum lifetimes, see Eq. (5.10), so the MIS oscillation amplitudes are expected to be suppressed as a result of electron heating. The electron temperature, which depends on the magnetic field, radiation frequency, and power, has been calculated assuming energy relaxation of electrons due to their interaction with acoustic phonons and is presented in Figure 5.6. Finally, to determine the electric field E_ω corresponding to our measurements, we have estimated for the microwave electric field to $E_\omega = 3.2$ V/cm and 7.9 V/cm (corresponding to -10 dB and -2 dB), respectively, and we applied these values for calculations of the magnetoresistance shown in Figure 5.4(b). The theoretical plots in Figure 5.4(b) reproduce all the basic features of the experimental magnetoresistance traces, in particular, a suppression and inversion of two MIS peaks around B =0.4 T, because of the contribution ρ_{in} with positive A_ω. Notice that the non-monotonic power dependence of the MIS peaks around 0.2 T is explained by the interplay of MIS/MIRO interference and heating effects. At low radiation power the enhancement of these peaks occurs because of the contribution ρ_{in} with negative A_ω. At high power, when the saturation effect becomes essential, a decrease in the Dingle factors due to the heating-induced increase in ν_{ee} becomes more important and the MIS peaks are suppressed. The expected mi-

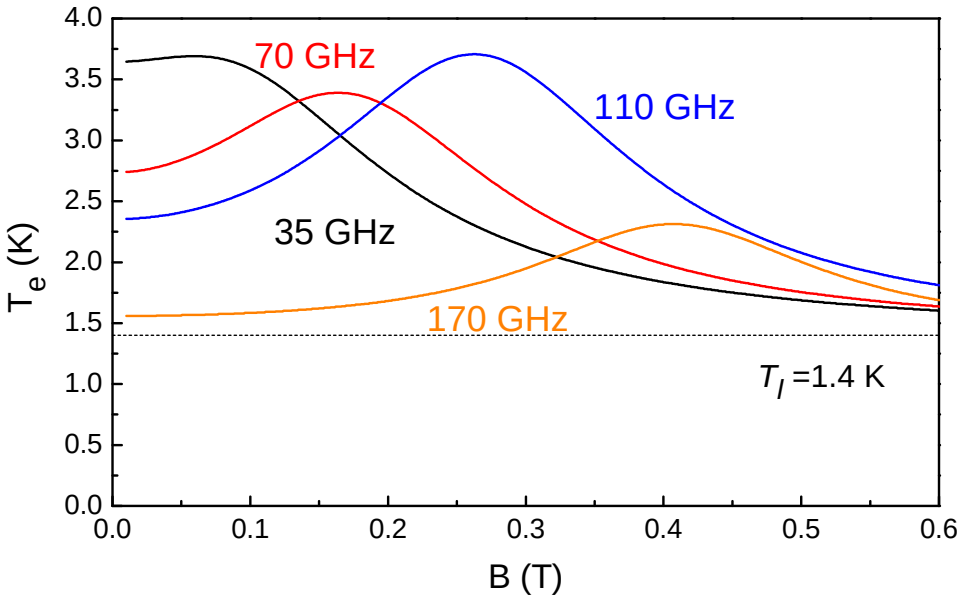

Figure 5.6: Electron temperature T_e for all frequencies of Figure 5.5 as a function of the magnetic field due to heating of electrons by the MW electric field.

crowave electric field in the frequency-dependent measurements shown in Figure 5.5(a) is $E_\omega \simeq 3$ V/cm. To get a closer resemblance of the theoretical magnetoresistance to the experimental plots, we slightly varied E_ω around this value and obtained the best fit at E_ω=3.5 V/cm for 35 GHz and 70 GHz, 4 V/cm for 110 GHz, and 2.2 V/cm for

170 GHz. The corresponding theoretical plots are presented in Figure 5.5(b). Since the lattice temperature for these measurements is 1.4 K, the heating effect appears to be considerable. For 35, 70, and 110 GHz, the calculated electron temperature in the vicinity of the cyclotron resonance is about 3.5 K, which is close to our experimental estimates obtained from suppression of the SdH oscillations. In general, a reasonably good agreement between theory and experiment at different frequencies suggests that the theoretical model applied for the calculations is reliable.

Hall resistance has also be investigated for all samples exposed to MW irradiation. Whereas MIROs have been reported, e.g. in Ref. [Mani04a], in systems with one occupied 2D subband.

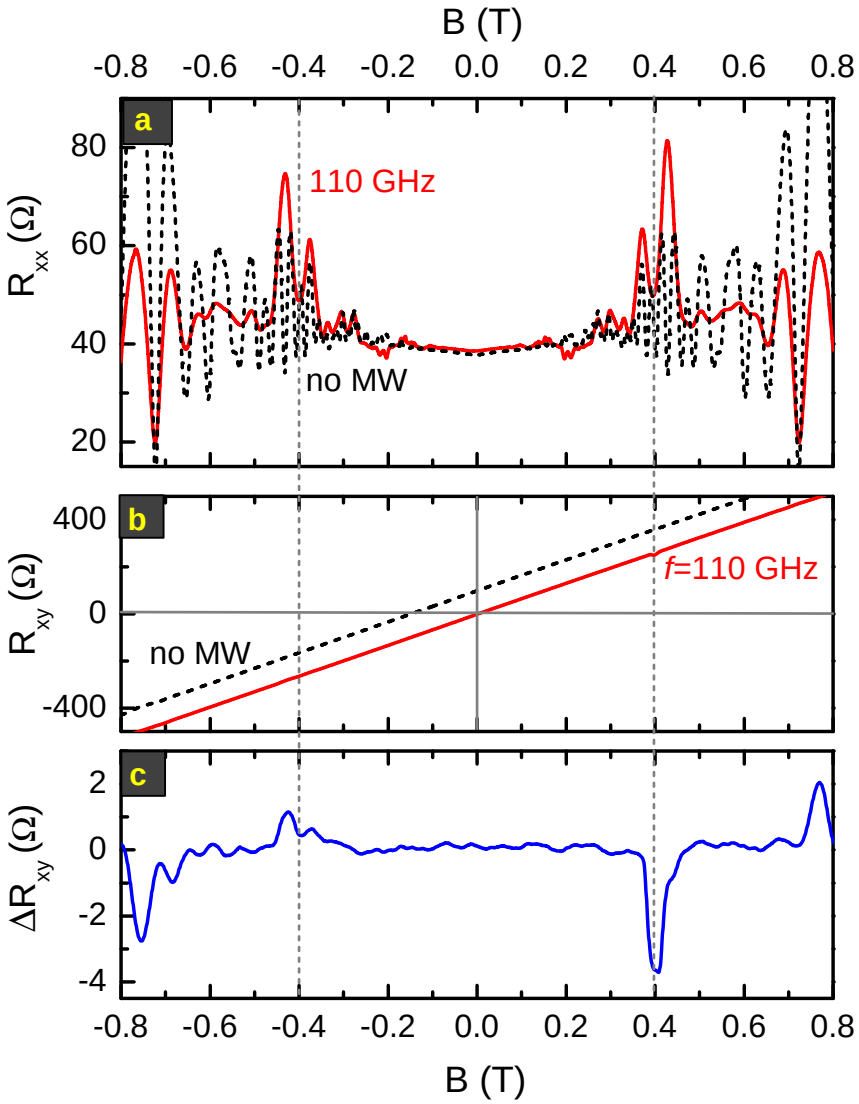

Figure 5.7: (a) Magnetoresistance in a TQW exposed to a MW irradiation of 110 GHz (attenuation 0 dB) at 1.4 K accompanied by MW-induced oscillations in Hall resistance (b). (c) Photoresistance exhibits oscillations correlated with longitudinal resistance at ±0.4 T.

In TQWs, additional features have also been identified in Hall resistance if the MIS oscillation picture is strongly changed by MW irradiation. In Figure 5.7 an example is presented for 110 GHz where MIS oscillations at B=0.4 T are enhanced. In R_{xy} a small change is visible at 0.4 T (positive B), see Figure 5.7(b). If we plot photoresistance $\Delta R_{xy} = R_{xy}^{MW} - R_{xy}$, this feature can be identified for ±0.4 T. As in Ref. [Mani04a], our signal vanishes for $B \to 0$ and we observe odd symmetry in ΔR_{xy} under field reversal. The odd symmetry rules out the possibility that ΔR_{xy} originates from a mixture from longitudinal resistance R_{xx} and transverse resistance R_{xy} due to misalignment of the Hall-voltage contacts.

Summary

This chapter has presented oscillations caused by intersubband scattering and modified by microwave (MW) irradiation in multi-subband systems. Theory, generalized to the multi-subband case, can be applied for an arbitrary number of subbands. We have performed experiments with three occupied 2D subbands in perpendicular magnetic fields. Such systems are realized in triple quantum wells (TQWs) with a high enough electron density. It has been demonstrated, both experimentally and theoretically, that the magnetoresistance of TQWs is qualitatively different from that for single-subband and two-subband systems, and contains a superposition of three oscillating terms whose frequencies are given by the subband separation energies Δ_{12}, Δ_{13}, and Δ_{23}. This occurs because the quantum contribution to the resistivity is essentially determined by electron scattering between the Landau levels of different subbands. By measuring the amplitude of MIS oscillations at different temperatures up to 30 K, we have established that temperature dependence of the electron-electron scattering rate follows the theoretically predicted T^2-law. The numerical constant λ in this dependence, $\lambda = 2.2$, is close enough to those determined from the MIS oscillations in two-subband systems, both in double quantum wells [Mamani08] ($\lambda = 3.5$) and in single quantum wells [Goran09] ($\lambda = 2.6$). Thus, the influence of electron-electron scattering on the quantum lifetime of electrons is not very sensitive to the number of occupied subbands.

Among the mechanisms of microwave photoresistance, the inelastic mechanism is found to be responsible for the observed magnetoresistance features. In spite of several approximations of the theory, in particular, those for description of elastic scattering, a good agreement is obtained between theoretical and experimental magnetoresistance traces by using an established estimate for the inelastic relaxation time. In experiments, the influence of microwaves decreases with an increasing number of subbands which is also connected to the quality (mobility) of the samples.

Chapter 6

Trilayer electron systems in high magnetic fields

Multi-component quantum Hall (QH) systems, which consist of multiple quantum wells separated by thin barriers, exhibit new interesting phenomena owing to many-body effects which are absent in pure single-layer systems [QH-effects97]. If the wells are in close proximity, interlayer electron-electron interaction creates new *correlated* states in strong magnetic fields. Studies have started 20 years ago in double quantum wells and of particular interest is the state at total filling factor ν=1 in a QH-bilayer system.
In this chapter, we first introduce quantum Hall effect in bilayer electron systems and present a summary of experimental and theoretical results, which are relevant for this thesis. We show that two parameters, interlayer separation d and magnetic length l_B, play an important role. Furthermore, we discuss the influence of a parallel magnetic field on multilayer systems which deserves a special attention and favors many-body correlation.
Further progress in physics of quantum Hall effects depends on experimental search of new many-body ground states which are different of those from bilayer systems. Therefore, we focus in the second part on trilayer electron systems, where three quantum wells are separated by thin barriers and coupled by tunneling. Whereas physics in bilayer systems has already been extensively studied, trilayer systems are at the beginning of both experimental and theoretical work. In order to find new many-body states, one has to suppress tunneling between the layers so that each electron moves only in a layer. This still allows electrons to interact with their neighbors in nearby planes if the layer separation is not too big, giving rise to new quantum Hall states of which some have been observed in experiments on double-layer systems.
In this thesis, we investigate triple quantum wells with high-electron density for the first time at temperatures of 50-100 mK and in magnetic fields up to 34 T. After introducing the particular behavior of quantum Hall effects in a perpendicular magnetic field in our trilayer systems, a parallel magnetic field reveals a collapse of the integer quantum Hall effect (QHE), emergent and reentrant fractional quantum Hall (FQH) states as well as new FQH states. We suggest, that the observed new FQH states might be attributed to new correlated states in trilayer electron systems.

6.1 Bilayer quantum Hall effect and correlated states in bilayer electron systems

The first and most simple candidate for multilayer systems is, of course, a bilayer electron system. The first and second part of this section present QHE in bilayer systems subjected to a perpendicular magnetic field and mainly discuss physics for total filling factor ν=1[1] as well as the importance of the ratio d/l_B and its consequences for transport. The last part introduces the influence of a parallel magnetic field on transport measurements which is one fundamental issue for our studies in trilayer electron systems.

Bilayer electron systems have proven extremely interesting physics due to their extra degree of freedom [QH-effects97]. When the interlayer separation d is small enough so that interlayer tunneling and/or Coulomb interactions become strong, new electronic configurations emerge. These configurations critically depend on the combination of interlayer effects with the physics of a single-layer 2D system. In strong perpendicular magnetic fields, new features of the integer and fractional quantum Hall effect exist, e.g. the destruction of the quantum Hall states at odd-integer filling factors [Boebinger90] and the appearance of a new fractional quantum Hall state at total filling factor ν=1 [Eisenstein92a]. Many other interesting phenomena can be studied in DQWs but they will not be a topic of this thesis, e.g. DQWs with separate contacts to each layer offer wide opportunities to study the transverse (layer-to-layer) electron transport [Eisenstein92b] and electron drag phenomena [Gramila91, Eisenstein92b]. Here we only focus on phenomena where the 2D layers are shunted. The following discussion about the destruction of QH-states at odd-integer filling factors, new fractional filling factors and the importance of parameters like d/l_B and tunneling gap Δ_{SAS} are based on the Refs. [Boebinger90, Eisenstein92a, Suen92] and especially on Ref. [Murphy93] as well as references therein.

6.1.1 New energy scales: Δ_{SAS} and Coulomb interaction

As it has been already shown in Chapter 1 for balanced DQWs, single-well electron wavefunctions "form" symmetric and antisymmetric wavefunctions, separated by the energy gap $\Delta_{SAS} = \varepsilon_{AS} - \varepsilon_S$ where ε_S (ε_{AS}) is the symmetric (antisymmetric) energy. This implies now the existence of three distinct energy gaps in DQWs which can be resolved in high magnetic fields, see Figure 6.1. In addition to cyclotron energy $\hbar\omega_c = \hbar eB_\perp/m^*$ and Zeeman energy $\Delta_Z = g^*\mu_B B_{tot}$, we have now the symmetric-antisymmetric energy gap Δ_{SAS}. The three energy gaps are labeled in a Landau fan diagram in the inset of Figure 6.1. All gaps can now be identified for the balanced DQW with a barrier thickness of d_b=1.4 nm (other sample parameters see Appendix A): ν=4 and ν=8 correspond to the cyclotron energy, ν=6 to the Zeeman energy and ν=3, ν=5 and ν=7 to

[1] Notation: the total filling in this chapter is given by $\nu = \sum_j \nu_j$ and partical filling factors from each layer are expressed by their layer index [e.g. the state 1/3 in one quantum well (here well with number 3, middle well) in a trilayer system is indicated by ν_3=1/3].

the symmetric-antisymmetric energy Δ_{SAS} in this range of magnetic field. Note that the Zeeman energy is proportional to the total magnetic field B_{tot} and the states at ν=4n+2 are ascribed to the Zeeman energy. The sample used in Figure 6.1 is an example for a strongly coupled bilayer system. The second new parameter is d/l_B and

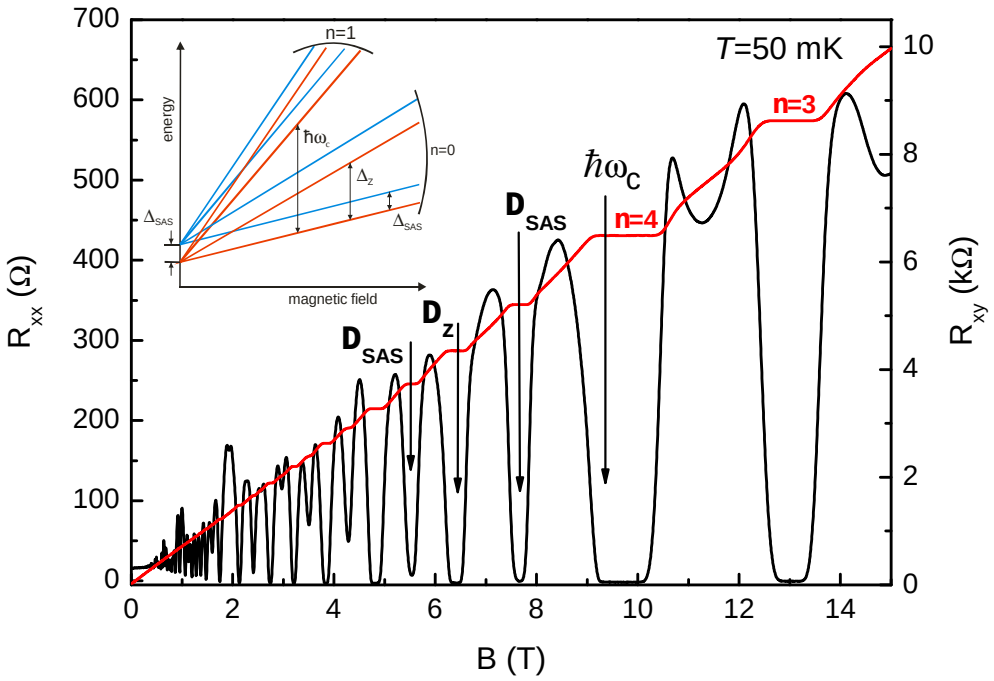

Figure 6.1: DQW with d_b=1.4 nm in a perpendicular magnetic field up to 15 T at a temperature of 50 mK. Filling factors can be attributed to corresponding energy gaps, see text. Inset: Landau fan diagram for a bilayer electron system.

is called "effective layer separation" which characterizes the relative importance of intralayer and interlayer Coulomb energies. d is the interlayer distance (center-to-center well separation) and determines the Coulomb energy ($e^2/4\pi\epsilon d$) of the electrons in different layers. $l_B = \sqrt{\hbar/eB}$ is the magnetic length and determines the mean separation between electrons within the same layer and thus characterizes the intralayer Coulomb energy ($e^2/4\pi\epsilon l_B$). The value of the parameter d/l_B is playing a crucial role and is now discussed in connection with the bilayer ν=1 QHE.

6.1.2 The bilayer ν=1 quantum Hall effect

In a balanced DQW-system with equal density in each layer, total filling factor ν=1 corresponds to the individual layers being at $\nu_1 = \nu_2$=1/2. It has been shown in Figure 1.7 that the state ν=1/2 does not show a plateau in Hall resistance. Note however, that this state in single-layer systems is described by the theory of composite fermions. When two layers are far way, they behave independent, i.e. each layer with ν=1/2. If they are

brought close together, the system can enter a new QH-state, unique for bilayer systems owing to interlayer tunneling and Coulomb interactions [Boebinger90, Eisenstein92a, Suen92]. This implies, that interlayer interactions are significant compared to intralayer interactions in close proximity. Electrons in both layers order in such a way to minimize the Coulomb interactions. These new states are called *correlated* states.

Two possibilities to obtain ν=1

The state ν=1 in a bilayer electron system can be obtained by two different ways. In the previous section it has been shown that Δ_{SAS} is the gap between the lowest symmetric and antisymmetric eigenstates. If the magnitude of Δ_{SAS} is large enough, the ground state in this bilayer system is just a fully filled Landau level of symmetric state electrons because Fermi energy ε_F is pinned in the gap giving rise to a QHE. An experimental work [Boebinger90] confirmed that odd-integer QH-states correspond to the Δ_{SAS}-gap. Filling factor ν=1 is destroyed in high magnetic fields. If the Δ_{SAS}-gap is destroyed, the DQW becomes essentially identical with a system of two independent single quantum wells with no interwell tunneling (in a single electron picture).
On the other hand, interlayer electron-electron interaction can produce a QHE at ν=1 even without tunneling, i.e. Coulomb interaction is sufficient to open a gap at ν=1. If d/l_B is large, the layers are much further apart than the electrons in each separate layer, and therefore intralayer interactions dominate. The system essentially consists of two separate single-layer 2DEGs with half-filled Landau levels, which are compressible states without any QHE. If the layers are brought close together, i.e. when d/l_B is small, the difference between inter- and intralayer interactions is in the order of d and l_B and hence also negligible. For this situation, the two half-filled Landau levels (LLs) are expected to act as one completely filled Landau level, and exhibit a QHE. If the layers are so far apart that the system can be considered as decoupled, no QHE is expected at ν=1 since no plateau has ever been observed at R_{xy}=$2h/e^2$ in a single layer 2D system (Figure 1.7).

Interplay between two distinct mechanisms and phase diagram

This interplay between two distinct mechanisms for producing a ν=1 plateau in bilayer electron systems has been extensively studied, and Murphy *et al.* [Murphy93] have established an experimental phase diagram for the double layer ν=1 QHE, shown in the inset of Figure 6.2. In their work, several samples with mostly barriers of 31 Å and 40 Å , and different Al concentration in order to vary Δ_{SAS} have been used. QHE at ν=1 in Figure 6.2 appears for the sample with d_b =31 Å whereas for the other sample with d_b =40 Å, QHE is absent. Both samples display minima at filling factors ν=2, 2/3 and 4/5. It must be noticed that the barrier width affects both the interlayer Coulomb interactions and the tunneling strength while the carrier concentration controls intralayer dynamics. This simple comparison of two samples does not explain the occurrence and the absence of QHE and Murphy *et al.* performed more experiments which enabled

them to distinguish between many-body regimes and tunneling. The inset of Figure 6.2 presents the phase diagram where the horizontal axis is the tunneling strength, parametrized by the ratio of Δ_{SAS} to the characteristic Coulomb energy (at ν=1). The vertical axis is the ratio of d to the magnetic length l_B, essentially the average intra- and interlayer Coulomb interactions. The solid (open) symbols in Figure 6.2 present samples where QHE at ν=1 appears (is absent). The dashed line indicates a well-defined boundary between a QHE phase at small d/l_B and a non-QHE phase at larger layer separation. However, the most interesting "message" of this phase diagram is that there is clear evidence that the ν=1 QHE evolves from a regime dominated by tunneling (right part with large Δ_{SAS}) to another where only Coulomb interactions are important (no tunneling, Δ_{SAS}=0). In other words, the bilayer QHE at ν=1 can exist even in the absence of a tunneling gap. Consequently, this energy gap arises entirely from many-body Coulomb interactions between the electrons. The possibility

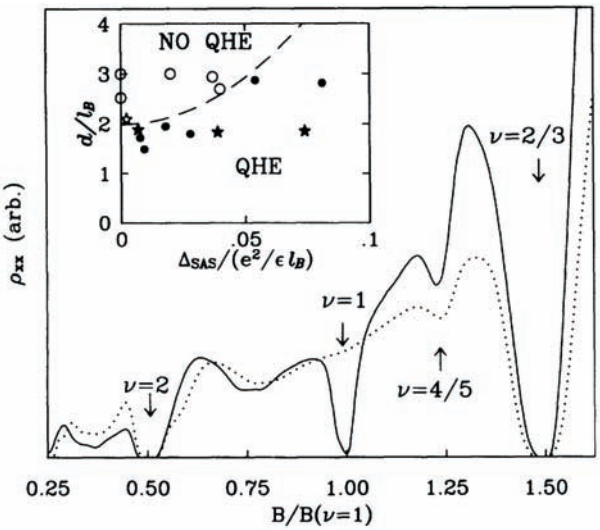

Figure 6.2: Resistivity as a function of magnetic field (normalized by B at ν=1) for two samples, see text, with slightly different carrier concentration exhibit different behavior at ν=1. Inset: phase diagram at ν=1 where solid symbols represent samples that show QHE at ν=1 and open symbols that do not. Figure is taken from Ref. [Murphy93].

of new correlated states that arise in Coulomb-coupled bilayer electron systems have been suggested first by Rezayi and Haldane [Rezayi87] and numerical studies for the state ν=1 have been reported in Ref. [Chakraborty87]. Actually, it was first Halperin in 1983 [Halperin83] and later Yoshioka and co-authors [Yoshioka89] who employed generalized Jastrow wavefunctions to outline new possible FQH states in bilayer systems in the absence of tunneling. In Ref. [Yoshioka89], the $\Psi_{1,1,1}$-state is proposed to be responsible for the bilayer ν=1-state which combines strong intralayer and interlayer correlations. This state is often interpreted in terms of a Bose-Einstein condensate of interlayer electron-hole pairs or an excitonic fluid. In addition, it has been also found in Ref. [Yoshioka89] that $\Psi_{3,3,1}$ is a candidate for the FQH state at ν=1/2 which

is quite similar to the Laughlin state 1/3 insofar that interlayer electron correlations are concerned containing interlayer correlations as well. Note that this state is only a candidate if the ratio d/l_b is in the order of unity.

6.1.3 Bilayer electron system in a tilted magnetic field

When in addition a magnetic field component $B_{\|}$ is applied, which is aligned parallel to the 2D plane, interlayer correlation has a profound influence on the physics of a bilayer electron system. It affects both the single-particle wavefunctions, as in the single-layer case, and the collective behavior of the system. We discuss the single-particle effect where electrons can travel along paths which enclose a magnetic flux, and pick up the associated Aharonov-Bohm phase. Furthermore, it has been shown in theory that the combination of a nonzero tunneling amplitude and an in-plane magnetic field gives rise to a commensurate-incommensurate phase transition driven by the in-plane field strength [Yang96].

In Ref. [Murphy93], a novel phase transition has been found for the ν=1-state in tilted magnetic fields. An in-plane magnetic field suppresses Δ_{SAS} with increasing tilt angle and hence tunneling between the layers. The unusal angle dependence for ν=1 has been attributed to a new phase transition in the ν=1-state. For its visualization, the pseudospin mechanism is now introduced. In pseudospin language, an electron in one 2D layer has pseudospin "up" and the one in the other layer has pseudospin "down". So the electron which is in the symmetric (antisymmetric) DQW state is an eigenstate of pseudospin σ=+1 (σ=-1) due to Pauli spin-algebra. It has been already mentioned above that without Coulomb interaction, the electron is in a symmetric eigenstate at ν=1 and we have a ground-state which is fully spin-polarized with Δ_{SAS} the amount of energy to flip electron's pseudospin.

In the presence of Coulomb interactions the energy gap is increased by exchange energy but the ground state remains polarized assuming small layer spacing. With an additional parallel magnetic field, it has been shown, e.g. in Ref. [Yang94] that the tunneling matrix element acquires a phase which advances linearly across the sample in the direction perpendicular to the parallel field. When the magnetic field is tilted with respect to the perpendicular direction, the transport gap at ν=1 is reduced, which is explained as a commensurate-incommensurate transition in the pseudospin configuration[2]. The consequences are illustrated in Ref. [Eisenstein95]. The direction in pseudospin space defining symmetric eigenstates is not longer orientated in, let's say $\vec{x}$ for $B_{\|}$=0, but instead rotates if one moves perpendicular to the parallel field component. Now, if the ν=1 ground state maintains the energetic advantage of tunneling, the pseudospin has to acquire a "texture" which is twisted. In Ref. [Eisenstein95] the wavelength of this texture is set by $B_{\|}$ which is required to inject one flux quantum between two layers: $\lambda_{co} = h/edB_{\|}$. Note that this twisting would have no observable effect if it were not for

[2] In the commensurate phase, the spins follow the rotation suggested by the tunneling term wheras for the incommensurate phase, we have a uniform spin orientation.

Coulomb interactions. Since the neighboring electrons have no longer precisely parallel pseudospin, the twisting costs exchange energy. With increasing parallel magnetic field, this cost rises and might exceed Δ_{SAS}. At exactly this point, the ground state becomes unstable against a phase transition [Yang94] to a (new) uniformly polarized many-body state (coherent state).

Oscillations of the tunneling amplitude

It has been shown that an in-plane field adds an Aharonov-Bohm phase to the tunneling amplitude which causes oscillations of the tunnel coupling between the electron states in the layers, see [Hu92, Yakovenko06, Gusev08], and suppression of this coupling for low Landau levels. In Ref. [Gusev08], several DQWs in tilted magnetic field have been investigated and strong magnetoresistance oscillations as a function of the in-plane magnetic field at filling factors ν=4n+3 and ν=4n+1 where n is the Landau level number have been found. With increasing in-plane magnetic field, the energy gap at ν=4n+3 and ν=4n+1 vanishes and reestablishes several times for n=2,3,4,... and this reentrance behavior originates from oscillations of the single-particle tunneling gap Δ_{SAS}. At these integer filling factors, longitudinal resistance R_{xx} depends exponentially on Δ_{SAS}, $R_{xx} \sim R_0 \exp(-\Delta_{SAS}/2k_BT)$. Figure 6.3 presents the interpretation of the oscillating tunneling gap as the Aharonov-Bohm (AB) effect in tilted magnetic fields [Yakovenko06]. First, in Figure 6.3(a) both layers separated by distance d in a tilted magnetic field are presented. In a perpendicular field, electron motion is described by cyclotron orbits with radius $R_c = \hbar k_F/eB_\perp$ with k_F the Fermi wavevector. The phase shift which leads to the oscillations of the effective interlayer tunneling amplitude appears owing to magnetic flux of the parallel component of the magnetic field through the area $S = 2R_c d$, see Figure 6.3(b). In Ref. [Boebinger91] is has been shown that in momentum space, the Fermi surfaces (circles) are shifted by $\Delta k_\parallel = eB_\parallel d/\hbar$ relative to each other due to the $B_\parallel$-component, see Figure 6.3(c). Tunneling occurs now at k_1 and k_2 due to energy and momentum conservation laws. Magnetic flux owing to

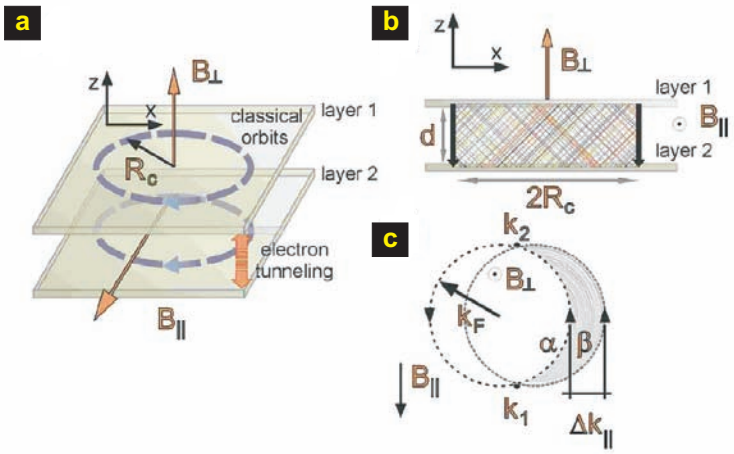

Figure 6.3: Aharonov-Bohm effect for the tunneling amplitude: (a) bilayer system in a tilted magnetic field, (b) side view where AB-effect for tunneling amplitude is produced by the magnetic flux through the shaded area and (c) Fermi circles shifted due to $B_\parallel$ by $\Delta k_\parallel$. Further explanations, see text. Figure taken from Ref. [Gusev08].

the perpendicular component of the magnetic field through the shaded area results in a constructive or destructive interference at the opposite turning points between trajectories α and β. AB-effect in real and momentum space leads to the same oscillations of tunneling amplitude with increasing tilt angle.

Additional new experimental works

Before we introduce trilayer electron systems, we mention briefly two additional experimental works where the influence of a parallel magnetic field on bilayer systems has been studied.

- Giudici *et al.* reported that the spin degree of freedom plays a decisive role in the bilayer ν=1 phase diagram [Giudici08]. It is pointed out that a parallel magnetic field increases the critical effective interlayer separation d/l_B from the usual value of 1.9 to 2.33, thus stabilising the coherent phase. The authors demonstrate in Ref. [Giudici08] (figure 2) that at a value of d/l_B=2.05, which is above the critical value observed with a perpendicular magnetic field, see inset of Figure 6.2, a minimum in the longitudinal resistance can be induced by tilting the bilayer system. Since the gap for this chosen sample is Δ_{SAS}=150 μK and therefore significantly below the temperature in the experiments, the charge gap in this sample cannot be due to the Δ_{SAS}-splitting, and has to be a consequence of the interlayer interactions. To conclude, the in-plane field stabilises the interlayer coherent state. Considering a simple model for the competition between the various energy scales, Giudici *et al.* suggest that the system is not fully spin-polarised in the case where $B_{\|}$=0 and an in-plane field increases B_{tot}. Hence, the Zeeman energy polarizes the spin further and strengthens the incompressible phase.

- Fukuda *et al.* report the finding of a commensurate-incommensurate phase transition, as well as an intermediate pseudospin soliton phase, all driven by the strength of $B_{\|}$ [Fukuda08]. They have found an anomalous peak in the longitudinal resistance with a sinusoidal dependence on the angle between the applied current and the in-plane field. The authors interpret this result as a soliton lattice, a stripe-like structure, aligned parallel to $B_{\|}$, in contrast with the usual stripe formation, which occurs perpendicular to $B_{\|}$. The existence of stripes in bilayer electron systems, see Ref. [Gusev07] and references therein, can be different from stripe phases in a single layer system.

6.2 Multilayer electron system: prediction for new correlated states

6.2.1 Candidates for correlated states in trilayer and multilayer systems

In multi-component quantum Hall systems, which consist of multiple quantum wells separated by (thin) tunneling barriers, a rich variety of new incompressible states can

be realized. Correlated FQH states exist in a certain interval of parameters determined by the ratio of interlayer separation d and the magnetic length l_B [Hanna96]. Such states in trilayer (or multilayer) electron systems appear at odd-denominator total filling factors and are different from correlated states in bilayer systems, but in both cases, multicomponent FQH-states can be obtained by the generalization of the Laughlin state [MacDonald90]. In Ref. [MacDonald90] (table 2) many new states are listed and the strongest FQHE is expected at ν=5/7 for a system with three closely spaced layers. It must be added that this state has a lower density in the middle layer than in the two side layers which obviously helps to lower the energy, i.e. we have filling factors $\nu_1 = \nu_3$=2/7 and ν_2=1/7 where ν_2 denotes the filling factor in the middle layer. All listed states in Ref. [MacDonald90] are expected to have the largest excitation gaps and hence they should be most robust against disorder and the first candidates seen in experiments.
Other theoretical works suggested several possible ground states in multilayer electron systems. One candidate for these ground states is a spontaneous coherent mini-band state in a superlattice quantum Hall system [Hanna02]. This state is an analog to the interlayer coherent state at filling factor ν=1 in bilayer electron systems. Another candidate for a possible ground state is a solid state phase (Wigner crystals) with different configurations depending on the interlayer separation [Qiu90]. Such phase transitions between different "Laughlin-like"-phases should be possible to observe in experiments. A further ground state, a so-called dimer state, is favored for a large number of layers with small interlayer distance [Shevchenko04]. The superlattice separates into pairs of adjacent interlayer coherent states, while such coherence is absent between layers of different pairs. The limit of a superlattice for many layers has been studied in Ref. [Qiu89]. Calculations indicate incompressible states as well as excitation gaps comparable to those in single-layer systems.
Last year, gapless layered three-dimensional fractional quantum Hall states in multilayer systems have been theoretically predicted. A three-dimensional (3D) multilayer FQH-state with average filling factor ν=1/3 per layer which is qualitatively distinct from a stacking of weakly coupled Laughlin states is built using the "*parton* construction". This new state supports gapped fermionic quasiparticles (with charge $e/3$) that might propagate both within and between n layers, in contrast to the quasi-particles in a multilayer Laughlin state which are confined within each layer [Levin09].
To summarize, there are many possibilities for multilayer FQH-states and hardly any of them has been explored neither in trilayer nor in multilayer electron systems.

6.2.2 Theoretical basics for studies in trilayer electron systems

Before we present our experimental studies in perpendicular and tilted magnetic fields, properties of trilayer systems are introduced. We also recapitulate the mentioned theoretical basics for bilayer systems which we employ for analysis in trilayer electron systems.
First, we discuss the energy diagram in Figure 6.4(a) and the Landau fan diagram in

Figure 6.4(b). In the energy diagram we have in addition to cyclotron energy $\hbar\omega_c$ and the Zeeman energy Δ_Z, subband splitting $\Delta_{jj'}$, illustrated by Δ_{23}. The Landau fan dia-

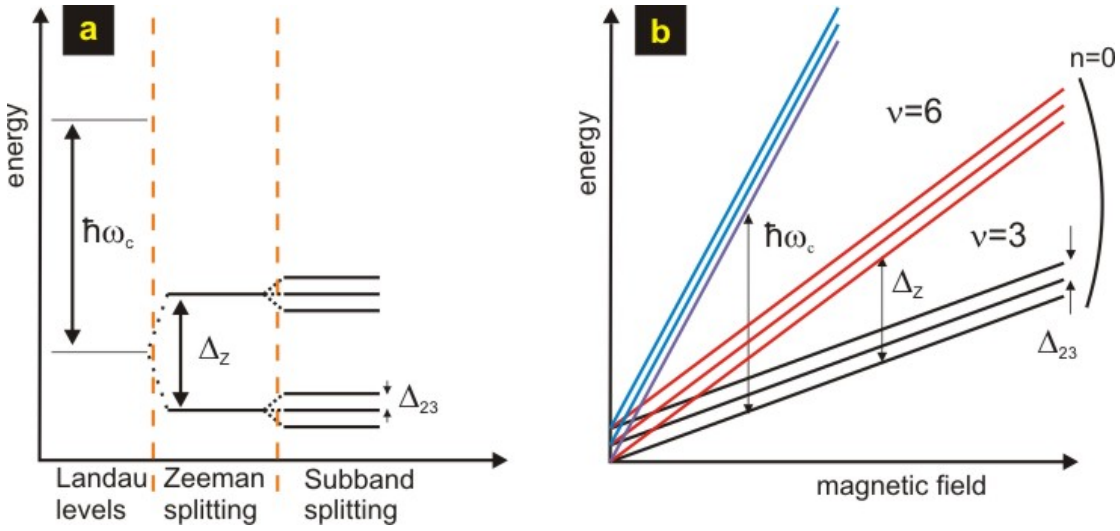

Figure 6.4: (a) Energy diagram with cyclotron energy ($\hbar\omega_c$), Zeeman energy ($\Delta_Z = g^*\mu_B B$) and subband energies ($\Delta_{jj'}$, marked here Δ_{23}). (b) Landau fan diagram for a TQW.

gram consists of spin split Landau levels separated by the subband gaps. These energies can be described by the expression $\hbar\omega_c(n+1/2) \pm \Delta_Z/2 + E_j$, where E_j $(j = 1, 2, 3)$ are the energies of quantization in the TQW potential.

The energy gaps as well as the corresponding single-electron wavefunctions can be estimated within the tight-binding model [Hanna96], see Chapter 5. For a symmetric structure, we can write

$$E_{1,3} = \frac{\varepsilon_c + \varepsilon_s}{2} \mp \sqrt{\frac{(\varepsilon_c - \varepsilon_s)^2}{4} + 2t^2}, \quad E_2 = \varepsilon_s, \tag{6.1}$$

where ε_s and ε_c are the energies of electrons in the side and central wells in the absence of tunneling, and t is the tunneling amplitude. Since $\varepsilon_c > \varepsilon_s$ and $t \neq 0$, one obtains a subband sequence $E_1 < E_2 < E_3$ and well-defined gaps for each spin-split Landau level. This is the case for $B_\parallel$=0.

If we apply in addition to the perpendicular component a parallel component of the magnetic field, the tunneling gap starts to oscillate due to the Aharonov-Bohm effect and is a pure single-particle phenomenon, as discussed for bilayer systems. The oscillation period $\Delta B_\parallel \simeq \hbar/edl_\perp$ is determined by the magnetic flux through the area $dl_\perp$, where $l_\perp = \sqrt{\hbar/eB_\perp}$ is the magnetic length associated with the perpendicular component of the magnetic field $B_\perp$. This effect should also occur in our trilayer electron systems and the resistance peaks (minima) correspond to a suppression (enhancement) of the tunneling gap. For the lowest Landau level (LL) $(n = 0)$ the gap is suppressed according to $t \propto \exp[-(B_\parallel/B_\parallel^c)^2]$, where $B_\parallel^c = (2/d)\sqrt{B_\perp \hbar/e}$ and does not oscillate. Since we have three populated 2D subbands, a parallel magnetic field might close the gap between two subbands of the lowest spin-split level whereas the other gap does not vanish. We show

now in experiments that this suppression of tunneling between two subbands gives rise to new FQH states.

6.3 Experimental studies of triple quantum wells

Experimental studies on trilayer electron systems, realized in triple quantum wells have been performed by Shayegan and co-workers in the 90s [Jo92, Shukla98]. The following sections present first the properties of TQWs and then experimental studies on our trilayer systems.

The first experimental work in 1992 [Jo92] reports on deep R_{xx} minima at fractional filling factors ν=7/5 and ν=5/7 which are particularly strong in triple-layer systems and have been already suggested theoretically [MacDonald90]. Another work presents a magnetic-field-induced triple-layer to bilayer-transition at high magnetic fields [Shukla98]. This transition occurs in the extreme quantum limit and is signaled by the appearance of strong FQH states which are characteristic for a bilayer electron system. The transition in Ref. [Shukla98] is attributed to a charge transfer from the center layer to the side layers and it is argued that the associated "Hartree" energy cost is compensated by the correlation energy gained in forming two incompressible FQH states in the side layers. Typical even-numerator FQH-states at ν=12/3, 4/5, 6/5, and 4/3 emerge which are those expected for a bilayer electron system.

6.3.1 Properties of investigated trilayer systems and energy gaps

Owing to the progress in fabrication of multiple 2D systems by MBE-technique, multicomponent QH-systems such as TQWs can be investigated now. In contrast to previous works [Jo92, Shukla98], we increase the total density in our trilayer system[3]. Due to a combined action of electron repulsion and confinement, the electrons tend to concentrate mostly in the side wells. The samples are symmetrically doped GaAs triple quantum wells with equal widths $d_W = 100$ Å of the side wells and a wider (230 Å) central well, separated by $Al_xGa_{1-x}As$ (x=0.35) barriers with thicknesses of $d_b = 14$ Å (wafer A) and $d_b = 20$ Å (wafer B)[4]. The trilayer electron systems are strongly coupled, see energy gaps in Table 5.1. The ratio d/l_B is 1.4 at B =1 T. All three layers are shunted by ohmic contacts. In order to increase the mobility, we have produced samples with high electron density $n_s = 9 \times 10^{11}$ cm^{-2} for both wafers. The samples have mobilities of $\mu = 5 \times 10^5$ cm^2/V s (wafer A) and 4×10^5 cm^2/V s (wafer B). While for both kinds of samples we obtain similar magnetoresistance, the thesis will focus mostly on samples with $d_b = 20$ Å. It should be added that all studies have been performed at $T = 50$ mK in a dilution refrigerator up to B=17 T and at $T \simeq 100$ mK in a Bitter-type coil up to B=34 T.

[3] A part of the results is presented in [Gusev09].

[4] All sample parameters are already presented in Chapter 5 and in Table 5.1, as well as in Appendix A, Table A.3.

As shown in Figure 6.1 for bilayer electrons systems, gaps can be identified in a measurement of longitudinal and Hall resistance in our TQWs. Figure 6.5 illustrates both resistances in a perpendicular magnetic field up to 32 T (inset 17 T) for a temperature of 100 mK (inset 50 mK) for a sample with a barrier width of d_b=2.0 nm. Within Figure 6.5, minimum at ν=6 is identified as the cyclotron gap, the minimum at $\nu = 3$ with the Zeeman gap and the minima at $\nu = 1$, $\nu = 2$, $\nu = 4$, and $\nu = 5$ with the subband gaps of the first LL ($n = 0$). Numerous scans have been done at various gate voltages V_g by sweeping the magnetic field in Hall-bar geometry with a top gate. It has been found that the topological diagram in the density-magnetic field plane correlates with the Landau level fan diagram in strong magnetic fields [Figure 6.4(b)]. Beyond integer

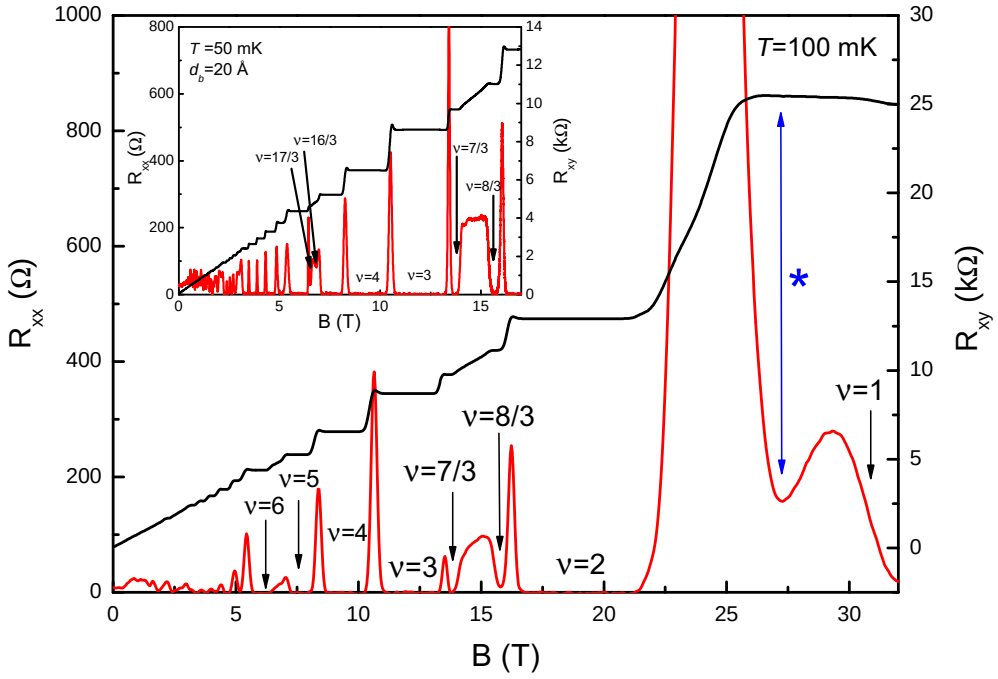

Figure 6.5: TQW with d_b=2.0 nm in a perpendicular magnetic field up to 32 T (inset 17 T) at a temperature of 100 mK (inset 50 mK). Filling factors can be attributed to corresponding energy gaps, see text. The minima marked with an asterisk in longitudinal resistance is not accompanied by a plateau in R_{xy}.

filling factors, we find in Figure 6.5 several minima in R_{xx} accompanied by plateaus in Hall resistance at fractional filling factors ν=17/3, 16/3, 8/3 and 7/3 for both wafers. Note that this observation clearly indicates the difference of trilayer electron systems (TQWs) from single layer systems (QWs) where FQH effect is developed for all Landau levels with filling factors ν <3. Moreover, the fractional states are observed only in the regions of transitions from ν=2 to ν=3 and from ν=5 to ν=6 which corresponds to filling of the upper subband for each spin sublevel of the first Landau level. Therefore it can be argued that since the FQH effect requires high mobility, this observation may

indicate that the mobilities are maximal for electrons in these upper subbands. Indeed, the electron wavefunction for an upper subband (j=3) is localized mostly in the central well, especially if t is small. Consequently, electrons of the upper subband experience less scattering and have the highest mobility, sufficient to form states with fractional filling factors. The minimum in longitudinal resistance at $B \simeq$27.5 T (marked with an asterisk in Figure 6.5) is not accompanied by a plateau in R_{xy}. This "state" is also very sensitive to temperature and its appearance might be attributed to a new correlated state at filling factor ν=1.

6.3.2 New FQH-states in a tilted magnetic field

In order to create favorable conditions for many-body correlations, the localization of electrons has to be increased. This can be done by applying a magnetic field $B_{\|}$ in the plane of 2D layers. For these measurements, a dilution refrigerator up to 17 T has been used and all samples have a barrier width of d_b=20 Å if no other values are given. Figure 6.6(a) presents the plot of R_{xx} in the tilt angle-perpendicular magnetic field plane. This plot clearly demonstrates that resistance minima corresponding to filling of the second Landau level at ν=7,9 and 10 vanish and reestablish with increasing tilt angle. This reentrant behavior originates from oscillations of the tunneling amplitude due to the Aharonov-Bohm effect [Gusev08]. Each resistance maximum corresponds to the suppression of the tunneling gap and each resistance minimum to the maximum of the tunneling amplitude.
The most intriguing observation in Figure 6.6(a) is the complete suppression of the minimum attributed to integer filling factor $\nu = 4$ at $\Theta \simeq 40°$. The corresponding $B_{\|}$ for these conditions is approximately equal to $B_{\|}^{c}$ and exponential suppression of the tunneling is expected. Note, that for this angle, we fulfill the condition for the appearance of new correlated states because the tunneling is suppressed exponentially and electron motion is confined to single layers. Consequently, correlation of electrons with nearby neighbors must be responsible for these new FQH-states. On the other hand, the state at $\nu = 5$ remains robust against increasing tilt angle. In Figure 6.6(b) longitudinal and Hall resistance are plotted for $\Theta = 0°$ and $\Theta = 49°$. We observe three new minima accompanied with quantized plateaus with denominator three and one of the plateaus is fully developed at $\Theta = 49°$ with filling factor $\nu = 10/3$ (accuracy 2%).
We explain the different sensitivity for different filling factors to $B_{\|}$ by the suppression of the tunneling amplitude ($t \to 0$). In this particular case, the gap between the two lowest subbands of each spin sublevel ($E_1 \to E_2 = \varepsilon_s$) are closed, while the gap between the upper and middle subbands decreases but does not vanish ($E_3 \to \varepsilon_c$).

In order to investigate this phenomenon more in detail, measurements with another wafer (also with $d_b = 20$ Å and in Hallbar-geometry) have been carried out to present the suppression of integer filling factor ν=4 (Figure 6.7) and temperature dependence of the new fractional state with filling factor ν=10/3 (Figure 6.8). Note that the mobility in Hallbar-geometry is slightly lower which has the consequence that the minimum at

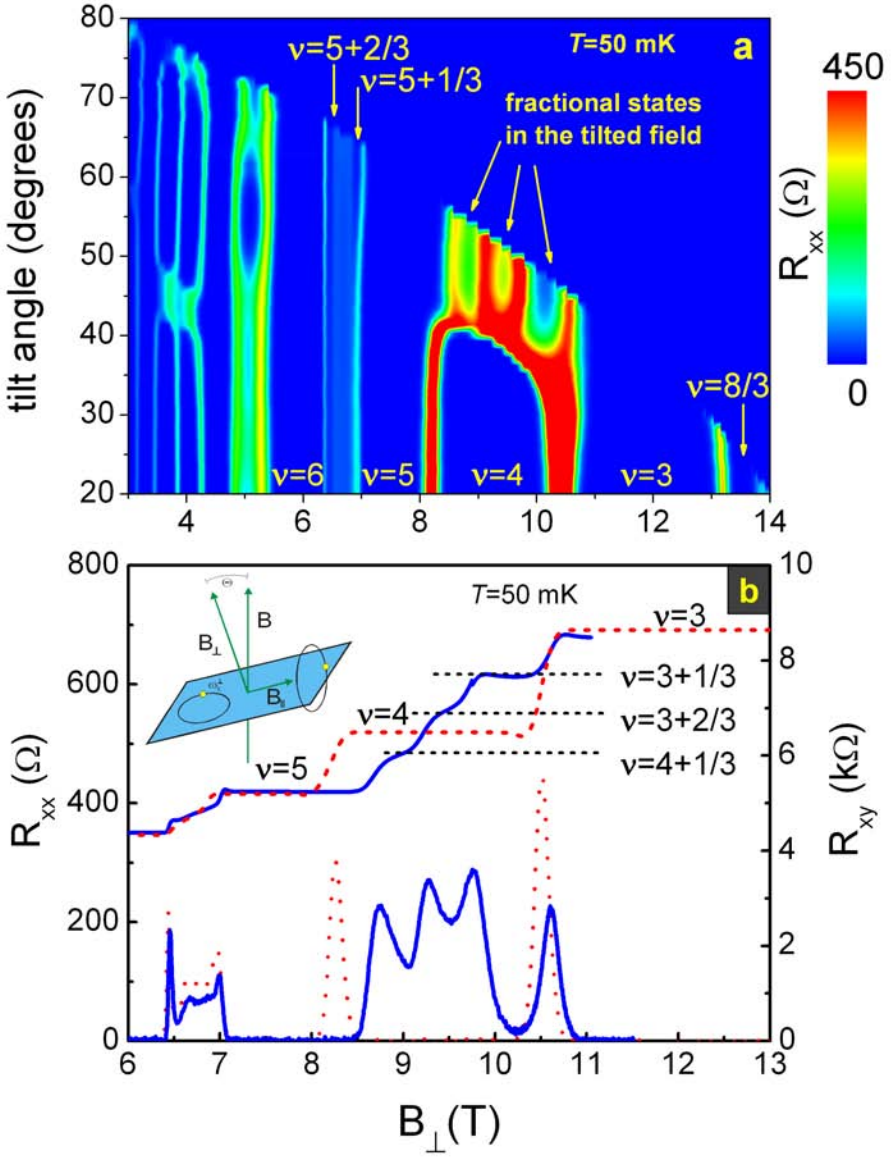

Figure 6.6: (a) Longitudinal resistance in the tilt angle-magnetic field plane for a trilayer electron system with a barrier thickness of d_b=2.0 nm. With increasing tilt angle ν=4 is suppressed an three new minima with denominator three are developed. (b) R_{xx} and R_{xy} as functions of the perpendicular magnetic field for $\Theta = 0°$ (red dashed, dotted) and $\Theta = 49°$ (blue) at T=50 mK. Inset: Schematic presentation of the sample rotation in the magnetic field.

ν=10/3 is not as profound as in Figure 6.6(b) for $\Theta = 49°$. First Figure 6.7(a) presents longitudinal resistance from $\Theta = 37°$ to $\Theta = 47°$ with $\Delta\Theta = 0.5°$. With increasing tilt angle, the wide minimum corresponding to ν=4 starts to narrow and the resistance maximum "separating" filling factors ν=4 and ν=3, develops into a new minimum which is later attributed to ν=10/3. This minimum becomes deeper with increasing tilt angle

but is not fully developed ($R_{xx}|_{\nu=4} \neq 0$) for this wafer. Starting from $\Theta = 45°$, this minimum remains unchanged up to $\Theta = 47°$ and is accompanied by a plateau in R_{xy}, see Figure 6.7(b). Note also that in Figure 6.7(b) the gap for ν=7 is suppressed due to Aharonov-Bohm effect. Figure 6.7(c) presents the complete suppression for ν=4. For $\Theta = 43.5°$, minimum is still visible as well as its corresponding plateau but if the tilt angle is increased by $\Theta = 0.5°$ to $\Theta = 44°$, $R_{xx}|_{\nu=4} \neq 0$. The plateau for $R_{xy} = h/4e^2$ vanishes at $\Theta = 45°$. Finally for $\Theta = 45.5°$, three new minima appear which are attributed to ν=10/3, ν=11/3 and ν=13/3 accompanied by plateaus in Hall resistance. Note, that the plateau at $R_{xy} = 3h/11e^2$ is not completely "flat". The next step is now to measure the

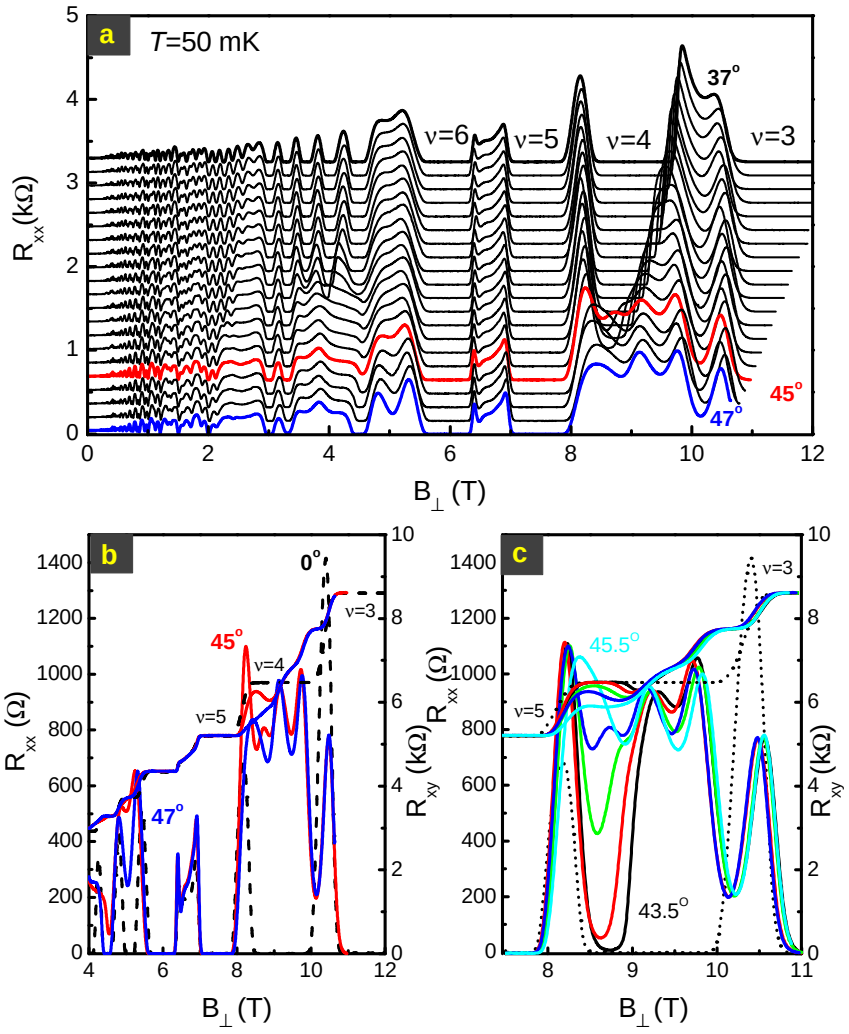

Figure 6.7: Evolution of new correlated states after collapse of ν=4. (a) Range from $\Theta = 37°$ to $\Theta = 47°$ where new states are developed for $\Theta = 45°$. (b) $\Theta = 0°$ (dashed), $\Theta = 45°$ and $\Theta = 47°$. (c) Zoom into (a) for the "transition" from integer filling factor ν=4 [at $\Theta = 0°$ (dotted)] to three new FQH-states with denominator three.

excitation gap of new FQH-states. Whereas the states ν=13/3 and ν=11/3 do not reveal

profound minima, the state ν=10/3 demonstrates strong temperature dependence and can hence be used to extract its excitation gap. In Figure 6.8(a), two measurements of longitudinal resistance at $\Theta = 45.5°$ for T=1.2 K and T=50 mK are presented. Figure 6.8(b) illustrates temperature dependence of longitudinal resistance as a function of perpendicular magnetic field from T=1.2 K to T=50 mK and the excitation gap for the new FQH-state at filling factor ν=10/3 is extracted to Δ=230 mK [Figure 6.8(c)]. Further evolution of the new states which replace integer QHE at filling factor ν=4 has

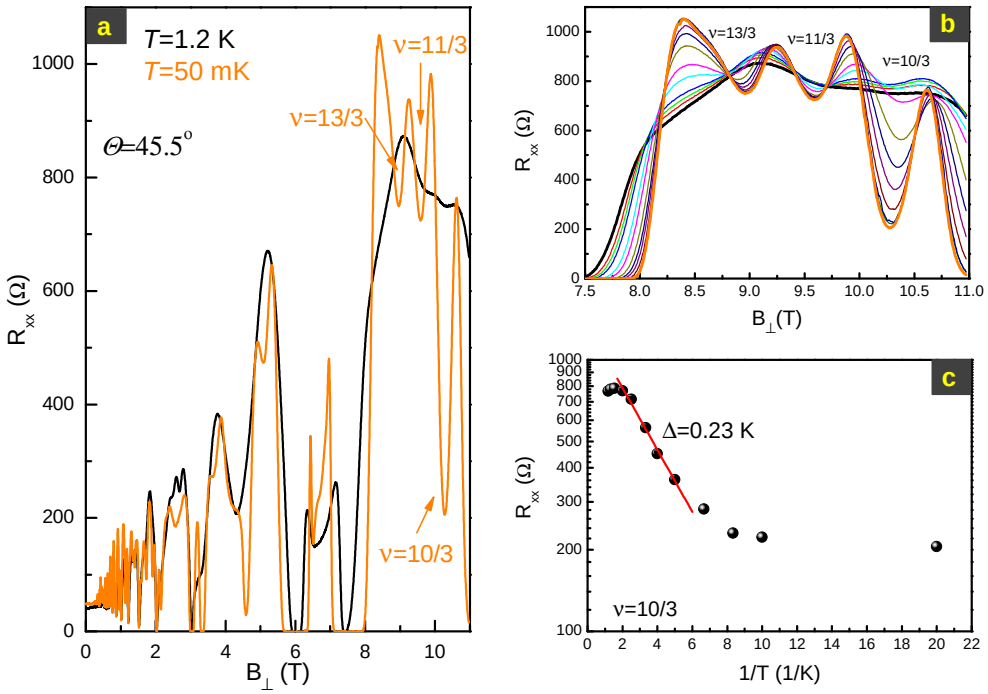

Figure 6.8: (a) Longitudinal resistance as a function of perpendicular magnetic field at $\Theta = 45.5°$ for 1.2 K (black) and 50 mK (orange). (b) Temperature dependence and development of new correlated states from 1.2 K to 50 mK. (c) Extraction of the gap for ν=10/3 to Δ=0.23 K.

to be studied in higher magnetic fields, shown in Figure 6.9. Longitudinal resistance as a function of perpendicular magnetic field from $\Theta = 32°$ to $\Theta = 66°$ has been measured for a sample in van der Pauw geometry. The temperature is 100 mK for all curves except the ones marked with an asterisk[5]. For $\Theta = 32°$, we observe integer QH-effect at ν=4. This state is suppressed for $\Theta = 42°$ and a new state with filling factor ν=10/3 appears. For $\Theta > 42°$, all new states are developed. A further increase in parallel magnetic field does not change longitudinal resistance up to an angle of $\Theta = 55°$. As it concerns

[5]These two traces correspond to the first trace at the beginning of a run in our resistive magnet. Due to heating during sweeps of magnetic field, the first trace each day has a lower temperature (∼50 mK) and all other sweeps have a constant temperature of T=100 mK.

other integer filling factors, ν=5, 6 and 8 remain unchanged whereas ν=7 exhibits the reentrance due to the Aharonov-Bohm effect with increasing parallel magnetic field. The wide region with R_{xx}=0 for filling factor ν=3, which corresponds to the Zeeman gap, becomes smaller with increasing tilt angle.

The evolution for all new states can be summarized as follows. For $\Theta = 57.5°$, the minimum attributed to ν=11/3 is less pronounced than for smaller angles and vanishes for $\Theta = 63°$ whereas the minimum at filling factor ν=13/3 still exhibits a kind of "shoulder" for $\Theta = 66°$, slightly shifted to a higher perpendicular magnetic field. The most profound state ν=10/3 seems to vanish for $\Theta > 60.5°$, but in fact, the minimum is combined with the minimum corresponding to integer filling factor ν=3. The angle $\Theta = 66°$ is the limit for our measurements where longitudinal resistance can be completely resolved.

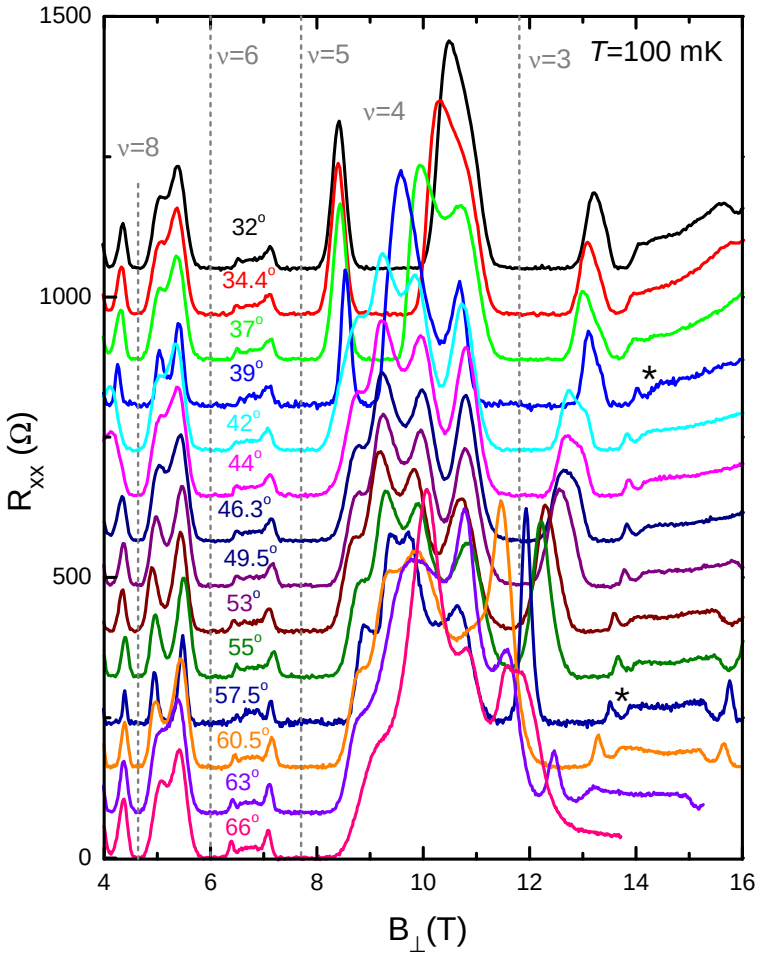

Figure 6.9: Vanishing of ν=4 and development of three new correlated states from $\Theta = 32°$ to $\Theta = 66°$. All measurements have been carried out at T=100 mK, except the ones marked with an asterisk, see text.

6.3.3 Reentrance effect of FQH states

This section discusses now magnetotransport in tilted magnetic fields for low filling factors (ν <4). New FQH states occur on the high-field side with respect to filling factor ν=5/2 and the state ν=7/3 exhibits reentrance.

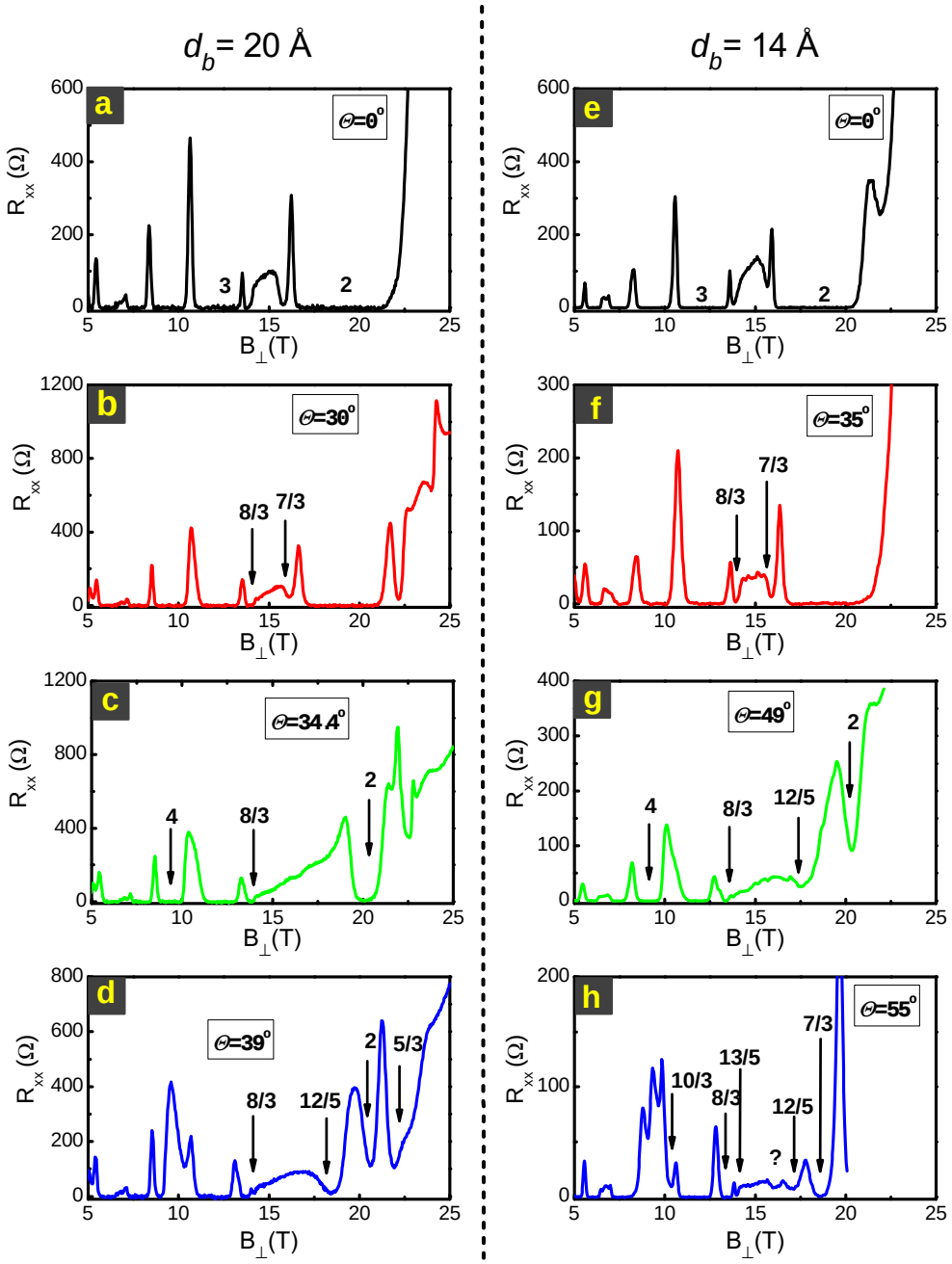

Figure 6.10: Longitudinal resistance as a function of the perpendicular magnetic field for two TQWs with d_b=2.0 nm (a,b,c,d) and d_b=1.4 nm (e,f,g,h) for different chosen tilt angles at T=100 mK. Several integer and fractional QH-states are labeled or marked with an arrow.

In Figure 6.10 a complete overview of longitudinal resistance as a function of perpendicular magnetic field is presented for two samples with d_b=2.0 nm (a,b,c,d) and d_b=1.4 nm (e,f,g,h) for different chosen tilt angles. First, one can observe again the collapse of integer minimum at ν=4 but in addition also the collapse of integer minimum at ν=2 with increasing in-plane magnetic field. Notice however, that the collapse of ν=4 and ν=2 appears for higher tilt angles in the TQW with a smaller barrier width. The fractional state $\nu = 7/3$ also collapses, see Figure 6.10(h) (but reappears at higher tilt angles), while the state $\nu = 8/3$ remains robust and is even improved for higher tilt angles. A further increase in Θ leads to other developed fractional states on the low-field and on the high-field side with respect to filling factor $\nu = 5/2$. Minima in longitudinal resistance which can be ascribed to $\nu = 12/5$ and $\nu = 13/5$ are also observed. Some additional minima appear for $\Theta \geq 30°$, see Figure 6.10(b,c) but they collapse with increasing tilt angles. We comment later on these states. Note that we also observe an additional feature in Figure 6.10(h) for $\Theta = 55.0°$ at $B_\perp = 16.1$ T which might be attributed to a higher odd-denominator FQH state.

The observation around filling factor $\nu = 5/2$ with new states and reentrance effect of $\nu = 7/3$ is now presented in detail for a sample with d_b=1.4 nm. In Figure 6.11 Hall resistance in (a,b) and longitudinal resistance (c,d) as functions of the perpendicular magnetic field are illustrated for several tilt angles Θ. We see a competition between the FQH states corresponding to $\nu = 7/3$ and $\nu = 12/5$ with increasing in-plane magnetic field. As Θ increases, the plateau at $R_{xy} = 3h/7e^2$ disappears for $\Theta > 32°$ and the plateau at $R_{xy} = 5h/12e^2$ emerges. The collapse of the plateau at $R_{xy} = 3h/7e^2$ correlates with the suppression of the integer plateau at $\nu = 2$ which is absent for $\Theta = 37°$. With increasing tilt angle, the plateau at $R_{xy} = 5h/12e^2$ develops very wide and its center is considerably shifted away from the corresponding fractional filling factor ν=12/5 towards higher $B_\perp$. The plateau at $R_{xy} = 5h/12e^2$ is best developed at $\Theta = 49.5°$, see Figure 6.11(b), but the minimum does not exhibit R_{xx}=0 [Figure 6.11(d)]. For $\Theta > 49.5°$ the plateau at $R_{xy} = 3h/7e^2$ reenters and becomes wide accompanied by vanishing longitudinal resistance, while the plateau at $R_{xy} = 5h/12e^2$ narrows. Both plateaus coexist for $\Theta > 49.5°$. This grouping is also observed for the low-field side, symmetric with respect to filling factor $\nu = 5/2$ for plateaus at $\nu = 8/3$ and $\nu = 13/5$. Both plateaus are continuously improved by the in-plane magnetic field. In the inset of Figure 6.11(b), a small plateau on the low-field side of filling factor $\nu = 12/5$ might be attributed to $R_{xy} = 7h/17e^2$ for $\Theta = 46.3°$.

The suppression of the plateaus at $R_{xy} = 3h/7e^2$ and $R_{xy} = h/2e^2$ as well as the emergence of $R_{xy} = 5h/12e^2$ is now discussed. In the presence of tunnel coupling, the gaps between subbands always exist. When the sample is now tilted, both effects of perpendicular and parallel magnetic fields have to be taken into account. An increase in the perpendicular magnetic field leads to a consecutive depopulation of subbands. Consequently, Hall resistance in the interval between filling factors $\nu = 3$ and $\nu = 2$ shows plateaus corresponding to fractional filling of the upper (third) subband at

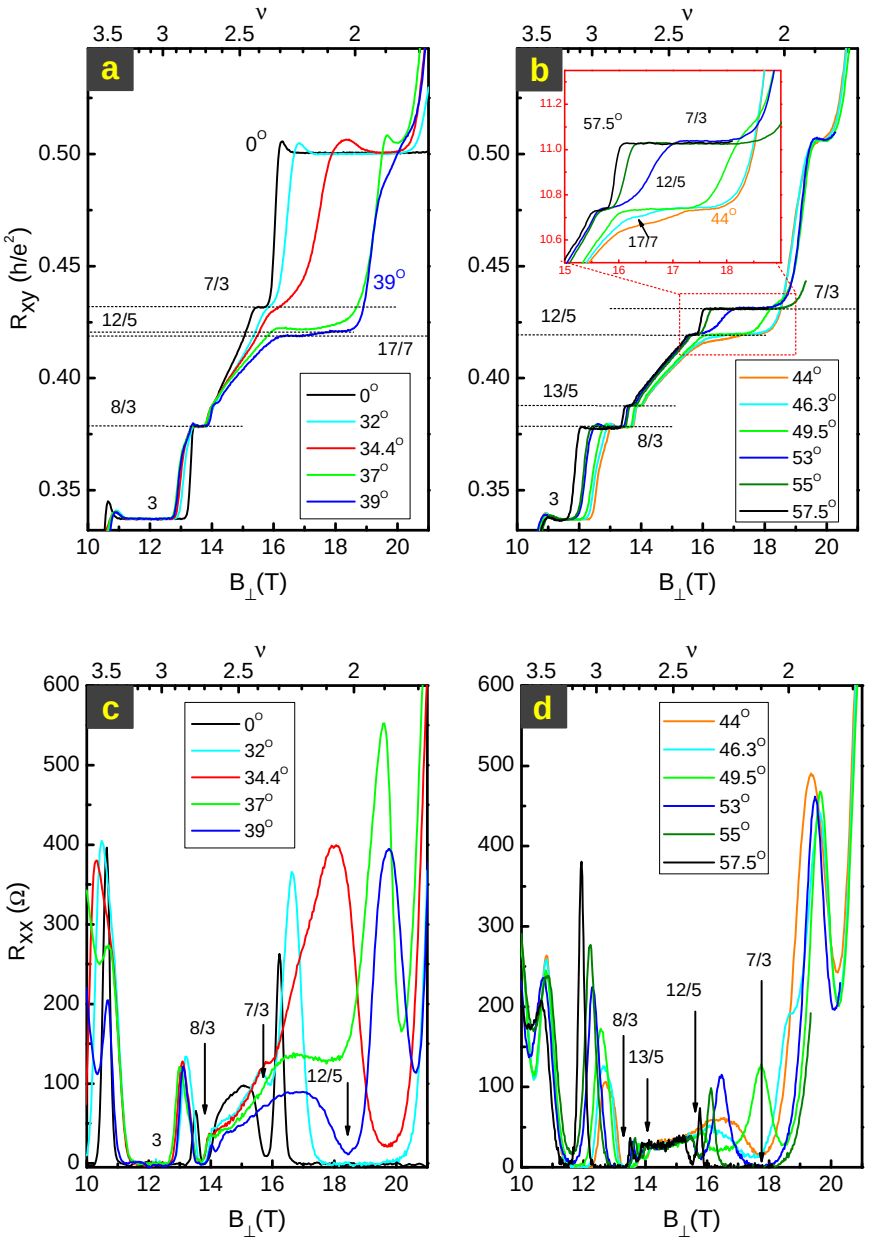

Figure 6.11: Hall resistance (a,b) and longitudinal resistance (c,d) present (i) reentrance of ν=7/3 and (ii) an emergent state at ν=12/5 at T=100 mK. For $\Theta > 34.4°$, the plateau at $R_{xy} = 3h/7e^2$ disappears and is replaced by $R_{xy} = 5h/12e^2$. Then for $\Theta = 53°$, the plateau at $R_{xy} = 3h/7e^2$ reappears and becomes very wide while the width of plateau $R_{xy} = 5h/12e^2$ decreases. A new plateau at $R_{xy} = 5h/13e^2$ also appears for $\Theta > 39°$. All plateaus are accompanied by minima in longitudinal resistance.

partial filling factors $\nu_3 = 2/3$ and $\nu_3 = 1/3$. If tunnel coupling is now cut off by the in-plane magnetic field ($E_1 = E_2 = \varepsilon_s$ and $E_3 = \varepsilon_c$), depopulation of the upper subband with increasing $B_\perp$ is accompanied, according to electrostatics, with a decrease of the separation ($\varepsilon_c - \varepsilon_s$) between the upper subband and lower subbands. This gap

decreases proportional to $-B_\perp$ until the subbands start to overlap. Then, both the partial filling of the upper subband ν_3 and the subband separation decrease much slowly with increasing $B_\perp$ since they are accompanied by the depopulation of lower subbands. Based on the estimations which have been carried out [Raichev09], the overlap regime becomes essential for ν <5/2. Therefore, the state at ν =8/3 and the emergent state at ν=13/5 are not affected. On the other hand, the depletion of the upper subband ν_3=1/3 corresponds to a strong overlap, while the depletion of ν_3=2/5 is characterized by a weak overlap of the subbands. Thus, the plateau $R_{xy} = 3h/7e^2$ is suppressed and replaced by $R_{xy} = 5h/12e^2$. The latter can still be explained as conventional FQH effect associated with a filling of the upper subband at ν_3=2/5. Since the partial filling of the upper subband slowly changes with $B_\perp$, this plateau becomes wide.
The observation around filling factor ν=5/2 cannot be fully explained. The origin of the reentrance for the FQH-effect at ν=7/3 with increasing parallel magnetic field differs from that in a single 2D layer, where the reentrance of FQH states is explained in terms of energy level crossing for composite fermions with spin [Du95]. Such a crossing cannot

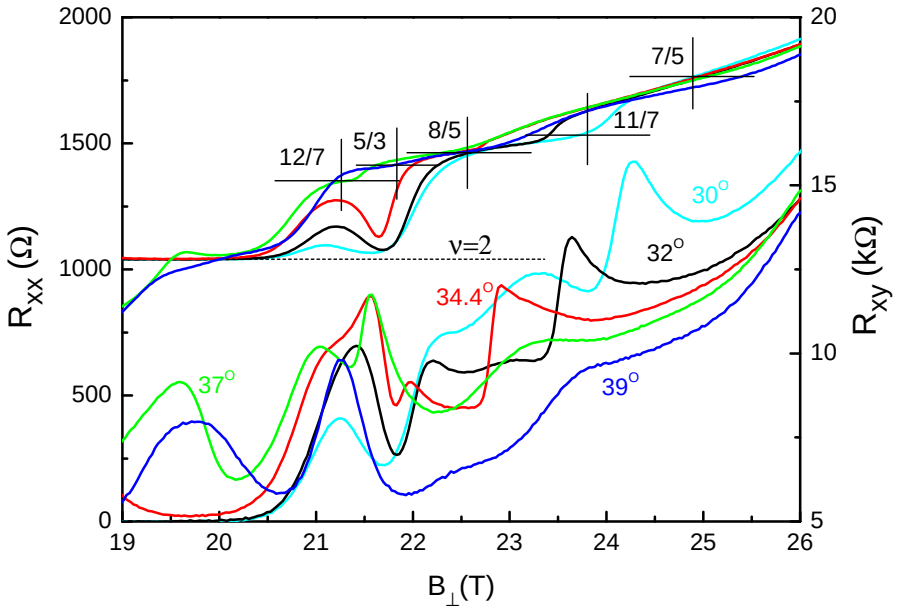

Figure 6.12: Longitudinal resistance as a function of perpendicular magnetic field reveals FQH-states between ν=1 and ν=2 which appear and vanish with increasing tilt angle from $\Theta = 30°$ to $\Theta = 39°$ (T=100 mK). Some minima are accompanied by plateaus or indicators of plateaus.

occur for the FQH states with lowest-order denominator three. Furthermore, a similar reentrance effect on the low-field side with respect to even-denominator filling ν >5/2 has not been observed. The suppression and disappearance of the plateau at ν=7/3 can be explained in terms of the influence of interlayer charge transfer on the conventional

FQH state in the upper subband. The emergence of the plateau at the same filling factor under the condition of *three partially occupied subbands* most probably signifies a new correlated state. Since this emergent plateau is sensitive to the in-plane field, we assume that interlayer correlations are essential. We also do not exclude a possibility that interaction effects in TQWs can lead to inhomogeneous correlated states which are similar to those discussed for bilayer quantum Hall systems [Cote02, Demler02, Wang03]. Finally, FQH-states which are observed in the region for ν <2 with increasing tilt angle are briefly mentioned and illustrated in Figure 6.12 for angles from $\Theta = 30°$ to $\Theta = 39°$. FQH-states can be attributed to ν=12/7, 8/5, 11/7 and 7/5. Note, that we observe neither fully developed minima in R_{xx} nor (flat) quantized plateaus in R_{xy} owing to a high temperature of 100 mK. The minima in R_{xy} which appear for $\Theta = 32°$ and $\Theta = 34.4°$ at $B_\perp \simeq$21.8 T might have the same origin as in Ref. [Eisenstein02] due to new insulating phases of two-dimensional electrons which are manifested as reentrant integer quantized Hall effects. In our case, we observe the reentrance of ν=2. The small shoulder at $B_\perp \simeq$21.8 T in longitudinal resistance might also be attributed to fractional filling factor ν=5/3 but there is no clear indication of a plateau in R_{xy}.

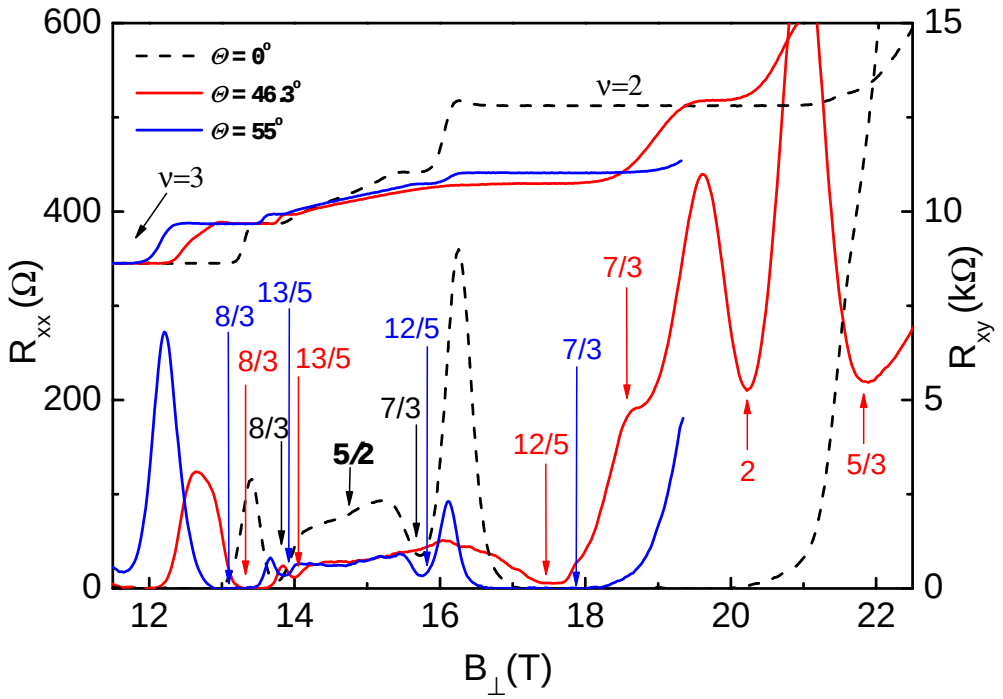

Figure 6.13: Overview for increasing tilt angle: longitudinal and Hall resistances for $\Theta = 0°$ (dashed), $\Theta = 46.3°$ and $\Theta = 55°$ present reentrance of the FQH state ν=7/3 and the appearance of the emergent FQH state ν=12/5.

In order to illustrate and summarize the behavior of FQH states around the even-denominator state ν=5/2, Figure 6.13 gives an overview for three chosen tilt angles $\Theta = 0°$ (dashed), $\Theta = 46.3°$ and $\Theta = 55°$. As discussed before, the states ν=7/3 and

ν=12/5 show unusually wide plateaus in Hall resistance and demonstrate reentrant and non-monotonic behavior with increasing in-plane field, respectively.

6.4 Outlook towards multilayer electron systems

In the previous section experimental results based on trilayer electron systems have revealed new correlated states when a parallel magnetic field suppresses tunneling between layers. Both wafers which have been studied have fixed well widths and differ only in the barrier width, and the results are qualitatively the same. Only the vanishing integer state ν=4 and the developing new fractional states ν=10/3, ν=11/3 and ν=13/3 appear for a slightly higher parallel magnetic field at $\Theta \simeq 50°$. The next step forward is now to vary either the well or the barrier widths or both at the same time. It is also desirable to decrease or even suppress the tunneling by an AlAs barrier. If the tunneling is completely suppressed, new FQH-states must be ascribed to many-body effects. Such studies are currently in progress.

Recently two theoreticians, Levin and Fisher, have suggested that fractional quantum Hall states can be much more three dimensional than the current understanding allows [Levin09]. They propose phases in which quasi-particles can move in three dimensions. This approach opens the possibility of constructing a completely new class of three-dimensional states for electrons in strong magnetic fields. The idea is also discussed by Burnell and Sondhi in Ref. [Burnell09]. These states are different from 3D multilayer Laughlin states [Laughlin83, Halperin83] and do not suffer from the limitation of a fixed number of electrons in each layer. The restriction of Laughlin states could be problematic for the description of certain multilayer systems, especially those with appreciable interlayer tunneling. The aim of Ref. [Levin09] is to find *candidate* ground states for the intermediate tunneling regime. Levin and Fisher suggest a ground state by spinless (or spin polarized) electrons with an average filling of ν=1/3 per layer and construct their candidate state using a "slave-particle" gauge theory approach known as the "parton construction". In the 3D limit, this candidate state exhibits unusual

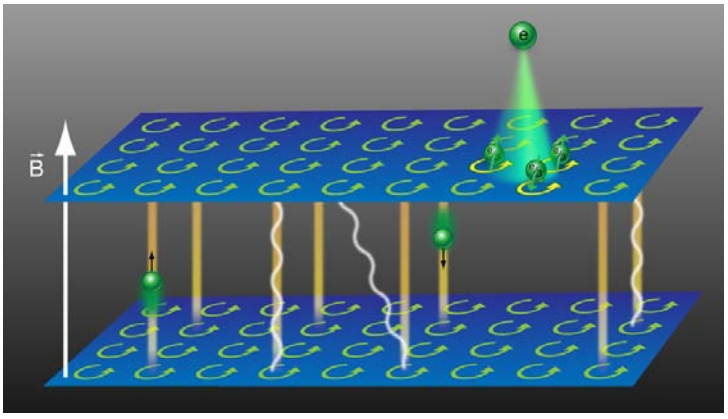

Figure 6.14: Parton construction where electrons are visualized as composed of partons, each with a charge of $e/3$: partons form cyclotron orbits whose number is a third of the electrons themselves. Three-dimensionality is introduced if partons hop between layers under certain conditions. Figure taken from Ref. [Burnell09].

physics since it supports two types of excitations. First, gapped charge $e/3$ fermionic quasiparticle excitations and second, gapless electrically neutral collective modes.
The parton construction is presented in Figure 6.14. In each layer, electrons are visualized as composed of partons living in cyclotron orbits, whose number is one third of the cyclotron orbits of the electrons themselves. When partons are confined to their layers, the state is described by multiple non-interacting copies of the 2D 1/3-filled quantum Hall state. Without confinement, the resulting states are different from both tunneling-dominated and correlation-dominated states. This fundamentally new approach is now open for theoretical and experimental work.

Summary

This chapter has discussed new correlated states which occur in electron systems which differ from a single-layer system. Owing to an extra degree of freedom, bilayer, trilayer and multilayer electron systems exhibit fractional QH-states which cannot be observed in conventional single-layer systems. In the introduction to bilayer systems, it has been shown that both the ratio of interlayer separation to magnetic length and the strength of the tunnel coupling play a crucial role. A parallel magnetic field has also a strong influence on magnetotransport which leads to a suppression of the tunneling gaps and localizes electrons in single layers. Therefore the occurrence of new states is a many-body phenomenon due to electron-electron interaction.
This thesis presented the first experimental studies in high-density trilayer electron systems realized in TQWs. In a tilted magnetic field, new states at ν=10/3, 11/3, and 13/3 have been found which replace integer filling factor ν=4. The observation of the collapse of $\nu = 4$ and $\nu = 2$, and the emergence of additional states at fractional filling factors in tilted magnetic fields for trilayer systems have been demonstrated. These states are developed with increasing in-plane magnetic field which suppresses tunneling, and some of them appear owing to many-body correlations in such multilayer systems. The states $\nu = 7/3$ and $\nu = 12/5$ show unusually wide plateaus in Hall resistance and demonstrate reentrant or non-monotonic behavior with increasing in-plane field.
Finally an outlook to further studies in trilayer electron systems has been given and a recent theoretical model using the *parton construction* is mentioned. More theoretical and experimental work in trilayer and multilayer electron systems is desirable, also in order to fully understand the origin of the results presented in this thesis.

Conclusion and outlook

This thesis has presented the first experimental and theoretical transport studies in multilayer electron systems subjected to a magnetic field and exposed to a continuous microwave (MW) irradiation. Owing to two or more occupied two-dimensional (2D) subbands, we observe in magnetoresistance intersubband oscillations which are a sign of coupling between the different layers. This peculiar oscillation picture is strongly modified if the sample is exposed to microwave irradiation. We explained experimental results by a generalization of the theory based on photoresistance mechanisms to multilayer electron systems and have found that for low temperature, the inelastic mechanism plays the dominant role [Wiedmann08, Wiedmann09b]. In particular, the inelastic mechanism also reveals that the conditions for absolute negative resistivity correlate with the appearance of zero-resistance states (ZRS) which have been found for the first time in a low-dimensional system (bilayer electron system) different from a conventional single-layer system [Wiedmann10b].
In addition, we have performed transport studies up to the highest magnetic field of 34 T in the Laboratoire National des Champs Magnétiques Intenses (LNCMI). Within these experiments at lowest possible temperature ($T < 100$ mK), we have shown new fractional quantum Hall states in trilayer electron systems which occur in the presence of a parallel component of the magnetic field and might be ascribed to new correlated states [Gusev09].

In order to confirm the response of a 2D electron system exposed to microwave excitation [Zudov01a], we have first investigated single-layer electron systems, where the motion of electrons is confined to one single layer. Experiments could reproduce the well-known microwave-induced resistance oscillations (MIROs) in samples with high electron density. Due to the low quality of the samples compared to the experimental work of other research groups [Mani02, Zudov03], we were not able to observe ZRS. However, and under particular conditions, i.e. high MW power and high temperature, we have found fractional MIROs with highest denominator so far observed [Wiedmann09a]. By applying two competing theoretical models [Dmitriev07b, Pechenezhskii07] we were able to explain the appearance of fractional MIROs up to ϵ=1/4 with the model of stepwise single-photon absorption [Pechenezhskii07]. Both models fail to give a complete explanation for the observed high-denominator features and further experimental and theoretical work is highly desirable.

The first step towards multilayer electron systems is to study bilayer electron systems formed by either double quantum wells or wide quantum wells. We have shown that

magneto-intersubband (MIS) oscillations occur in both types of bilayer electron systems. Double quantum wells exposed to microwave irradiation exhibit a peculiar oscillation picture which is strongly correlated with microwave frequency. We have interpreted this oscillation picture as an interference of the MIS oscillations with MIROs. We have demonstrated that the quantum component of magnetoresistance, which is directly affected by the microwaves, is "visualized" in bilayer (multilayer) systems by the enhancement, damping or inversion of MIS oscillation amplitude [Wiedmann08]. The changes in amplitude caused by a variation of temperature or microwave intensity are visible in the behavior of single or groups of MIS oscillations. We have successfully explained our experimental results within the inelastic mechanism of photoresistance as a result of the microwave-induced change of the isotropic part of the electron distribution function for low temperatures [Dorozhkin03, Dmitriev05].
Owing to the visualization of photoresistance in the change of MIS oscillation, we have an advantage in data analysis compared to single-layer systems since MIS oscillation period is typically smaller than the period of the MIROs. Temperature dependent magnetoresistance exposed to a constant microwave electric field and frequency has demonstrated that the inelastic mechanism alone fails to explain photoresistance for T >4 K. For higher temperatures, we have shown that microwave-induced resistance can even not be fully attributed to a sum of inelastic and discplacement mechanism [Ryzhii70, Durst03], i.e. a previously unaccounted microscopic mechanism, not yet considered and discussed in theory, might be responsible for this deviation [Wiedmann10a].
In addition, high microwave power and temperature have revealed the interference of MIS oscillations and fractional MIROs.

In a high-quality bilayer electron system formed by wide quantum wells, we have discovered the first evidence for zero-resistance states in a 2D bilayer electron system exposed to microwave irradiation. The crucial difference compared to single-layer system is that inverted MIS oscillations evolve into ZRS. We have performed experiments for different microwave frequency, electric field strength and temperature. The manifestation of ZRS in bilayer systems is distinct from the case of single-layer systems, due to a peculiar magnetotransport picture of a two-subband system, where quantum magnetoresistance is modulated by MIS oscillations. Since the vanishing resistance develops for inverted MIS peaks, the ZRS intervals are narrow, and these states are very sensitive to microwave frequency. In our samples, we have identified four different MIS oscillations which evolve into zero-resistance states.
The observed zero-resistance can be described as a consequence of current instability under absolute negative resistivity. We have demonstrated in calculations based on theoretically proposed microscopic photoresistance mechanisms, namely inelastic and displacement mechanism, that the conditions of absolute negative resistivity correlate with the appearance of ZRS. The dominant contribution for our experimental conditions is the inelastic mechanism of photoresistance [Wiedmann10b]. By demonstrating experimentally that the phenomenon of zero-resistance states is not limited to single-layer 2D

electron systems, and, theoretically, that the presence of intersubband scattering in bilayers is not an obstacle for the negative resistivity, we can suggest that similar physical mechanisms might lead to ZRS in multilayer or quasi-3D electron systems.

The successful description of magnetoresistance and microwave-induced resistance for bilayer systems has been extended to the case of multilayers. We have developed a theory for multiple subbands which can be applied for magnetotransport studies. In addition and based on the inelastic mechanism of microwave photoresistance, we can fully analyze magnetoresistance exposed to microwave irradiation changing parameters like microwave frequency, power and temperature. Within this context, we have tested our model on trilayer electron systems and found an excellent agreement between experiment and theory. Low-field magnetotransport in three-subband systems both with and without microwave excitation is a useful step towards understanding the influence of energy spectrum and scattering mechanisms on the transport properties of low-dimensional electrons [Wiedmann09b].

In this thesis, we have successfully explained MIROs in bi- and multilayer electron systems based on bulk properties of 2D electron systems [Wiedmann08, Wiedmann09b, Wiedmann10a]. In addition, we have demonstrated the applicability of microscopic bulk mechanisms for the occurrence of ZRS [Wiedmann10b].
Concerning the nature of a near-contact oscillating contribution, we point out that this contribution should be first understood theoretically, and further experimental investigations have to be carried out. The absence of clear knowledge of what happens near the contacts under microwave irradiation does not enable us to give detailed information about this phenomenon.

Furthermore, we have investigated magnetotransport in trilayer electron systems subjected to high magnetic fields up to 34 T. In order to find new correlated states, we have suppressed tunneling of electrons between the layers by applying a parallel magnetic field [Gusev09], as it has been done in previous studies by other groups in bilayer systems. In experiments, we have observed that integer quantum Hall effect at filling factor ν=4 is replaced by three new fractional quantum Hall states with denominator three. As a consequence of confined electrons in each layer, the origin of these new states might appear due to correlation of electrons with nearby neighbors. In addition we have found and discussed emergence and reentrance of new states with respect to charge transfer from the central to the side wells due to electrostatics. While convincing results have been obtained for both trilayer electron systems, several questions can not be fully answered yet. More theoretical and experimental work is desirable in order to understand the origin of these emergence and reentrance phenomena.

Having investigated extensively transport phenomena in such multilayer electron systems in magnetic fields and under microwave excitation, this work can serve as a starting point for future investigations.

Outlook

As far as fundamental experiments are concerned, the next consequent step is to study the reponse of bi- and multilayer electron systems subjected to microwaves and to a strong dc electric field. Such kind of studies have been carried out in single-layer systems [Hatke08, Khodas08, Lei08]. Based on this work where we have demonstrated the interference of MIS oscillations with MIROs, and on a recent experimental and theoretical work which explains the response of a bilayer electron system to high dc fields [Mamani09b], such studies are straightforward.
With a continuous improvement of sample quality, we assume that it is possible to observe ZRS formed by double quantum wells. Generally, the possibility should not be excluded that two or more inverted MIS oscillations in bilayer electron systems might evolve into ZRS for samples with higher mobility.

The microwave-induced change in Hall resistance has been mentioned throughout this work, but a systematic study has not been carried out and is beyond the scope of this thesis. The prediction of the violation of Onsager relations based on microscopic mechanisms of photoresistance has not yet been proved experimentally until now, even not in single-layer systems [Dmitriev07a].

Another interesting subject is the fact that for ZRS induced by microwave irradiation, the sample spontanuously breaks into current domains [Andreev03]. Based on the current domain picture, the understanding of zero-resistance states requires a proof of the existence of such current domains. Thus, the knowledge of the current distribution in the sample which exhibits ZRS is the key to solve the question of the microscopic mechanism and the grouping of domains. An image of the current distribution is thought to be the most straightforward method to achieve information of current distribution. Such an image can be obtained by scanning Hall probe microscopy.

The reponse of a low-dimensional electron system to a high-frequency electromagnetic field can be used to identify and detect frequency and the strength of the applied electric field. Applications can be realized in frequency detectors and high-frequency devices since it has been shown in this work that multilayer electron systems are extremely sensitive to radiation frequency.

Precise ideas and an outlook for future experiments in trilayer and multilayer electron systems have been already presented in Chapter 6. The main intention beyond fundamental experimental studies and the proof of new theoretical models, is to control tunneling between layers by external gates. This manipulation by an external electric field can also be used to control spin polarization which is the fundamental aspect of spintronics. Thus, such effects may find application in various spintronic devices.

Appendix A

Investigated samples

This appendix presents the type of samples used in this thesis. Quantum wells (QWs), double quantum wells (DQWs) and triple quantum wells (TQWs) have one parameter in common: high carrier density. In order to increase conductivity $\sigma = 1/\rho = en_s\mu$ in a 2D system, see Eq. (1.20), one idea is to use short-period AlAs/GaAs superlattices [Friedland96]. This concept allows one to obtain samples with high mobility and high electron density.

Concept of superlattices

Modulation doped heterostructures, including GaAs/AlGaAs heterojunctions and GaAs quantum wells with high mobility are the objective of intensive research. The necessity of high quality samples has been extensively discussed in this thesis with respect to transport experiments and measurements of microwave-induced resistance oscillations and zero-resistance states. In conventional GaAs/AlGaAs heterostructures, the regions of charge transport and the doping regions are separated by an undoped AlGaAs layer, called spacer. If the spacer is increased, the scattering by the random potential becomes weaker and thus electron mobility at the interface increases. At the same time, however, electron density of free charge carriers in the 2DEG decreases. Decreasing the spacer thickness increases density and inevitably leads to a loss in electron mobility.
In order to suppress remote impurity scattering, the distance of dopants from the conducting channel has to be increased but this, already mentioned, reduces the electron density. Friedland *et al.* have developed a method for both the enhancement of carrier concentration and reduction of remote impurity scattering in GaAs single quantum wells. This concept significantly increases the conductivity. The barriers of the GaAs quantum well are formed by AlAs/GaAs short-period superlattices. In AlAs/GaAs short-period superlattices, the lowest conduction band state can be formed by the X-conduction band state of the AlAs layer (X-electrons) [Holtz90]. This new method reduces impurity scattering in a remotely doped GaAs single quantum well using heavy-mass X electrons in barriers to smooth the potential fluctuations of the ionized Si dopants.
The presence of superlattices implies the presence of X electrons located close to the dopant layer. X electrons have a rather high effective mass and therefore they screen the ionized impurities due to a high screening capability. The heavy mass also implies

a low mobility. It must be added that they are also strongly localized and do not contribute to the conductivity. Consecutive investigations in Ref. [Friedland96], e.g. the photoluminescence as well as self-consistent calculations confirm their existence in the AlAs/GaAs superlattice barriers.

The concept of Ref. [Friedland96] is applied to the samples which have been investigated in this thesis. All wafers have been grown by Askhat K. Bakarov in the Institute of Semiconductor Physics in Novosibirsk, Russia. In this thesis, we only present a sketch for a DQW structure in Figure A.1 where the different layers are visible. Both QWs, which are separated by a barrier of AlGaAs, are sandwiched by GaAs/AlAs superlattices. One can clearly identify the short-period AlAs/GaAs superlattice barriers which surround the two quantum wells. The structures under study were grown by molecular beam epitaxy (MBE) on (100) GaAs substrates. The red regions indicate doping with silicon (Si).

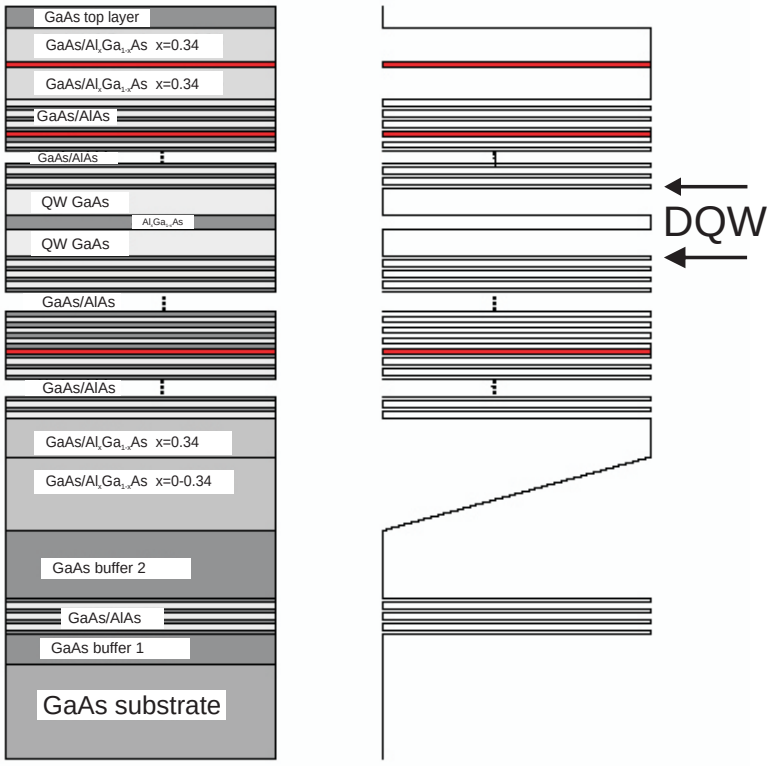

Figure A.1: Sketch of a high-density double quantum well system: high density and sufficiently high mobilites are obtained using AlAs/GaAs superlattices.

Sample geometry and list of samples

For transport experiments, two sample geometries have been used in this work, presented in Figure A.2. Samples in Hall-bar geometry consist of six contacts. For our samples, L/W=2.5. For high field measurements we also use samples in van-der Pauw geometry (square specimens) with four contacts. The chemical potential for each contact is denoted with μ_i.

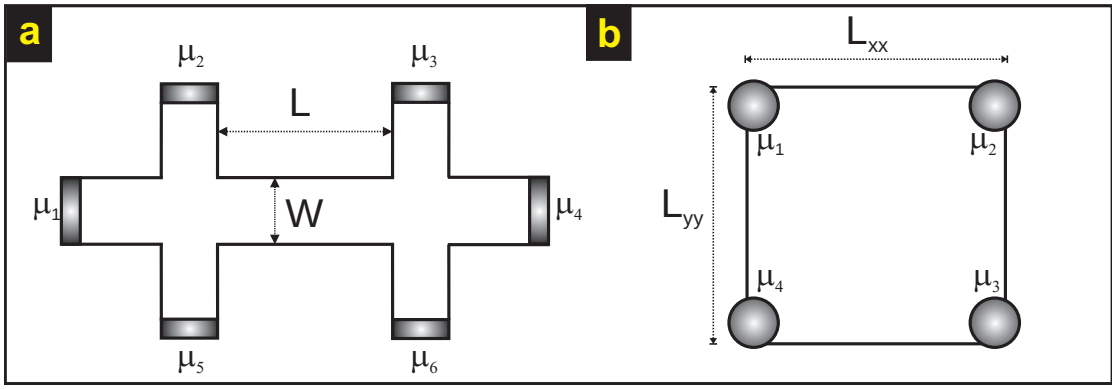

Figure A.2: Sketch of sample geometry used in this thesis: (a) Hall-bar with six contacts, (b) square specimens in van der Pauw geometry with four contacts. μ_i is the chemical potential for each contact.

Samples in van-der Pauw geometry are simply cut from a wafer whereas we have used special masks to define our Hall-bar geometry in photolitography.

All samples which have been studied during this thesis are summarized in the following tables. For each sample, well width(s) and barrier width(s) d_b for multilayer systems, electron density n_s and mobility μ are given. We start with single-layer systems in Table A.1, then bilayer electron systems in Table A.2 where also the type (either double quantum well or wide quantum well is indicated) and finish with trilayer electron systems in Table A.3. For TQWs, central well width is indicated with w_c and lateral well width with w_l. The last column in each table refers to the chapter where the samples have been used.

Type	well width (Å)	n (cm^{-2})	μ (cm^2/Vs)	Chapter
QW	140	$7.5 \cdot 10^{11}$	$1.2 \cdot 10^6$	1, 2
QW	140	$9.75 \cdot 10^{11}$	$1.6 \cdot 10^6$	2

Table A.1: Sample parameters and characterization for single-layer systems.

Type	well width (Å)	d_b (Å)	n (cm^{-2})	μ (cm^2/Vs)	Chapter
DQW	140	14	$9.32 \cdot 10^{11}$	$1.0 \cdot 10^6$	1, 3, 6
DQW	140	14	$12 \cdot 10^{11}$	$1.4 \cdot 10^6$	3
DQW	140	21	$9.8 \cdot 10^{11}$	$0.9 \cdot 10^6$	3
DQW	140	30	$9.2 \cdot 10^{11}$	$0.9 \cdot 10^6$	3
WQW	450	-	$9.1 \cdot 10^{11}$	$1.9 \cdot 10^6$	4

Table A.2: Sample parameters and characterization for bilayer systems.

Type	w_c (Å)	w_l (Å)	d_b (Å)	n (cm^{-2})	μ (cm^2/Vs)	Chapter
TQW	230	100	14	$9.0 \cdot 10^{11}$	$5.0 \cdot 10^5$	5, 6
TQW	230	100	20	$9.0 \cdot 10^{11}$	$4.0 \cdot 10^5$	5, 6

Table A.3: Sample parameters and characterization for trilayer systems.

Appendix B

Experimental methods and measurement techniques

This appendix describes the experimental technique which has been used to perform all investigations in this thesis. The first part briefly introduces fundamentals of cryogenic systems. The second and third part focus on measurement technique and the microwave setup.

B.1 Cryogenics

Within this thesis, three different types of cryostats with superconducting magnets have been constantly used: a ^{4}He-cryostat with a toploading variable temperature insert (VTI) which enables measurements between 1.4 K and 300 K up to 17 T, a ^{3}He cryostat (300 mK - 4.2 K) up to 15 T, and a dilution refrigerator (40 mK - 1.4 K) up to 17 T. All systems resemble each other by the fact that they possess the same architecture: a helium bath containing a superconducting bobbin surrounded by a bath of liquid nitrogen. For readers interested in "low-temperature physics" and technique, we recommend the book [Enss and Hunklinger]. All toploading systems possess a probe with rotation to measure in perpendicular and parallel magnetic fields.

The first cryostat is a ^{4}He bath cryostat with a toploading variable temperature insert (VTI). In principle one uses the properties of temperature and pressure of liquid ^{4}He. The sample which is located in a probe is cooled down by thermal conduction through the ^{4}He exchange gas. The flow of liquid ^{4}He from the main bath to the VTI is controlled by a needle valve. In order to decrease temperature, the vapour in the VTI is pumped and temperatures down to

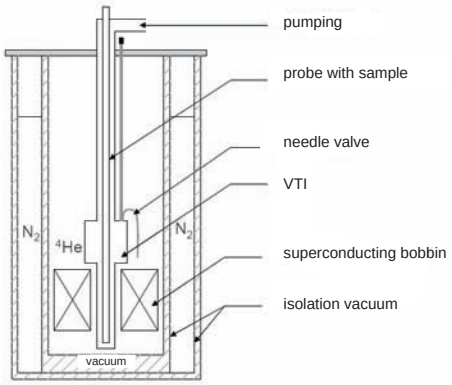

Figure B.1: Sketch of our VTI cryostat.

1.4 K are possible with our system.
Below 2.172 K, ^{4}He becomes superfluid and the effectiveness of pumping decreases rapidly. This is the reason why this system allows not to acquire very low temperatures. In Figure B.1, a sketch of a VTI presents the main parts. For higher temperature, one has to control the temperature by the gas flow and by a heater of type ITC4 (provided by Oxford Instruments). This VTI is also used for microwave measurements with specially fabricated probes.

For lower temperature, a ^{3}He cryostat has been employed, especially for temperature dependent magnetoresistance measurements in the range from 300 mK to 1.4 K. A ^{3}He-system has two advantages over ^{4}He. First, with modest pumping systems, high vapour pressure allows lower temperature (0.3 K). ^{3}He - a fermion - does not possess the problem created by the creeping superfluid film which induced a heat transfer from warm to cold parts of the system. The idea of a ^{3}He cryostat, see Figure B.2, is to condense ^{3}He gas by bringing it in contact with a pumped ^{4}He reservoir (1-K pot). The sample is placed in direct contact with the ^{3}He. Our ^{3}He evaporation system possesses an adsorption pump (cryopump). In this case, ^{3}He that is condensed in the ^{3}He pot (sample space in Figure B.2) and is adsorbed onto the cold surface of a sinter of charcoal powder. This cryopump is thermally anchored at the 1-K pot which provides the required temperatures. If the ^{3}He pot is empty and pumping is finished, the charcoal pump is pulled to a warmer region (in our system around 40 K). Upon warming, ^{3}He is desorbed from the powder and then condenses in the ^{3}He pot.

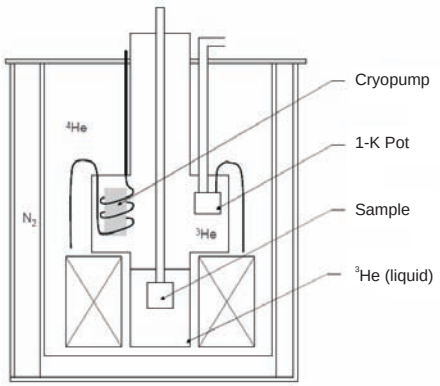

Figure B.2: Sketch of a ^{3}He cryostat.

For lower temperatures, a dilution refrigerator has been used. A dilution refrigerator is a cryogenic device, which uses a mixture of two helium isotopes: ^{3}He and ^{4}He. The principle of operation relies on the specific properties of dilute ^{3}He/^{4}He mixtures. The phase diagram of liquid helium is shown in Figure B.3(a).
For temperatures below the triple point (830 mK), ^{3}He/^{4}He mixture will separate because of their different densities into two vertical liquid phases, divided by a phase boundary. The upper phase is called the ^{3}He rich phase, because it contains mostly ^{3}He. The second phase is called the ^{4}He rich phase, because it is mostly superfluid ^{4}He. However, this phase will always be composed of at least 6.5% ^{3}He, no matter what temperature (even at absolute zero). Between both phases a thermodynamic equilibrium is prevailed. The ^{3}He atoms in the ^{3}He-rich phase have a lower entropy than ^{3}He atoms in

the ^{4}He-rich phase. The cooling process takes place in the mixing chamber, see Figure B.3(b), and consists of a transfer of ^{3}He atoms from the ^{3}He-rich phase into the dilute phase. This transfer can be referred to as an evaporation into the quasivacuum of the superfluid ^{4}He. The ^{3}He circuit at work of a dilution refrigerator is shown in Figure

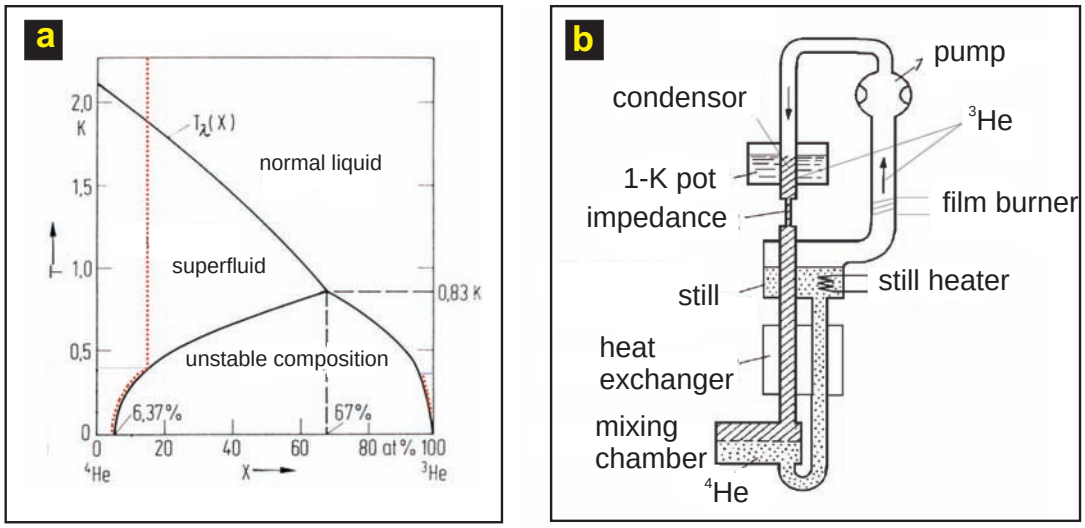

Figure B.3: (a) Phase diagram of helium. The red line indicates a concentration of 15%. (b) ^{3}He circuit at work in a dilution refrigerator.

B.3(b). It is necessary to realize a sufficiently high circulation of ^{3}He, while maintaining a low heat at the mixing chamber. After the gas is condensed in the condenser at 1.4 K (temperature of the 1-K pot), the liquid helium passes an impedance. If a ^{3}He atom from the concentrated upper phase now passes the phase boundary to the diluted lower phase, a quasi-evaporation is taking place. The energy which is necessary for this transition will be withdrawn from the environment as heat and therefore temperature in the mixing chamber decreases. The concentration difference of ^{3}He in both phases in the dilution refrigerator will be kept constant by continuously evacuating ^{3}He from the diluted phase (still heater) to ensure a constant temperature in the mixing chamber. The ^{3}He-^{4}He equilibrium of the mixture is assured through constantly recirculated ^{3}He atoms from the concentrated phase. The film burner avoids a thermal coupling of the still with warmer parts with ascending superfluid liquid helium. During the measurement the sample is in the mixing chamber fixed on the probe. Our system used during the thesis makes it possible to obtain temperatures between 40 mK and 1 K for samples directly placed in the mixing chamber.

B.2 Measurement technique

A transport measurement is actually a measurement of the voltage/resistance as a function of different parameters: magnetic field, temperature and samples exposed to microwave irradiation. The measurement of a small signal is always superimposed on noise. The noise of a measured signal is determined by the Signal-to-noise ratio (SNR). At low

temperatures it must be avoided that the applied current heats the system (2DEG), therefore the measured voltage should not exceed the thermal excitation $V < k_B T/e$. To improve the SNR, measurements with Lock-In detection, which is widely used in standard transport measurements, have been carried out. This idea is based on the modulation of the excitation current and a subsequent detection of the voltage drop at the modulation frequency ω (here we use a modulation frequency around 13 Hz). Lock-In amplifiers are also known as phase sensitive detectors. The alternative currents (AC), especially in the mK-range, are in the order of 10 nA to 1.0 μA. To improve the SNR further, low-noise preamplifiers have been used.

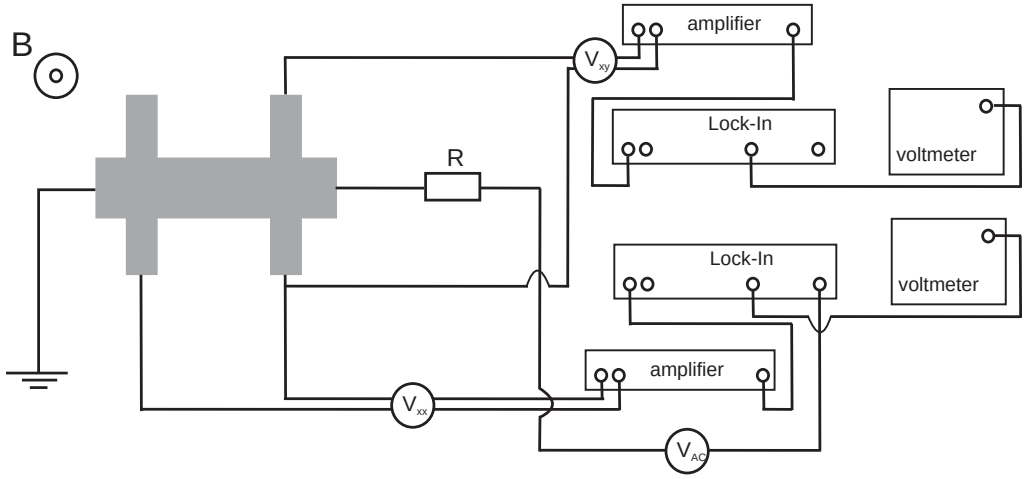

Figure B.4: Sketch of a typical transport measurement presented in this thesis.

In Figure B.4 we sketch the measurement scheme for all experiments in this thesis. The resistance R is chosen between 1 and 100 MΩ, and the excitation voltage is V_{AC}=1 V.

B.3 Microwave measurements

A general overview about microwave engineering can be found in Ref. [Pozar98].

Microwave generators

The term microwaves refers to alternating current signals with frequencies between 300 MHz and 300 GHz corresponding to a wavelength between $\lambda = c/f$ =1 m and 1 mm. The frequency range to our disposal and in this thesis is 32.7 to 170 GHz. The MW sources are backward wave oscillators and are also called carcinotron or backward wave tubes. In principle, this generator is a vacuum tube that is used to generate microwaves up to the THz range. Carcinotron generators belong to the travelling-wave tube family with a wide electronic tuning range.
The generators are G440XE Sweep Generators from `Elmika` equipped each with an attenuator in order to change the MW power from no attenuation (0 dB, highest MW power) to full attenuation (-75 dB, no MW power). The technical data of the generators

used during this thesis, their frequency range, power range and rectangular output are presented in Table B.1.

Generator	Frequency range (GHz)	Power range (mW)	Output area (mm^2)
G4406E	32.7-55	25-130	WR-22 (5.69 x 2.84)
G4404E	55-85	30-85	WR-15 (3.76 x 1.88)
G4403E	75-110	30-100	WR-10 (2.54 x 1.27)
G4402E	110-170	10-35	WR-6 (1.62 x 0.82)

Table B.1: Characteristics of the microwave generators with a rectangular output.

MW power and attenuation

In general, MW power (in mW) at the output of the waveguide can be calculated by taking into account the losses of attenuation and waveguide for each frequency. For our four generators, we have a different MW power for each frequency without attenuation (0 dB). Tables, provided by `Elmika` can be used to estimate the MW power (in mW) at the end (output) of the waveguide.
Within this thesis, we use for power-dependent measurements in experiments the value of the attenuation (attenuator) in decibel (dB) which we translate in a MW electric field after our calculation or fitting procedure.

Experimental setup

The cryogenic system for microwave measurement is a VTI cryostat (temperature range from 1.4 to 300 K) equipped with two different types of probes. In order to deliver microwave irradiation from the MW source down to the sample, we use a circular waveguide which is also integrated in both probes. The advantage of a waveguide is a high power handling capability and a lower loss rate in comparison with coaxial cables. An image of the experimental setup is presented in Figure B.5. Starting from the MW generator equipped with an attenuator, see Figure B.5(a), the microwaves are guided in a cylindrical waveguide with a diameter of 1 mm and a total lenght of 4.5 m down to the sample [Figure B.5(b)]. This construction provides a minimal damping of the MW power[1].
With our experimental setup we can either expose the sample to indeterminate polarization or linear polarization. In order to expose samples to linear polarization, special devices have been used in this work. Starting from the generator, microwaves pass the attenuator and are then "transformed" from the rectangular output into the circular waveguide by a special fabricated brass inset with an internal profile (from rectangular input to circular output), see Figure B.6. For all measurements which have been carried out in this thesis, an indeterminate polarization has been used, i.e. a waveguide with an open circular output [marked with an asterisk in Figure B.6(a)] if no special remark on

[1] A waveguide lenght of 4.5 m leads to an additional damping of 9 dB.

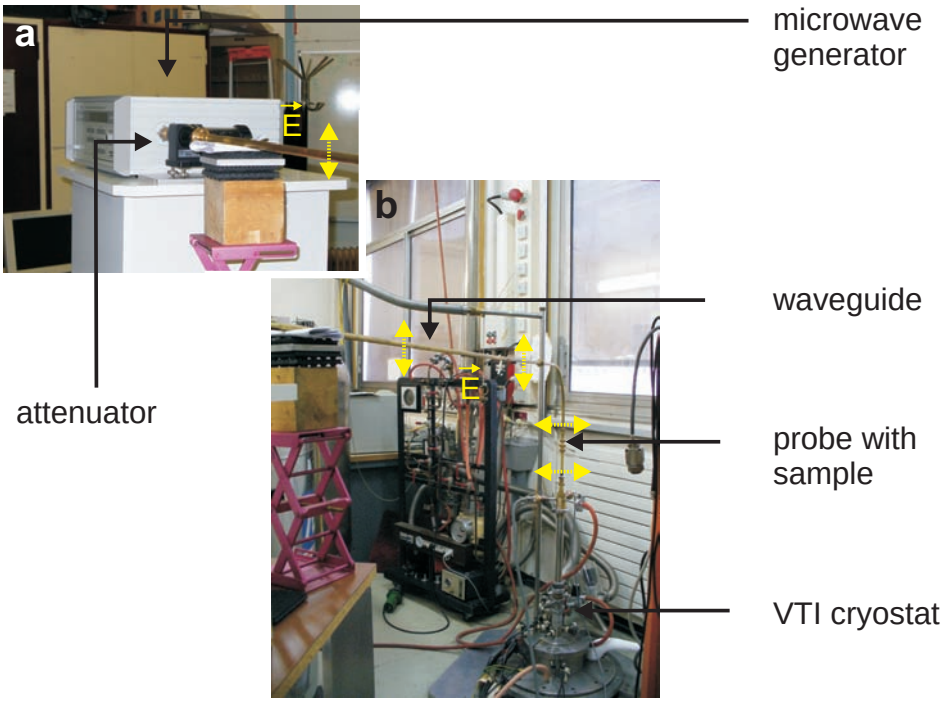

Figure B.5: Setup for MW experiments: (a) MW generator with attenuator and (b) VTI with probe and waveguide.

linear polarization is mentioned in the chapters. The possibility of linear polarization enables us to prove microwave effects which are sensitive to linear polarization. The special construction of a second brass inset which is placed at the end of the waveguide enables measurements with linear polarization, see Figure B.6(a) for generators from 55 to 170 GHz. The sample for all measurements is placed 1-2 mm away from the end of the waveguide (Faraday configuration).

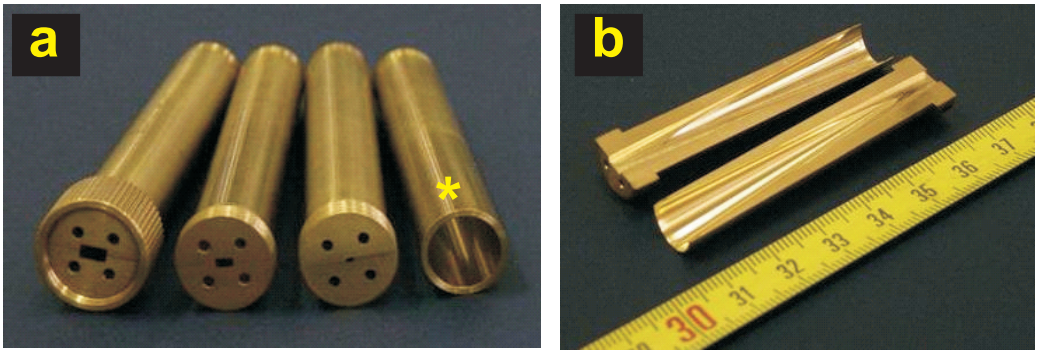

Figure B.6: (a) Brass inset for the microwave waveguide: By adding such an inset at the end of the waveguide, the microwaves penetrating the sample are linear polarized. (b) Internal profile of such a brass inset.

For measurements with linear polarization, the orientation of the linear polarized MWs is kept constant. As a consequence and to obtain different orientations of linear polarization, the orientation of the sample holder (with the sample) is changed from $\Theta = 0°$ to $\Theta = 90°$ (special probe). It should be noticed that due to the rectangular output of the waveguide for measurements with linear polarization, the MW flux on the surface of the sample is different for different orientations. Thus, a constant MW electric field is controlled by a constant damping of Shubnikov-de Haas (SdH) oscillations. In Figure B.5 the wavevector for linear polarization is sketched starting from the generator to the cryostat. The wavevector $\vec{E}$ is orientated either parallel or perpendicular to the direction of the current for samples in Hall-bar geometry, see Figure 1.2, and for van der Pauw geometry (Figure A.2).

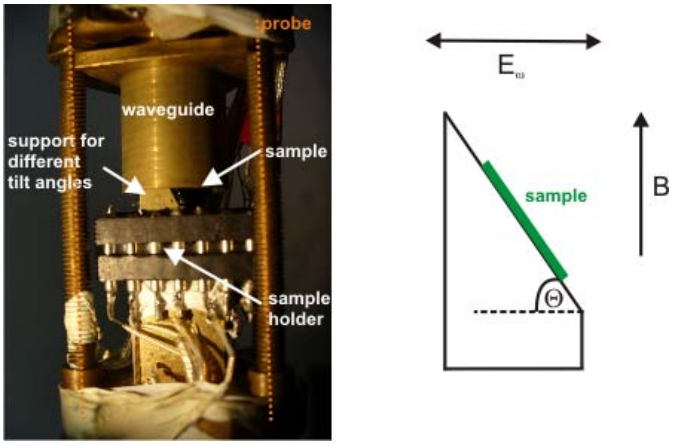

Figure B.7: MW measurements in tilted magnetic fields.

In Chapter 4 studies in tilted magnetic fields and exposed to a continuous microwave irradiation have been discussed. An image of this configuration is shown in Figure B.7. The dotted lines mark the probe. The sample is placed on a special support for measurements in tilted magnetic fields (here $\Theta = 60°$). The sample itself is fixed only by wires on the sample holder. Due to different types of sample holders with different (fixed) tilt angles, we are able to measure from perpendicular magnetic field (Faraday configuration) to almost $\Theta = 80°$. It has been shown in Chapter 4 that the influence of MWs at higher tilt angles is decreased owing to a reduced microwave "flux".

Extraction of the microwave electric field strength

To extract the MW electric field E_ω is one fundamental issue of photoresistance measurements in 2D systems. A well-known method to estimate the MW electric field is to compare the measurement of magnetoresistance of samples under MW excitation with measurements where only a strong dc field (dc current) is applied. This idea is widely discussed in literature and have been applied to measurements in single-layer systems [Wiedmann09a]. We have also compared this method with the fitting procedure for mul-

tilayer systems and have obtained a reasonable agreement. Heating of the electrons due to either MW electric fields or high dc current, leads to damping of SdH oscillations. If $\omega\tau \ll 1$, it can be assumed that the absorption of MW power P_ω and dc current "power" P_{dc} is the same at B=0 (Joule heating). Thus for $\omega_c\tau > 1$ where SdH oscillations can be observed, one can equalize $P_\omega(B)$ with $P_{dc}(B)$ and calculate the microwave electric field E_ω using

$$P_\omega = \frac{1}{2}\sigma_0 E_\omega^2 \tag{B.1}$$

with $\sigma_0 = R_0^{-1}(L/W)$ the lattice resistivity. The striking point is the assumption that both MW and dc fields are equivalent.

Notice, that in experiments we do not know the exact value of the MW electric field when we perform measurements. Therefore, we have to carry out power-dependent measurements (different MW attenuations) to ensure first that we are not in the saturated regime. If we compare magnetotransport curves exposed to different MW frequencies, we have to ensure a constant MW electric field for all frequencies. This is provided by a constant amplitude of SdH oscillations.

Limits of our theoretical model for multilayer electron systems

We have shown in this thesis, that we are able to extract the microwave electric field E_ω *in-situ* from our measurements by fitting experimental traces to theory in multilayer electron systems. An example is presented in Figure B.8 for a bilayer electron system at 85 GHz and for different attenuations. This model is valid for intermediate or low MW power, i.e. MIS oscillations of the corresponding multilayer electron systems are not yet in a saturated regime (are not damped after enhancement or vice versa). In our example, see Figure B.8(b), we can apply this procedure for attenuations $\leq$-5 dB, for higher MW power, shadded area in Figure B.8(b), MIS oscillations are already saturated.

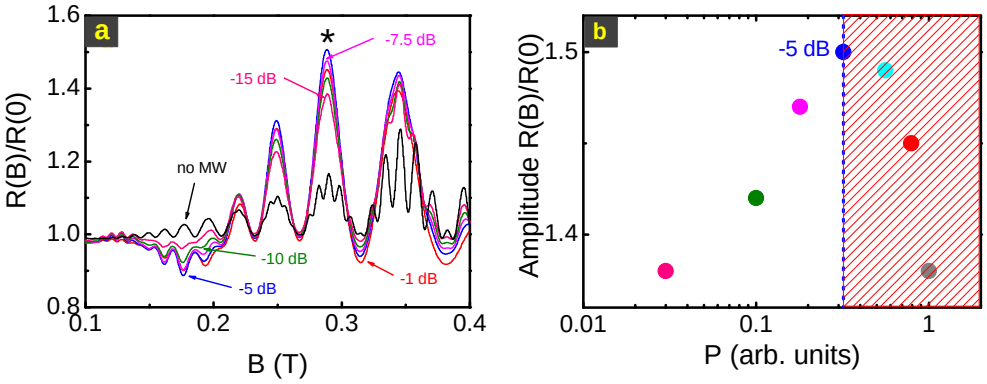

Figure B.8: Example for the extraction of the MW electric field for a bilayer electron system.

Bibliography

[Andreev03] A. V. Andreev, I. L. Aleiner, and A. J. Millis,
Phys. Rev. Lett. **91**, 056803, (2003).

[Andreev08] I. V. Andreev, V. M. Murav'ev, I. V. Kukushkin, J. H. Smet, K. von Klitzing, and V. Umansky,
JETP Letters **88**, 616, (2008).

[Beenakker91] C. W. J. Beenakker and H. van Houten,
Solid State Physics **44**, 1, (1991).

[Berk95] Y. Berk, A. Kamenev, A. Palevski, L. N. Pfeiffer, and K. W. West,
Phys. Rev. B **51**, 2604, (1995).

[Boebinger90] G. S. Boebinger, H. W. Jiang, L. N. Pfeiffer, and K. W. West,
Phys. Rev. Lett. **64**, 1793, (1990).

[Boebinger91] G. S. Boebinger, A. Passner, L. N. Pfeiffer, and K. W. West,
Phys. Rev. B **43**, 12673, (1991).

[Buettiker88] M. Buettiker,
Phys. Rev. B **38**, 9375, (1988).

[Burnell09] Fiona J. Burnell and Shivaji L. Sondhi,
Physics **2**, 49, (2009).

[Bykov06] A. A. Bykov, A. K. Bakarov, D. R. Islamov, and A. I. Toropov,
JETP Letters **84**, 391-394, (2006).

[Bykov09] A.A. Bykov,
JETP Letters **89**, 575, (2009).

[Casimir45] H. B. G. Casimir,
Rev. Mod. Phys. **17**, 343, (1945).

[Chakraborty87] T. Chakraborty and P. Pietilainen,
Phys. Rev. Lett. **59**, 2784, (1987).

[Chepelianskii09] A. D. Chepelianskii and D. L. Shepelyansky,
Phys. Rev. B **80**, 241308(R), (2009).

[Chiu76] K. W. Chiu, T. K. Lee, and J. H. Quinn,
Surf. Sci. **58**, 182, (1976).

[Chklovskii92] D. B. Chklovskii, B. I. Shklovskii, and L. I. Glazman,
Phys. Rev. B **46**, 4026, (1992).

[Coleridge89] P. T. Coleridge, R. Stone, and R. Fletcher,
Phys. Rev. B **39**, 1120, (1989).

[Cote02] R. Cote, H. A. Fertig, J. Bourassa, and D. Bouchiha,
Phys. Rev. B **66**, 205315, (2002).

[Demler02] E. Demler, D.-W. Wang, S. Das Sarma, and B. I. Halperin,
Sol. St. Commun. **123**, 243, (2002).

[Dmitriev05] I. A. Dmitriev, M. G. Vavilov, I. L. Aleiner, A. D. Merlin, and D. G. Polyakov,
Phys. Rev. B **71**, 115316, (2005).

[Dmitriev07a] I. A. Dmitriev, A. D. Merlin, and D. G. Polyakov,
Phys. Rev. B **75**, 245320, (2007).

[Dmitriev07b] I. A. Dmitriev, A. D. Merlin, and D. G. Polyakov,
Phys. Rev. Lett. **99**, 206805, (2007).

[Dmitriev09] I. A. Dmitriev, M. Khodas, A. D. Merlin, D. G. Polyakov, and M. G. Vavilov,
Phys. Rev. B **80**, 165327, (2009).

[Dorozhkin03] S. I. Dorozhkin,
JETP Letters **77**, 577, (2003).

[Dorozhkin05] S. I. Dorozhkin, J. H. Smet, V. Umansky, and K. von Klitzing,
Phys. Rev. B **71**, 201306(R), (2005).

[Dorozhkin07] S. I. Dorozhkin, J. H. Smet, K. von Klitzing, L. N. Pfeiffer, and K. W. West,
JETP Letters **86**, 543, (2007).

[Drude00] P. Drude,
Annalen der Physik **1**, 369, (1900).

[Du95] R. R. Du, A. S. Yeh, H. L. Stormer, D. C. Tsui, L. N. Pfeiffer, and K. W. West,
Phys. Rev. Lett. **75**, 3926, (1995).

[Durst03] A. C. Durst, S. Sachdev, N. Read, and S. M. Girvin,
Phys. Rev. Lett. **91**, 086803, (2003).

[Durst04] Adam C. Durst and Steven M. Girvin,
Science Volume **304**, 1752, (2003).

[Eisenstein90] J. P. Eisenstein and H. L. Störmer,
Science **248**, 1510, (1990).

[Eisenstein92a] J. P. Eisenstein, G. S. Boebinger, L. N. Pfeiffer, K. W. West, and S. He,
Phys. Rev. Lett. **68**, 1383, (1992).

[Eisenstein92b] J. P. Eisenstein,
Microstruct. **12**, 107, (1992).

[Eisenstein95] J. P. Eisenstein,
Brazilian Journal of Physics **26**, 1, (1995).

[Eisenstein02] J. P. Eisenstein, K. B. Cooper, L. N. Pfeiffer, and K. W. West,
Phys. Rev. Lett. **88**, 076801, (2002).

[Enss and Hunklinger] C. Enss and S. Hunklinger,
Low-TemperaturePhysics, ISBN-10 3-540-23164-1 Springer Berlin Heidelberg New York, ISBN-13 978-3-540-23164-6 Springer Berlin Heidelberg New York, (2005).

[Fedorych09] O. M. Fedorych, S. Moreau, M. Potemski, S. A. Studenikin, T. Saku, and Y. Hirayama,
Intern. Journ. Mod. Phys. **23**, 2698, (2009).

[Finkler09] I. G. Finkler and I. B. Halperin,
Phys. Rev. B **79**, 056803, (2009).

[Fletcher00] R. Fletcher, Y. Feng, C. T. Foxon, and J. J. Harris,
Phys. Rev. B **61**, 2028, (2000).

[Friedland96] K.-J. Friedland, R. Hey, H. Kostial, R. Klann, and K. Ploog,
Phys. Rev. Lett. **77**, 4616, (1996).

[Fukuda08] A. Fukuda, D. Terasawa, M. Morino, K. Iwata, S. Kozumi, N. Kumada, Y. Hirayama, Z. F. Ezawa, and A. Sawada,
Phys. Rev. Lett. **100**, 016801, (2008).

[Giudici08] P. Giudici, K. Muraki, N. Kumada, Y. Hirayama, and T. Fujisawa,
Phys. Rev. Lett. **100**, 106803, (2008).

[Giuliani82] G. F. Giuliani and J. J. Quinn,
Phys. Rev. B **26**, 4421, (1982).

[Gramila91] T. J. Gramila, J. P. Eisenstein, A. H. MacDonald, L. N. Pfeiffer, and K. W. West,
Phys. Rev. Lett. **66**, 1216, (1991).

[Greiter91] M. Greiter, X.-G. Wen, and F. Wilczek,
Phys. Rev. Lett. **66**, 3205, (1991).

[Goran09] A. V. Goran, A. A. Bykov, A. I. Toropov, and S. A. Vitkalov,
Phys. Rev. B **80**, 193305, (2009).

[Gurevich61] V. L. Gurevich and Yu. A. Firsov,
Sov. Phys. JETP **13**, 137, (1961).

[Gusev07] G. M. Gusev, A. K. Bakarov, T. E. Lamas, and J. C. Portal,
Phys. Rev. Lett. **99**, 126804, (2007).

[Gusev08] G. M. Gusev, C. A. Duarte, T. E. Lamas, A. K. Bakarov, and J. C. Portal,
Phys. Rev. B **78**, 155320, (2008).

[Gusev09] G. M. Gusev, S. Wiedmann, O. E. Raichev, A. K. Bakarov, and J. C. Portal,
Phys. Rev. B **80**, 161302(R), (2009).

[Halperin83] B.I. Halperin,
Helv. Phys. Acta **56**, 75, (1983).

[Halperin93] B. I. Halperin, P. A. Lee, and N. Read,
Phys. Rev. B **47**, 7312, (1993).

[Hanna96] C. B. Hanna and A. H. MacDonald,
Phys. Rev. B **53**, 15981, (1996).

[Hanna02] C. B.Hanna, J. C. Dias-Velez, and A. H. MacDonald,
Phys. Rev. B **65**, 115323, (2002).

[Hatke08] A. T. Hatke, H.-S. Chiang, M. A. Zudov, L. N. Pfeiffer, and K. W. West,
Phys. Rev. B **77**, 201304(R), (2008).

[Hatke09a] A. T. Hatke, M. A. Zudov, L. N. Pfeiffer, and K. W. West,
Phys. Rev. Lett. **102**, 066804, (2009).

[Hatke09b] A. T. Hatke, M. A. Zudov, L. N. Pfeiffer, and K. W. West,
Phys. Rev. Lett. **102**, 086808, (2009).

[Haug93] R. J. Haug,
Semicond. Sci. Technol. **8**, 131, (1993).

[Holtz90] M. Holtz, R. Cingolani, K. Reimann, R. Muralidharan, K. Syassen, and K. Ploog,
Phys. Rev. B **41**, 3641, (1990).

[Hu92] J. Hu and A. H. MacDonald,
Phys. Rev. B **46**, 12554, (1992).

[Iñarrea05] J. Iñarrea and G. Platero,
Phys. Rev. Lett. **94**, 016806, (2005).

[Jain89] J. K. Jain,
Phys. Rev. Lett. **63**, 199, (1989).

[Jain90] J. K. Jain,
Phys. Rev. B **41**, 7653, (1990).

[Jo92] J. Jo, Y. W. Suen, L. W. Engel, M. B. Santos, and M. Shayegan,
Phys. Rev. B **46**, 9776, (1992).

[Khodas08] M. Khodas and M. G. Vavilov,
Phys. Rev. B **78**, 245319, (2008).

[Laughlin83] R. B. Laughlin,
Phy. Rev. Lett. **50**, 1395, (1983).

[Lei06] X. L. Lei and S. Y. Liu,
Appl. Phys. Lett. **88**, 212109, (2006).

[Lei08] X. L. Lei and S. Y. Liu,
Appl. Phys. Lett. **93**, 082101, (2008).

[Levin09] M. Levin and M. P. A. Fisher,
Phys. Rev. B **79**, 235315, (2009).

[Lifshits56] I. M. Lifshits and A. Kosevich,
Zh. Eksp. Teor. Fiz 29, 730 (1955); Sov. Phys. JETP **2**, 636, (1956).

[Ma91] Y. Ma, R. Fletcher, E. Zaremba, M. D'Iorio, C. T. Foxon, and J. J. Harris,
Phys. Rev. B **43**, 9033, (1991).

[MacDonald90] A. H. MacDonald,
Surf. Sci **229**, 1, (1990).

[Mamani08] N. C. Mamani, G. M. Gusev, T. E. Lamas, A. K. Bakarov, and O. E. Raichev,
Phys. Rev. B **77**, 205327, (2008).

[Mamani09a] N. C. Mamani, G. M. Gusev, E. C. F. da Silva, O. E. Raichev, A. A. Quivy, and A. K. Bakarov,
Phys. Rev. B **80**, 085304, (2009).

[Mamani09b] N. C. Mamani, G. M. Gusev, O. E. Raichev, T. E. Lamas, and A. K. Bakarov,
Phys. Rev. B **80**, 098762, (2009).

[Mani02] R. G. Mani, J. H. Smet, K. von Klitzing, V. Narayanamurti, W. B. Johnson, and V. Umansky,
Nature **420**, 646, (2002).

[Mani04a] R. G. Mani, V. Narayanamurti, K. von Klitzing, J. H. Smet, W. B. Johnson, and V. Umansky,
Phys. Rev. B **69**, 161306(R), (2004).

[Mani04b] R. G. Mani, J. H. Smet, K. von Klitzing, V. Narayanamurti, W. B. Johnson, and V. Umansky,
Phys. Rev. Lett. **92**, 146801, (2004).

[Mani05] R. G. Mani,
Phys. Rev. B **72**, 075327, (2005).

[Mani08] R. G. Mani,
Appl. Phys. Lett. **92**, 102107, (2008).

[Mikhailov04] S. A. Mikhailov,
Phys. Rev. B **70**, 165311, (2004).

[Mikhailov06] S. A. Mikhailov and N. A. Savostianova,
Phys. Rev. B **74**, 045325, (2006).

[Moore91] G. Moore, and N. Read,
Nucl. Phys. B **360**, 362, (1991).

[Murphy93] S. Q. Murphy, J. P. Eisenstein, G. S. Boebinger, L. N. Pfeiffer, and K. W. West,
Phys. Rev. Lett. **72**, 728, (1994).

[Onsager31] L. Onsager,
Phys. Rev. **38**, 2265, (1931).

[Pechenezhskii07] I. V. Pechenezhskii, S. I. Dorozhkin and I. A. Dmitriev,
JETP Letters **85**, 86, (2007).

[Polyanovsky88] V. Polyanovsky,
Poluprovodn. **22**, 2230, (1988).

[Pozar98] David M. Pozar,
Microwave Engineering, John Wiley and Sons, (1998).

[QH-effects97] Perspectives in quantum Hall effects, edited by S. Das Sarma and A. Pinzuk,
John Wiley and Sons, New York, (1997).

[Qiu89] X. Qiu, R. Joynt, and A. H. MacDonald,
Phys. Rev. B **40**, 11943, (1989).

[Qiu90] X. Qiu, R. Joynt, and A. H. MacDonald,
Phys. Rev. B **42**, 1339, (1990).

[Raichev08] O. E. Raichev,
Phys. Rev. B **78**, 125304, (2008).

[Raichev09] O. E. Raichev,
private communications, -, (2009).

[Raikh94] M. E. Raikh and T. V. Shahbazyan,
Phys. Rev. B **49**, 5531 - 5540, (1994).

[Rezayi87] E. H. Rezayi and F. D. M. Haldane,
Bull. Am. Phys. Soc. **32**, 892, (1987).

[Ryzhii70] V. I. Ryzhii,
Fiz. Tverd. Tela (Leningrad) 11, 2577 (1969); Sov. Phys. Solid State **11**, 2078, (1970).

[Ryzhii86] V. I. Ryzhii, R. A. Suris, and B. S. Shchamkhalova,
Fiz. Tekh. Poluprovodn. 20, 2078 (1986); Sov. Phys. Semicond. **20**, 1299, (1986).

[Sander98] T. H. Sander, S. N. Holmes, J. J. Harris, D. K. Maude, and J. C. Portal,
Phys. Rev. B **58**, 13856, (1998).

[SdH30] L. Shubnikov and W. J. de Haas,
Leiden Commun. **207**, 3, (1930).

[Sedrakyan08] T. A. Sedrakyan and M. E. Raikh,
Phys. Rev. Lett. **100**, 086808, (2008).

[Shevchenko04] S. I. Shevchenko, D. V. Fil, and A. A. Yakovleva,
Low Temp.Phys. **30**, 321, (2004).

[Shukla98] S. P. Shukla, Y. W. Suen, and M. Shayegan,
Phys. Rev. Lett. **81**, 693, (1998).

[Smet05] J. H. Smet, B. Gorshunov, C. Jiang, L. Pfeiffer, K. West, V. Umansky, M. Dressel, R. Meisels, F. Kuchar, and K. von Klitzing,
Phys. Rev. Lett. **95**, 116804, (2005).

[Stoermer92] H. L. Störmer,
Physica B **177**, 401, (1992).

[Studenikin04] S. A. Studenikin, M. Potemski, P. T. Coleridge, A. S. Sachrajda, Z. R. Wasilewski,
Solid State Comm. **129**, 341-345, (2004).

[Studenikin05] S. A. Studenikin, M. Potemski, A. Sachrajda, M. Hilke, L. N. Pfeiffer, and K. W. West,
Phys. Rev. B **71**, 245313, (2005).

[Studenikin07] S. A. Studenikin, A. S. Sachrajda, J. A. Gupta, and Z. R. Wasilewski, O. M. Fedorych, M. Byszewski, D. K. Maude, M. Potemski, M. Hilke, K. W. West, and L. N. Pfeiffer,
Phys. Rev. B **76**, 165321, (2007).

[Suen92] Y. W. Suen, L. W. Engel, M. B. Santos, M. Shayegan, and D. C. Tsui,
Phys. Rev. Lett. **68**, 1379, (1992).

[Tsui80] D. C. Tsui, Th. Englert, A. Y. Cho, and A. C. Gossard,
Phys. Rev. Lett. **44**, 341, (1980).

[Tsui82] D. C. Tsui, H. Stormer, and A. C. Gossard,
Phys. Rev. Lett. **48**, 1559, (1983).

[Vasiliadou93] E. Vasiliadou, G. Muller, D. Heitmann, D. Weiss, K. von Klitzing, H. Nickel, W. Schlapp, and R. Losch,
Phys. Rev. B **48**, 17145, (1993).

[Vavilov04a] M. G. Vavilov and I. L. Aleiner,
Phys. Rev. B **69**, 035303, (2004).

[Vavilov04b] M. G. Vavilov, I. A. Dmitriev, I. L. Aleiner, A. D. Mirlin, and D. G. Polyakov,
Phys. Rev. B **70**, 161306(R), (2004).

[vonKlitzing80] K. v. Klitzing, G. Dorda, and M. Pepper,
Phys. Rev. Lett. **45**, 494, (1980).

[vonKlitzing04] K. von Klitzing,
Séminaire Poincaré **2**, 1-16, (2004).

[Wang03] D.-W. Wang, E. Demler, and S. Das Sarma,
Phys. Rev. B **68**, 165303, (2003).

[Wiedmann08] S. Wiedmann, G. M. Gusev, O. E. Raichev, T. E. Lamas, A. K. Bakarov, and J. C. Portal,
Phys. Rev. B **78**, 121301(R), (2008).

[Wiedmann09a] S. Wiedmann, G. M. Gusev, O. E. Raichev, A. K. Bakarov, and J. C. Portal,
Phys. Rev. B **80**, 035317, (2009).

[Wiedmann09b] S. Wiedmann, N. C. Mamani, G. M. Gusev, O. E. Raichev, A. K. Bakarov, and J. C. Portal,
Phys. Rev. B **80**, 245306, (2009).

[Wiedmann10a] S. Wiedmann, G. M. Gusev, O. E. Raichev, A. K. Bakarov, and J. C. Portal,
Phys. Rev. B **81**, 085311, (2010).

[Wiedmann10b] S. Wiedmann, G. M. Gusev, O. E. Raichev, A. K. Bakarov, and J. C. Portal,
Phys. Rev. Lett. **105**, 026804, (2010).

[Wiedmann10c] S. Wiedmann, G. M. Gusev, O. E. Raichev, A. K. Bakarov, and J. C. Portal,
submitted to Phys. Rev. B, -, (2010).

[Willett87] R. L. Willett, J. P. Eisenstein, H. L. Stormer, D. C. Tsui, A. C. Gossard, and J. H. English,
Phys. Rev. Lett. **59**, 1776, (1987).

[Willett04] R. L. Willett, L. N. Pfeiffer, and K. W. West,
Phys. Rev. Lett. **93**, 026804, (2004).

[Yakovenko06] V. M. Yakovenko and B. K. Cooper,
Physica E **34**, 128, (2006).

[Yang94] Kun Yang, K. Moon, L. Zheng, A. H. MacDonald, S. M. Girvin, D. Yoshioka, and Shou-Cheng Zhang,
Phys. Rev. Lett. **72**, 732, (1994).

[Yang96] Kun Yang, K. Moon, Lotfi Belkhir, H. Mori, S. M. Girvin, A. H. MacDonald, L. Zheng, and D. Yoshioka,
Phys. Rev. B **54**, 11644, (1996).

[Yang06] C. L. Yang, R. R. Du, L. N. Pfeiffer, and K. W. West,
Phys. Rev. B **74**, 045315, (2006).

[Yoshioka89] D. Yoshioka, A. H. MacDonald, and S. M. Girvin,
Phys. Rev. B **39**, 1932, (1989).

[Zudov01a] M. A. Zudov, R. R. Du, J. A. Simmons, and J. R. Reno,
Phys. Rev. B **64**, 201311(R), (2001).

[Zudov01b] M. A. Zudov, I. V. Ponomarev, A. L. Efros, and R. R. Du, J. A. Simmons, and J. L. Reno,
Phys. Rev. Lett. **86**, 3614, (2001).

[Zudov03] M. A. Zudov, R. R. Du, L. N. Pfeiffer, and K. W. West,
Phys. Rev. Lett. **90**, 046807, (2003).

[Zudov04] M. A. Zudov,
Phys. Rev. B **69**, 041304(R), (2004).

[Zudov06] M. A. Zudov, R. R. Du, L. N. Pfeiffer, and K. W. West,
Phys. Rev. B **73**, 041303(R), (2006).

List of publications

Publications in international journals

2010

- S. Wiedmann, G. M. Gusev, O. E. Raichev, A. K. Bakarov, and J. C. Portal, "Zero-resistance states in bilayer electron systems", Phys. Rev. Lett. **105**, 026804, 2010

- S. Wiedmann, G. M. Gusev, O. E. Raichev, A. K. Bakarov, and J. C. Portal, "Crossover between distinct mechanisms of microwave photoresistance in bilayer electron systems", Phys. Rev. B **81**, 085311, 2010
  also recited in the Virtual Journal of Nanoscale Science & Technology, Volume 21, Issue 8, February 22, 2010

2009

- S. Wiedmann, N. C. Mamani, G. M. Gusev, O. E. Raichev, A. K. Bakarov, and J. C. Portal, "Magnetoresistance oscillations in multilayer electron systems - triple quantum wells", Phys. Rev. B **80**, 245306, 2009

- G. M. Gusev, S. Wiedmann, O. E. Raichev, A. K. Bakarov, and J. C. Portal, "Emergent and reentrant fractional quantum Hall effect in trilayer systems in a tilted magnetic field", Phys. Rev. B **80**, 161302(R), 2009

- S. Wiedmann, G. M. Gusev, O. E. Raichev, A. K. Bakarov and J. C. Portal, "High order fractional microwave-induced resistance oscillations in two-dimensional systems", Phys. Rev. B **80**, 035317, 2009
  also recited in the Virtual Journal of Nanoscale Science & Technology, Volume 20, Issue 5, August 3, 2009

2008

- S. Wiedmann, G. M. Gusev, O. E. Raichev, T. E. Lamas, A. K. Bakarov, and J. C. Portal,
  "Interference oscillations of microwave photoresistance in double quantum wells",
  Phys. Rev. B **78** , 121301(R), 2008

Conference Proceedings

2010

- S. Wiedmann, G. M. Gusev, O. E. Raichev, A. K. Bakarov, and J. C. Portal,
  "Microwave induced magnetoresistance oscillations and inelastic scattering time in double quantum wells",
  Physica E **42** , 1075-1077, 2010
- S. Wiedmann, N. C. Mamani, G. M. Gusev, O. E. Raichev, A. K. Bakarov, and J. C. Portal,
  "Magneto-intersubband oscillations in triple quantum wells",
  Physica E **42** , 1088-1090, 2010
- S. Wiedmann, G. M. Gusev, O. E. Raichev, A. K. Bakarov, and J. C. Portal,
  "Integer and fractional microwave induced resistance oscillations in a 2D system with moderate mobility",
  Physica E **42** , 1078-1080, 2010
- S. Wiedmann, G. M. Gusev, O. E. Raichev, A. K. Bakarov, and J. C. Portal,
  "Microwave induced magnetoresistance oscillations and inelastic scattering time in double quantum wells",
  accepted in Physica E 2010

2008

- S. Wiedmann, G. M. Gusev, O. E. Raichev, T. E. Lamas, A. K. Bakarov, and J. C. Portal,
  "Magnetoresistance oscillations in double quantum wells under microwave irradiations",
  Int. Journal of Mod. Phys. **B** , 2943, 2008

Further parts of this thesis are considered for publication.

Participations and presentation in international conferences, workshops and schools

2nd EuroMagNET Summer School, Science in High Magnetic Fields (5-11 Sept. 2010, Ameland, the Netherlands)

- "Fractional quantum Hall effect in trilayer electron systems in a tilted magnetic field" *(contributed oral presentation)*

19th International Conference on the Application of High Magnetic Fields in Semiconductor Physics and Nanotechnology (HMF-19) (Fukuoka, Japan, 2010)

- "Zero-resistance states in bilayer electron systems induced by microwave irradiation" *(contributed oral presentation)*
- "Emergent fractional quantum Hall effect at even denominator 3/2 in the triple quantum well in the tilted magnetic field" *(contributed poster presentation)*
- "Charge transfer in trilayer electron systems in a strong magnetic field" *(contributed poster presentation)*
- "A new kind of magnetoresistance oscillations in wide quantum well bilayers" *(contributed poster presentation)*

30th International Conference on the Physics of Semiconductors (ICPS 2010)

- "Microwave-induced zero-resistance states in bilayer electron systems" *(contributed oral presentation)*
- "Interlayer Aharonov-Bohm interference in tilted magnetic fields in a wide quantum well" *(contributed poster presentation)*

International Conference on Electronic Properties of Two-Dimensional Systems (EP2DS 18) and International Conference on Modulated Semiconductor Structures (MSS 14) (Kobe, Japan, 2009)

- "Integer and fractional microwave induced resistance oscillations in a 2D system with moderate mobility" *(contributed poster presentation)*
- "Magneto-intersubband oscillations in triple quantum wells" *(contributed poster presentation)*
- "Magnetoresistance oscillations in triple quantum wells under microwave irradiation" *(contributed poster presentation)*
- "Microwave induced magnetoresistance oscillations and inelastic scattering time in double quantum wells" *(contributed poster presentation)*

- "Fractional quantum Hall effect in trilayer systems in a tilted magnetic field" *(contributed poster presentation)*

International Workshop on Semiconductor and Carbon Based Nanostructures on Magnetic Fields (LCMI Grenoble, France, 2008)

- "Magnetoresistance oscillations in double quantum wells under microwave irradiation" *(oral presentation)*

18th International Conference on high magnetic fields in semiconductor physics and technology (São Pedro, Brazil, 2008)

- "Magnetoresistance oscillations in double quantum wells exposed to microwave irradiation" *(contributed oral and poster presentation)*

Acknowledgement

First of all, I thank Michel Dyakonov and André Raymond, the two "rapporteurs" of my PhD thesis for their evaluation and comments. I also thank the president of my jury, Guy Le Lay, and the "examinateurs" Georges Bremond and Rodolfo Jalabert.
This work has been carried out at the Laboratoire National des Champs Magnétiques Intenses (LNCMI) in Grenoble. I thank our Director Geert Rikken, his predecessor Jean-Louis Tholence and Vice-Director Claude Berthier for their constant support and their help which was one key element for the success of this work.

During my three years, I worked in the well-equipped laboratory of Jean-Claude Portal (directeur de thèse) in the group of mesoscopic physics. His financial support enabled me to join the international conferences EP2DS/MSS 2009 in Kobe, ICPS 30 in Seoul and HMF 19 in Fukuoka 2010.

The results of scientific research, which are presented within the scope of this thesis, would not have been possible without assistance and discussions with many other people. So I wish to thank everyone, who supported me and contributed to this work.

A prerequisite for this thesis was the offer of Guennadii Gusev from Instituto de Física da Universidade de São Paulo, beginning of 2008 to start the work on microwave studies in multilayer electron systems. I wish to thank him, not only for this possibility but more important for all scientific discussions in Grenoble and São Paulo. Thanks to modern communication tools, which have been used frequently, the distance has been overcome easily. Thanks for sharing your time and your knowledge; I can say that I have benefited greatly from both. Also unforgettable were the night shifts at LNCMI which we spent together on studies of trilayer electron systems. Guena, thank you so much for all!
The present work would not have been possible without a close collaboration to Oleg Raichev, theoretical physicist at Institute of Semiconductor Physics, NAS of Ukraine, due to a continuous exchange between experimental results, theoretical models and data analysis. Thank you very much Oleg for all these exchanges and discussions during my PhD. Your input enabled me to connect all experimental results to theory and I am sure that readers will benefit from it.
In addition to an excellent equipment to perform experiments, high-quality samples are necessary. I thank Ashkat Bakarov from the Institute of Semiconductors in Novosibirsk who did an excellent job in sample growth.

During my PhD, it was a great pleasure to work, discuss and exchange knowledge with all colleagues at the LNCMI-CNRS who gave scientific and technical support. I would like

to thank especially Steffen Krämer, Vincent Renard and Arlei Borba Antunes. Danke Steffen for all scientific and technical advice, and for sharing your knowledge with me. Many thanks also for proofreading this manuscript and many interesting and useful comments. Merci Vincent, first for introducing me into our experimental systems when I arrived, all scientific discussions we had and in particular merci for all your advice. Thanks also for proofreading my documents in French. Obrigado Arlei that I got to know you. We shared so much time in the LNCMI, including scientific and technical discussions. Your death in 2010 was a shock for everybody. I will never forget the time we spent together and you will be always in my mind.
Muchas gracias to Niko Churata Mamani (IFUSP) for all the fantastic time we spent together not only by doing measurements which we have performed in low and high fields, and all discussions which resulted in a nice friendship.

I gratefully acknowledge the entire technical and administrative staff of the LNCMI, in particular Gilbert Arnaud for his help, discussions and his advice on all our cryogenics systems. Many thanks also to Robert Pankow for his technical support solving daily technical problems in the lab and the new sample holder for M9 experiments. Thanks also to Jean Florentin who built up the waveguide, brass tubes etc. for the MW measurements before I arrived in Grenoble.
Special thanks to Eric Mossang and Christiane Warth-Martin, not only for their efficient planning of magnet time, but especially for many discussions and their support. Merci beaucoup Eric for proofreading many documents I have written in French.
During my work here in LNCMI, I got many advice, tricks and had lots of discussions which were useful for measurement technique from many people here in the lab. Thanks to Benjamin Piot, Duncan Maude, Marek Potemski, Paulina Plochocka, Johannes Schneider, Clément Faugeras, Anne-Laure Barra, Luc Ronayette, Francesco Aimo and Ilya Sheikin. I also thank Rachel Graziotti, Gislaine Menéroud, Elisabeth Rochat, Amélie Pic and Cécile Vannier for all help in the administrative problems including their help with visitors. Merci also to Thomas Dolmazon and Sébastian Buisson for solving problems in informatics.

In my time as PhD student, I was local contact in the group of mesoscopic physics in our lab and for high-field experiments from 2008-2010. I was also able to exchange knowledge with our visitors Celso de Araujo Duarte (IFUSP), Evguenii Olshanetsky, Dima Kozlov (Institute of Semicondutor Physics Novosibirsk), Alain Nogaret, Pedro Saraiva, Sam Littlejohn (University of Bath), Dimity Ivanov, Alexander Federov and Vladimir Popov (Chernogolovka, Moscow). Special thanks also to Ze Don Kvon from the Institute of Semiconductor Physics in Novosibirsk.
Finally, I have to thank all unnamed people all around the world for stimulating scientific discussions during conferences, meetings or in free-time. Thank you all!

Last but not least, I acknowledge my friends and my family for their support during my entire life which was and is crucial that the present work has been successfully done.

Résumé and abstract

Résumé

Ce travail de thèse présente l'étude de l'influence du nouveau degré de liberté quantique, causé par le couplage tunnel entre les couches, sur les propriétés de transport des multi-puits quantiques dans un champ magnétique, à basse température, et sous irradiation micro-ondes. De nouvelles oscillations de résistance sont observées dans les systèmes d'électrons bi- et multicouches. Elles résultent d'une interférence entre les oscillations des sous-bandes et celles induites par les micro-ondes. Des états à résistance nulle apparaissent lorsque les systèmes bicouches de haute qualité sont exposés à une irradiation micro-ondes même en présence d'une diffusion additionnelle. Le mécanisme inélastique de la photorésistance est la contribution dominante à basse température et sous un champ électrique modéré. Ce modèle confirme l'intégrité des estimations théoriques pour le temps de relaxation inélastique et conduit à une explication satisfaisante de la photorésistance dans les systèmes d'électrons bi-et multicouches. Dans un champ magnétique intense, la suppression de l'effet tunnel entre les couches provoque de nouveaux états corrélés à cause d'une interaction électron-électron entre les différentes couches. Dans cette thèse, les systèmes électroniques tricouches, formés par de triples puits quantiques révèlent de nouveaux états de l'effet Hall Quantique fractionnaire si l'effet tunnel est supprimé par une composante parallèle du champ magnétique aux très basses températures (de l'ordre du mK).

Mots clés: systèmes d'électrons multicouches, magnétotransport, oscillations induites par micro-ondes, états à résistance nuls, effet Hall quantique entier et fractionnaire, états corrélés.

Abstract

This work is devoted to the investigation of the influence of the additional quantum degree of freedom caused by tunnel coupling on transport properties of multilayer electron systems in magnetic fields, at low temperatures and under microwave excitation. Microwave-induced resistance oscillations in bi- and multilayer electron systems are the consequence of an interference of magneto-intersubband and microwave-induced resistance oscillations which leads to peculiar oscillations in magnetoresistance. High-quality bilayer systems exposed to microwave irradiation exhibit zero-resistance states even in the presence of intersubband scattering. The inelastic mechanism of microwave photoresistance is found to be the dominant contribution at low temperatures and moderate microwave electric field. This model confirms the reliability of theoretical estimates for the inelastic relaxation time and leads to a satisfactory explanation of photoresistance in bi- and multilayer electron systems. In high magnetic fields, the suppression of tunnelling between layers causes new correlated states owing to electron-electron interaction in neighboured layers. In this thesis, trilayer electron systems formed by triple quantum wells reveal new fractional quantum Hall states if tunnelling is suppressed by a parallel component of the magnetic field at mK temperatures.

Key words: multilayer electron systems, magnetotransport, microwave-induced resistance oscillations, zero-resistance states, integer and fractional quantum Hall effect, correlated states.